Universidade de Aveiro Departamento de Física
2010

Rui Miguel Oliveira Meleiro

Dispositivos e Técnicas de Processamento Óptico para Redes Ópticas de Nova Geração

Optical Processing Devices and Techniques for Next Generation Optical Networks

Universidade de Aveiro Departamento de Física
2010

Rui Miguel Oliveira Meleiro

Dispositivos e Técnicas de Processamento Óptico para Redes Ópticas de Nova Geração

Optical Processing Devices and Techniques for Next Generation Optical Networks

dissertação apresentada à Universidade de Aveiro para cumprimento dos requisitos necessários à obtenção do grau de Doutor em Física, realizada sob a orientação científica do Doutor Paulo Sérgio de Brito André, Professor Auxiliar do Departamento de Física da Universidade de Aveiro e Investigador Auxiliar do Instituto de Telecomunicações e do Doutor Jorge Costa de Sousa Castro, Investigador Sénior da Unidade de Telecomunicações e Multimédia do Instituto de Engenharia de Sistemas e Computadores do Porto.

Apoio financeiro da Nokia Siemens Networks Portugal S.A.

Nokia Siemens Networks

Apoio financeiro da Fundação para a Ciência e Tecnologia através da bolsa SFRH/BDE/15565/2005.

FCT Fundação para a Ciência e a Tecnologia
MINISTÉRIO DA CIÊNCIA, TECNOLOGIA E ENSINO SUPERIOR

Para ser grande, sê inteiro: nada
Teu exagera ou exclui.

Sê todo em cada coisa. Põe quanto és
No mínimo que fazes.

Assim em cada lago a lua toda
Brilha, porque alta vive.

Ricardo Reis, in Odes

Dedico este trabalho à minha mãe; ao meu pai; à minha irmã.

o júri

presidente

Doutor Jorge Ribeiro Frade
Professor Catedrático da Universidade de Aveiro

Doutor João de Lemos Pinto
Professor Catedrático da Universidade de Aveiro

Doutor Henrique Manuel de Castro Faria Salgado
Professor Associado da Faculdade de Engenharia da Universidade do Porto

Doutor Adolfo da Visitação Tregeira Cartaxo
Professor Associado do Instituto Superior Técnico da Universidade Técnica de Lisboa

Doutor Paulo Miguel Nepomuceno Pereira Monteiro
Professor Associado da Universidade de Aveiro e Investigador Coordenador da Nokia Siemens Networks Portugal, S.A.

Doutor José Maria Longras Figueiredo
Professor Auxiliar da Faculdade de Ciência e Tecnologia da Universidade do Algarve

Doutor Paulo Sérgio de Brito André
Professor Auxiliar Convidado da Universidade de Aveiro e Investigador Auxiliar do Instituto de Telecomunicações

Doutor Jorge Costa de Sousa Castro
Investigador Sénior do Instituto de Engenharia de Sistemas e Computadores do Porto

agradecimentos

Porque devo agradecer a outras pessoas a finalização deste trabalho? Porque acredito que devemos agradecer a quem nos ajuda e nos faz feliz. Por isso, aqui estão os meus agradecimentos. Mais pessoas do que as que aqui enumero merecem um agradecimento. A essas, agradecerei pessoalmente.
Queria agradecer ao meu orientador, o Doutor Paulo André, pelo pragmatismo e por me ajudar a manter focado ao longo deste trabalho. Queria agradecer também ao meu co-orientador, o Doutor Jorge Castro, por me ter indicado os caminhos e referências que eu decidi seguir ou não, pelo espírito sempre crítico e construtivo, e pelo apoio incansável. Por vezes fui um aluno de doutoramento difícil, mas espero que, após as contas feitas, tenhamos todos ganho. Outra pessoa que também contribuiu forte e positivamente para o curso deste trabalho foi o Alvaro Buxens, que merece um sentido obrigado.
Agradeço também ao Doutor Paulo Monteiro por ter reunido uma equipa de pessoas excelentes com quem tive o privilégio de trabalhar na Nokia Siemens Networks. Quero agradecer particularmente a algumas pessoas dessa equipa, que se tornaram meus grandes amigos após cinco anos de interdependência. Começo pelos meus colegas de mesa. Ao João Pedro, que esteve sempre calmo ao meu lado. Ao Tiago Silveira, com quem não tive o prazer de fazer trabalho conjunto, mas a quem tive a oportunidade de admirar o génio tumultuoso. À Sílvia Pato, com quem tive o prazer de fazer frutuoso trabalho conjunto e que me custou abandonar. Ao Rui Morais, ao seu génio inventivo, às horas passadas em conjunto no laboratório e às mil e uma ideias que um dia vão acontecer. Aos Doutores Daniel Fonseca e Ruben Luís, que foram meus mentores, nunca hesitaram em me dizerem o que precisava de ouvir sempre que necessário, e que foram exemplos de tenacidade para mim. À Lara Pellegrino, minha companheira de viagem de doutoramento na UA. Ao José Pina, meu camarada e conselheiro do Matlab. Ao João Gomes, também meu companheiro de viagem, se bem que por outros caminhos. Ao Pedro Inácio, o matemático de serviço, que ainda não venceu a probabilidade, mas está quase. À Ana Ferreira por ser tão companheira. Aos novatos do grupo João Santos e Filipe Ferreira a quem desejo o maior sucesso na aventura que é o doutoramento.
Aos meus amigos de Viseu por me trazerem à realidade de vez em quando. Agradeço muito especialmente à Catarina, uma motivadora nata.
Agradeço à minha família, tios, avós, por me sorrirem sempre, em particular à Inês e ao Diogo, apesar de ser o 'primo ausente'.
Agradeço também aos meus pais e irmã...

palavras-chave

Interferómetro Mach-Zehnder baseado em amplificadores ópticos de semicondutor (MZI-SOA), conversão de comprimento de onda, conversão de formato, processamento óptico, compressão e descompressão de pacotes, comutação temporal, diafonia com sinais distorcidos.

resumo

Este trabalho surge do interesse em substituir os nós de rede óptica baseados maioritariamente em electrónica por nós de rede baseados em tecnologia óptica. Espera-se que a tecnologia óptica permita maiores débitos binários na rede, maior transparência e maior eficiência através de novos paradigmas de comutação. Segundo esta visão, utilizou-se o MZI-SOA, um dispositivo semicondutor integrado hibridamente, para realizar funcionalidades de processamento óptico de sinal necessárias em nós de redes ópticas de nova geração.

Nas novas redes ópticas são utilizados formatos de modulação avançados, com gestão da fase, pelo que foi estudado experimentalmente e por simulação o impacto da utilização destes formatos no desempenho do MZI-SOA na conversão de comprimento de onda e formato, em várias condições de operação. Foram derivadas regras de utilização para funcionamento óptimo. Foi também estudado o impacto da forma dos pulsos do sinal no desempenho do dispositivo.

De seguida, o MZI-SOA foi utilizado para realizar funcionalidades temporais ao nível do bit e do pacote. Foi investigada a operação de um conversor de multiplexagem por divisão no comprimento de onda para multiplexagem por divisão temporal óptica, experimentalmente e por simulação, e de um compressor e descompressor de pacotes, por simulação. Para este último, foi investigada a operação com o MZI-SOA baseado em amplificadores ópticos de semicondutor com geometria de poço quântico e ponto quântico. Foi também realizado experimentalmente um permutador de intervalos temporais que explora o MZI-SOA como conversor de comprimento de onda e usa um banco de linhas de atraso ópticas para introduzir no sinal um atraso seleccionável.

Por fim, foi estudado analiticamente, experimentalmente e por simulação o impacto de diafonia em redes ópticas em diversas situações. Extendeu-se um modelo analítico de cálculo de desempenho para contemplar sinais distorcidos e afectados por diafonia. Estudou-se o caso de sinais muito filtrados e afectados por diafonia e mostrou-se que, para determinar correctamente as penalidades que ocorrem, ambos os efeitos devem ser considerados simultaneamente e não em separado. Foi estudada a escalabilidade limitada por diafonia de um comutador de intervalos temporais baseado em MZI-SOA a operar como comutador espacial. Mostrou-se também que sinais afectados fortemente por não-linearidades podem causar penalidades de diafonia mais elevadas do que sinais não afectados por não-linearidades.

Neste trabalho foi demonstrado que o MZI-SOA permite construir vários e pertinentes circuitos ópticos, funcionando como bloco fundamental de construção, tendo sido o seu desempenho analisado, desde o nível de componente até ao nível de sistema. Tendo em conta as vantagens e desvantagens do MZI-SOA e os desenvolvimentos recentes de outras tecnologias, foram sugeridos tópicos de investigação com o intuito de evoluir para as redes ópticas de nova geração.

keywords

Mach-Zehnder interferometer based on semiconductor optical amplifiers (MZI-SOA), wavelength conversion, format conversion, optical processing, packet compression and decompression, time slot interchanging, crosstalk and distorted signals.

abstract

The main motivation for this work is the desire to upgrade today's opaque network nodes, which are plagued by inherent limitations of its constitutive electronics, by all-optical transparent network nodes. The all-optical promise consists in delivering ever higher bit rates, more transparency, and unsurpassed efficiency associated to sophisticated all-optical switching paradigms. In this light, the integrated MZI-SOA has been selected as the fundamental building block for this investigation of all-optical processing techniques and functions necessary for developing the next generation all-optical networks.

Next generation optical networks will use advanced phase-managed modulation formats. Accordingly, the first simulation and experimental investigation assesses the performance of MZI-SOA based wavelength and format converter circuits for advanced modulation formats. Rules are derived for ensuring optimal MZI-SOA operation. The impact of the pulse shape on both the wavelength and format conversion processes is also addressed.

More complex MZI-SOA based implementations of bit-level, and packet-level, time domain processing functions are analysed. A MZI-SOA based wavelength division multiplexing to time division multiplexing converter is experimentally investigated and compared to similar simulation results. The performance of packet compressor and decompressor circuit schemes, based on quantum well and quantum dots SOA devices, is analysed through simulation techniques. A MZI-SOA wavelength converter based selectable packet delay time slot interchanger, which uses an optical delay line bank, is experimentally demonstrated.

Finally, the impact of crosstalk on all-optical networks is studied analytically, experimentally, and through simulations. An extant analytical model for assessing the performance of crosstalk impaired signals is improved for dealing also with distorted signals. Using the extended model, it is shown that heavily filtered signals are more seriously affected by crosstalk than unfiltered signals. Hence, accurate calculation of penalties stemming from both filtering and crosstalk, must model these effects jointly. The crosstalk limited scalability of a MZI-SOA space switched time slot interchanger is also assessed employing this method. An additional study points to the conclusion that crosstalk caused by signals impaired by non-linear effects can have a more significant detrimental impact on optical systems performance than that of the crosstalk caused by a signal unimpaired by non-linearities.

On the whole, it has been demonstrated that the MZI-SOA is a suitable building block for a variety of optical processing circuits required for the next generation optical networks. Its performance capabilities have been established in several optical circuits, from the component up to the system level. Next steps towards the implementation of next generation optical networks have been suggested according to the recent developments and the MZI-SOA's strengths and drawbacks, in order to pursue the goal of higher bit rate, more transparent, and efficient optical networks.

Table of contents

List of figures

List of tables

List of acronyms and abbreviations

2R	re-amplification and re-shaping
3R	re-amplification, re-shaping and re-timing
AMI	alternate mark inversion
AMI38	alternate mark inversion with 38% duty cycle
AOLS	all-optical label swapping
ASE	amplified spontaneous emission
ATT	variable attenuator
B2B	back-to-back
BER	bit error rate
BERT	bit error rate tester
BMR	burst mode receiver
BPSK	binary phase shift keying
CH	carrier heating
CIP	Centre for Integrated Photonics
CRU	clock recovery unit
CS67	carrier suppressed return to zero with 67% duty cycle
CS-RZ	carrier suppressed return to zero
CW	continuous wave
DCM	dispersion compensation modules
demux	demultiplexer
DI	delay interferometer
DISC	delay interferometer signal converter
DPSK	differential phase shift keying
DWDM	dense wavelength division multiplexing
EAM	electro-absorption modulator
ECP	eye closure penalty
EDFA	Erbium doped fibre amplifier
EF	electrical filter
EOP	eye opening penalty
ER	extinction ratio
FEC	forward error correction
FOCS	fully inline and optimized post-compensation scheme
FSK	frequency shift keying
FWHM	full width at half maximum
FWM	four-wave mixing
GVD	group velocity dispersion
ISI	intersymbolic interference
ISOL	isolator
MCB	modified Chernoff bound
MCB-EA	modified Chernoff bound with eye aperture data
MEMS	micro-electro-mechanical systems
MGF	moment generating function
MLL	mode-locked laser
MMI	multi-mode interferometers
MUFINS	Multi-Functional Integrated Arrays of Interferometric Switches
mux	multiplexer
MZI-QDSOA	Mach-Zehnder interferometer based on quantum dot semiconductor optical amplifier

MZI-SOA	Mach-Zehnder interferometer based on semiconductor optical amplifier
MZM	Mach-Zehnder modulator
NOLM	non-linear optical loop mirror
NRZ	non-return to zero
NSN	Nokia Siemens Networks
OADM	optical add/drop multiplexer
OBPF	optical band pass filter
OBS	optical burst switching
OCDMA	optical code division multiplexing access
OCS	optical circuit switching
ODB	optical duo-binary
ODL	optical delay line
OEO	optical-electrical-optical
OOK	on-off keying
OPS	optical packet switching
OSA	optical spectrum analyser
OSNR	optical signal to noise ratio
OTDM	optical time division multiplexing
OXC	optical cross-connect
PC	polarization controller
PD	photodetector
PDF	probability density function
PDG	polarization dependent gain
PED	packet envelope detector
PG	pattern generators
PID	proportional, integral, and differential
PMD	polarization mode dispersion
PPLN	periodically poled Lithium Niobate
PRBS	pseudorandom bit sequence
PRBSG	pseudorandom bit sequence generator
PS	phase shifters
PSK	phase shift keying
QDSOA	quantum dot semiconductor optical amplifier
QPSK	quaternary phase shift keying
ROADM	reconfigurable optical add/drop multiplexer
RZ	return to zero
RZ33	return to zero with 33% duty cycle
RZ50	return to zero with 50% duty cycle
SGM	self gain modulation
SHB	spectral hole burning
SLALOM	semiconductor laser amplifier in a loop mirror
SOA	semiconductor optical amplifier
SPM	self phase modulation
SSMF	standard single mode fibre
SXR	signal to crosstalk ratio
TDM	time division multiplexing
TOAD	terahertz optical asymmetric demultiplexer
TSI	time slot interchanger
Tx	transmitter
UNI	ultrafast nonlinear interferometer
VLSI	very large scale integration
VODL	variable optical delay line

WC	wavelength conversion/converted
WDM	wavelength division multiplexing
XGM	cross gain modulation
XPM	cross phase modulation
XPR	cross polarization rotation

List of symbols

	Chapter 2
a_N	material gain
e	electron charge
$E_{\beta,0}$	mean carrier energy
f_p	frequency of the probe signal
G	amplifier gain
g	SOA local gain
h	logarithmic integral SOA gain
h_0	unsaturated logarithmic integral SOA gain
h_{CH}	logarithmic integral SOA gain compression due to carrier heating
h_N	logarithmic integral SOA gain from the carrier recombination
h_{SHB}	logarithmic integral SOA gain compression due to SHB
I	SOA bias current
L	SOA length
$N(t)$	total SOA carrier density
N_0	density of available states in optically coupled region
n_β	local carrier density of carrier type β
$\overline{n}_\beta$	local carrier density of carrier type β in equilibrium
$P(t,z)$	optical power at time t and longitudinal coordinate z
P_{in}	optical power at SOA input
P_s	saturation power parameter
$S(t)$	photon density
T	time delay
T_L	lattice temperature
T_β	carrier temperature
t	time
U_β	total energy density
V	SOA active region volume
v_g	group velocity
z	longitudinal SOA coordinate
α	alpha-factor or linewidth enhancement factor
α_{CH}	alpha-factor or linewidth enhancement factor from carrier heating
α_N	alpha-factor or linewidth enhancement factor from carrier depletion
β	carrier type: electrons ($\beta=e$) and holes ($\beta=l$)
$\Delta\phi$	phase rotation
ε_{CH}	nonlinear gain suppression factors for carrier heating
ε_{SHB}	nonlinear gain suppression factors for SHB
λ	wavelength
λ_{in}	input wavelength
λ_{out}	output wavelength
$\tau_{H,\beta}$	temperature relaxation time, (without β, electrons are assumed)
τ_s	carrier lifetime
$\tau_{SHB,\beta}$	carrier-carrier scattering times (without β, electrons are assumed)
$\phi(t,z)$	optical phase at time t and longitudinal coordinate z

Ω	difference between the frequencies of the probe and pump signals

	Chapter 3
a	fitting parameter
b	fitting parameter
G_0	unsaturated SOA gain
i_1, i_2, i_3, i_4	SOA driving currents
i_T	Peltier cell driving current
V_1, V_2, V_3, V_4	voltages applied to the phase shifters
V_T	thermistor voltage
P_{cont}	optical power of the signal at the control input of the MZI-SOA
P_{int}	optical power of the signal at the interferometric input of the MZI-SOA
P_s	saturation power parameter
α_N	alpha-factor or linewidth enhancement factor from carrier heating
α_{CH}	alpha-factor or linewidth enhancement factor from carrier depletion
ε_{CH}	nonlinear gain suppression factors for carrier heating
ε_{SHB}	nonlinear gain suppression factors for SHB
τ_H	temperature relaxation time
τ_s	carrier lifetime
τ_{SHB}	carrier-carrier scattering times

	Chapter 4
a	fitting parameter
B	baud rate
b	fitting parameter
ECP	eye closure penalty
i_0	samples of the ‘0’ level at the sampling instant
i_1	samples of the ‘1’ level at the sampling instant
$\bar{i}_0$	average of the samples i_0
$\bar{i}_1$	average of the samples i_1
k	index
N	baud rate compression ratio
n_p	number of symbols in the packet
M	number of optical delay lines
r	correlation coefficient
T_p	packet duration
T_s	symbol period
$\Delta\varphi_A$, $\Delta\varphi_B$	phase mismatch of optical delay line A and B, respectively
λ	wavelength
$\wedge$	set intersection operation

Chapter 5

$A_k^{(0)}$, $A_k^{(1)}$	amplitude of the electric field envelope of the k^{th} crosstalk interferer conditioned to a '0' and '1' bit, respectively
$A_k(t)$	amplitude of the electric field envelope of the k^{th} crosstalk interferer
$A_s^{(0)}$, $A_s^{(1)}$	amplitude of the electric field envelope of the signal conditioned to a '0' and '1' bit, respectively
$A_s(t)$	amplitude of the electric field envelope of the signal
A_x	amplitude of the electric field envelope of the crosstalk interferer (all crosstalk channels are identical)
$A_x^{(0)}$, $A_x^{(1)}$	crosstalk interferer electric field amplitude conditioned to a '0' and '1' bit, respectively (all crosstalk channels are identical)
BER_0, BER_1	BER for bits '0' and '1', respectively
BER_{Dopt}	BER for a bit sequence with optimized decision threshold
c.c.	complex conjugate
C_k^N	number of k combinations from a set of N
D	decision threshold
D_{opt}	optimized decision threshold
$\vec{E}_k$	electric field of the k^{th} crosstalk interferer
$\vec{E}_{pd}$	electrical field of the optical signal at the photodetector input
$\vec{E}_s$	electric field of the signal
e_k	value of the k^{th} experimental data point
G	amplifier gain
h	Planck constant
$H_e(f)$	electric filter frequency response
$h_e(t)$	electric filter impulse response
$H_o(f)$	optical filter frequency response
$h_o(t)$	optical filter impulse response
$i(t)$	output current of the receiver electrical filter
I_0	zero order modified Bessel function of the first kind
$i_{ASE\text{-}ASE}(t)$	current of the ASE-ASE beating
i_k	sampled k^{th} crosstalk interferer current at the receiver output
$i_{pd}(t)$	photodetector output current
i_s	sampled signal current at the receiver output
$i_{s\text{-}ASE}(t)$	current of the signal-ASE beating
$i_{s\text{-}x}(t)$	current of the signal-crosstalk beating
i_x	sampled crosstalk current at the receiver output (all crosstalk channels are identical)
$i_{x\text{-}x}(t)$	current of the crosstalk-crosstalk beatings
K	number of experimental or simulation data points
k	index
k_{Gr}	Bragg grating coupling coefficient
L	number of '0' or '1' bits in a binary sequence
l	index
L_{Gr}	Bragg grating length
$m_0(z_0)$, $m_1(z_1)$	signal dependent part of the MCB for bits '1' and '0', respectively
$M_{ASE}(z)$	moment generating function of the ASE beatings
$MCB^{(0)}$,$MCB^{(1)}$	Modified Chernoff Bound for bits '0' and '1', respectively

$MCB_l^{(0)}$,$MCB_l^{(1)}$	Modified Chernoff Bound for bit *l* conditioned to be a '0' and '1', respectively
MCB_{seq}	Modified Chernoff Bound for a bit sequence
$MCB_{seq,Dopt}$	Modified Chernoff Bound for a bit sequence with optimized decision threshold
$M_{el}(z)$	moment generating function of the electrical Gaussian noise
$M_i^{(0)}(z)$, $M_i^{(1)}(z)$	moment generating function of the photodetector current *i(t)* conditioned to be a '0' and '1' bit, respectively
$M_i(z)$	moment generating function of the photodetector current *i(t)*
$M_X(z)$	signal–crosstalk beating moment generating function
N	number of crosstalk channels
n	number of TSI stages
$\vec{n}(t)$	ASE electric field filtered at the receiver optical filter ouput
$n_{el}(t)$	post-detection electrical Gaussian noise
$\vec{n}_{in}(t)$	ASE electric field arriving at the receiver pre-detection filter
n_{sp}	spontaneous-emission factor
N_{spans}	number of fibre spans
$\vec{p}_s$	signal electric field polarization
p_k	k^{th} crosstalk interferer electric field polarization
P_{fibre}	signal power at fibre input
S_{ASE}	amplified spontaneous emission spectral density
s_k	value of the k^{th} simulation data point
t	time
T_p	packet duration
X	contrast ratio
z	moment generating function parameter
z_0, z_1	moment generating function parameter for bits '0' and '1', respectively
$\Delta\theta_{sk}$	phase difference between signal and k^{th} crosstalk interferer
v	optical field frequency
$\phi_s(t)$	signal electric field phase
$\phi_k(t)$	k^{th} crosstalk interferer electric field phase
$\sigma^2_{ASE-ASE}$	ASE–ASE beating variance
σ_{el}^2	variance of the electrical noise after electrical filtering
σ_k	standard deviation of the k^{th} experimental data point
σ^2_{s-ASE}	signal–ASE beating variances
$\sigma_{tot}^{(0)}$, $\sigma_{tot}^{(1)}$	total standard deviation for bits '0' and '1', respectively
χ^2	reduced chi-squared
ω_s	signal electric field frequency
ω_k	k^{th} crosstalk interferer electric field frequency

Appendix A

χ	susceptibility
ε	relative electrical permittivity
k_0	wave number
$\vec{E}$	electrical field

t,t'	time
x,y,z	Cartesian coordinates
$A(z,t)$	optical wave envelope
$F(x,y)$	optical mode profile
$\hat{k}$	polarization direction
v_g	group velocity
α	linewidth enhancement factor or alpha-factor
g	SOA local gain
P	optical power
ϕ	optical phase
G	SOA amplifier gain
h	integral logarithmic SOA gain

Appendix B	
	See Chapter 2, plus:
t_0	time at the beginning of the simulation time vector

Appendix D	
n	logarithm of base 2 of the binary sequence size

Appendix E	
k	index
N	baud rate compression ratio
T	time delay
T_p	packet duration
T_s	symbol period

Appendix F	
	See Chapter 5

Chapter 1 Introduction

1.1 Context

The advent of digital telecommunications has been preponderant in the recent history of Humanity. The International Telecommunications Union has estimated that in 2008 there were 61 mobile phone subscriptions per 100 inhabitants in the world, while 23% of the world's population used the Internet and 11% had a broadband connection [1]. We have now grown to be used to being connected anywhere, anytime and with large enough bandwidth to access our email, to browse the web, to chat over an instant messaging service, to make a phone call, to listen or watch an audio or video stream, among several other services the Internet provides us with. The user content generated websites, such as blogs, video hosting sites, online marketplaces and also social networking sites, have changed the way we use the Internet, since everyone can very easily publish personal content online and make it available to a very large number of people. One other major use of the internet is file sharing, namely through peer-to-peer applications. All this variety of services has rendered the Internet as almost indispensable for the regular daily life.

As a consequence of the Internet, traffic in telecommunications networks has changed from being mainly local and low bandwidth intensive to world wide and large bandwidth consuming. Telecommunication service providers have to deliver an increasingly larger amount of bandwidth, either wired or wirelessly, at a low price to the end user. As a result, telecommunication system vendors have nowadays the challenge of providing networks that have high transmission capacity, are simple to set up and operate, support a multitude of network services, are flexible, reliable and fault tolerant, and all this at a low cost per transmitted bit. Moreover, energy consumption is becoming a key factor when operators pick the supplying vendor, for both cost and environmental impact reasons.

It is foreseen that the current technology, based on electrical processing, of network nodes is not scalable at the present rate of growth of bandwidth demand [2]. In fact, router capacity has been growing 2-fold every 18 months, just barely enough to keep up with the

4-fold traffic demand increase over three years of AT&T, one of the largest network operators in the world [3]. Optical technology seems to alleviate the electronic processing limitations, enabling more scalable network nodes. However, optical technology performance is not yet comparable to its electronic counterpart for system vendors to employ it in a commercial system.

In this context, this Thesis intends to contribute towards implementing the new generation of optical networks, by studying all-optical devices and techniques, which hold the promise of being the right technology to build larger capacity, more energy efficient, cheaper and more transparent optical networks.

1.2 Motivation

The optical fibre is the principal enabler of the large data transmission capacity we have today, with reported capacity times distance product of 112×10^{15} km×bit/s [4], achieved with 155 wavelength channels at 100 Gb/s over 7200 km. This record represents an increase of over seven orders of magnitude over 35 years, since the beginning of optical telecommunications [5]. Dense wavelength division multiplexing (DWDM) and time domain multiplexing (TDM) are key technologies for achieving such high transmission bit rates, of the order of tens of terabits per second. Typically, at the network node, the incoming data are converted to the electrical domain, the data headers are processed and the data are then forwarded to the correct output port. With a data rate of tens of terabits per second per fibre arriving at a network node, it is a hard task for the electronics to handle such amount of data due to the limited electronic bandwidth of the order of tens of gigabit per second per channel. Therefore, there is a bottleneck effect, where the fibre provides very large bandwidth capacity, but at the network nodes there are not enough processing capabilities to take advantage of the fibre capacity.

Despite the very large increase of fibre data transmission capacity and different technologies involved, the optical network nodes have always been based in optical-electrical-optical (OEO) conversion, until the adoption of optical add/drop multiplexers (OADM). This was the first optical solution to be adopted, where the traffic is routed in the optical domain, on a wavelength basis. The next solutions, which are currently being adopted, are the reconfigurable OADM (ROADM) and the optical cross connect (OXC),

where the OADM functionality is retained, with the added capability of remotely re-routing the traffic without local user intervention. Although, the OADM, ROADM and OXC provide wavelength routing, neither regeneration nor routing at a finer granularity are possible. Therefore, all-optical processing schemes are being proposed to avoid OEO conversion and take advantage of the optical processing capabilities. Regeneration, wavelength conversion, packet routing, optical TDM, bit-wise logic, and various other functions have been demonstrated all-optically, as will be described in detail in the next chapter. By and large, all-optical processing is seen to be key in future optical networks.

All-optical processing functions have been mainly achieved by exploiting non-linear effects on both fibres and semiconductors. The semiconductor optical amplifier (SOA) stands out from other all-optical processing devices since it is integrable, provides gain and requires small optical input powers for non-linear operation. Due to the SOA integrability, interferometric structures have been proposed, which have stable operation when compared to their fibre-based counterparts. The integrated SOA structures allow more optical processing functions than the SOA alone, and at a faster bit rate, as will be shown in the next chapter. In particular, the Mach-Zehnder interferometer with a SOA in each arm (MZI-SOA), and moreover, MZI-SOA integrated arrays have been used to demonstrate several all-optical functions at 40 Gb/s. Therefore, both the SOA and the MZI-SOA are considered key elements for all-optical processing sub-systems and consequently for future generation optical networks. For this reason, the MZI-SOA was chosen to be the centrepiece of the optical processing study here presented.

This Thesis addresses some questions regarding the utilization of all-optical sub-systems in optical networks that had been unanswered. For instance, long haul optical transmission systems are now adopting more advanced modulation formats instead of the usual optical on-off keying, either with non return to zero (NRZ) or return to zero (RZ) pulses. It is imperative that all-optical circuits are capable of operating with more advanced formats, and therefore study on this matter is required. Chapter 3 presents work on this topic. Another issue regarding the adoption of all-optical circuits is the scalability of the optical devices, since no OEO regeneration occurs in between all optical processing blocks, and consequently optical impairments accumulate in each stage. This is particularly important if the electronic routers are to be replaced by optical routers. Optical routers will have several functional blocks, such as WDM to OTDM converters, packet compressors

and decompressors, or time slot interchangers, depending on the network switching paradigm. The performance of these optical processing sub-systems is analysed in chapter 4.

The issue of optical impairments accumulation is very critical and is relevant even to the simplest of optical nodes, the OADM. The OADM, the ROADM, the OXC, and also the more advanced all-optical nodes, such as those based on MZI-SOA devices, introduce optical crosstalk degrading the optical performance, which is the main subject of chapter 5. The impact of crosstalk on optical networks has been extensively studied, but most studies analyse the impact of crosstalk considering perfect signal shapes either for the signal being degraded, or the signal causing the degradation. However, in a real network, both the signals that are impaired by crosstalk and the signals that cause crosstalk are impaired by transmission effects, such as chromatic dispersion, non-linear transmission effects, and optical filtering. At the end of the transmission link, all impairments are combined, resulting in potentially severe degradation of the signal performance. It is not certain that the resulting performance penalty can be calculated from the penalty resulting from each of the impairments taken separately, and then added together for a combined effect assessment. As a matter of fact, penalties usually add super-linearly, and the combined effects of different impairments should be carefully analysed.

1.3 Thesis objectives and outline

The goal of this Thesis is to contribute to the advancement of optical technology enabling the future generations of optical networks. Optical processing is believed to be the path to this goal and therefore all-optical devices and circuits were studied for this purpose. The MZI-SOA shows very attractive optical processing capabilities and therefore one objective is to investigate its optical processing capabilities with more advanced optical modulation formats. Sub-systems for processing packets in the time domain, such as time slot interchangers (TSI), packet compressors and decompressors based on these devices will also play an important role and have been investigated. A characteristic of interferometric based optical processing circuits is the crosstalk between outputs, which can significantly degrade the performance of the optical signals. In this Thesis the impact of crosstalk generated by these devices is analysed and the scalability of optical processing

architectures is assessed. Finally, the combined effect of crosstalk with other transmission impairments, such as dispersion, non-linear effects and narrow filtering is analysed.

The following structure in six chapters was adopted to describe the studies:

This first introductory chapter exposes the social and technological context of the Thesis, as well as the motivation and objectives behind the work here presented. It is expected to motivate the reader for the next chapters where the deeper and more arduous content lies.

The second chapter introduces the reader to the devices used for all-optical processing and, particularly to the SOA and MZI-SOA fundamentals. The state of the art of SOA based optical processing, SOA interferometers and, particularly, of MZI-SOA is overviewed, whilst contextualizing them in the work presented on the following chapters. Additionally, a mathematical model for simulation and performance estimation of these devices is briefly explained.

The third chapter starts off with the experimental characterization of MZI-SOA devices. The mathematical methods, together with the experimental characterisation data, provide the starting point for obtaining results on the advanced format conversion in the MZI-SOA. Experimental and simulation results are given for wavelength and format conversion using the MZI-SOA, and rules of operation are derived.

In the fourth chapter, the MZI-SOA is used in time domain processing circuits by making extensive use of wavelength conversion. An all-optical multi-format converter and time multiplexer is proposed and its performance is investigated. Then, MZI-SOA based optical packet compressor and decompressor circuits for phase shift keyed modulated packets are analysed. In this simulation study, the cascadability of the packet compressor and decompressor pair and the operating margins of some their parameters are assessed. The use of phase modulated packets imposes constraints on the optical circuits that are also addressed in this chapter. Finally, a time slot interchanger is presented based on the MZI-SOA acting as a wavelength converter and a bank of optical delay lines that are addressed by the wavelength. Experimental results on the performance of this architecture are presented.

The fifth chapter concerns itself with the impact of optical crosstalk in some optical network scenarios. A computationally fast method for estimating the bit error rate of a signal impaired by distortion, amplified stimulated emission noise, and in-band crosstalk,

is presented and compared to semi-analytical, and Monte Carlo simulations, as well as with experimental results. This method along with both semi-analytical and experimental methods are then used to estimate the performance of an optical signal impaired by crosstalk and transmission effects such as chromatic dispersion, non-linear effects, and both narrow optical and electrical filtering. Then, a crosstalk-impaired MZI-SOA based time slot interchanger switching unit architecture is analysed. The scalability of the architecture which is limited by optical crosstalk is investigated numerically, and an improved architecture is proposed to mitigate the crosstalk. Finally, the scenario where the signal that causes the crosstalk is itself impaired by transmission effects is considered, and its impact on the network performance is analysed.

The main conclusions of the work are summarised in the final chapter. Future work following from the work presented in the Thesis is also suggested in the concluding paragraphs.

The bibliographic references are listed at the end of each chapter.

1.4 Main contributions

This work has been performed within a PhD programme in an industrial environment at Nokia Siemens Networks Portugal, S.A. (NSN) (formerly Siemens, S.A.) in the optical research group. NSN is a global company offering telecommunication solutions for operators. The PhD programme in partnership with a company presents an additional challenge which is to do research with the ultimate goal of incorporating resulting knowledge in a product. As a system integrator, NSN is particularly interested in research that might yield more efficient and cost effective networks. This goal has clearly been present throughout the work, which has motivated a research path starting at the component level, the MZI-SOA device, leading up to a sub-system level and finally to a network level, justifying the layout of this Thesis, as described in section 1.3. A consequence of the immersion of this work within an industrial context has resulted in scientific knowledge and in intellectual property in the form of patents, both of benefit to the company.

Some of the work was developed within the European Union Framework Programme 6 project IST-2-004222, called Multi-Functional Integrated Arrays of

Interferometric Switches (MUFINS). The MUFINS project aimed to develop MZI-SOA devices that can be used as a basic building block for larger and more complex optical processing circuits. It is shown in this project that the MZI-SOA gates, when properly combined together, are suitable for a vast number of different useful applications in telecommunications, logics and computing. Within the framework of this project, a joint experiment with the National Technical University of Athens was done to demonstrate the time slot interchanger functionality based on MZI-SOA gates. The results of this collaboration are presented in section 4.4.

During the work performed within the PhD programme, a total of two international patent applications [6, 7], one technical report [8], and three magazine [9, 10, 11] and nine conference proceedings publications [12, 13, 14, 15, 16, 17, 18, 19, 20] were achieved. The main scientific contributions that have arisen from the PhD programme are the following:

Experimental demonstration based on a 40 Gb/s MZI-SOA of a) wavelength conversion of a NRZ signal, b) optical format conversion of a CS-RZ and NRZ signal to RZ, and c) CS-RZ wavelength conversion using an additional electro-optic modulator [14].

Demonstration of an experimental MZI-SOA based format converter to short pulses and time domain multiplexer from 40 Gb/s to 120 Gb/s [16].

Numerical study of the scalability of two time slot interchanger architectures based on MZI-SOA switching elements [13].

Experimental implementation of a multi stage time slot interchanger based on wavelength conversion with MZI-SOA, at 10 Gb/s [18].

Demonstration of a MZI-SOA based all-optical packet compressor and decompressor for phase modulated packets and study of their cascadability, for compression from 10 to 40 Gb/s and from 40 Gb/s to 160 Gb/s, and subsequent decompression [15].

Study of the phase requirements of the compressor and decompressor circuits arising from the use of phase modulated packets, instead of amplitude modulated packets.

Development of a novel computationally fast method for estimating the bit error rate of a signal impaired by optical in-band crosstalk, amplified spontaneous emission noise and shape distortion [10].

Study of the combined effect of crosstalk, chromatic dispersion, self-phase modulation, and both optical and electrical narrow filtering, on the signal performance [10].

Study of the crosstalk penalties when the crosstalk signal itself is impaired by optical filtering, chromatic dispersion, and self-phase modulation [12, 9].

Additionally, one magazine [11] and three conference proceedings [17, 19, 20] publications, in authorship or co-authorship, have also resulted from related work.

1.5 References

[1] International Telecommunication Union, *Measuring the Information Society - The ICT Development index*. 2009. Available online at http://www.itu.int/ITU-T/ict/publications/idi/2009/material/IDI2009_w5.pdf.

[2] I. Keslassy, S. Chuang, K. Yu, D. Miller, M. Horowitz, O. Solgaard, and N. McKeown, "Scaling Internet routers using optics (extended version)," tech. rep., Stanford HPNG Tech. Rep. TR03-HPNG-080101 (Stanford University, 2003), available online at http://yuba.stanford.edu/techreports/TR03-HPNG-080101.pdf.

[3] K. Tse, "AT&T's photonic network," *in Proc. Optical Fiber Communication Conference (OFC)*, vol. NMC1, 2008.

[4] M. Salsi, H. Mardoyan, P. Tran, C. Koebele, E. Dutisseuil, G. Charlet, and S. Bigo, "155x100Gbit/s coherent PDM-QPSK transmission over 7,200km ," *in Proc. Optical Fiber Communication Conference (OFC)*, p. PD2.5, 2009.

[5] E. Desurvire, "Capacity Demand and Technology Challenges for Lightwave Systems in the Next Two Decades," *IEEE/OSA Journal of Lightwave Technology*, vol. 24, no. 12, pp. 4697–4710, 2006.

[6] R. Meleiro, J. M. Santos, P. Inácio, M. Hajduczenia, M. M. Freire, J. Castro, and P. P. Monteiro, "Automatic Topology Discovery for Passive Optical Networks," Tech. Rep. 08104626.0, 2008P00693EP, Nokia Siemens Networks Oy, July 2008. European patent application number 2008P00693EP (First Filling).

[7] L. Pellegrino, R. Meleiro, D. Fonseca, R. Morais, P. Monteiro, P. André, "Method for data processing in an optical network component and optical network component", Nokia Siemens Networks Oy, European Patent Application number PCT/EP2009/052541

[8] D. Fonseca, R. Meleiro, "Apparatus to distinguish presence of optical signal power from amplified spontaneous emission noise", Nokia Siemens Networks Portugal, S.A., 2009, Internal Technical Report

[9] R. Meleiro, A. Buxens, D. Fonseca, J. Castro, P. André, and P. Monteiro, "Impact of self phase modulation on in-band crosstalk penalties," *IEEE Photonics Technology Letters*, vol. 20, no. 8, pp. 644–646, 2008.

[10] R. Meleiro, J. Castro, D. Fonseca, P. André, and P. Monteiro, "In-band crosstalk penalties in optical networks with narrow optical and electric filtering," *Optics Express*, vol. 17, no. 6, pp. 4605–4610, 2009.

[11] S. Pato, R. Meleiro, D. Fonseca, P. Andre, P. Monteiro, and H. Silva, "All-Optical Burst-Mode Power Equalizer Based on Cascaded SOAs for 10-Gb/s EPONs," *IEEE Photonics Technology Letters*, vol. 20, no. 24, pp. 2078–2080, 2008.

[12] R. Meleiro, A. Buxens, J. Castro, P. André, and P. Monteiro, "Impact of Dispersion and Self Phase Modulation on Crosstalk in Optical WDM Networks," *in Proc. of Conference on Telecommunications - Conftele*, pp. 557–560, 2007.

[13] R. Meleiro, J. Castro, P. Andre, and P. Monteiro, "Performance Study of a Time Slot Interchanger Based on a MZI-SOA in the Switch Configuration," *in Proc. International Conference on Transparent Optical Networks*, p. We.P.11, 2007.

[14] R. Meleiro, D. Fonseca, J. Pina, J. Castro, P. Andre, and P. Monteiro, "40 Gb/s CS-RZ to RZ format conversion using a MZI-SOA integrated switch," *in Proc. Pacific Rim Conference on Lasers and Electro-Optics (CLEO/Pacific Rim)*, vol. ThD3-5, pp. 1414–1415, 2007.

[15] R. Meleiro, J. Pina, H. Silva, J. Castro, P. Andre, and P. Monteiro, "All-optical RZ-DPSK packet compressor and decompressor based on MZI-quantum-dot-SOA," *in Proc. International Conference on Transparent Optical Networks*, p. Mo.D1.4, 2008.

[16] R. Meleiro, R. Morais, J. Castro, P. André, and P. Monteiro, "On all-optical 3×40Gb/s WDM to 120 Gb/s OTDM conversion based on MZI-SOA," *Proc Symp. on Enabling Optical Networks - SEON*, June 2008.

[17] R. Meleiro, R. Morais, P. Monteiro, J. Castro, P. Marques, and P. André, "Laser multi-comprimento de onda com auto-estabilização devido a mistura de quatro ondas em fibra altamente não linear de Bi," *in Proc. 15ª Conferência Nacional de Física (FISICA 2006)*, p. OL1, 2006.

[18] O. Zouraraki, D. Petrantonakis, K. Yiannopoulos, R. Meleiro, L. Sadeghioon, A. Poustie, G. Maxwell, E. Varvarigos, K. Vlachos, P. Monteiro, *et al.*, "Optically-Addressable Packet Timeslot Interchanger Using a Quadruple Switch Array," *in Proc. Optical Fiber Communication Conference (OFC)*, p. OTuB3, 2007.

[19] R. Morais, R. Meleiro, P. Monteiro, and P. Marques, "OTDM-to-WDM conversion based on wavelength conversion and time gating in a single optical gate," *in Proc. Optical Fiber Communication Conference (OFC)*, vol. OTuD5, 2008.

[20] P. Monteiro, J. Pedro, S. Pato, J. Gomes, R. Morais, J. Santos, R. Meleiro, H. Rohde, and R. Winkelmann, "Challenges and trends in optical networking: A bottom-up approach," *Broadband Communications, Networks and Systems, 2008. BROADNETS 2008. 5th International Conference on*, pp. 460–469, 2008.

Chapter 2 Optical processing devices, optical systems, and their modelling

This chapter describes the state of the art of all-optical processing with MZI-SOA devices, and contextualizes the work presented in the following chapters within the extant scientific literature. This chapter overviews all-optical processing devices, with an emphasis on the SOA. Its basic operation is described, and more complex SOA based all-optical processing devices, are also reviewed, including the MZI-SOA which stands out for its compactness and versatility. Next, several optical processing functions based on the MZI-SOA are presented. Finally, SOA and MZI-SOA mathematical models are described, for modelling the performance of more complex SOA and MZI-SOA based all-optical circuits.

2.1 All-optical processing devices

Optical processing is generally understood as the manipulation of the characteristics of a light signal, whereas all-optical signal processing consists in manipulating the characteristics of a light beam (probe) by means of another optical signal (pump). Light modulation by an electro-optic modulator, or light steering by micro-electro-mechanical systems (MEMS) are examples of optical processing, but not of all-optical processing, since both the modulator and the MEMS are controlled by electrical signals. On the other hand, wavelength conversion in a non-linear optical fibre, or clock recovery in a mode-locked laser, are both examples of all-optical processing since only optical signals are involved.

All-optical processing is seen as a key technology for next generation optical communication networks [1, 2, 3, 4]. Several authors have highlighted the limited scalability of the current electronic switching paradigm which may be unable to cope with a continued exponential traffic growth [1, 2, 3]. Router size and energy consumption will become unacceptably large if the current technology is employed to extend routers capacity to the 100 Tb/s range [5, 2]. In fact, the internet energy consumption was

currently estimated to be about 0.4% of the total energy consumption in broadband enabled countries [1]. All-optical processing will enable moving away from the current electric packet switching and forwarding network paradigm, towards optical switching which provides better scalability and less energy consumption [2, 3, 4]. All-optical processing network nodes have the further advantage of a reduced latency, when compared to their digital electronic counterparts.

Ultimately, one would like to develop an optical transistor, i.e., the optical domain counterpart of the electronic transistor, for building all-optical networks. The optical transistor would enable the design of large integrated optical circuits capable of performing complex operations at the network nodes, such as regeneration, header recognition, routing, etc., mimicking the impact of electronic VLSI circuits in today's network nodes. The relevant characteristics of a suitable transistor are its size, compactness, switching energy, switching time, wavelength range, and cost [7]. The size, compactness, and cost factors, as in electronics, highlight the importance of the integrability of all-optical devices. This is one crucial advantage of the SOA relatively to other non-integrable all-optical processing devices.

Several suitable types of devices exist for all-optical processing. Among them are fibre based devices, where 1 m to 1000 m spans of optical fibre are used for optical processing via the Kerr effect. Although very small lengths of fibre have been used in optical processing [8], tens or even hundreds of meters of fibre are used more often. However, even the shortest pieces of fibre, are still considered too bulky for building all-optical sub-systems, and are not integrable [4]. Therefore, several alternative devices have been developed with smaller form factors based on material waveguides, which are potentially integrable. Several materials exhibit strong enough non-linearity with respect to the optical input power for performing optical processing, which only require short waveguides of only a few millimetres or centimetres in length for the non-linear effects to become significant. Such devices are based on photonic crystals [9], chalcogenide glass [10], and silicon [11], among other materials. A list of a few materials for nonlinear processing can be found in reference [12]. Although showing promising processing capabilities, they are still very immature and, consequently, only a few processing capabilities have been demonstrated. Semiconductor devices share with the passive

waveguides, the advantage of being integrable, but have the additional advantages of providing gain to the input optical signal and requiring lower input signal powers.

The SOA is rightfully regarded as one of the most promising all-optical processing devices for future optical networks [4, 13], and, consequently, has been selected for carrying out the investigation on all-optical processing described in this Thesis.

2.2 The SOA

The SOA is an optoelectronic device, which under suitable conditions can amplify an input light signal, as defined by Connelly [14]. Several commercial SOAs are currently available [15, 16, 17, 18, 19, 20], for various applications, both for the 1300 nm and 1550 nm bands. These SOAs can provide large gain, and exhibit high saturation power, low polarization gain dependence, and moderate noise figures. Due to its amplifying capability, the SOA has also been used as an optical amplifier, in addition to a non-linear processing device. Table 2-1 presents a comparison of typical SOA and erbium doped fibre amplifier (EDFA) characteristics.

Table 2-1 Comparison of typical Erbium doped fibre amplifier (EDFA) and SOA characteristics, from [14] with updates from [4].

Feature	EDFA	SOA
Maximum internal gain (dB)	30-50	30
Insertion loss (dB)	0.1 - 2	6 – 10
Polarization sensitivity	No	Weak (< 2 dB)
Pump source	Optical	Electrical
3 dB gain bandwidth (nm)	30	30 – 50
Non-linear effects	Negligible	Yes
Recovery time of gain compression	100 μs	1- 10^3 ps
Saturation output power (dBm)	15-30	5-20
Noise figure (dB)	3 – 5	6 – 12
Integrated circuit compatible?	No	Yes
Functional device possibility?	No	Yes

The basic SOA structure is depicted in Fig. 2.1. It consists of an optical semiconductor waveguide for confining the light to a given region. When an electric current is applied to the semiconductor, the conduction band carriers are excited and electron-hole pairs are formed, as illustrated in Fig. 2.2. When the electron-hole pairs recombine due to stimulated emission, the input light pulse is amplified. Unfortunately,

there is also recombination of electron-hole pairs through spontaneous emission, in which case a noise photon is added to the signal. Further amplification of spontaneous emission photons leads to noise being added to the signal, referred to as amplified spontaneous emission (ASE) noise.

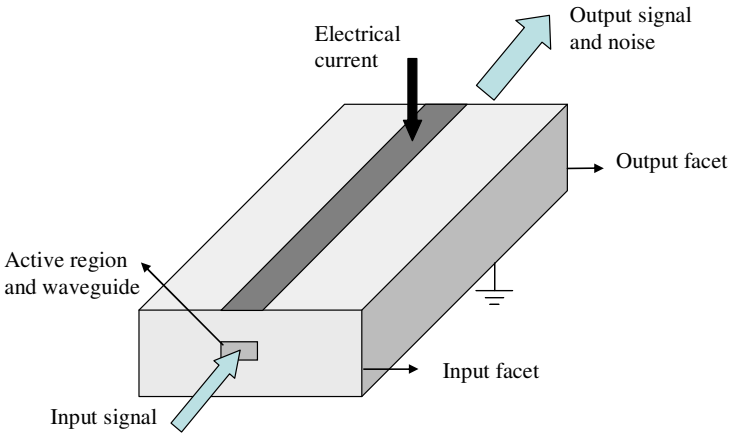

Fig. 2.1 SOA structure schematics.

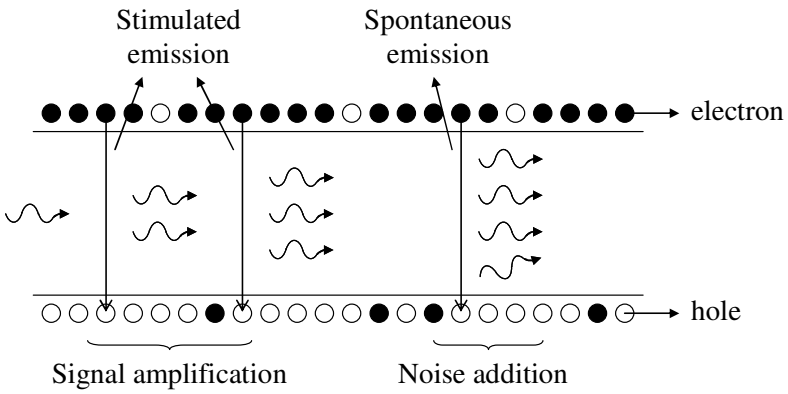

Fig. 2.2 Stimulated and spontaneous emission in a two level system.

Other important phenomena affect the signal amplification. When the power of the signal travelling inside the SOA becomes too high, a significant number of electron-hole pairs are recombined and the number of electron-hole pairs can become depleted. When that happens, stimulated emission and signal amplification cannot proceed, as there are not enough electron-hole pairs to recombine. The SOA becomes saturated, its gain is reduced, and consequently the output optical signal power remains constant even if the input power is increased. Fig. 2.3 shows the typical SOA steady-state gain saturation curve as a function of the output signal power. When the output signal power depends in a non-linear way on the input power of the same signal, i.e., when the input signal is causing gain

variations, the phenomenon is called self gain modulation (SGM). However, when the SOA gain is depleted, due to electron-hole pair recombination, the optical medium density changes and, as a consequence of the Kramers-Kronig relations, so does the refractive index. The refractive index dependence on the output signal power is also depicted in Fig. 2.3. Since the refraction index of the material changes, the signal amplitude variation also causes a change in the signal phase. Similarly to the SGM case, this phenomenon is called self phase modulation (SPM). Both phenomena enable one signal to modulate itself when travelling inside a SOA and can be used to perform non-linear processing [21]. The same principle can be used to modulate the amplitude and phase of another secondary signal, called probe, inside the SOA, if the wavelength of the latter signal is within the range of influence of the gain reduction and phase change caused by the first (pump) signal. Hence, the probe signal experiences both cross gain modulation (XGM) and cross phase modulation (XPM).

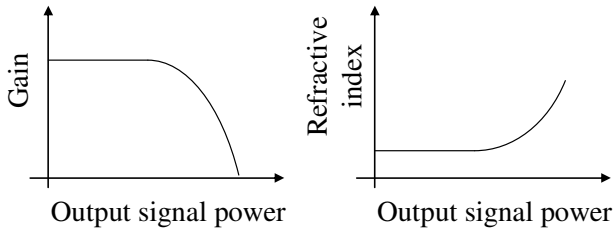

Fig. 2.3 Typical gain saturation and refractive index curve of a SOA as a function of the output signal power.

Additionally, when two or three different wavelength signals are present in a SOA, new signals appear spaced by the wavelength difference of the incoming signals. This effect is called four-wave mixing (FWM) and is due to gain modulation of the incoming signals at the beat frequency.

Another phenomenon occurring in the SOA is the polarization rotation. Since the modulation of the refraction index of the SOA depends on the polarization, different polarizations will suffer different phase modulations. Hence, a signal travelling inside a saturated SOA can have orthogonal polarization directions affected by phase modulation to different extents, causing a polarization rotation. When a pump signal is causing polarization rotation on a probe signal, the phenomenon is usually called cross polarization rotation (XPR).

A direct application of XGM is wavelength conversion, as depicted in Fig. 2.4. If a signal (pump) with high power is input to the SOA, along with a second CW smaller

power probe signal, at a different wavelength, the high power mark levels of the first signal will cause XGM on the probe and low output power is obtained at the output. Conversely, the SOA gain is large during the space levels of the original signal, and large output probe power is attained. Therefore, the original data information is converted to the probe wavelength, even if inverted. Moreover, the extinction ratio of the output signal is limited by the achieved gain compression, which can be unsatisfactory. Due to these drawbacks, better performing methods have been devised, particularly those exploiting XPM [22].

The setup for wavelength conversion in a SOA using XPM is similar to the setup for exploiting XGM, and is shown in Fig. 2.5. The XPM phenomenon by itself does not cause any change in the signal amplitude, only in the phase. Therefore, in XPM-based wavelength conversion, it is also necessary to convert the phase modulation of the probe at the SOA output to an intensity modulation. One way to do this is to use an offset filter at the SOA output relatively to the probe wavelength, so that only one side-band is transmitted. This side-band alone is an amplitude modulated signal, with the same data polarity as the input signal.

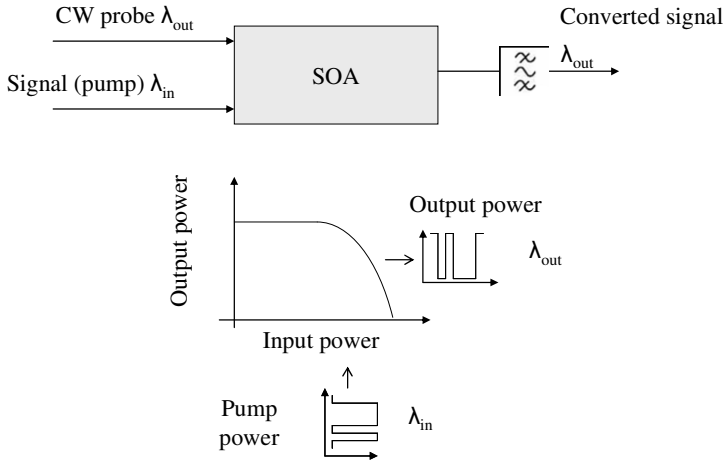

Fig. 2.4 Wavelength conversion through XGM in a SOA.

The FWM phenomenon can also be exploited to perform wavelength conversion, which is depicted in Fig. 2.6. When two different wavelengths are present inside the SOA, the gain of the SOA is modulated by the total power of the input signals. The total power has one component which is the beating of both input signals. Therefore, the SOA gain is modulated at the frequency of the beating between the two input signals. As a consequence, new signals appear at the SOA output, at frequencies that are distanced from

the input signals by the beating frequency. Again, by filtering only one of these generated new frequencies, wavelength conversion of the original signal can be obtained.

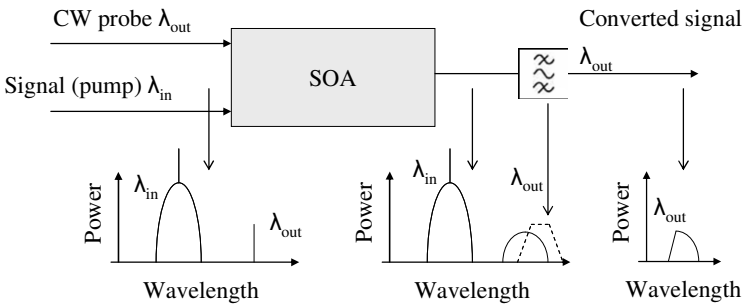

Fig. 2.5 Wavelength conversion through XPM in a SOA.

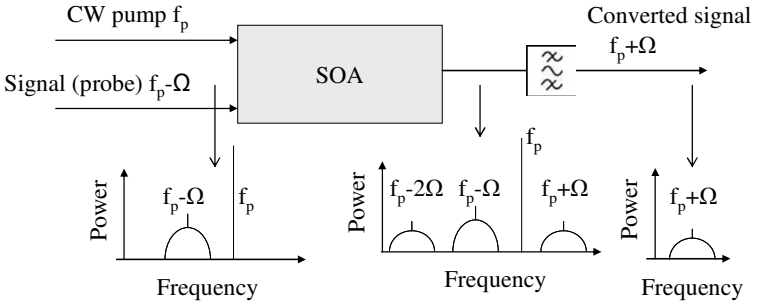

Fig. 2.6 Wavelength conversion using four-wave mixing in SOA.

The wavelength conversion based on XGM and XPM has the advantage over the FWM conversion method that the output signal wavelength is the wavelength of the probe, whereas the FWM creates a new wavelength. Also, the FWM efficiency is both very low and polarization dependent in SOAs. Therefore, XPM and XGM are exploited more often than the FWM in SOAs.

Both the XPM and XGM effects are based on the SOA carrier dynamics and therefore the maximum bit rate at which wavelength conversion can be done is limited by carrier dynamics characteristics. In the wavelength conversion through XGM, the pump signal marks saturate the SOA gain, resulting in a low power state (space) imprinted in the probe. As pointed out earlier, wavelength conversion through XGM inverts the data polarity. If a zero follows in the input signal bit stream, the SOA gain will recover from saturation, and a high power level will show up at the SOA output. However, for large bit rates, where the bit period approaches the gain saturation recovery time, the gain will recover in the bit slot of the next bit, as illustrated in Fig. 2.7. If the gain recovery time is

similar or larger than the bit slot, the gain will not be fully recovered from the previous bit and consequently the power values of each bit will be influenced by the previous bits. This is known as a patterning effect, and causes the eye diagram of the output signal to have a smaller aperture than the input eye diagram, with inevitable penalties. Consequently, the maximum bit rate at which both the XGM and XPM based wavelength conversion can be performed is limited to the SOA gain recovery time. The typical maximum bit rate of XGM based wavelength conversion using a quantum-well SOA is 10 Gb/s to 40 Gb/s [23], and 160 Gb/s using a quantum-dot SOA [24].

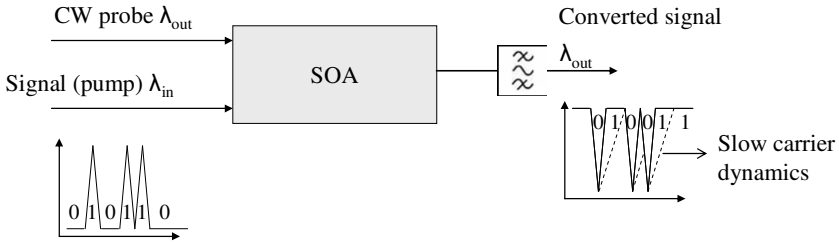

Fig. 2.7 Wavelength conversion through XGM in a SOA with slow carrier dynamics resulting in patterning effects.

2.3 SOA-based devices for optical processing

In the previous section it has been explained how the gain recovery time, which is determined by the carrier recovery dynamics, limits the maximum bit rate at which wavelength conversion is possible in a SOA. The SOA can be engineered to have faster carrier dynamics and hence faster response [25], [26]. However, at some point, the material becomes the limiting factor of the carrier dynamics speed [23]. In this situation, either a different material must be used, or optical processing methods can be employed to countervail this fundamental limitation. As observed earlier, using quantum dots SOAs instead of quantum-well SOAs allows faster wavelength conversion due to their reduced gain recovery time. In chapter 4, optical processing functions will be investigated using both types of SOAs. However, the quantum-dot SOAs have not been available until quite recently, and are not available commercially. Therefore, optical processing schemes have been devised to allow faster operation of the SOAs. Some selected examples will be presented hereafter. Naturally, the maximum benefit results from combining the latest materials with such processing techniques.

2.3.1 Delay interferometer signal converter

One of the simplest and fastest wavelength conversion schemes is the delay interferometer signal converter (DISC) [27], [28]. This scheme is a particular implementation of the wavelength converter based on XPM presented in Fig. 2.5. It uses the same setup, but the optical filter consists of an asymmetrical Mach-Zehnder interferometer, having a delay and phase shift in one of its arms. The DISC schematic is depicted in Fig. 2.8 as well as its working principle. A pump signal and a CW probe are fed to the SOA, where XGM and XPM take place. At the SOA output, the CW probe is amplitude and phase modulated by the pump carrying the data. Each time a signal pulse arrives, a large phase shift is imprinted by the SOA on the probe. The SOA recovers between pulses during which the phase shift is varying slowly. This signal is then fed to the Mach Zehnder delay interferometer (DI), which creates two signal replicas, delays one of them, and adds them together at the output. As depicted in Fig. 2.8 b), at the times corresponding to the arrival of a signal pulse, the two replicas in the DI will have a significantly different phase and therefore there will be a pulse at the DI output. On the other hand, when no signal pulse was present, the phase is changing slowly and hence the two replicas have a similar phase. Little light is output in this case. Therefore, the input data is converted to the probe wavelength with the original polarity.

The operation of this configuration can be understood by representing the involved signals and devices in the base band, and considering the limited bandwidth wavelength conversion by the SOA as a low pass filtering action on the incoming signal, as shown in Fig. 2.8 c). The DI acts as a high pass filter, since it eliminates the slowly changing phase components of the signal, like the derivative operation. Hence, combining the transfer function of the SOA and the DI, the resulting total wavelength conversion transfer function has larger bandwidth, compared to that of the SOA alone, effectively mitigating the effect of the SOA slow gain recovery.

Experimental results with this technique have demonstrated wavelength conversion at bit rates from 10 Gb/s [27], 80 Gb/s [29] to 640 Gb/s [30], which is the current record for the highest bit rate of wavelength conversion. Demultiplexing has also been demonstrated with the DISC technique [31].

Although this technique enables very high bit rate wavelength conversion, its main drawback is that it needs an optical filter, the DI, fine tuned to the probe wavelength. A control system would be required to both tune the wavelength of the optical filter and to track the signal wavelength, which is complex and costly, and therefore not realistic in a practical network scenario. Other methods exist that do no require this kind of fine tuned filtering. Moreover, this technique does not permit more advanced functionalities due to its lack of additional operational degrees of freedom.

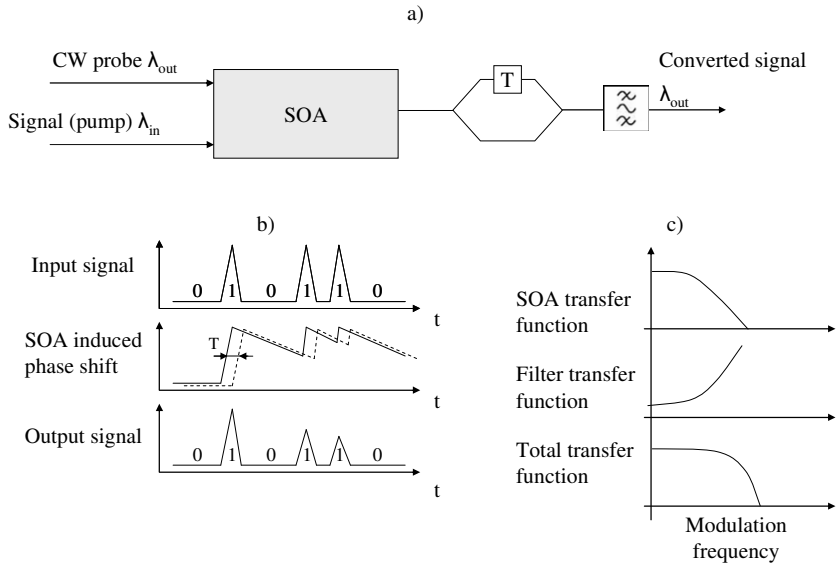

Fig. 2.8 a) Delay interferometer signal converter (DISC) scheme, b) DISC operating principle, c) DISC transfer function model.

2.3.2 Non-linear optical loop mirror

Another device used for signal processing is the non-linear optical loop mirror (NOLM) [32, 33], depicted in Fig. 2.9. This configuration is also known as the terahertz optical asymmetric demultiplexer (TOAD), when operating as a demultiplexer, or else as the semiconductor laser amplifier in a loop mirror (SLALOM), when the nonlinear element is a SOA. The SOA-based NOLM is a Sagnac interferometer with a SOA inside the interferometer. The SOA is placed in an asymmetric position inside the loop relatively to the input/output coupler. An additional coupler is placed between the SOA and the input/output coupler so that the pump signal can be fed in to the loop. While the probe is split by the input/output coupler and passes the SOA twice, the pump only passes the SOA once. Since the SOA is placed with some offset relatively to the loop middle point, the two

probe replicas pass the SOA at different times. When a pump pulse arrives at the SOA it will cause XPM on the two probe replicas. However, one of the probe replicas arrives at the SOA sooner than the other and therefore the part of the clockwise and counter-clockwise propagating replicas that experience the SOA induced phase shift arrives at the input/output coupler also at different times. As in the DISC, the input/output coupler adds a part of the probe that is affected by XPM while the other replica remains unaffected. Hence, a light pulse exits the NOLM. When no pump pulse is present, the SOA induced phase is recovering slowly. In this situation, the phase is nearly identical in both replicas and almost no light exits the NOLM, achieving wavelength conversion, again without data inversion.

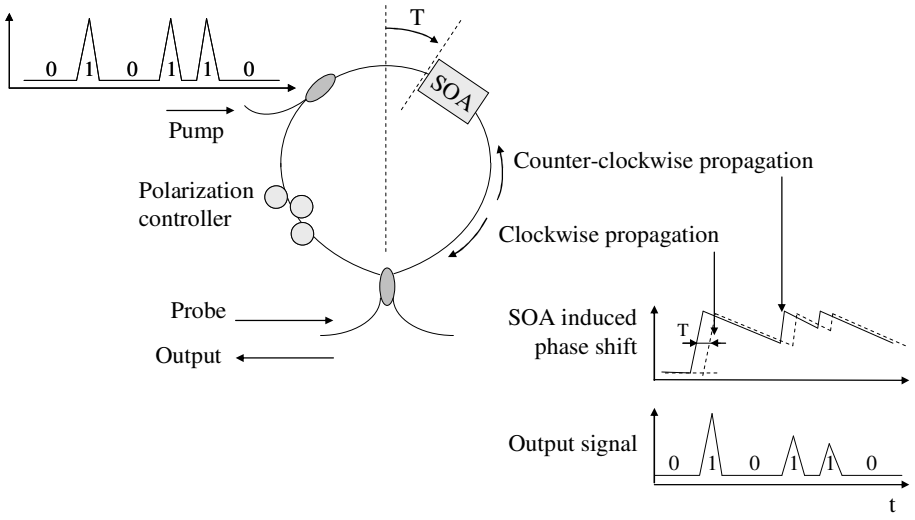

Fig. 2.9 Non-linear optical loop mirror (NOLM) and operating principle schematics.

The NOLM has the significant advantage over the DISC that it does not need a fine tuned optical filter. However, the NOLM requires control of the polarization inside the Sagnac interferometer, since both replicas must have the same polarization to interfere. The NOLM is typically built with optical fibre, which is sensitive to the environmental conditions. Therefore, polarization tracking inside the loop is compulsory, which makes it less practical for real world applications. Wavelength conversion of both RZ and NRZ pulses, and demultiplexing of OTDM signals [34] have been demonstrated using the NOLM [35].

2.3.3 The MZI-SOA, a SOA based Mach-Zehnder interferometer

Both wavelength conversion configurations presented earlier have disadvantages such as the need for optical filter fine tuning, or polarization tracking, which compromise the stability of such devices in a real world application. The MZI-SOA has the advantage over both the DISC and the NOLM of doing away with both the fine tuned optical filter and the polarization controller inside the interferometer [36].

The MZI-SOA, as the DISC and the NOLM, exploits XPM in the SOAs and is depicted with its operating principle in Fig. 2.10. The MZI-SOA is a Mach-Zehnder interferometer with a SOA in each interferometer arm. Two additional ports are connected directly one for each SOA, which do not directly take part in the interferometric action. The probe is fed into one of the interferometer inputs which is then split and fed to the two SOAs. A polarization controller is used at the interferometer input if either the waveguides or the SOAs are polarization sensitive. The SOA outputs are then combined and the chosen interferometer output port is optically filtered to reject the pump signal. The pump signal is split into two replicas before being fed to the SOAs. One is delayed by an amount of time T relatively to the other. A pulse of the non-delayed pump replica arrives first at the SOA and causes a phase shift on the probe through XPM. There is a phase difference between the two probe signals coming out of the SOAs while the pulse of the delayed pump replica does not arrive at the other SOA. Hence, an output pulse arises at the filtered output of the MZI-SOA. When the delayed pump pulse arrives at the SOA, it induces a phase shift on the probe crossing the SOA, and therefore both probes crossing the two SOAs will have a similar phase. Hence, there will be destructive interference at the filtered output and light no longer exits at the MZI-SOA output.

The MZI-SOA operation, as well as the other interferometer-based optical processing devices, can be described by the concept of switching window [37, 38, 39]. Whenever the phase between the probe replicas in each of the interferometer's arms is different, the switching window is open, i.e., and light comes out of the interferometer. When the phase is the same in both arms, the switching window is closed. The method described before, where each of the SOAs receives a pump pulse, is called push-pull or differential method of operation, because it uses two pump replicas [40]. One opens the interferometer's switching window, and the delayed replica closes it. The MZI-SOA can

also be operated with only one pump replica, i.e., not using the push-pull mode. In this case, the maximum bit rate is limited by the gain recovery, similarly to the case of wavelength conversion with a single SOA. Further mechanisms have been devised to reduce the patterning effects, such as the use of asymmetrical interferometers [41], or bidirectional propagation of the input data signal [42].

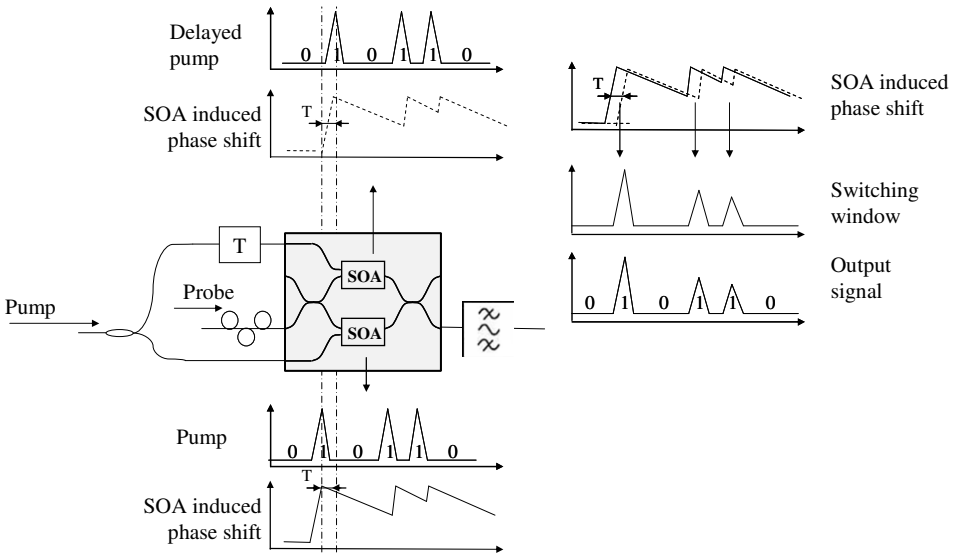

Fig. 2.10 MZI-SOA schematic and operating principle.

The interferometric input of the MZI-SOA is usually coupled to a locally generated signal, although it may be polarization dependent. Therefore it does not require an active polarization controller inside the interferometer, as is the case with the NOLM. Furthermore, polarization independence relatively to the control data input has been demonstrated [43]. The MZI-SOA has also demonstrated superior performance in demultiplexing applications at a high 160 Gb/s bit rate [38], and in logic applications [44]. Another significant advantage of the MZI-SOA is that it has been either hybridly [45] or monolithically [46] integrated. Further to the stability advantage, the integrated devices also have a small form factor, and the possibility of integrating several of these devices in a single chip [47] exists, e.g., MZI-SOA devices with passive devices [48], MZI-SOA with passive devices and linear amplifier SOAs [49], or with other active devices such as lasers [50]. This makes it possible to design larger circuits for performing more advanced functions than the wavelength conversion [51], which will be addressed in the next section.

2.4 Optical processing functions

Wavelength conversion is the simplest optical processing function, but several other functions have also been performed with the MZI-SOA and similar optical processing devices. Some of them are now presented, which will be revisited in the following chapters.

2.4.1 Format conversion

The increase of bit rates in optical networks has set more stringent demands in transmission distances and OSNR margins. In order to cope with tougher requirements, advanced modulation formats have been proposed. However, each modulation format has its own share of advantages and hence is more suitable for a particular scenario. Whereas a comprehensive overview can be found in reference [52], a brief presentation of some modulation formats will be given here. For example, the NRZ-OOK format, usually known as NRZ, has the simplest transmitter and receiver structure and therefore is more adequate for low cost access networks. However, the optical duobinary (ODB), which is still an intensity modulation format, but has a correlated phase shift between bits, has increased tolerance to optical filtering and chromatic dispersion, and therefore has advantages in networks with a narrow equivalent optical filter and reduced chromatic dispersion compensation. Nonetheless, at higher bit rates, the RZ formats have longer reaches in transmission links by taking profit of an appropriate combination of group velocity dispersion (GVD) and self phase modulation (SPM) management. Particularly, the CS-RZ format, due to the π phase shift in every bit, has increased tolerance to non-linear effects. Additionally, RZ formats have the advantage of lower OSNR requirement relatively to NRZ formats due to its lower duty cycle. However, in what concerns the OSNR, phase modulated formats have an even larger advantage when detected differentially, with the differential phase shift keying (DPSK) gaining much popularity.

With all the currently available formats, format conversion between different optical network hierarchies or simply between transmission links using different formats arises as a natural necessity, with the SOA-based devices being good candidates for the job. A few examples of extant work on this matter are now presented in brief. Several

demonstrations of duty cycle adaptation of pure intensity modulated formats have been done in SOA based gates, such as the conversion of RZ-OOK to NRZ [53, 54], or the conversion from NRZ to RZ-OOK [55]. Additionally, phase management has been introduced in a purely intensity modulated format in the NRZ format conversion to vestigial side-band modulation [21] and to CS-RZ [56, 57] in SOAs or SOA-based interferometers. Furthermore, RZ-OOK to CS-RZ conversion was demonstrated in a NOLM [57]. Intensity modulation to phase modualtion conversion of a NRZ signal to RZ-BPSK and to RZ-QPSK was also shown in a MZI-SOA [58, 59]. The interest in differentially detected phase modulation formats has led to the demonstration of regeneration of DPSK signals [60, 61, 62], which effectively utilizes intensity modulation RZ-OOK format conversion to RZ-BPSK.

The previous demonstrations of format conversion make extensive use of the capabilities of SOA-based devices, namely the MZI-SOA, to handle both phase and intensity. The particular reduced chirp property of the MZI-SOA, comparing to other nonlinear gates, have also been exploited advantageously to wavelength convert the payload of a FSK/IM label/payload signal [63].

Conversion between several formats has been demonstrated, with the extant studies focusing more on the demonstration of the functionality rather than on the performance of the format conversion scheme. In chapter 3, format conversion performance in the MZI-SOA will be compared using different modulation formats to investigate the characteristics that determine the conversion performance. From this point forth, when referring to the RZ format, RZ-OOK should be understood.

2.4.2 Multiplexing, demultiplexing, logic and switching

Novel techniques and circuits are required to cope with the increase of the bit rate of individual wavelength channels. Specifically, some networks have been proposed where a number of tributaries are time domain multiplexed and demultiplexed using all-optical techniques – optical time division multiplexing (OTDM) –, which allow the use of lower bit rate electrical transmitters and receivers. In its simplest form, optical multiplexing of tributaries can be achieved by coupling together the tributaries if only with appropriate timing, duty cycle and modulation format. If the timing of the tributaries is not unsuitable,

more complex circuits, usually not all-optical, are required for adapting the incoming tributaries to the requirements of the higher bit rate network [64]. If the timing is suitable, wavelength and duty cycle can be adapted by all-optical means [65, 66, 67]. Nevertheless, these existing circuits lack some of the advantages of the MZI-SOA, such as polarization insensitiveness, gain and integrability. Therefore a more suitable alternative MZI-SOA based circuit will be presented in Chapter 4.

On the other hand, optical time division demultiplexing of a higher bit rate signal to a lower bit rate signal, represented in Fig. 2.11, is also required in OTDM networks. For this functionality, both the high bit rate signal and a demultiplexing gating signal are fed to an optical gate. The demultiplexing signal is a periodic signal matching the timing of the higher bit rate signal bits that are to be demultiplexed. The optical gate can be any one of the devices presented earlier. Demultiplexing in these gates can be performed in two different ways.

The first uses the input data as the probe and the demultiplexing gating signal as the pump. In this case, it is as if the 'data' of the demultiplexing signal is wavelength converted to the probe, which is the true input data. Light pulses appear at the gate output only when the demultiplexing gating signal is present, i.e., every four bits as in the example depicted in Fig. 2.11. However, the probe also contains data, as opposed to a CW signal. Therefore, at the times when there is a pulse in the demultiplexing gating signal, the corresponding input data bit will show up at the gate output, and all the other input data bits will be discarded.

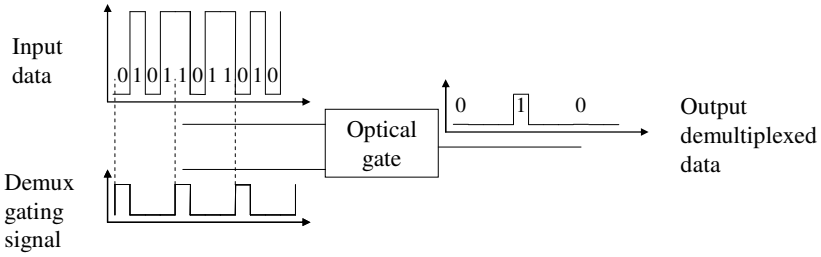

Fig. 2.11 Optical time demultiplexing.

The second way of performing optical time division demultiplexing using an optical gate uses the input data as the pump, and the demultiplexing gating signal as the probe. Again, this can be understood as a wavelength conversion of the input signal to the probe, which is a gating signal instead of a CW. Therefore, there will be data conversion

only in the presence of a pulse in the demultiplexing gating signal, and hence only the desired bits are demultiplexed.

The main difference between the two demultiplexing techniques is in the signal bit rate. On the one hand, in the demultiplexing application, the gating signal has a lower rate than the incoming data signal. On the other hand, the SOAs of the MZI-SOA gate must have a suitable recovery time for handling the bit rate of the pump signal. Therefore, the most advantageous situation as far as the speed is concerned, is to use the signal with the lowest repetition rate as pump, i.e., the gating signal in the control port, since the SOAs do not need to respond as quickly as in the case of a high bit rate data signal.

Demultiplexing has been performed with this MZI-SOA configuration since early in 1995, from 40 Gb/s to 5 Gb/s [68], from 80 Gb/s to 10 Gb/s [69], from 160 Gb/s to 10 Gb/s [70] and from 320 Gb/s to 10 Gb/s [71]. In chapter 4, this functionality of the MZI-SOA will be exploited in a larger optical circuit to perform packet decompression, and will be presented at a later stage. The alternative mode of operation, where the higher bit rate data signal is fed to the control port of the MZI-SOA, is also useful because it can be used to simultaneously demultiplex the incoming OTDM signal and convert it to lower bit rate WDM tributaries [72]. Furthermore, the MZI-SOA has been applied to OTDM networks for performing conversion from 40G OTDM to 4x10G WDM [73], as well as OTDM add and drop of tributaries [74], and demultiplexing with optical clock recovery after transmission [75].

It has been seen that optical time demultiplexing with an optical gate is conceptually similar to wavelength conversion, provided that a gating signal is used instead of a CW signal. In fact, there is only light at the output, when both pump and probe signals are present. From a logical point of view, this is equivalent to the AND operation between the two input signals. Calling the pump and probe data signals A and B, only when both A and B have a logical 1 will there be also a logical 1 at the optical gate output, as depicted in Fig. 2.12.

Other logical operations can be performed using the described optical processing devices. However, these generally require more complex circuits compared to the AND operation. For example, the XOR operation can be performed using the MZI-SOA, with the configuration depicted in Fig. 2.13. The MZI-SOA is not used in the push pull configuration, although the two control ports are used. Each input signal is fed to one of

the control ports acting as pumps, while a CW probe is fed to the interferometric port of the MZI-SOA. In this configuration, there is no push-pull so the gain of the SOAs must recover within the bit slot. When one, and only one, of the input signal contains a mark or logical 1, the corresponding SOA introduces a phase difference between the two arms of the interferometer, and a mark appears at the interferometer output, corresponding to a logical 1. When both inputs correspond to logical 0s, there is no phase difference between the arms of the MZI-SOA and a logical 0 results at the output. When the two input signals are logical 1s, both induce a phase shift in each arm of the MZI-SOA. However, since a shift is introduced in both arms, the phase difference between both arms is zero and therefore a logical 0 is output. Hence, this configuration implements logical XOR operation. It is also possible to use the push-pull technique to perform the XOR operation. However it involves feeding a delayed replica of each input signal to the other control port [76], resulting in a more complex structure.

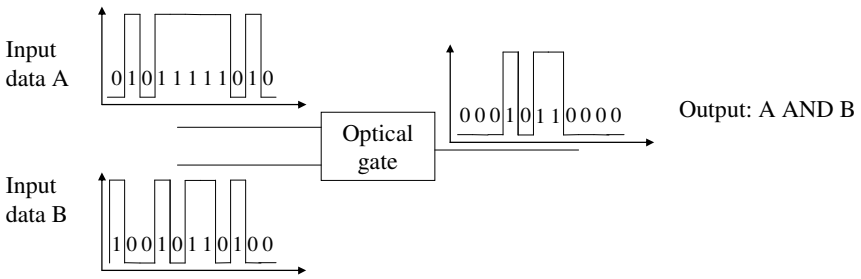

Fig. 2.12 AND logical operation with optical gate.

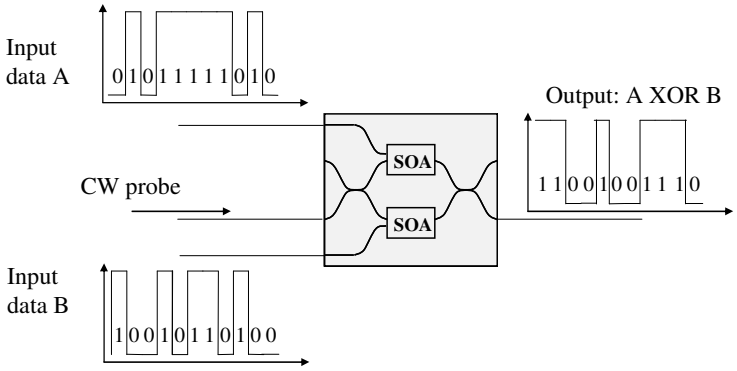

Fig. 2.13 Logical XOR operation in MZI-SOA.

Experimental results with the MZI-SOA based XOR gate have demonstrated better performance than with other interferometric gate at 40 Gb/s [44].

Other logical operations can be achieved with the MZI-SOA, such as the NOR, the OR, and the NAND logical operations, usually requiring more than one gate [77].

Several proposed types of all-optical networks rely on space switching to route packets or bursts over the network. Fast optical packet switches are required, for maximising the network efficiency, since the required guardband time durations can be decreased. Due to both the fast switching time of the MZI-SOA and its pair of output gates, it can also be used as a 1×2 space switch for this application. A 2×2 space switch can also be devised, making use of the two interferometric input ports, as shown in Fig. 2.14.

In the 2×2 space switch configuration, two data signals are fed separately to each of the interferometric inputs of the MZI-SOA. If no light pulse is present in the control port, there is zero phase difference between the arms of the MZI-SOA meaning that, relatively to each one of the input ports, there will be constructive interference on one of the output ports, and destructive interference on the other. Therefore, the incoming signals at inputs 1 and 2 are output at the output ports 1 and 2, respectively. However, in the presence of a control signal, a phase difference arises between both arms of the MZI-SOA. If this phase difference is set to be π, the opposite interference condition to the case without control signal will occur at the outputs of the MZI-SOA. In this case, the signals in input ports 1 and 2 emerge at output ports 2 and 1, respectively. Therefore, a 2×2 space switch is obtained, whose state, either bypass or switch, can be set by the control port.

As an example, depicted in Fig 2.14, data blocks A and B arrive at the input port 1, while data blocks C and D arrive at the input port 2. Blocks A and C arrive at the same time, as well as blocks B and D. At the time that blocks A and C arrive, no control signal is present, and therefore blocks A and C are forwarded to output ports 1 and 2, respectively. Blocks B and D arrive when the control signal is present and so they are switched to ports 2 and 1, respectively. The 1×2 space switch is a particular case of the 2×2 where only one input is used.

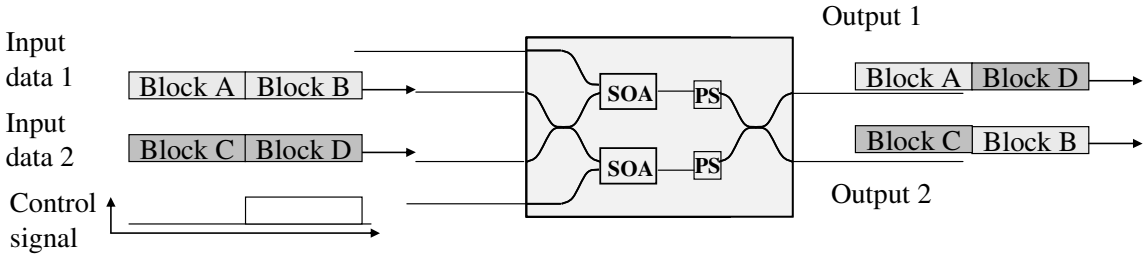

Fig. 2.14 MZI-SOA acting as 2×2 space switch with phase shifters (PS) [78].

The main problem with the space switch configuration is that the contrast ratio of the output ports is imperfect, i.e. the input signals are not completely switched to the desired output port, and some power leaks to the wrong output port. This is due both to the difficulty of setting an exact π phase difference between both arms and to the resulting gain compression of the SOAs. To facilitate optimizing the extinction ratio of both switch outputs, phase shifters are introduced in both arms of the MZI-SOA [78]. The consequence of the imperfect extinction ratio is that crosstalk is introduced in the signals, which may lead to very severe crosstalk penalties when the crosstalk is inband, i.e., has the same optical frequency as that of the signal. In chapter 5, the MZI-SOA will be used as a space switch and its performance is affected by crosstalk.

Switches with 20 dB of extinction ratio have been achieved by using unbalanced bias currents of the SOAs and phase shifters [79, 80].

2.4.3 Regeneration

The signal quality is also affected by other impairments, in addition to the crosstalk. Transmission of optical signals over large distances accumulates ASE noise, and other transmission impairments such as dispersion and nonlinear effects, either intra-channel or inter-channel, such as SPM, XPM and FWM. Although some transmission impairments can be compensated, such as dispersion and, partially, SPM, there is a significant degradation of the signal after transmission over long distances. When the signal quality is unsuitable, usually measured in terms of BER, or eye opening, the signal needs to be regenerated. Full regeneration of a signal generally comprises three operations: re-amplification, re-shaping and re-timing. All-optical re-amplification has become commonplace with the advent of the EDFA, and the SOA has recently been employed as a multi-channel pre-amplifier [81]. Re-shaping and re-timing are harder to achieve all-optically, since they must process each individual bit, as shown in Fig. 2.15. The re-shaping function must change the shape of each bit by redistributing optical noise, and removing distortion and amplitude jitter. The re-timing function resets each bit to the correct time inside the bit slot, and removes timing jitter.

Regenerators that perform re-amplification and re-shaping are commonly called 2R regenerators, while regenerators that also perform re-timing are called 3R regenerators. 3R regenerators usually include a clock recovery block for re-timing the regenerated data.

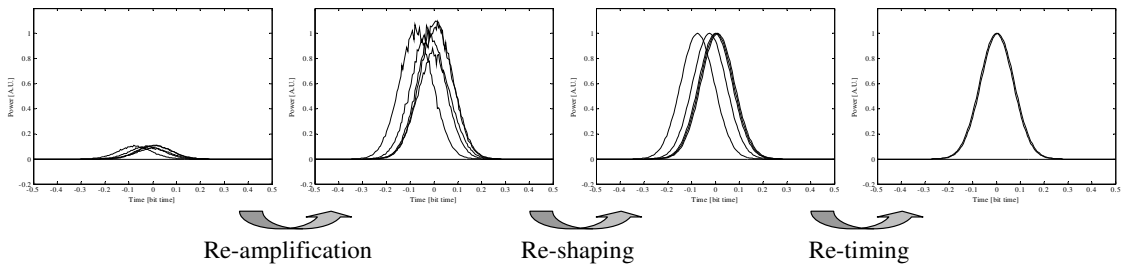

Fig. 2.15 3R regeneration steps: re-amplification, re-shaping and re-timing.

2R regeneration can be achieved by exploiting the MZI-SOA non-linear power transfer function. Fig. 2.16 depicts a 2R regenerator configuration and a MZI-SOA sine like power transfer function. The 2R regeneration function is achieved by exploiting the two flat regions of the nonlinear transfer function. The amplitude noise in the 1 pulses is compressed, and the power of each individual pulse equalized, as illustrated in the example of Fig. 2.16 b). The same happens to the space symbols, whose power can also be reduced, thereby increasing the signal extinction ratio. The regenerator transfer function should be as steep as possible, like a step function, to maximize the regenerative capabilities [82, 83, 84]. However, it is known that no optical 2R regenerator solely described by a nonlinear transfer function can correct errors or improve the BER right at the regenerator's output port. However, a 2R regenerator does help improve the overall BER of links with long spans of fibre after the regenerator [85].

2R regeneration has been performed with MZI-SOAs, at 2.5 Gb/s [86], where its ability to redistribute ASE noise has been demonstrated. More recently, the MZI-SOA has been used to regenerate signals impaired by crosstalk [87], polarization mode dispersion (PMD), [88], and coherent interference from optical code division multiplexing access (OCDMA) [89].

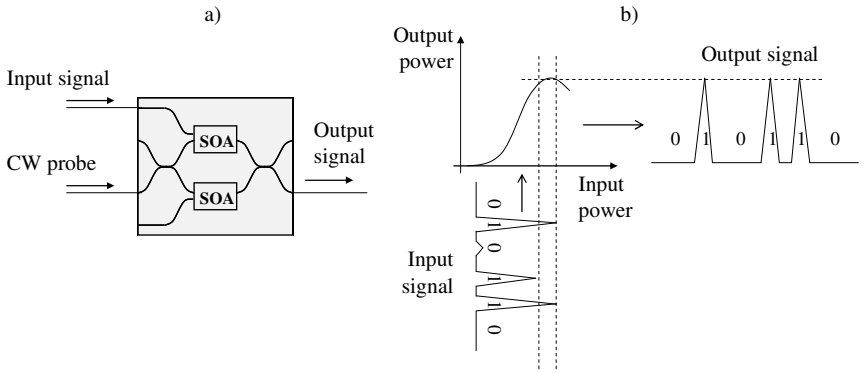

Fig. 2.16 a) Simple (non differential) 2R regeneration configuration with MZI-SOA. b) A typical MZI-SOA power transfer function used for 2R regeneration.

Although 2R regeneration reshapes the signal and removes noise, the re-timing functionality is sometimes critical to avoid accumulation of timing jitter which can cause error floors. Therefore, MZI-SOA based 3R regeneration has also been investigated.

3R regeneration also requires clock recovery which requires additional circuit parts. The 3R regeneration is typically performed by a clock recovery unit followed by a MZI-SOA based 2R regenerator, as depicted in Fig. 2.17 a). The clock recovery unit recovers an optical clock signal from the degraded signal and feeds it to the 2R regenerator, which modulates the clock with the data.

3R regeneration has also been demonstrated using an electronic phase locked loop for recovering an optical clock signal that is then fed to the MZI-SOA [90]. The regenerative capabilities of this optical circuit have also been demonstrated in loop experiments from 10 Gb/s to 40 Gb/s, over several thousands of kilometres [82, 91, 92].

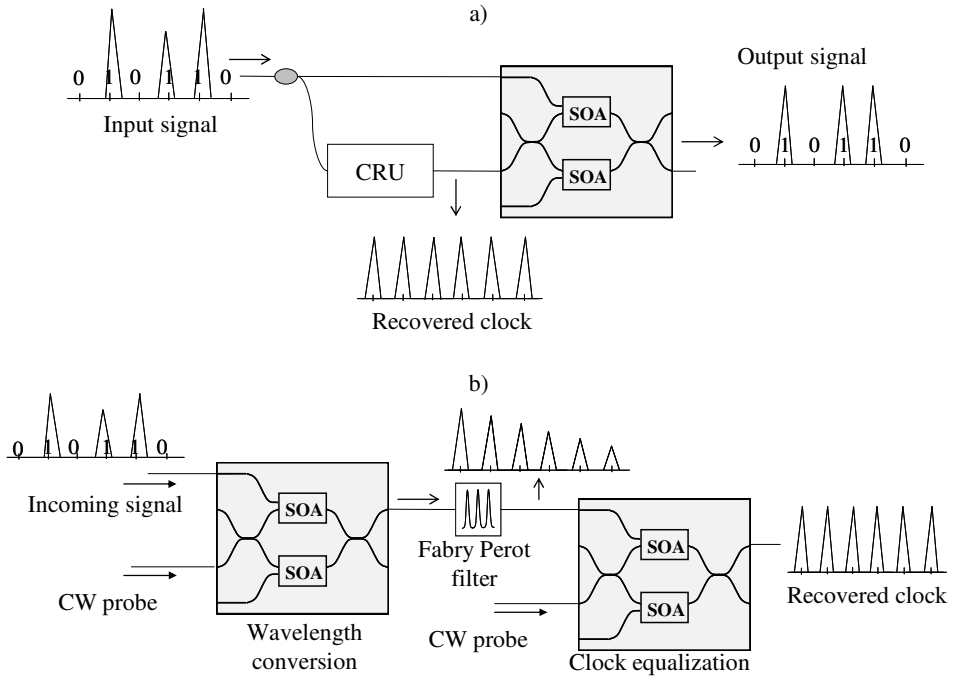

Fig. 2.17 a) 3R regeneration scheme with MZI-SOA and clock recovery unit (CRU). b) CRU based on a Fabry-Perot filter and MZI-SOA for clock equalization.

The clock recovery unit can also consist of an optical Fabry-Perot filter for extracting the clock spectral components of the degraded signal, as shown in Fig. 2.17. The main advantage of the Fabry-Perot filter over the electronic circuit is its very fast clock acquisition time of only a few bits [93], which is particularly useful in packet or burst applications, as is described below. The output of the Fabry-Perot is an exponentially

fading clock signal that is unfortunately unsuitable for direct modulation. Hence, its power is equalized before remodulation by an additional MZI-SOA gate. Since the Fabry-Perot filter requires that the wavelength of the optical signal to be filtered to match the filter's transfer function, it is customary to use a wavelength conversion stage before the Fabry-Perot filter [94]. The wavelength conversion stage can be performed by a MZI-SOA gate which ensures that the adequate signal wavelength is fed to the Fabry-Perot filter.

When a circuit is established in an optical circuit switched network, the optical power of the channel is adjusted and kept constant until the circuit is interrupted. However, in an optical burst or packet switched network, switching occurs at packet or burst level and hence packets or bursts arriving from different node sources may have different optical powers. Therefore, power equalization of packets and bursts is essential in these networks. In this case also, the non-linear transfer function of the MZI-SOA is useful for equalizing the powers of different packets. As in the case of the 2R regenerator, the MZI-SOA flat power transfer function region can be exploited to minimize the differences between the powers of incoming packets. So, only an additional MZI-SOA gate is required for equalizing the power of incoming packets, before the individual bit reshaping (2R regeneration), or re-shaping and re-timing (3R regeneration) [95]. This all-optical circuit is known as an optical burst mode receiver (BMR). The typical schematic of a 3R regenerator BMR is shown in Fig. 2.18. The 2R BMR is similar to the 3R BMR without the clock recovery part.

2R BMRs have been demonstrated with a single MZI-SOA gate with an unbalanced interferometer, which are capable of suppressing a 9 dB power variation between packets [96]. A loop experiment where the BMR successively equalizes the power of packets circulating around the loop has also been reported [97, 98].

The 3R BMR has now been extensively studied, showing remarkable regenerative capabilities, by removing severe error floors due to packet-to-packet power fluctuations [99, 100, 101]. The presented 3R BMR has been performed using four integrated MZI-SOAs in the same chip (quad MZI-SOA gates), demonstrating the integration potential of the MZI-SOA gates. A four wavelength 3R BMR has been demonstrated using three quadruple MZI-SOA gates [102]. The Fabry-Perot fast clock acquisition is crucial in the 3R BMR application, because it minimises packet clock recovery overheads.

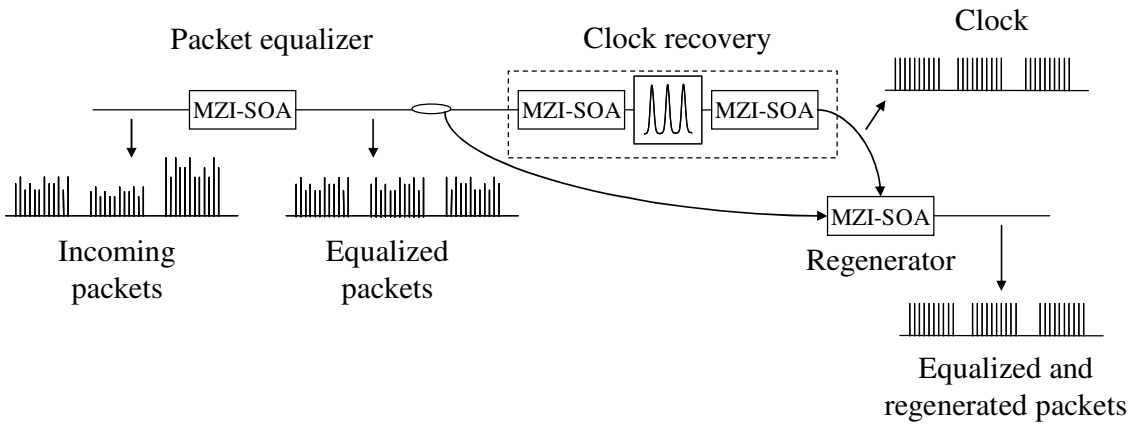

Fig. 2.18 Burst mode receiver based on MZI-SOA and clock recovery on a Fabry-Perot filter.

2.4.4 Further applications in OBS and OPS networks

In either optical packet switching (OPS) or optical burst switching (OBS) networks, data is transmitted in packets or bursts. At each network node, the packets or the bursts are sent to their next destination according to the information contained in the packet or burst header. In-band signalling can be used, in which case the headers are sent immediately before the transmitted data in the same wavelength, or at the same time, using orthogonal modulations. Alternatively, in out-of-band signalling, the header is sent much before the transmitted data, i.e. the payload, in a different wavelength. In-band signalling is employed in all-optical label swapping (AOLS) networks, in which, at each network node, the payload is separately processed from the label, both all-optically [103, 104, 105]. The switching matrix is configured according to the label information, and a new label is appended to the payload and forwarded to the next destination. In these network architectures, an optical circuit is needed to separate the label from the payload of incoming packets, so that the payload goes to the switching matrix while the label is sent to the node control layer for processing.

A MZI-SOA based packet payload label separation circuit has been proposed for RZ formatted packets where the payload follows the header in time and both share the same wavelength [106]. The circuit is composed of a clock recovery circuit and an optical 1×2 switch, as depicted in Fig. 2.19. The clock recovery unit operates as explained earlier, and recovers a clock signal of about the duration of the incoming packet. This part of the circuit is sometimes also called a packet envelope detector (PED) [107]. The clock signal

and a replica of the incoming packet are fed to a MZI-SOA gate operating as a 1×2 space switch. The clock signal acts as the control of the switch, while the packet is fed to the interferometric port. The clock signal is delayed relatively to the incoming packet so that the clock signal may reach the switch at the beginning of the payload. Hence, when the label arrives at the switch, there is no control signal present and the label is forwarded to the unswitched port of the MZI-SOA. On the other hand, when the payload arrives, so does the clock signal, who changes the switch state, forwarding the payload to the switched port of the MZI-SOA. The label and the payload are detached as a result, and ready for processing by the label processing unit and switching matrix, respectively.

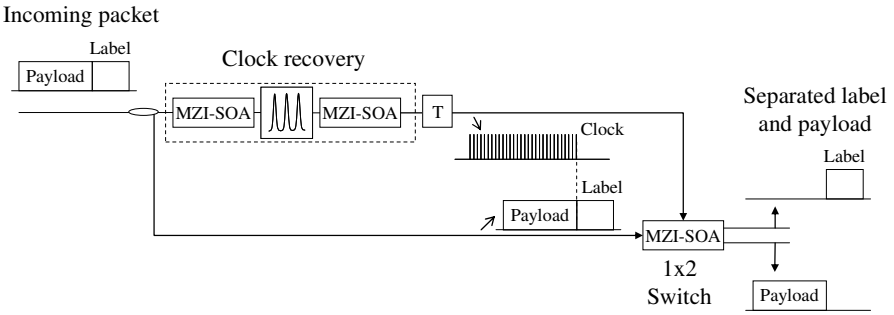

Fig. 2.19 Packet label/payload separation circuit based on MZI-SOA devices.

Experimental results of the packet label and payload separation with MZI-SOA gates at 40 Gb/s have shown a power penalty below 2 dB [106]. An earlier circuit based on the ultrafast nonlinear interferometer (UNI) has been implemented, at 10 Gb/s [108]. A front-end for an all-optical label switching has also been presented, that includes data regeneration in addition to the packet and label separation function [47].

OPS and OBS networks exploit and benefit from statistical multiplexing. However, typically, packets or bursts arriving at network nodes, directed to the same output fibre link contend for the same transmission resources. Contending packets or bursts may be lost, unless a contention resolution mechanism is employed. Contention resolution involves, first of all, detecting the presence of contending packets or bursts. Afterwards, wavelength conversion, or other contention resolution strategies, can be used to resolve conflicts. One MZI-SOA based circuit has been presented for resolving contention by wavelength conversion [109], and is depicted in Fig. 2.20. The circuit resolves contention between two packet streams heading for the same output fibre link. The circuit resolves the contention by converting one of the contending packets into another wavelength on the same output fibre link. The first packet stream is split into two and one part is fed to a PED, which is

described earlier. The other part is directly forwarded to the output. The PED output drives an optical 1×2 space switch and a wavelength conversion unit. The second packet stream is fed to the optical 1×2 space switch, which steers the incoming packets to the output if there is no contention and no packet from the first stream is detected in the PED (P3 in the example of Fig. 2.20). If there is contention and the PED detects a packet in the first stream, the 1×2 space switch steers the packet from the second stream to the wavelength conversion stage (P2 in Fig. 2.20). The wavelength converter converts the wavelength of the incoming packet using the envelope detection signal from the PED. Finally, the wavelength converted packet is sent to the output, where it joins the packet with the original wavelength from the first stream.

Other alternative SOA based implementations of such functionality exist, for example, using cross-coupled injection-locked wavelength converters [110].

An alternative technique for resolving contention uses buffering, for delaying one of the contending packets. More specifically, synchronous OPS or OBS slotted network architectures have also been proposed [111, 112]. In this case, the packet is allocated a suitable empty time slot, before being sent to the next node, thus preventing packet or burst collision and improving the network performance. Optical processing circuits for delaying the packets or burst are required to reallocate them to empty slots. For this purpose, time slot interchangers, which basically delay a packet or burst by a selectable amount of time, have been proposed using SOAs as wavelength converters using recirculating buffers [113] or selectable delays [114], or even current-driven switches [115]. The MZI-SOA is an excellent candidate for designing such functionality and therefore a wavelength converter MZI-SOA based time slot interchanger is presented and evaluated in chapter 4. Additionally, an alternative space switched MZI-SOA based time slot interchanger architecture is analysed in chapter 5.

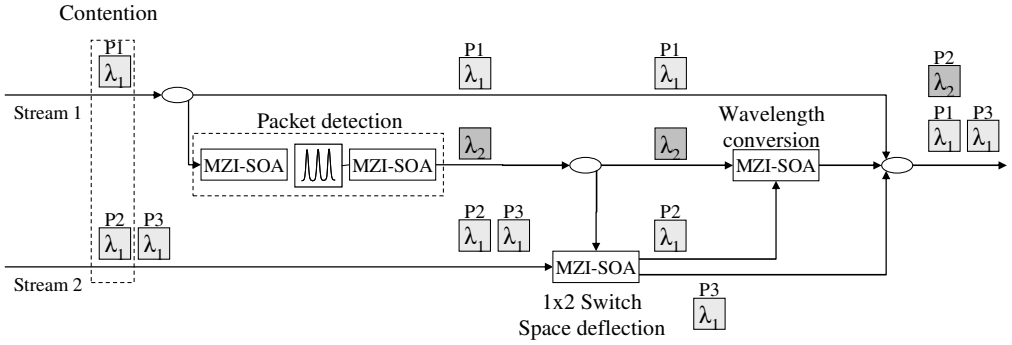

Fig. 2.20 MZI-SOA based packet contention resolution circuit.

The collection of optical processing circuits presented in this Thesis demonstrates the flexibility of the MZI-SOA gates and, more importantly, their usefulness to future generation optical networks. A few more functionalities performed with the MZI-SOA are now enumerated, without much detail, as a reference for the reader.

The MZI-SOA device has been used as a self-switching device [95], low loss power coupler [116], optical flip-flop [117], and pulse compressor [118]. It has also been employed to do data multicasting [119], simultaneous payload wavelength conversion and label re-rewriting [120], label stripping [121], and pattern recognition [122]. This list does not purport to be complete or exhaustive. The intention is to demonstrate the wide range of applications that can be addressed with the MZI-SOA gate, and hence its universality.

2.4.5 The performance of all-optical processing circuits

Up to this point, optical processing circuits have been presented only from a functional perspective. However, their usefulness ultimately depends on their performance, in the sense that the output signal must have enough quality for conveying information reliably to subsequent detection or other circuits. As amplifying circuit elements, SOAs introduce ASE noise, and OSNR degradation will occur as the signal passes through several MZI-SOAs in the optical circuits. Other impairments detrimental to the signal quality are also caused by the MZI-SOA, depending on its mode of operation.

It was already mentioned that MZI-SOAs operating as space switches, add crosstalk to the signal, although, clearly, crosstalk is not exclusive of the MZI-SOA space switch. Large penalties can result when the crosstalk has the same optical frequency as the signal. The penalties increase further when more than one space switch is required, such as in a large switching matrix. Typically, the receiver has a limited tolerance to crosstalk and therefore only a certain penalty can be tolerated. Hence, the space switch size, or, equivalently, the number of individual space switches must be limited depending on the penalty they introduce. This is an important aspect of optical circuits operation, since they must compare favourably to their electronic counterparts. This aspect is all the more important if other impairments exist that also affect the signals suffering crosstalk, such as the group velocity dispersion (GVD) or SPM arising in long-haul transmission. It is widely recognized that the operating margins of the network are reduced as transmission distances

and bit rates increase, and more and more impairments kick in and affect the signal performance [123]. Certainly, the regenerators described earlier can improve the signal quality, if only at the expense of additional complex circuitry and associated cost. Therefore, it is imperative to accurately characterize the impact of such impairments to minimize the number of regenerators in the network and/or to extend the signal range. Hence, chapter 5 is dedicated to the analysis of crosstalk in some relevant network scenarios. There, a method is derived for calculating the BER of a signal impaired by pulse distortion, e.g., due to filtering, and, simultaneously, crosstalk and ASE. A MZI-SOA space switched based time slot interchanger is analysed, and the maximum time slot interchanger size (i.e., the number of permissible individual space switches) is assessed. Moreover, this method enables the performance estimation of a network with both narrow filtering and crosstalk, which is used to calculate the maximum permissible number of optical add-drop multiplexers.

Crosstalk is not an issue when the MZI-SOA is operated in a non-switching mode, i.e., when the MZI-SOA is operated with one interferometric input and output. However, in this case, the pump signal saturates the SOAs and the dynamics of the SOA gain recovery can influence the shape of the output signal as the bit rate increases. Moreover, the shape of the input signals may influence the performance of the particular MZI-SOA application. Clearly, the output signal quality depends both on the input signal and on the operating conditions and the MZI-SOA device parameters. Inter-symbolic interference occurs when the MZI-SOA operates in such a way where the gain recovery affects the next bit, and, consequently, the signal performance is degraded. As the signal travels across several MZI-SOA devices, its shape will be successively affected by each of the MZI-SOA temporal response. The MZI-SOA based optical processing circuits investigated in chapters 3 and 4 fall under such conditions. Therefore, it is crucial to model the temporal response of the MZI-SOA accurately. Accordingly, the following section presents a SOA mathematical time-model for modelling both the SOA and MZI-SOA based circuits.

2.5 SOA and MZI-SOA models

Several models have been proposed to describe the SOA operation. Reference [124] presents a comparison of the features of several SOA models. The most basic feature of

SOA modelling is the gain saturation as a function of the input power. The gain saturation models can be either dynamic or static. Dynamic models can predict the SOA operation with high bit rate signals in nonlinear regime, whereas static models can provide useful physical insight of the phenomena in the SOA and are also applicable in the linear regime (amplification). Some models resort to the carrier density to calculate the gain, while other models directly calculate the gain from optical input power. Some models account for the spectral shape, i.e., the gain dependence on the wavelength, while others simply assume a constant gain over the wavelength region of interest, usually a few nanometers for accommodating the simulated signals. However, for multi-channel simulations, the wavelength dependence may become relevant. A spatial description of the signal transmission through the SOA is also desirable when the SOA is long or when in deep saturation, which causes the carrier spatial distribution to be very non-uniform along the length of the SOA. Some models divide the SOA in several sections to account for this effect, while other resort to analytical integration of the carrier density spatial profile. Although the analytical integration of the spatial profile of the carrier density results in a much faster computation, sometimes approximations are made, and both co-propagation and counter-propagation of optical beams are not considered. The gain recovery must be accurately modelled at very high bit rates, where the SOA time response is critical. In this case, both the slower inter-band effects and the intra-band effects play an important role and have to be considered. Intra-band effects can be taken into account by using effective parameters that compress the gain, but a more accurate description requires separate time equations for the different effects.

Appendix A describes the derivation of tractable amplifier equations for both the amplitude and phase of a signal travelling inside a SOA. The key equations are

$$P(t,L) = G(t)P(t,0) \tag{2.1}$$

for the optical power at the output and input of the SOA *P(t, L)* and *P(t,* 0*)*, respectively, and

$$\phi(t,L) = -\frac{\alpha}{2}\ln[G(t)] + \phi(t,0) \tag{2.2}$$

for the phase, where

$$G(t) = e^{h(t)} \tag{2.3}$$

is the amplifier gain taken as the relation of the output and input powers and

$$h(t) = \int_0^L g(t,z)dz \quad . \tag{2.4}$$

g is the local SOA gain, t the time and z the longitudinal coordinate of the SOA, ranging from 0 to L. The spatial dependence of G and h (see Appendix A) has been dropped since the main interest is the value of these quantities at the SOA output facet, at $z=L$.

The model of the dependence of the gain g on the input optical signal adopted in this work has been proposed in references [125, 126]. The derivation is lengthy and not straightforward, and hence it is not reproduced here, but the main ideas are illustrated in what follows.

The model aims to describe the inter-band carrier depletion, and the intra-band phenomena of carrier heating (CH) and spectral hole burning (SHB). Carrier depletion is due to the recombination of electrons in the conduction band with holes in the valence band. The recovery of this kind of depletion is typically achieved by electrical pumping and has a time scale of between tens of picoseconds and nanoseconds, depending on the SOA operating conditions and fabrication method. When a light pulse enters the SOA, free carriers recombine resulting in carrier depletion such that the remaining carriers are left with an energy distribution that is not in equilibrium. For a narrow band optical pulse, only the electron-hole pairs that have an energy difference that matches the photon energy recombine and provide optical gain. As a result, a spectral hole in the energy distribution arises, hence the name SHB. Through fast (sub-picosecond) carrier scattering, the carrier energy is distributed, tending to an equilibrium distribution and the spectral hole disappears. However, the new equilibrium distribution is a Fermi distribution with a higher temperature (depending on the pulse wavelength [124]) than the lattice temperature, thus the name of carrier heating. Through phonon emission, the carrier temperature cools down to the lattice temperature in a picosecond time scale. Electrical pumping restores the recombined carriers to their initial distribution, in the absence of an optical pulse.

The equations that model these phenomena are given by [125]

$$\frac{\partial N(t)}{\partial t} = \frac{I}{eV} - \frac{N(t)}{\tau_s} - v_g g(t) S(t) \tag{2.5}$$

$$\frac{\partial n_\beta(t)}{\partial t} = -\frac{n_\beta(t) - \overline{n}_\beta}{\tau_{SHB,\beta}} - v_g g(t) S(t) \tag{2.6}$$

$$\frac{\partial T_\beta(t)}{\partial t} = \left(\frac{\partial U_\beta(t)}{\partial T_\beta(t)}\right)^{-1}\left(\frac{\partial U_\beta(t)}{\partial N(t)} - E_{\beta,0}\right) v_g g(t) S(t) - \frac{T_\beta(t) - T_L}{\tau_{h,\beta}} \quad . \tag{2.7}$$

Equation (2.5) is the rate equation of the total free carriers in the medium. It states that the total carrier density N varies in time due to electrical pumping, spontaneous emission and stimulated emission. I, e, and V are the pumping current, electron charge and the volume of the active SOA region, respectively. τ_s is the carrier lifetime, v_g is the group velocity of the light beam and S is the photon density inside the SOA.

The second equation, Eq. (2.6), quantifies the variation of the local carrier density n_β, for carriers that have an energy difference corresponding to the incoming light energy and hence are effectively coupled to the incoming light. The symbol β=e,l, represents electrons and holes, respectively. The variation of the local carrier densities depends on two parts. One part is responsible for compensating deviations from the equilibrium value, $\bar{n}_\beta$, through carrier-carrier scattering, with carrier-carrier scattering times, $\tau_{SHB,\beta,}$, associated to the SHB effect. The other part is the stimulated emission which causes the carrier density deviation from equilibrium. The equilibrium value of the local carrier density $\bar{n}_\beta$ depends on the total carrier density and also on the carrier temperatures T_β.

The last equation, Eq. (2.7), relates the variations of the electron and hole temperatures T_β (carrier heating) arising from the re-distribution of the carriers energy due to stimulated emission, which heats the carriers, and the phonon emission that thermalises the carriers to the lattice temperature T_L. U_β is the total energy density, $E_{\beta,0}$ is the mean carrier energy, and $\tau_{H,\beta}$ are the temperature relaxation times.

For deriving practical equations of the SOA dynamics, the local gain g is expressed as a function of the carrier densities as

$$g = \frac{a_N}{v_g}\left(n_e + n_l + N_0\right) \tag{2.8}$$

where a_N is the material gain and N_0 is the density of available states in optically coupled region. The task now is to translate a variation of total and local carrier densities and temperature in a variation of gain. For the total and local carrier density equations this is achieved with Eq. (2.8), while for the temperature equation, the temperature variation is related to the consequent local densities change. The resulting equations are [125, 126]

$$\frac{\partial h_N}{\partial t} = -\frac{h_N}{\tau_s} - \frac{1}{P_s \tau_s}\left[G(t)-1\right]P_{in}(t) + \frac{h_0}{\tau_s} \tag{2.9}$$

$$\frac{dh_{SHB}}{dt} = -\frac{h_{SHB}}{\tau_{SHB}} - \frac{\varepsilon_{SHB}}{\tau_{SHB}}\left[G(t)-1\right]P_{in}(t) - \frac{dh_{CH}}{dt} - \frac{dh_N}{dt} \tag{2.10}$$

$$\frac{\partial h_{CH}}{\partial t} = -\frac{h_{CH}}{\tau_H} - \frac{\varepsilon_{CH}}{\tau_H}\left[G(t)-1\right]P_{in}(t) \tag{2.11}$$

$$h = h_N + h_{CH} + h_{SHB} \tag{2.12}$$

where h_N represents the logarithmic integral SOA gain from the carrier recombination and h_{CH} and h_{SHB} represent the logarithmic integral gain compression due to carrier heating and SHB, respectively. The logarithmic integral gains are defined, for each term, according to Eq. (2.4). ε_{SHB} and ε_{CH} are the nonlinear gain suppression factors for SHB and carrier heating, respectively, and h_0 is the unsaturated logarithmic integral SOA gain. P_s is the saturation power parameter and P_{in} is the optical power at the SOA input.

Due to the nature of the carrier heating, the phase shift due to the gain compression from carrier heating is different from the phase shift from the carrier depletion. Hence, the total phase shift is written as a contribution of the two phenomena, while SHB does not contribute at all

$$\Delta\phi = -\frac{\alpha_N}{2}h_N - \frac{\alpha_{CH}}{2}h_{CH} \tag{2.13}$$

where α_N and α_{CH} are the linewidth enhancement factors for the gain compression due to carrier depletion and carrier heating, respectively.

Equations (2.1) and (2.13) defining the gain and phase rotation of a signal inside the SOA, the set of equations (2.9) – (2.12) that enable the calculation of the SOA gain, and appropriate initial conditions for solving the differential equations, together provide a useful model to investigate the SOA performance in system applications. Appendix B discusses initial conditions in more detail.

The SOA model can also be straightforwardly used to build a MZI-SOA model for simulating the MZI-SOA non-linear processing capabilities that is used in the following chapters. Recall from the schematics of Fig. 2.10, that the MZI-SOA has one SOA in each interferometer arm. The two interferometer inputs, where the optical signals are fed to the MZI-SOA, are connected through a 2×2 ports directional coupler. The outputs of the directional coupler are then coupled in a Y junction to the control inputs of the MZI-SOA.

The outputs of the Y junctions each lead to one SOA. The two SOA outputs are then coupled together in a second 2×2 ports directional coupler. The outputs of the directional coupler are the two MZI-SOA outputs. The directional couplers introduce a 90º phase shift between the two split or coupled signals. An experimental characterization of an MZI-SOA, as well as of its constitutive SOAs, is described in the next chapter. Parameters for the simulation model are drawn from that characterization and simulation results are compared to experimental observations.

The simulation models of the SOA and MZI-SOA produce the time dependence of the optical signal describing the devices dynamics. These models enable a comparison between the simulated signals and the experimental signals analysed either by the oscilloscope or the optical spectrum analyser. However, the quantity of most interest that characterizes the quality of an optical signal is the BER. In order to have a BER estimate of a simulated signal, the noise created throughout the system under study can be taken into account either by generating random samples or analytically, usually known as the Monte Carlo or the semi-analytical simulation, respectively. The Monte Carlo simulation is generally recognized as the most accurate simulation method. However, it requires a significant number of simulation runs and therefore considerable computational time to obtain meaningful results. This is even more applicable as the BER values of interest are smaller, as more simulation runs are necessary. Alternatively, the semi-analytical simulation requires only one simulation run, since its results stem from an analytical description of the noises present in the system. The noise probability density functions (PDF) at the receiver can be accurately modelled, usually at the expense of considerable computational effort. Fortunately, approximate methods have been devised for estimating the BER of an optical signal which are both accurate and simple enough so that the computational effort remains small.

The Gaussian approximation for the noise at the receiver stands out for its simplicity, while retaining adequate accuracy, as long as the variances are correctly modelled [127, 128]. The method presented in reference [127] allows to accurately calculate the variances due to ASE and electrical noise for arbitrary optical and electrical filter shapes, for an intensity modulated signal impaired by intersymbolic interference. This method as proved to be fast to compute and to provide accurate results when compared to more rigorous methods [127, 129] or to experimental results [128], and

therefore it shall be used throughout this Thesis to estimate the BER of an intensity modulated signal. Naturally, from the moment that the BER can be calculated, a power penalty or OSNR penalty can be promptly determined by varying, respectively, the signal input power or the OSNR fed to the receiver.

2.6 References

[1] J. Baliga, R. Ayre, K. Hinton, W. Sorin, and R. Tucker, "Energy Consumption in Optical IP Networks," *IEEE/OSA Journal of Lightwave Technology*, vol. 27, pp. 2391–2403, July, 2009.

[2] D. J. Blumenthal and M. Usami, "Optical signal processing: The roadmap towards high-speed optical packet/burst switching," *in Proc. European Conference on Optical Communication (ECOC)*, p. 5.6.1, 2009.

[3] M. Zukerman, "Increasing scope for circuit switching in the optical internet," *in Proc. International Conference on Transparent Optical Networks*, p. Mo.D2.1, 2009.

[4] A. Poustie, "SOA-based All-optical Processing," *in Proc. Optical Fiber Communication Conference (OFC)*, p. OWF1, March 2007.

[5] G. Epps, D. Tsiang, and T. Boures, "System power challenges," *in proc. of Cisco Routing Research Seminar*, 2006.

[6] I. Keslassy, S. Chuang, K. Yu, D. Miller, M. Horowitz, O. Solgaard, and N. McKeown, "Scaling Internet routers using optics (extended version)," tech. rep., Stanford HPNG Tech. Rep. TR03-HPNG-080101 (Stanford University, 2003), available online at http://yuba.stanford.edu/techreports/TR03-HPNG-080101.pdf.

[7] K. E. Stubkjaer, "Technologies for optical processing," *in Proc. Optical Fiber Communication Conference (OFC)*, p. OMV1, Feb. 2008.

[8] J. Lee, K. Kikuchi, T. Nagashima, T. Hasegawa, S. Ohara, and N. Sugimoto, "All fiber-based 160-Gbit/s add/drop multiplexer incorporating a 1-m-long Bismuth Oxide-based ultra-high nonlinearity fiber," *OSA Optics Express*, vol. 13, no. 18, pp. 6864–6869, 2005.

[9] K. Asakawa, Y. Sugimoto, Y. Watanabe, N. Ozaki, A. Mizutani, Y. Takata, Y. Kitagawa, H. Ishikawa, N. Ikeda, K. Awazu, *et al.*, "Photonic crystal and quantum dot technologies for all-optical switch and logic device," *New Journal of Physics*, vol. 8, no. 208, pp. 1–26, 2006.

[10] M. Pelusi, V. Ta'eed, M. Lamont, S. Madden, D. Choi, B. Luther-Davies, and B. Eggleton, "Ultra-High Nonlinear As_2S_3 Planar Waveguide for 160-Gb/s Optical Time-Division Demultiplexing by Four-Wave Mixing," *IEEE Photonics Technology Letters*, vol. 19, no. 19, pp. 1496–1498, 2007.

[11] V. Almeida, C. Barrios, R. Panepucci, and M. Lipson, "All-optical control of light on a silicon chip," *Nature*, vol. 431, no. 7012, pp. 1081–1084, 2004.

[12] A. Driessen, H. Hoekstra, F. Horst, G. Krijnen, B. Offrein, J. van Schoot, P. Lambeck, and T. Popma, "All-optical integrated optic devices: a hybrid approach," *IEE Proceedings-Optoelectronics*, vol. 145, no. 4, pp. 227–235, 1998.

[13] A. Poustie, "Semiconductor devices for all-optical signal processing," *in Proc. European Conference on Optical Communication (ECOC)*, vol. We3.5.1, 2005.

[14] M. Connelly, *Semiconductor Optical Amplifiers*. Kluwer Academic Publishers, 2002.

[15] CIP - Centre for Integrated Photonics, *Online at www.ciphotonics.com*.

[16] Alphion, *Online at www.alphion.com*.

[17] QPhotonics, *Online at www.qphotonics.com*.

[18] InPhenix, *Online at www.inphenix.com*.

[19] Covega, *Online at www.covega.com*.

[20] Amphotonix, *Online at www.kamelian.com*.

[21] T. Silveira, A. Teixeira, A. Ferreira, and P. Monteiro, "All-Optical Vestigial Sideband Generation Using a Semiconductor Optical Amplifier," *IEEE Photonics Technology Letters*, vol. 18, no. 21, pp. 2212–2214, 2006.

[22] K. Stubkjaer *et al.*, "Semiconductor optical amplifier-based all-optical gates for high-speed optical processing," *IEEE Journal of Selected Topics in Quantum Electronics*, vol. 6, no. 6, pp. 1428–1435, 2000.

[23] T. Akiyama, M. Sugawara, and Y. Arakawa, "Quantum-dot semiconductor optical amplifiers," *Proceedings of the IEEE*, vol. 95, pp. 1757–1766, Sept. 2007.

[24] G. Contestabile, A. Maruta, S. Sekiguchi, K. M. M. Sugawara, and K. Kitayama, "160 Gb/s Cross Gain Modulation in Quantum Dot SOA at 1550 nm," *in Proc. Optical Fiber Communication Conference (OFC)*, p. PD1.4, 2009.

[25] C. Joergensen, S. Danielsen, K. Stubkjaer, M. Schilling, K. Daub, P. Doussiere, F. Pommerau, P. Hansen, H. Poulsen, A. Kloch, M. Vaa, B. Mikkelsen, E. Lach, G. Laube, W. Idler, and K. Wunstel, "All-optical wavelength conversion at bit rates above 10 Gb/s using semiconductor optical amplifiers," *IEEE Journal of Selected Topics in Quantum Electronics*, vol. 3, pp. 1168–1180, Oct 1997.

[26] Y. Miyazaki, T. Miyahara, K. Takagi, K. Matsumoto, S. Nishikawa, T. Hatta, T. Aoyagi, and K. Motoshima, "Polarization-insensitive SOA-MZI monolithic all-optical wavelength converter for full C-band 40Gbps-NRZ operation," *in Proc. European Conference on Optical Communication (ECOC)*, p. Th3.4.2, 2006.

[27] Y. Ueno, S. Nakamura, K. Tajima, and S. Kitamura, "New wavelength converter for picosecond RZ pulses," *in Proc. European Conference on Optical Communication (ECOC)*, vol. 1, pp. 657–658, Sep 1998.

[28] M. Nielsen, J. Mork, J. Sakaguchi, R. Suzuki, and Y. Ueno, "Reduction of nonlinear patterning effects in SOA-based all optical switches using optical filtering," *in Proc. Optical Fiber Communication Conference (OFC)*, p. OThE7, 2005.

[29] Y. Ueno, S. Nakamura, and K. Tajima, "Penalty-free error-free all-optical data pulse regeneration at 84 Gb/s by using a symmetric-Mach-Zehnder-type semiconductor regenerator," *IEEE Photonics Technology Letters*, vol. 13, pp. 469–471, May 2001.

[30] M. Galili, H. Mulvad, L. Oxenlowe, H. Ji, A. Clausen, and P. Jeppesen, "640 Gbit/s wavelength conversion," *in Proc. Optical Fiber Communication Conference (OFC)*, p. OTuD4, 2008.

[31] S. Nakamura, Y. Ueno, and K. Tajima, "168-Gb/s all-optical wavelength conversion with a symmetric-Mach-Zehnder-type switch," *IEEE Photonics Technology Letters*, vol. 13, pp. 1091–1093, Oct 2001.

[32] J. Sokoloff, P. Prucnal, I. Glesk, and M. Kane, "A terahertz optical asymmetric demultiplexer (TOAD)," *IEEE Photonics Technology Letters*, vol. 5, no. 7, pp. 787–790, 1993.

[33] M. Eiselt, W. Pieper, and H. Weber, "SLALOM: semiconductor laser amplifier in a loop mirror," *IEEE/OSA Journal of Lightwave Technology*, vol. 13, no. 10, pp. 2099–2112, 1995.

[34] S. Diez, R. Ludwig, and H. Weber, "Gain-transparent SOA-switch for high-bitrate OTDM add/dropmultiplexing," *IEEE Photonics Technology Letters*, vol. 11, no. 1, pp. 60–62, 1999.

[35] J. Yu, X. Zheng, C. Peucheret, A. Clausen, H. Poulsen, and P. Jeppesen, "All-optical wavelength conversion of short pulses and NRZ signals based on a nonlinear optical loop mirror," *IEEE/OSA Journal of Lightwave Technology*, vol. 18, no. 7, pp. 1007–1017, 2000.

[36] B. Mikkelsen, K. Jepsen, M. Vaa, H. Poulsen, K. Stubkjaer, R. Hess, M. Duelk, W. Vogt, E. Gamper, E. Gini, P. Besse, H. Melchior, S. Bouchoule, and F. Devaux, "All-optical wavelength converter scheme for high speed RZ signal formats," *IEE Electronics Letters*, vol. 33, pp. 2137–2139, Dec 1997.

[37] R. Schreieck, M. Kwakernaak, H. Jackel, E. Gamper, E. Gini, W. Vogt, and H. Melchior, "Ultrafast switching dynamics of Mach-Zehnder interferometer switches," *IEEE Photonics Technology Letters*, vol. 13, pp. 603–605, Jun 2001.

[38] C. Schubert, J. Berger, S. Diez, H. Ehrke, R. Ludwig, U. Feiste, C. Schmidt, H. Weber, G. Toptchiyski, S. Randel, *et al.*, "Comparison of interferometric all-optical switches fordemultiplexing applications in high-speed OTDM systems," *IEEE/OSA Journal of Lightwave Technology*, vol. 20, no. 4, pp. 618–624, 2002.

[39] R. Schreieck, M. Kwakernaak, H. Jackel, and H. Melchior, "All-optical switching at multi-100-Gb/s data rates with Mach-Zehnder interferometer switches," *IEEE Journal of Quantum Electronics*, vol. 38, pp. 1053–1061, Aug 2002.

[40] R. Hess, M. Duelk, W. Vogt, E. Gamper, E. Gini, P. Besse, H. Melchior, B. Mikkelsen, K. Jepsen, M. Vaa, *et al.*, "Novel method for all-optical wavelength conversion of RZ pulses for penalty free operation over the entire EDFA window using a monolithically integrated Mach-Zehnder interferometer," *in Proc. Opt. Amplifiers and Applications*, 1997.

[41] Q. Xu, M. Yao, Y. Dong, W. Cai, and J. Zhang, "Experimental demonstration of pattern effect compensation using an asymmetrical Mach-Zehnder interferometer with SOAs," *IEEE Photonics Technology Letters*, vol. 13, pp. 1325–1327, Dec 2001.

[42] M. Hattori, K. Nishimura, R. Inohara, and M. Usami, "Bidirectional Data Injection Operation of Hybrid Integrated SOA–MZI All-Optical Wavelength Converter," *IEEE/OSA Journal of Lightwave Technology*, vol. 25, no. 2, pp. 512–519, 2007.

[43] J.-Y. Emery, M. Picq, F. Poingt, F. Gaborit, R. Brenot, M. Renaud, B. Lavigne, and A. Dupas, "Optimised 2R all-optical regenerator with low polarisation sensitivity penalty (<1 dB) for optical networking applications," *in Proc. Optical Fiber Communication Conference (OFC)*, p. MB4, 2001.

[44] X. Yang, A. Mishra, R. Manning, R. Webb, G. Maxwell, A. Poustie, and R. Harmon, "Comparison of All-Optical XOR Gates at 42.6 Gbit/s," *in Proc. European Conference on Optical Communication (ECOC)*, p. P062, 2007.

[45] G. Maxwell, B. Manning, M. Nield, M. Hadow, C. Ford, M. Clements, S. Lucas, P. Townley, R. McDougall, S. Oliver, R. Cecil, L. Johnston, I. Poustie, R. Webb, I. Lealman, L. Rivers, J. King, S. Perrin, R. Moore, I. Reid, and D. Scrase, "Very low coupling loss, hybrid-integrated all-optical regenerator with passive assembly," *in Proc. European Conference on Optical Communication (ECOC)*, p. PD3.5, Sept. 2002.

[46] R. Hess, J. Leuthold, J. Eckner, C. Holtmann, and H. Melchior, "All-optical space switch featuring monolithic InP-waveguide semiconductor optical amplifier interferometer," *in Proc. Opt. Amplifiers and Applications, Davos, Switzerland*, p. PD 2, June 1995.

[47] P. Zakynthinos, D. Apostolopoulos, O. Zouraraki, D. Petrantonakis, G. Theophilopoulos, A. Poustie, G. Maxwell, and H. Avramopoulos, "Single Chip Quad MZI array in a 40 Gb/s AOLS Front-end," *in Proc. Optical Fiber Communication Conference (OFC)*, p. OWH7, March 2007.

[48] G. Maxwell, R. McDougall, R. Harmon, M. Nield, L. Rivers, A. Poustie, F. Gunning, M. Yang, A. Ellis, R. Webb, and R. Manning, "WDM-enabled, 40 Gb/s hybrid integrated all-optical regenerator," *in Proc. European Conference on Optical Communication (ECOC)*, vol. 6, p. Th4.2.2, Sept. 2005.

[49] R. McDougall, G. Maxwell, R. Harmon, A. Poustie, L. Rivers, and P. Townley, "40Gb/s hybrid integrated all-optical SOA-MZI regenerator incorporating separately optimised SOAs on-chip time delays and WDM combiners," *in Proc. European Conference on Optical Communication (ECOC)*, p. Th3.4.6, 2006.

[50] M. Masanovic, V. Lal, J. Barton, E. Skogen, L. Coldren, and D. Blumenthal, "Monolithically integrated Mach-Zehnder interferometer wavelength converter and widely tunable laser in InP," *IEEE Photonics Technology Letters*, vol. 15, no. 8, pp. 1117–1119, 2003.

[51] M. Renaud, D. Keller, N. Sahri, S. Silvestre, D. Prieto, F. Dorgeuille, F. Pommereau, J. Emery, E. Grard, and H. Mayer, "SOA-based optical network components," *in Proc. 51st Electronic Components and Technology Conference*, pp. 433–438, 2001.

[52] P. Winzer and R. Essiambre, "Advanced optical modulation formats," *Proceedings of the IEEE*, vol. 94, no. 5, pp. 952–985, 2006.

[53] T. Silveira, A. Teixeira, G. Tosi Beleffi, D. Forin, P. Monteiro, H. Furukawa, and N. Wada, "All-Optical Conversion From RZ to NRZ Using Gain-Clamped SOA," *IEEE Photonics Technology Letters*, vol. 19, no. 6, pp. 357–359, 2007.

[54] L. Banchi, M. Presi, A. D'Errico, G. Contestabile, and E. Ciaramella, "All-Optical 10 and 40 Gbit/s RZ-to-NRZ Format and Wavelength Conversion Using Semiconductor Optical Amplifiers," *IEEE/OSA Journal of Lightwave Technology*, vol. 28, no. 1, 2010.

[55] X. Yang, A. Mishra, R. Manning, R. Webb, and A. Ellis, "All-optical 42.6 Gbit/s NRZ to RZ format conversion by cross-phase modulation in single SOA," *Electronics Letters*, vol. 43, no. 16, pp. 890–892, 2007.

[56] T. Silveira, A. Ferreira, A. Teixeira, and P. Monteiro, "40-Gb/s Multichannel NRZ to CSRZ Format Conversion Using an SOA," *IEEE Photonics Technology Letters*, vol. 20, no. 19, pp. 1597–1599, 2008.

[57] W. Li, M. Chen, Y. Dong, and S. Xie, "All-optical format conversion from NRZ to CSRZ and between RZ and CSRZ using SOA-based fiber loop mirror," *IEEE Photonics Technology Letters*, vol. 16, no. 1, pp. 203–205, 2004.

[58] K. Mishina, A. Maruta, S. Mitani, T. Miyahara, K. Ishida, K. Shimizu, T. Hatta, K. Motoshima, and K. Kitayama, "NRZ-OOK-to-RZ-BPSK Modulation-Format Conversion Using SOA-MZI Wavelength Converter," *IEEE/OSA Journal of Lightwave Technology*, vol. 24, no. 10, pp. 3751–3758, 2006.

[59] K. Mishina, S. Nissanka, A. Maruta, S. Mitani, K. Ishida, K. Shimizu, T. Hatta, and K. Kitayama, "All-optical modulation format conversion from NRZ-OOK to RZ-QPSK using parallel SOA-MZI OOK/BPSK converters," *Optics Express*, vol. 15, no. 12, pp. 7774–7785, 2007.

[60] J. Wang, Y. Jiao, R. Bonk, W. Freude, and J. Leuthold, "Regenerative Properties of Bulk and Quantum Dot SOA Based All-Optical Mach-Zehnder Interferometer DPSK Wavelength Converters," *in Proc. Photonics in Switching, Herakleion, Greece*, vol. O4.5, 2006.

[61] I. Kang, C. Dorrer, L. Zhang, M. Rasras, L. Buhl, A. Bhardwaj, S. Cabot, M. Dinu, X. Liu, M. Cappuzzo, *et al.*, "Regenerative all optical wavelength conversion of 40-Gb/s DPSK signals using a semiconductor optical amplifier Mach-Zehnder interferometer," *in Proc. European Conference on Optical Communication (ECOC)*, vol. 6, p. Th 4.3.3, 2005.

[62] B. Sartorius, C. Bornholdt, J. Slovak, M. Schlak, C. Schmidt, A. Marculescu, P. Vorreau, S. Tsadka, W. Freude, and J. Leuthold, "All-optical DPSK wavelength converter based on MZI with integrated SOAs and phase shifters," *in Proc. Optical Fiber Communication Conference (OFC)*, p. OWS6, 2006.

[63] I. Monroy, E. Verdurmen, S. Sulur, A. Koonen, H. de Waardt, G. Khoe, N. Chi, P. Holm-Nielsen, J. Zhang, and C. Peucheret, "Performance of a SOA-MZI wavelength converter for label swapping using combined FSK/IM modulation format," *Optical Fiber Technology*, vol. 10, no. 1, pp. 31–49, 2004.

[64] C. W. Chow, A. D. Ellis, and F. Parmigiani, "Time-division-multiplexing using pulse position locking for 100 Gb/s applications," *Optics Express*, vol. 17, pp. 6562–6567, 2009.

[65] P. Almeida, P. Petropoulos, F. Parmigiani, M. Ibsen, and D. Richardson, "OTDM Add-Drop Multiplexer Based on Time-Frequency Signal Processing," *IEEE/OSA Journal of Lightwave Technology*, vol. 24, no. 7, pp. 2720–2732, 2006.

[66] M. Hayashi, H. Tanaka, K. Ohara, T. Otani, and M. Suzuki, "OTDM transmitter using WDM-TDM conversion with an electroabsorption wavelength converter," *IEEE/OSA Journal of Lightwave Technology*, vol. 20, no. 2, pp. 236–242, 2002.

[67] T. Ohara, H. Takara, I. Shake, K. Mori, K. Sato, S. Kawanishi, S. Mino, T. Yamada, M. Ishii, I. Ogawa, *et al.*, "160-Gb/s OTDM transmission using integrated all-optical MUX/DEMUX with all-channel modulation and demultiplexing," *IEEE Photonics Technology Letters*, vol. 16, no. 2, pp. 650–652, 2004.

[68] E. Jahn, N. Agrawal, M. Arbert, H. Ehrke, D. Franke, R. Ludwig, W. Pieper, H. G. Weber, and C. M. Weinert, "40 Gbit/s All-Optical Demultiplexing Using a Monolithically Integrated Mach-Zehnder Interferometer with Semiconductor Laser Amplifiers," *IEE Electronics Letters*, vol. 31, no. 21, pp. 1857–1858, 1995.

[69] R. Hess, M. Carccia-Gross, W. Vogt, E. Gamper, P. Besse, M. Duelk, E. Gini, H. Melchior, B. Mikkelsen, M. Vaa, *et al.*, "All-optical demultiplexing of 80 to 10 Gb/s signals with monolithic integrated high-performance Mach-Zehnder interferometer," *IEEE Photonics Technology Letters*, vol. 10, no. 1, pp. 165–167, 1998.

[70] S. Nakamura, Y. Ueno, K. Tajima, J. Sasaki, T. Sugimoto, T. Kato, T. Shimoda, M. Itoh, H. Hatakeyama, T. Tamanuki, and T. Sasaki, "Demultiplexing of 168-Gb/s data

pulses with a hybrid-integrated symmetric Mach-Zehnder all-optical switch," *IEEE Photonics Technology Letters*, vol. 12, pp. 425–427, Apr 2000.

[71] S. Nakamura, Y. Ueno, and K. Tajima, "Error-free all-optical demultiplexing at 336 Gb/s with a hybrid-integrated symmetric-Mach-Zehnder switch," *in Proc. Optical Fiber Communication Conference (OFC)*, p. FD3, 2002.

[72] D. Wolfson, A. Kloch, T. Fjelde, C. Janz, B. Dagens, and M. Renaud, "40-Gb/s all-optical wavelength conversion, regeneration, and demultiplexing in an SOA-based all-active Mach-Zehnder interferometer," *IEEE Photonics Technology Letters*, vol. 12, pp. 332–334, Mar 2000.

[73] S. Fischer, M. Duelk, M. Puleo, R. Girardi, E. Gamper, W. Vogt, W. Hunziker, E. Gini, and H. Melchior, "40-Gb/s OTDM to 4×10 Gb/s WDM conversion in monolithic InP Mach-Zehnder interferometer module," *IEEE Photonics Technology Letters*, vol. 11, no. 10, pp. 1262–1264, 1999.

[74] A. de Melo, S. Randel, and K. Petermann, "Mach–Zehnder Interferometer-Based High-Speed OTDM Add–Drop Multiplexing," *IEEE/OSA Journal of Lightwave Technology*, vol. 25, no. 4, pp. 1017–1026, 2007.

[75] T. Miyazaki, H. Sotobayashi, and W. Chujo, "Synchronous optical demultiplexing and sampling of 80-Gb/s OTDM signals by optically recovered clock using mode-locked laser diode and symmetric Mach-Zehnder switch," *IEEE Photonics Technology Letters*, vol. 14, no. 12, pp. 1734–1736, 2002.

[76] R. Webb, R. Manning, G. Maxwell, and A. Poustie, "40 Gbit/s all-optical XOR gate based on hybrid-integrated Mach-Zehnder interferometer," *IEE Electronics Letters*, vol. 39, no. 1, pp. 79–81, 2003.

[77] J. Kim, J. Kang, T. Kim, and S. Han, "All-optical multiple logic gates with XOR, NOR, OR, and NAND functions using parallel SOA-MZI structures: theory and experiment," *IEEE/OSA Journal of Lightwave Technology*, vol. 24, no. 9, pp. 3392–3399, 2006.

[78] F. Ratovelomanana, N. Vodjdani, A. Enard, G. Glastre, D. Rondi, R. Blondeau, A. Dupas, L. Billes, and J. Simon, "Regeneration improvement in all-optical wavelength converter, based on a mach-zehnder interferometer, by means of phase-shifter section," *IEE Electronics Letters*, vol. 33, pp. 1629–1630, Sep 1997.

[79] J. Leuthold, J. Eckner, C. Holtmann, R. Hess, and H. Melchior, "All-optical 2× 2 switches with 20 dB extinction ratios," *IEE Electronics Letters*, vol. 32, no. 24, pp. 2235–2236, 1996.

[80] K. Morito, J. Leuthold, and H. Melchior, "Dynamic analysis of MZI-SOA all optical switches for balanced switching," *Integrated Optics and Optical Fibre Communications, 11th International Conference on, and 23rd European Conference on Optical Communications*, vol. 2, pp. 81–84, 1997.

[81] R. Nagarajan, M. Kato, S. Hurtt, A. Dentai, J. Pleumeekers, P. Evans, M. Missey, R. Muthiah, A. Chen, D. Lambert, *et al.*, "Monolithic, 10 and 40 Channel InP Receiver Photonic Integrated Circuits with On-Chip Amplification," *in Proc. Optical Fiber Communication Conference (OFC)*, p. PD32, 2007.

[82] B. Lavigne, D. Chiaroni, P. Guerber, L. Hamon, and A. Jourdan, "Improvement of regeneration capabilities in semiconductor optical amplifier-based 3R regenerator," *in Proc. Optical Fiber Communication Conference (OFC)*, p. TuJ3, 1999.

[83] O. Leclerc, B. Lavigne, E. Balmefrezol, P. Brindel, L. Pierre, D. Rouvillain, and F. Seguineau, "Optical regeneration at 40 Gb/s and beyond," *IEEE/OSA Journal of Lightwave Technology*, vol. 21, pp. 2779–2790, Nov. 2003.

[84] J. Mork, F. Ohman, and S. Bischoff, "Analytical expression for the bit error rate of cascaded all-optical regenerators," *IEEE Photonics Technology Letters*, vol. 15, pp. 1479–1481, Oct. 2003.

[85] M. Rochette, J. Kutz, J. Blows, D. Moss, J. Mok, and B. Eggleton, "Bit-error-ratio improvement with 2R optical regenerators," *IEEE Photonics Technology Letters*, vol. 17, pp. 908–910, April 2005.

[86] B. Mikkelsen, S. Danielsen, C. Joergensen, R. Pedersen, H. Poulsen, and K. Stubkjaer, "All-optical noise reduction capability of interferometric wavelength converters," *IEE Electronics Letters*, vol. 32, no. 6, pp. 566–567, 1996.

[87] Y. Ku, K. Chan, W. Hung, C. Chan, L. Chen, and F. Tong, "Homodyne crosstalk tolerance enhancement by all-active MZI-SOA wavelength converters," *in Proc. Pacific Rim Conference on Lasers and Electro-Optics (CLEO/Pacific Rim)*, p. W4A(13)4, 2003.

[88] Y. Akasaka, Z. Zhu, Z. Pan, and S. Yoo, "PMD mitigation application of MZI-SOA based optical 2R regeneration in the receiver," *in Proc. Optical Fiber Communication Conference (OFC*, p. JWA22, 2005.

[89] T. Silveira, A. Teixeira, N. Kataoka, A. Ferreira, N. Wada, X. Wang, T. Miyazaki, and P. Monteiro, "MZI-SOA-based 2R regeneration of OCDMA signals with multiaccess interference noise," *Microwave and Optical Technology Letters*, vol. 50, no. 6, p. 1521, 2008.

[90] S. Fischer, M. Dulk, E. Gamper, W. Vogt, E. Gini, H. Melchior, W. Hunziker, D. Nesset, and A. Ellis, "Optical 3R regenerator for 40 Gbit/s networks," *IEE Electronics Letters*, vol. 35, pp. 2047–2049, Nov 1999.

[91] B. Lavigne, P. Guerber, C. Janz, A. Jourdan, and M. Renaud, "Full validation of an optical 3R regenerator at 20 Gbit/s," *in Proc. Optical Fiber Communication Conference (OFC)*, p. ThF7, 2000.

[92] B. Lavigne, P. Guerber, P. Brindel, E. Balmefrezol, and B. Dagens, "Cascade of 100 optical 3R regenerators at 40 Gbit/s based on all-active Mach Zehnder interferometers," *in Proc. European Conference on Optical Communication (ECOC)*, p. We.F.2.6, 2001.

[93] D. Tsiokos, P. Bakopoulos, O. Zouraraki, G. Maxwell, A. Poustie, and H. Avramopoulos, "Integrated MZI-based All-Optical Clock and Data Recovery for Asynchronous Variable Packet Length Traffic," *in Proc. European Conference on Optical Communication (ECOC)*, p. We4.P.022, 2005.

[94] D. Tsiokos, P. Bakopoulos, A. Poustie, G. Maxwell, and H. Avramopoulos, "Jitter reduction in 40 Gbit/s all-optical 3R regenerator using integrated MZI-SOA switches," *IEE Electronics Letters*, vol. 42, no. 14, pp. 817–819, 2006.

[95] E. Patent, J. vanderTol, J. Binsma, Y. Oei, E. Bente, and M. Smit, "Self-Switching in Mach–Zehnder Interferometers With SOA Phase Shifters," *IEEE Photonics Technology Letters*, vol. 17, no. 11, pp. 2301–2303, 2005.

[96] G. Kanellos, N. Pleros, D. Petrantonakis, P. Zakynthinos, H. Avramopoulos, G. Maxwell, and A. Poustie, "40 Gb/s 2R Burst Mode Receiver with a single integrated SOA-MZI switch," *OSA Optics Express*, vol. 15, no. 8, pp. 5043–5049, 2007.

[97] G. Kanellos, D. Klonidis, N. Pleros, P. Zakynthinos, D. Apostolopoulos, A. Poustie, G. Maxwell, H. Avramopoulos, and I. Tomkos, "Cascaded operation of a 2R burst-mode regenerator with data exhibiting 6 dB power variation," *in Proc. Optical Fiber Communication Conference (OFC)*, p. OWP4, 2007.

[98] P. Zakynthinos, G. Kanellos, D. Klonidis, D. Apostolopoulos, N. Pleros, A. Poustie, G. Maxwell, I. Tomkos, and H. Avramopoulos, "Cascaded Operation of a 2R Burst-Mode Regenerator for Optical Burst Switching Network Transmission," *IEEE Photonics Technology Letters*, vol. 19, no. 22, pp. 1834–1836, 2007.

[99] G. Kanellos, D. Petrantonakis, D. Tsiokos, P. Bakopoulos, P. Zakynthinos, N. Pleros, D. Apostolopoulos, G. Maxwell, A. Poustie, and H. Avramopoulos, "All-optical 3R burst-mode reception at 40 Gb/s using four integrated MZI switches," *IEEE/OSA Journal of Lightwave Technology*, vol. 25, no. 1, pp. 184–192, 2007.

[100] D. Petrantonakis, G. Kanellos, P. Zakynthinos, D. Apostolopoulos, N. Pleros, and H. Avramopoulos, "40-Gb/s 3R Burst Mode Regenerator Using Four Integrated MZI Switches," *IEEE Photonics Technology Letters*, vol. 19, no. 5, pp. 288–290, 2007.

[101] D. Petrantonakis, G. Kanellos, P. Zakynthinos, N. Pleros, D. Apostolopoulos, and H. Avramopoulos, "A 40 Gb/s 3R burst-mode receiver with 4 integrated MZI switches," *in Proc. Optical Fiber Communication Conference (OFC)*, p. PD25, 2006.

[102] P. Zakynthinos, D.Petrantonakis, D. Apostolopoulos, A. Poustie, G. Maxwell, and H. Avramopoulos, "Four-Wavelength 3R Burst Mode Regenerator Using Three Integrated Quad MZI Arrays," *in Proc. Optical Fiber Communication Conference (OFC)*, p. OWK5, 2008.

[103] D. Blumenthal, B. Olsson, G. Rossi, T. Dimmick, L. Rau, M. Anovi, O. Lavrova, R. Doshi, O. Jerphagnon, J. Bowers, *et al.*, "All-optical label swapping networks and technologies," *IEEE/OSA Journal of Lightwave Technology*, vol. 18, no. 12, p. 2058, 2000.

[104] K. Vlachos, I. Monroy, A. Koonen, C. Peucheret, and P. Jeppesen, "STOLAS: switching technologies for optically labeled signals," *IEEE Communications Magazine*, vol. 41, no. 11, pp. S9–15, 2003.

[105] F. Ramos, E. Kehayas, J. Martinez, R. Clavero, J. Marti, L. Stampoulidis, D. Tsiokos, H. Avramopoulos, J. Zhang, P. Holm-Nielsen, *et al.*, "IST-LASAGNE: Towards All-Optical Label Swapping Employing Optical Logic Gates and Optical Flip-Flops," *IEEE/OSA Journal of Lightwave Technology*, vol. 23, no. 10, pp. 2993–3011, 2005.

[106] D. Apostolopoulos, D. Petrantonakis, O. Zouraraki, E. Kehayas, N. Pleros, and H. Avramopoulos, "All-Optical Label/Payload Separation at 40 Gb/s," *IEEE Photonics Technology Letters*, vol. 18, pp. 2023–2025, Oct.1, 2006.

[107] L. Stampoulidis, E. Kehayas, H. Avramopoulos, Y. Liu, E. Tangdiongga, and H. Dorren, "40 Gb/s fast-locking all-optical packet clock recovery," *in Proc. Optical Fiber Communication Conference (OFC)*, p. OThE2, 2005.

[108] C. Bintjas, N. Pleros, K. Yiannopoulos, G. Theophilopoulos, M. Kalyvas, H. Avramopoulos, and G. Guekos, "All-optical packet address and payload separation," *IEEE Photonics Technology Letters*, vol. 14, no. 12, pp. 1728–1730, 2002.

[109] L. Stampoulidis, E. Kehayas, D. Apostolopoulos, P. Bakopoulos, K. Vyrsokinos, and H. Avramopoulos, "On-the-Fly All-Optical Contention Resolution for NRZ and RZ Data Formats Using Packet Envelope Detection and Integrated Optical Switches," *IEEE Photonics Technology Letters*, vol. 19, no. 8, pp. 538–540, 2007.

[110] S. Rangarajan, Z. Hu, L. Rau, and D. Blumenthal, "All-optical contention resolution with wavelength conversion for asynchronous variable-length 40 Gb/s optical packets," *IEEE Photonics Technology Letters*, vol. 16, pp. 689–691, Feb. 2004.

[111] E. Varvarigos, "The "packing" and the "scheduling packet" switch architectures for almost all-optical lossless networks," *IEEE/OSA Journal of Lightwave Technology*, vol. 16, no. 10, pp. 1757–1767, 1998.

[112] J. Ramamirtham and J. Turner, "Time sliced optical burst switching," vol. 3, no. 30, pp. 2030–2038, 2003.

[113] Y. Liu, M. Hill, R. Geldenhuys, N. Calabretta, H. de Waardt, G.-D. Khoe, and H. Dorren, "Demonstration of a variable optical delay for a recirculating buffer by using all-optical signal processing," *IEEE Photonics Technology Letters*, vol. 16, pp. 1748–1750, July 2004.

[114] Z. Pan, J. Cao, Y. Bansal, V. Tsui, S. Fong, Y. Zhang, J. Taylor, H. Lee, M. Jeon, V. Akella, S. Yoo, K. Okamoto, and S. Kamei, "All-optical programmable time-slot-interchanger using optical-label switching with tunable wavelength conversion and N by N arrayed waveguide grating routers," *in Proc. Optical Fiber Communication Conference (OFC)*, pp. 267–268, Mar 2002.

[115] E. Burmeister and J. Bowers, "Integrated gate matrix switch for optical packet buffering," *IEEE Photonics Technology Letters*, vol. 18, no. 1/4, p. 103, 2006.

[116] J. van der Tol, H. de Waardt, and Y. Liu, "A Mach-Zehnder-interferometer-based low-loss combiner," *IEEE Photonics Technology Letters*, vol. 13, no. 11, pp. 1197–1199, 2001.

[117] R. Clavero, F. Ramos, J. Martinez, and J. Marti, "All-optical flip-flop based on a single SOA-MZI," *IEEE Photonics Technology Letters*, vol. 17, pp. 843–845, April 2005.

[118] M. Nielsen and B. Dagens, "Experimental and theoretical demonstration of amplifying pulse compression using an SOA-based Mach-Zehnder interferometer," *in Proc. Lasers and Electro-Optics Society Annual Meeting (LEOS)*, vol. 2, pp. 677–678, 2004.

[119] N. Yan, T. Silveira, A. Teixeira, A. Ferreira, E. Tangdiongga, P. Monteiro, and A. Koonen, "40 Gbit/s wavelength multicast via SOA-MZI and applications," *Electronics Letters*, vol. 43, no. 23, 2007.

[120] V. Lal, M. L. Masanovic, J. A. Summers, G. Fish, and D. J. Blumenthal, "Monolithic wavelength converters for high-speed packet-switched optical networks," *IEEE Journal of Selected Topics in Quantum Electronics*, vol. 13, pp. 49–57, Jan.-feb. 2007.

[121] M. Xin, M. Chen, H. Chen, and S. Xie, "Optical Code Label Stripping based on SOA-MZI in Optical Packet Switching Networks," *IEEE/OSA Journal of Lightwave Technology*, vol. 27, no. 15, pp. 3212–3219, 2009.

[122] R. Webb, X. Yang, R. Manning, G. Maxwell, A. Poustie, S. Lardenois, and D. Cotter, "42Gbit/s All-Optical Pattern Recognition System," *in Proc. Optical Fiber Communication Conference (OFC)*, p. OTuL2, 2008.

[123] D. Kilper, R. Bach, D. Blumenthal, D. Einstein, T. Landolsi, L. Ostar, M. Preiss, and A. Willner, "Optical Performance Monitoring," *IEEE/OSA Journal of Lightwave Technology*, vol. 22, pp. 294–304, January 2004.

[124] L. Occhi, *Semiconductor Optical Amplifiers made of Ridge Waveguide Bulk InGaAsP/InP: Experimental Characterization and Numerical Modelling of Gain, Phase, and Noise*. PhD thesis, Eidgenössische Technische Hochschule Zürich, 2002.

[125] A. Mecozzi and J. Mork, "Saturation effects in nondegenerate four-wave mixing between short optical pulses in semiconductor laser amplifiers," *IEEE Journal of Selected Topics in Quantum Electronics*, vol. 3, no. 5, pp. 1190–1207, 1997.

[126] D. Cassioli, S. Scotti, and A. Mecozzi, "A time-domain computer simulator of the nonlinear response of semiconductor optical amplifiers," *IEEE Journal of Quantum Electronics*, vol. 36, no. 9, pp. 1072–1080, 2000.

[127] J. L. Rebola and A. V. T. Cartaxo, "Gaussian approach for performance evaluation of optically preamplified receivers with arbitrary optical and electrical filters," *IEE Proceedings-Optoelectronics*, vol. 146, pp. 135–142, June 2001.

[128] M. Pfennigbauer, M. M. Strasser, M. Pauer, and P. J. Winzer, "Dependence of optically preamplified receiver sensitivity on optical and electrical filter bandwidths-measurement and simulation," *IEEE Photonics Technology Letters*, vol. 14, no. 6, pp. 831–833, 2002.

[129] M. Leiria, J. L. Rebola, and A. V. T. Cartaxo, "Gaussian approach to the performance assessment of optical multiplexer-demultiplexer concatenation in transparent optical networks," *IEE Proceedings-Optoelectronics*, vol. 151, no. 3, pp. 157–165, 2004.

Chapter 3 Format and wavelength conversion in MZI-SOA

3.1 Introduction

Recent trends in optical networks are that the different hierarchies in the optical network become closer and less isolated from each other, in an attempt to reduce complexity and cost. One such example is the use of the same transmission platform and equipment type both in the backbone and in the metro network. One straightforward advantage is that OEO transponders, that before would interface both networks, can be swiftly removed and replaced by a transparent connection, provided that proper wavelength assignment and planning is performed and the same wavelength can be used in both hierarchies. However, if different wavelengths are used in both hierarchies, an OEO transponder is required to perform wavelength and possibly format conversion, without any electronic overhead processing. In this case, the OEO transponder can be replaced by an all-optical wavelength and format converter such as the MZI-SOA. This would translate in a significant cost reduction since in 40 Gb/s networks OEO transponders have the largest fraction of the total cost. Format conversion plays a special role in interfaces of different hierarchies of optical networks, since typically, higher network hierarchies use more complex modulation and pulse formats, such as the optical duobinary (ODB), RZ and carrier-suppressed RZ (CS-RZ) which are optimised for performance, whereas lower network hierarchies use simple NRZ mainly due to the lower cost. Hence, wavelength conversion with format conversion is of great interest under the discussed scenario. Additionally, several optical circuits based on the MZI-SOA have been proposed and demonstrated using the RZ format. Therefore, it is important to assess the MZI-SOA performance with other formats to validate the operation of the optical processing circuits with different modulation formats.

This chapter is dedicated to the wavelength and format conversion in the MZI-SOA. The results here reported provide a comparative study of the wavelength and format

conversion capabilities of the MZI-SOA between selected modulation formats. These functionalities of the MZI-SOA will be studied using the simulation model explained in the previous chapter, and also experimentally, in a device manufactured by the Centre for Integrated Photonics (CIP) [1].

In section 3.2, an experimental static characterization of the SOAs in the MZI-SOA is performed, in order to obtain numerical parameters to use in the simulation model. Then, in section 3.3, an investigation of the dynamic properties of the MZI-SOA will be performed, and namely the wavelength conversion performance will be studied as a function of the signal bit rate to estimate the maximum possible bit rate of the wavelength conversion within given penalty limits. It will be shown that the maximum operating bit rate is 40 Gb/s and therefore this will be the chosen bit rate for all the remaining analysis.

The performance of the wavelength and format conversion depends on the format of the incoming signal, as well as on the powers of the signal. The impact of these factors on the wavelength conversion performance will be investigated in section 3.4 and an operating region of the powers fed to the MZI-SOA will be defined both through experiment and simulation. The numerical model will be then be benchmarked against the experimental observations of the BER as function on the input powers. At this point, not only wavelength conversion to a CW beam will be studied as in section 3.4, but also using a short pulse beam as the probe signal in section 3.5.

Then, in order to have a good characterization of the signal shape on the conversion performance, the effect of the extinction ratio of the input signal on the wavelength conversion performance will be analysed in section 3.6. Additionally, different signal formats will be applied to the MZI-SOA to investigate the impact of the duty-cycle on the performance of the conversion. Finally, the width of the probe pulses will be varied and the impact on the conversion performance will be observed. At the end, overall conclusions drawn about this topic are presented.

3.2 Static MZI-SOA and SOA characterization

The SOA model presented in the previous chapter provides a mathematical description of its operation, but, to draw relevant conclusions regarding the SOA utility in

an optical network, accurate numerical parameters are necessary. This section addresses SOA characterization and match between the simulation model and experimental findings.

The derivation of the SOA parameters can be a complex and lengthy process, since a large number of variables are present in the system. Therefore, the base SOA parameters were obtained from the same work where the SOA model was initially derived [2]. Then, these parameters were tweaked in order to improve the match between experimental observations and simulation results. At the end, only the output saturation power and the alpha factor values needed to be adapted. Table 3-1 presents the SOA parameters used throughout this chapter.

Table 3-1 SOA model numerical parameters.

Unsaturated gain	G_0	26	dB
Saturation power parameter	P_s	8.6	dBm
Carrier lifetime	τ_s	70	ps
Carrier-carrier scattering time	τ_{SHB}	0.12	ps
Temperature relaxation time	τ_H	0.48	ps
Nonlinear gain suppression due to spectral hole burning	ε_{SHB}	1.17	W^{-1}
Nonlinear gain suppression due to carrier heating	ε_{CH}	1.95	W^{-1}
Alpha factor from carrier depletion	α_N	3.5	
Alpha factor from carrier heating	α_{CH}	0.94	

A picture of the packaged MZI-SOA device used in this work is shown in Fig. 3.1. The package contains a chip with two MZI-SOA structures [3]. The MZI-SOA is hybridly integrated with the following parts: a silica motherboard that contains the optical waveguides such as the couplers and the Y junctions; a silicon daughterboard where the SOAs are fitted and which is used to be passively assembled in the motherboard; the active elements, i.e. the SOAs, that are assembled in the daughterboard; and a V-groove to ease fibre pigtailing of the motherboard [4].

Fig. 3.2 presents a functional schematic of the dual MZI-SOA chip with the SOAs, phase shifters, the Peltier cell, and the thermistor. The chip temperature is measured in the thermistor and a proportional, integral, and differential (PID) control loop actuates on the Peltier cell to keep the chip temperature stable at the desired value. All measurements were done at a temperature setting of 25ºC. Fig. 3.3 shows a picture of a prototype box that included temperature control and SOA current and phase shifter bias electronics.

The couplers in the experimental devices have shown splitting ratios deviated from the ideal 50:50 ratio, closer to 40:60. The effect of this unbalancing is a reduction of the

on/off ratio at the MZI-SOA output. However, this can be contravened by using phase shifters in the MZI-SOA arms [5], which are featured in the experimental device. It is expected however, that future MZI-SOA devices will have splitting ratios closer to 50:50, due to the use of multi-mode interferometers (MMI), instead of directional couplers [6]. Hence, in the simulation it is considered that the coupling ratio is the ideal 50:50, but phase shifters are not considered. The experimental method of biasing the MZI-SOA that is described in the next subsection ensures that the MZI-SOA is properly biased to optimise the non-inverting output of the wavelength converter.

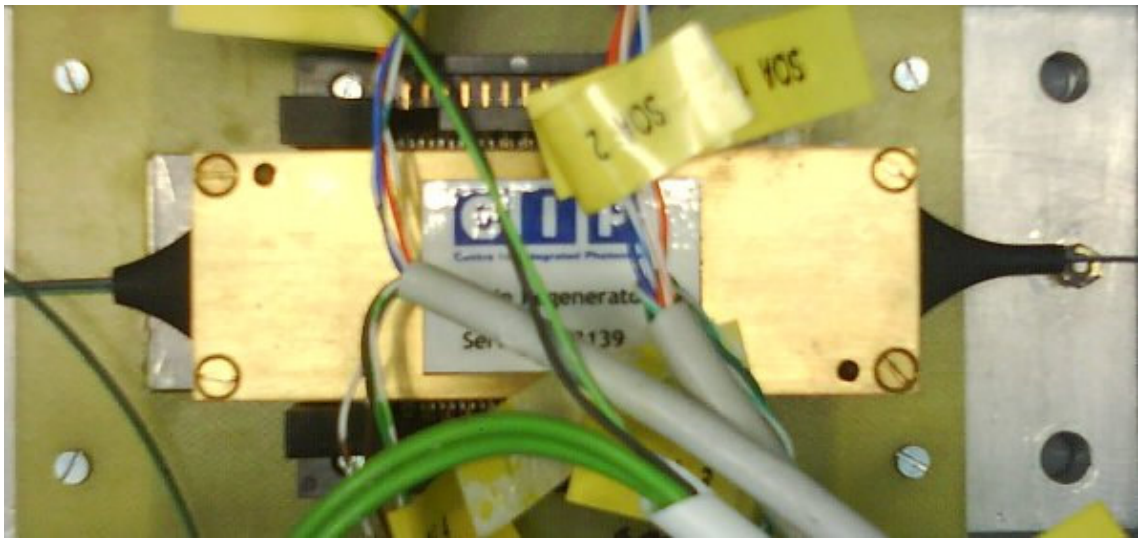

Fig. 3.1: Dual MZI-SOA device used to obtain experimental results. A ribbon of 8 fibres enters the MZI-SOAs on the left (4 fibres per MZI-SOA, 2 control and 2 interferometric inputs), and a ribbon of 4 fibre exits on the right (2 fibres per MZI-SOA, all interferometric outputs).

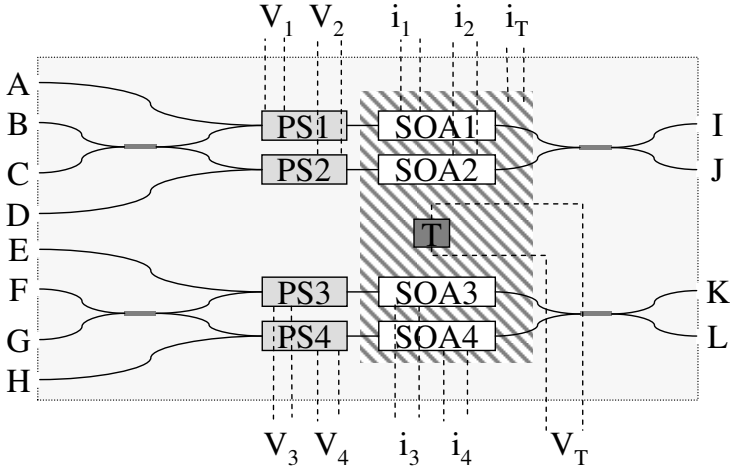

Fig. 3.2 Dual MZI-SOA chip schematic. Solid lines represent optical waveguides, while dashed lines represent electrical connections. PS represents the phase shifters, T represents the thermistor, and the shaded area with diagonal lines represents the Peltier cell. $V_{1,2,3,4}$ represents the voltages applied to the phase shifters and $i_{1,2,3,4}$ denote currents applied to the SOAs. V_T is the voltage created by a thermocouple and i_T is the current applied to the Peltier cell.

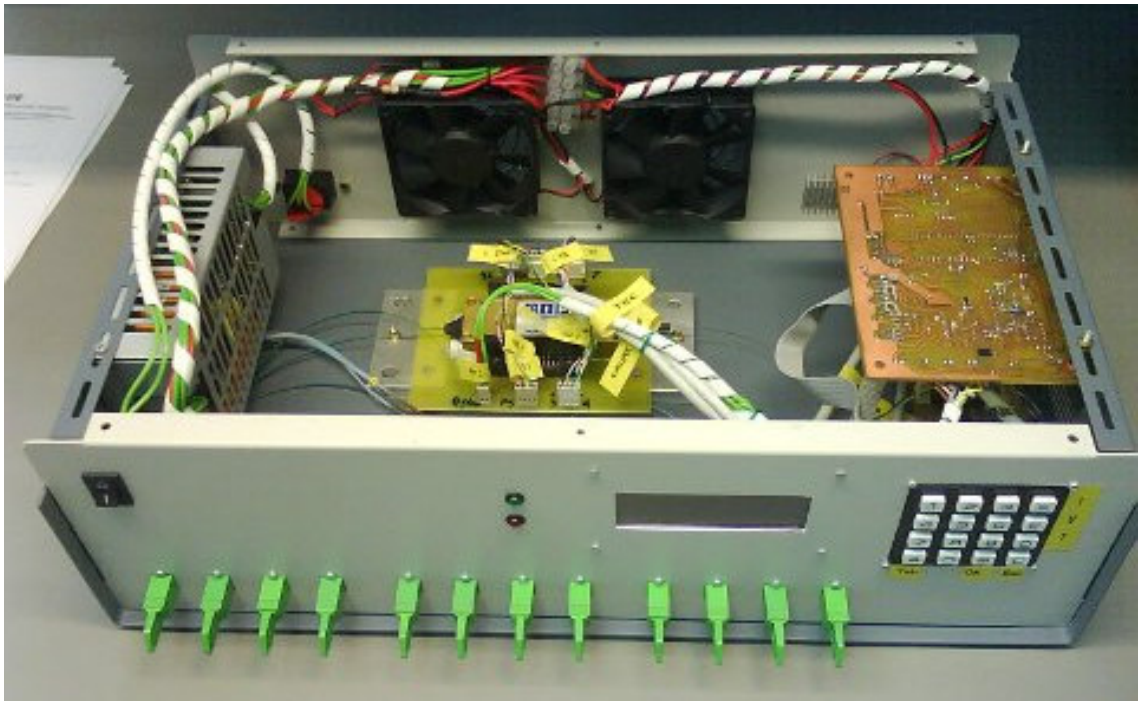

Fig. 3.3 MZI-SOA driving box. The MZI-SOA sits in the middle of the box. The temperature control, SOA bias and phase shifter bias electronics board is on the right, and the power supply unit is on the left. The front plate contains the interface dial, numerical display, and the input (8) and output (4) fibre connectors.

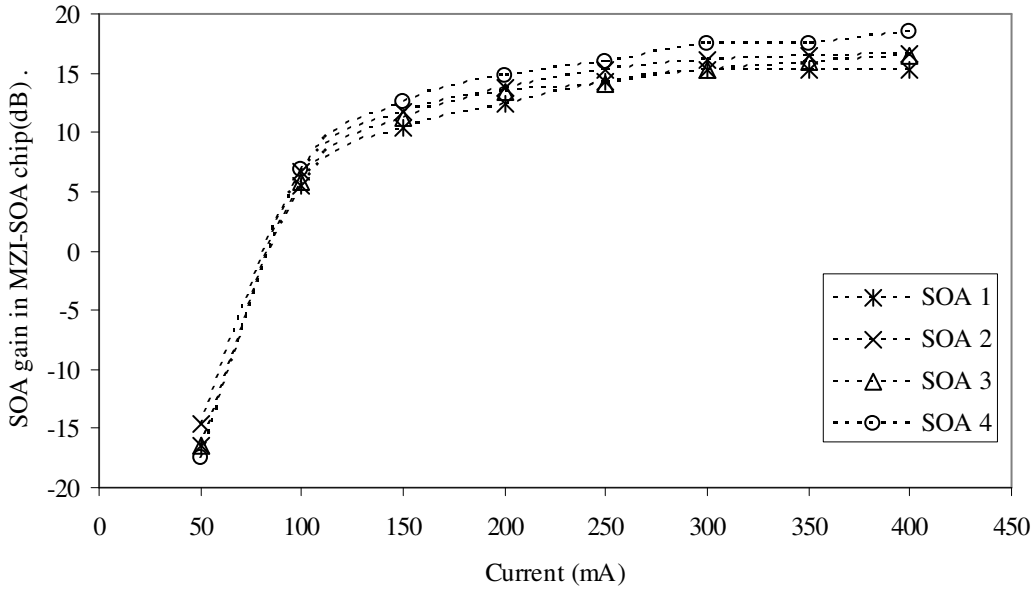

Fig. 3.4 SOA gain at 1550 nm as a function of the driving current. The gain is measured at the input and output facets of the MZI-SOA. The lines are guides for the eyes.

The SOA becomes faster at higher currents [7] and hence the highest possible operating current was used. The datasheet allows a maximum current of 400 mA per device, but a safety margin of 50 mA has been applied. Therefore, the SOA current was set to 350mA and will be kept fixed in all upcoming experimental tests. Also, no performance improvement has been noticed when increasing the current from 350 to 400 mA. Moreover, less cooling effort from the Peltier cell was required at 350 mA due to less SOA heating.

The SOA gain has also been measured as function of the wavelength at 1550 nm and at the C band limits (1530 and 1560 nm). These measurements are presented in Fig. 3.5, and with the ASE profile of the SOAs in Fig. 3.6, they provide a good indication on the spectral capabilities of the gain of the SOAs. It can be observed that the maximum gain is around 1560 nm, while the -3 dB bandwidth of the ASE power ranges from 49 to 54 nm. For operation in the C band, the SOA gain should be maximum near the band centre so that the gain difference between the maximum and minimum gain within the C band is minimized.

The SOA model used in this work does not explicitly depend on the wavelength. In 40 Gb/s simulations with 64 samples per bit, the simulation window spans 2.56 THz, which is about 20 nm at 1550 nm. Around plus and minus 10 nm of the considered operation wavelength of 1550 nm, the gain does not vary significantly and therefore the gain can be considered constant in the simulations. However, at higher bitrates and thus larger simulation windows, the gain might not be constant enough for this approximation to hold. As it will be seen shortly, at bitrates higher than 40 Gb/s the MZI-SOA is not capable of wavelength conversion within reasonable penalty margins, and therefore the wavelength independent gain approximation can be used. Still, the SOA modelling can capture the effect of operation at different wavelengths by using the measured unsaturated gain at each wavelength. In that situation, not only the gain changes, but also the gain-phase coupling, or alpha factor, changes [8]. However, wavelength dependence will not be addressed in this work. Studies on wavelength dependence can be found elsewhere [8, 9].

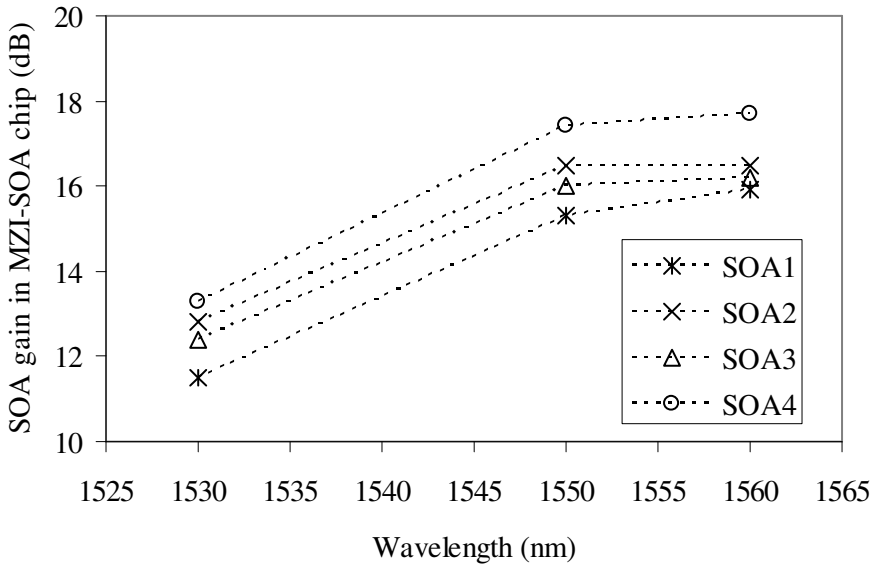

Fig. 3.5 SOA gain as a function of the wavelength. The gain is measured at the input and output facets of the MZI-SOA. The lines are guides for the eyes.

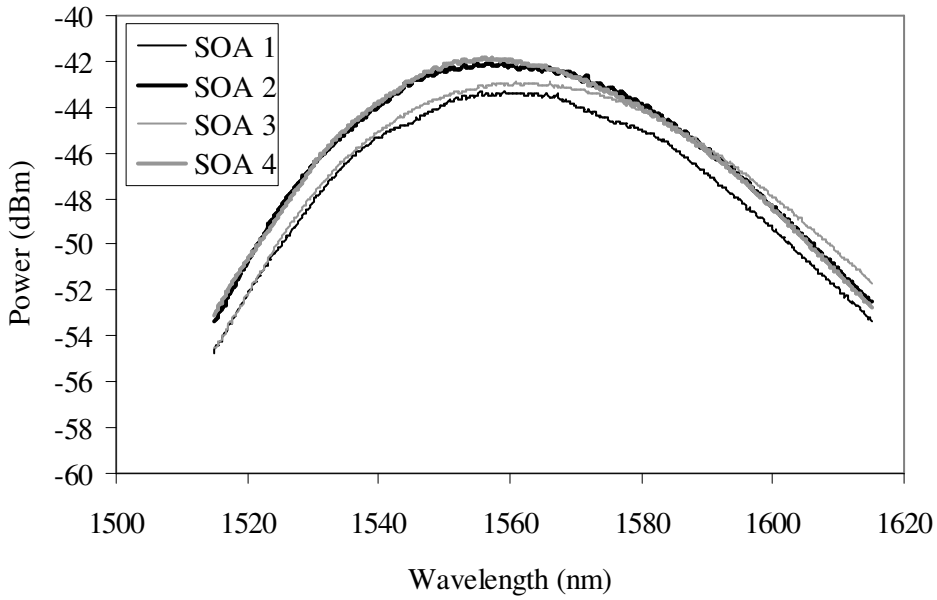

Fig. 3.6 Optical spectra of SOA generated ASE.

The SOAs' gain is now plotted in Fig. 3.7 as a function of the input CW laser power, both for the experiment and simulation. First of all, it can be noticed that the SOA gain in the MZI-SOA chip is around 10 dB smaller than the SOA unsaturated gain simulation parameter. This is due to the 3 dB losses per coupler at two couplers plus a Y junction, and 1 dB of additional excess loss due to waveguide loss. It should be noted that

the SOA unsaturated gain of 26 dB already includes the fibre to chip coupling loss and therefore this additional loss is not added to the SOA gain in MZI-SOA chip.

As for the dependence of the gain saturation on the input power, there is a good match between the experimental and simulation results, even if the experimental curves show a more distinct separation between the unsaturated and the saturated regime at around -15 to -10 dBm of input power. The simulation curve shows a much smoother transition between these two regions and the slope difference between the unsaturated and saturated regimes is also not as large as in the experimental results. The reason for this discrepancy is the mathematical model of gain saturation inside the SOA, since the numerical parameters do not change the slope of the curve of gain saturation.

The characterization of the SOA is of immense importance but also of great interest is the power transfer curve of the MZI-SOA. The static switching capabilities of the MZI-SOA were also investigated by using a CW beam at the interferometric port, acting as a probe, and another CW beam of variable power at the control port, acting as the saturating pump. The MZI-SOA transmissivity was obtained by measuring the power exiting at both output ports of the MZI-SOA and normalizing it to its maximum value. Transmissivity values and not absolute power values are presented so that the effect of insertion losses of additional components such as optical filters, isolators, etc., is removed. Indeed, the important variable for the MZI-SOA operation description is the transmissivity and not the absolute power, since, typically, there will be an amplifying stage such as an EDFA at the SOA output to control the power to the next stage of an optical processing circuit. The MZI-SOA transmissivity results are plotted in Fig. 3.8 for the two output ports of the MZI-SOA and for both the experiment and the simulation. There is a reasonable match between simulation and experiment which will now be analysed. At small pump powers, the non-inverting port transmissivity is very low and increases until it reaches a maximum value. Afterwards, as the pump power continues to increase, the transmissivity starts to decline. The maximum of the transmissivity of the non-inverting port is attained when the phase of the probe in MZI-SOA arms is such that, at the output, the waves travelling in both MZI-SOA arms interfere constructively with the same phase. If the pump power is different than the one required to attain this phase condition, the constructive interference is no longer perfect and therefore the output power declines. The exact opposite happens at the inverting output port of the MZI-SOA. When the phase between both interferometer paths

is such that at the output destructive interference occurs, the transmitted power is minimum. Whenever this phase condition is not achieved, the transmitted power is larger than the minimum. The minimum transmissivity predicted by the simulation is 5 dB lower than the observed one in the experiment. This is mainly due to the polarization effects and coupler asymmetry that are not modelled in the simulation. Even in the simulation there is still some light transmitted at the minimum transmission due to the gain unbalancing of the SOAs in the interferometer arms. The experimental and the simulation curves also differ in about 1 dB on the power at which the minimum/maximum transmissivity is found for the inverting/non-inverting ports. This is attributed to the discrepancy observed between the SOA gain saturation curves of Fig. 3.7 and also on the alpha factor, which is only an approximate value, and furthermore, this alpha factor model is approximate has received criticisms due to its linear approximation nature [10]. The same reasons also explain the difference between the experimental and simulation curves in the region of transition from low to high transmissivity of the non-inverting output.

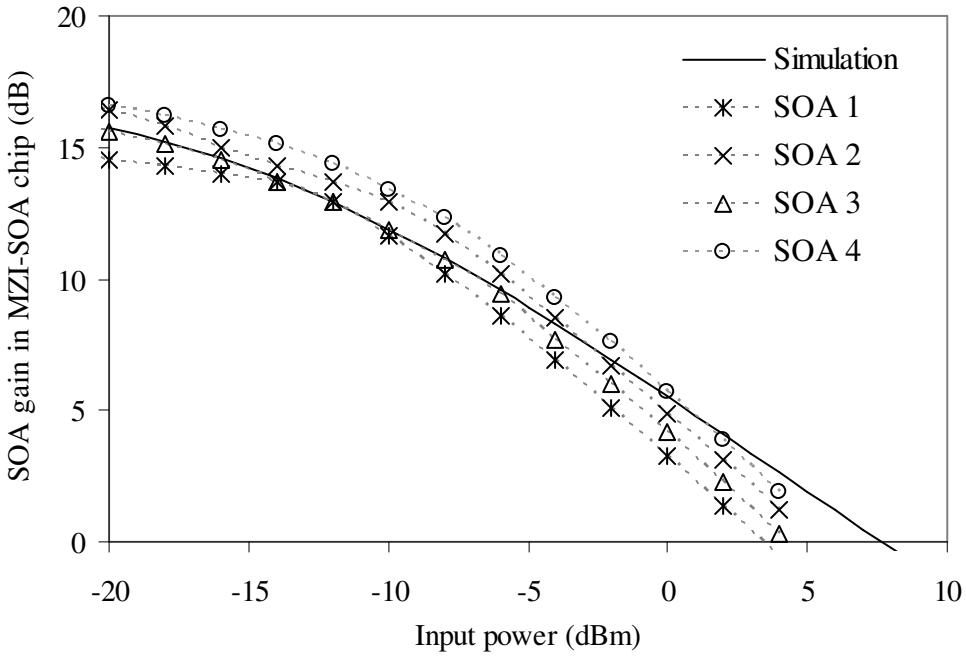

Fig. 3.7 SOA gain measured at the MZI-SOA input and output facets, i.e. including coupler and guide loss. The dotted lines are guides for the eyes.

One other discrepancy between the experimental and simulation observations is the behaviour of the non-inverting output at very low powers. Whereas the simulation foresees an ever decreasing transmissivity for decreasing pump powers, in the experiment, the transmissivity reaches a plateau which bounds the minimum transmissivity attainable for this output port. This is typical of a Mach-Zehnder interferometer structure, where the destructive interference condition is limited by the polarization of the signals, and mainly amplitude balancing between both arms.

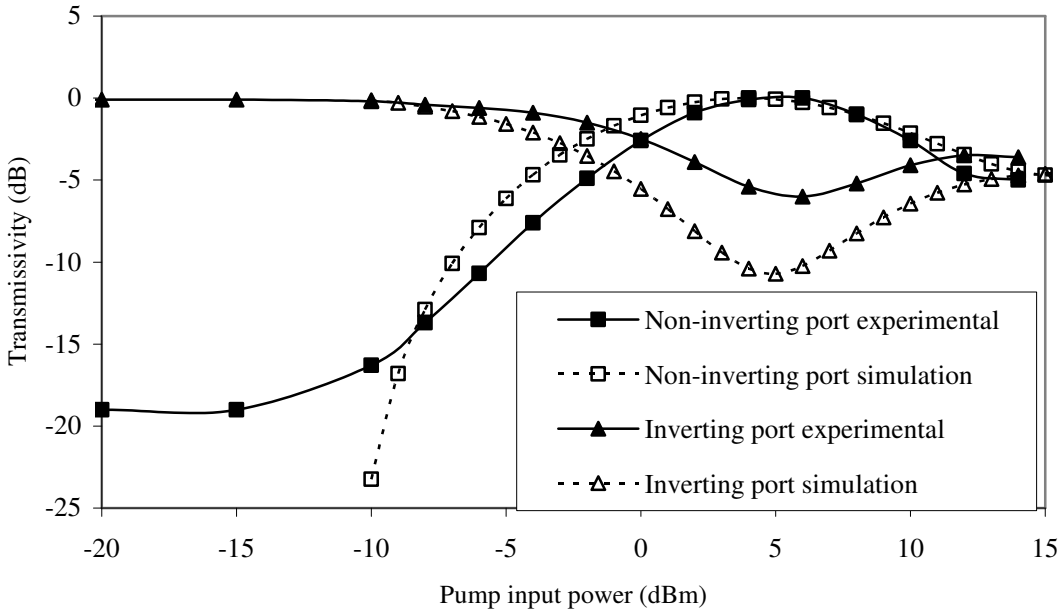

Fig. 3.8 Static power transfer function of the MZI-SOA: transmissivity as a function of the applied switching power on the control port, for both MZI-SOA output ports. The lines are guides for the eyes.

Furthermore, in the case of active interferometers (with amplifiers) such as the MZI-SOA, the SOAs generate SOA which contribute to a power floor at the MZI-SOA output port that cannot be removed. All these factors were not considered in the simulation model and hence the simulation forecasts ideal null transmissivity in the absence of pump power.

Even though the match between the simulation and experimental curves is not perfect, this characterization is enough to draw some useful conclusions. First of all, due to the very asymmetric operation of the inverting and non-inverting ports of the MZI-SOA, and specifically due to the very low on/off ratio of the inverting port, the operation of the

MZI-SOA as a switch will be severely impaired. This topic will be studied more thoroughly in chapter 5.

As for the applications of the MZI-SOA that involve only one output port, such as wavelength conversion, the MZI-SOA performance is promising. Keeping in mind that the transfer function analysed so far is static, for an input signal with '1' at 2 dBm and '0' level at -6 dBm, thus having 8 dB of extinction ratio, the output converted signal will have an extinction ratio of 10 dB or 9.5 dB, considering the experimental or simulation transfer function, respectively. The increase of extinction ratio of the converted signal relatively to the input signal is in particular one of the main interests in these devices due to the possibility of increasing the signal quality.

The next sections of this chapter will study the dynamic performance of the MZI-SOA to exploit it as a wavelength and format converter.

3.3 Dynamic MZI-SOA characterization

After the static gain characterization, the dynamic properties of the MZI-SOA are now investigated in this section. Conversion of NRZ and RZ signals was performed at bitrates from 5 to 80 Gb/s both in the push-pull and non push-pull configurations. Experimental eye diagrams have been obtained and compared to the simulation eye diagrams as a complement to the previous static SOA and MZI-SOA characterization. The OSNR penalty was then calculated by simulation to assess the maximum bit rate at which the MZI-SOA can operate for a maximum given OSNR penalty.

The generic wavelength conversion setup is shown in Fig. 3.9 and a picture of the respective experimental setup is shown in Fig. 3.10. It contains a CW laser beam that is fed to the interferometric input port through attenuator ATT1 and then through a polarization controller (PC) and an isolator (ISOL) to avoid reflections and consequent lasing in the SOA.

Several different transmitters were used that produced either NRZ or RZ signals at different bitrates. Details of the transmitter are presented in Appendix C. The transmitter output signal is input to a power coupler that divides it into the two control ports. Before each control port there is an attenuator (ATT2 and ATT3) and before the pull control port (#2) there is also a variable optical delay line (VODL). When control port #2 is connected,

the MZI-SOA is operated in push-pull mode. Otherwise, if non push-pull mode is desired, control port #2 is disconnected. By definition, the control signal power is the power that is input to the coupler in front of the transmitter in Fig. 3.9.

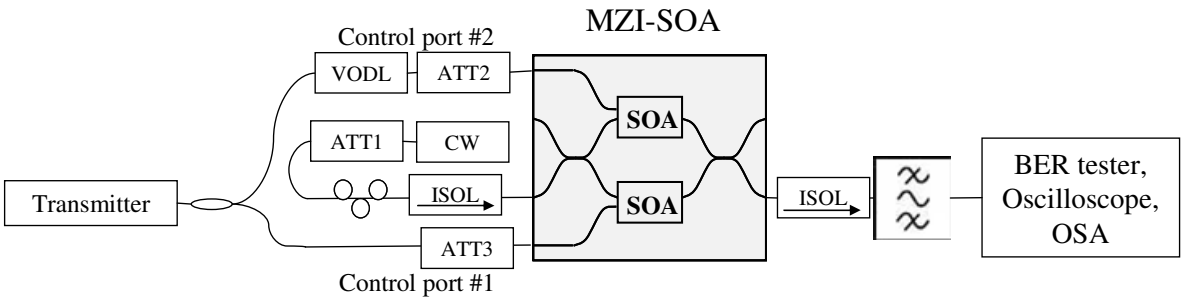

Fig. 3.9 Wavelength and format conversion setup to obtain eye diagrams and determine the BER of the MZI-SOA converted output.

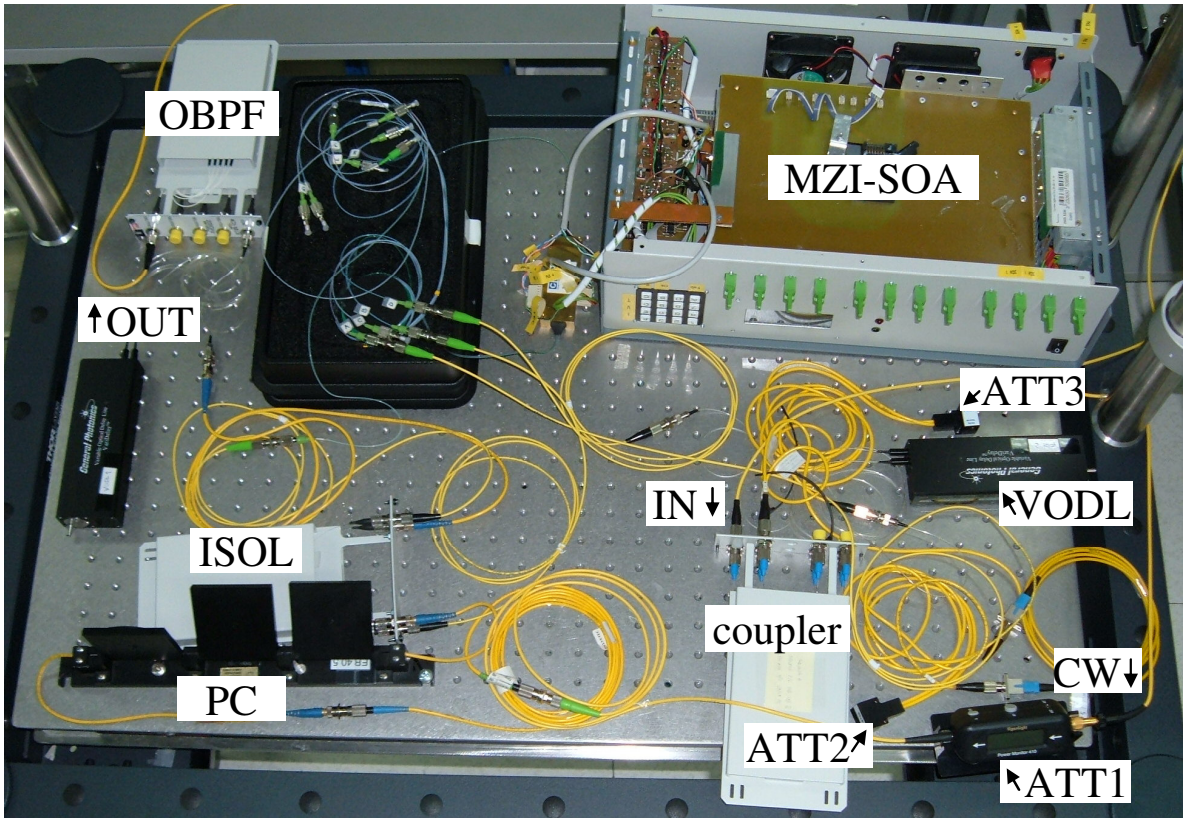

Fig. 3.10 Picture of the experimental setup to perform wavelength conversion in the MZI-SOA. OBPF – optical band pass filter; ISOL – isolator; PC – polarization controller; ATT – Variable attenuator; VODL – Variable optical delay line. IN and CW represent the ingress points of the signal to be wavelength converted and the CW beam, respectively, and OUT represents the egress point of the wavelength conversion output signal.

The MZI-SOA output is first passed through an isolator before being filtered by a 130 GHz bandwidth optical pass-band filter to reject the original control signal and also ASE noise. The output is connected to the BER tester, oscilloscope, or optical spectrum analyser (OSA). In this picture, the MZI-SOA is outside the MZI-SOA control box because the equipment was still in development stage.

The simulation setup mimicked the experimental setup except for the isolators and the polarization controller. No isolators are needed, since the models consider forward propagation only. Also, the polarization controller is not necessary in the simulation since only one polarization is considered. Thus, it is important to keep the polarization correctly aligned in the experiment to avoid the effects of polarization dependent gain/loss and delay.

The binary sequence size is 2^7=128 bits, as it was the best compromise between computational time and accuracy, according the study presented in Appendix D. 64 samples per bit are used, which is again a compromise between computational time and accurate description of the pulse temporal profile (1.6% of the bit time).

For the BER measurements of the following sections, the photoreceiver is modelled as an ideal square law device followed by a low pass 3rd order Bessel filter with a bandwidth of 87.5% of the bit rate at -3dB. At 40 Gb/s the bandwidth is 35 GHz, which matches well the experimental characterization.

Often, the performance of the input signal will be referred to as back to back, since it is obtained by bypassing the wavelength converter and directly connecting the transmitter to the BER tester through an optical filter properly tuned to the signal wavelength.

Operating the MZI-SOA device requires a number of optimisations such as the phase shifters voltage, polarization, input powers of the interferometric signal, control signal (push and pull, if applicable) and delay of pull signal. A blind search of the optimum operation point of these parameters is not effective and therefore an algorithm has been derived to locate the best operating point.

First, without any control signal, the power at the output of the MZI-SOA was minimized by scanning the voltage of the phase shifters and the polarization of the CW beam. It was observed that for minimum MZI-SOA transmissivity, the phase shifter

voltage in combination with polarization control was always the same, so it was kept constant in all tests, except for minor fine adjustments. Still, due to polarization drift, the polarization of the interferometric signal had to be adjusted to minimize the transmitted power in every test run. The CW beam power was set to be as high as possible as the equipment and safety recommendations would allow, working as a holding beam [11].

Then, the control signal would be connected. If non push pull mode was used, the power of the control signal would be varied between 0 and -10 dB relatively to the power of the interferometric signal. The chosen control power was the one that maximized eye opening or minimized the BER, if applicable. Later on, the power optimisation will be explored with greater detail. If the push-pull mode was employed, the same power rule was adopted to the push signal, while the power of the pull signal would be typically 5-8 dB lower. The delay would be typically 50 to 70% of the bit period, e.g. 12.5 to 17.5 ps at 40Gb/s. Then a search would be run over these three parameters, with the same optimisation criteria as in the non push-pull mode.

It was observed that the polarization of the control signal did not impact significantly the performance of the wavelength conversion, due to the low polarization dependent gain (PDG) of the SOAs of less than 1 dB. On the other hand, changing the polarization of the CW beam fed to the interferometric input port after the initial setting changed the extinction ratio of the output signal. Hence, the polarization of the interferometric signal was used as a fine tune.

In the simulation, as mentioned before, there are no phase shifters and only one polarization is modelled. Therefore, the optimisation process becomes simpler, but, still, the powers of the signal and the delay and attenuation of the pull arm must be optimised. The algorithm to obtain these parameters is explained hereafter.

The delay and attenuation of the pull arm have been varied in order to obtain the value that minimizes the BER. In the non push-pull configuration, the control power determines the conversion performance once the probe power is fixed. However, in the push-pull configuration, there is interplay between the control power, and the delay and attenuation of the pull arm. It is impractical to scan all three simulation parameters and so, the following methodology is adopted to optimise the performance. The delay is varied, and for each delay, the control power is also varied, because the optimum power depends on the delay. The delay that results in the lowest BER at the optimum control power is

chosen. Then, with fixed delay, the attenuation is scanned, again also scanning the control power. The attenuation that minimizes the BER is chosen as the optimum one. Then, the delay is again varied to ensure that, for the optimum attenuation, the optimum delay has not changed. It is verified that convergence to the correct minimum is achieved.

The optimum values are 15 ps of delay and 6.4 dB of attenuation at 40 Gb/s, which will be used to obtain the forthcoming results. For other bit rates, the delay was scaled accordingly.

The wavelength conversion performance will now be investigated for different bit rates. In the following experimental results, the power was optimised on the basis of the eye diagram only, since BER measurements were not performed. A more accurate power dependence investigation will be done afterwards. Wavelength conversion of 10 and 20 Gb/s NRZ signals was performed without the push-pull configuration and the eye diagrams are presented in Fig. 3.11 and Fig. 3.12, respectively. There is a good match between the shape of the experimental and simulation eye diagrams. The experimental 10 Gb/s eye diagram shows less patterning than the simulated eye diagram in the ‘0’ level. This is attributed to polarization effects that are not modelled in the simulation. As mentioned before, due to the interferometric process, the polarization setting impacts the power that is transmitted in the absence of control signal. Therefore, in the “0”, the polarization setting plays a significant role in the eye diagram shape and hence the match between experiment and simulation is worse. As for the temporal behaviour, at 10 Gb/s, bit patterning starts to be observed due to the gain recovery of the SOAs, while at 20 Gb/s the eye closure due to patterning is already significant. Wavelength conversion in these conditions but at a bit rate of 40 Gb/s produced a closed eye diagram at the output, as could be expected by the eye diagrams at 20 Gb/s. Thus, the MZI-SOA operation without the push-pull configuration is limited to a bit rate of 20 Gb/s.

For that reason, the push pull configuration was employed in order to achieve acceptable operation at higher bit rates. 40 Gb/s operation was also attempted with the push-pull configuration and the NRZ format. However, the NRZ format is not suitable for the push pull configuration and again very considerable eye closure was observed as the Fig. 3.13 shows. In these conditions the match between the experiment and simulation is significantly deteriorated. Both the experimental and simulated eye diagrams show broadened bit transitions due to strong bit patterning, but the experimental eye diagram

shows a very low extinction ratio. The power offset of the '0' could not be removed by polarization adjustment and is believed to be due to ASE noise. It should be noted that due the limited gain recovery speed, the SOA acts as a low pass filter. In other words, higher frequencies are wavelength converted in the SOA with less efficiency when compared to lower frequencies. The purpose of the push-pull and interferometer structure is to reduce the amplitude of the low frequencies relatively to the higher frequencies of the SOA wavelength converted signals. This is achieved by 'subtracting' the converted pull signal from the converted push signal. However, as the bit rate increases, higher frequencies are converted with decreasing efficiency relatively to the lower frequencies. In order to compensate for this, low frequencies need to be subtracted to a larger extent. Consequently, since more power is subtracted to the push-arm signal as the bit rate increases, less power is outputted from the MZI-SOA. As a result, the conversion power efficiency is penalized and the signal to noise ratio of the output signal decreases.

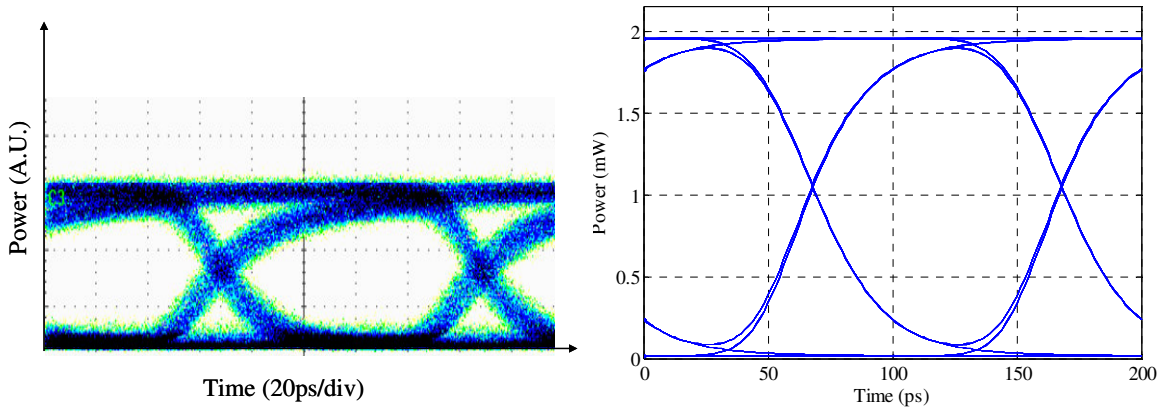

Fig. 3.11 Experimental (left) and simulated (right) eye diagrams of wavelength conversion of a 10 Gb/s NRZ signal without push-pull.

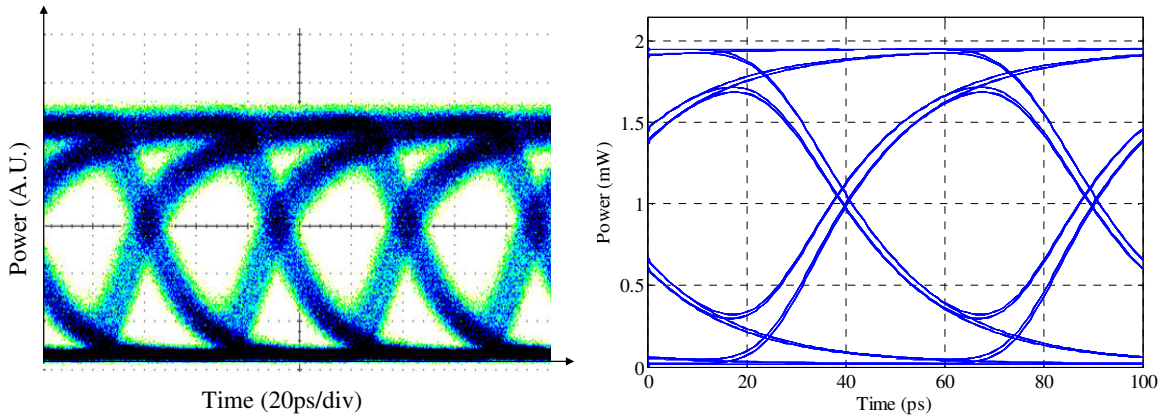

Fig. 3.12 Experimental (left) and simulated (right) eye diagrams of wavelength conversion of a 20 Gb/s NRZ signal without push-pull.

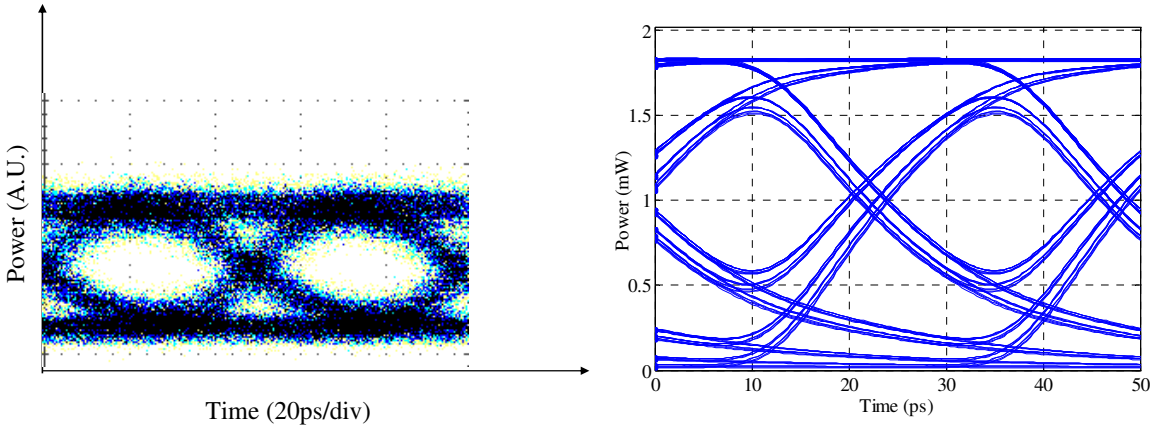

Fig. 3.13 Experimental (left) and simulated (right) eye diagrams of wavelength conversion of a 40 Gb/s NRZ signal using the push-pull configuration.

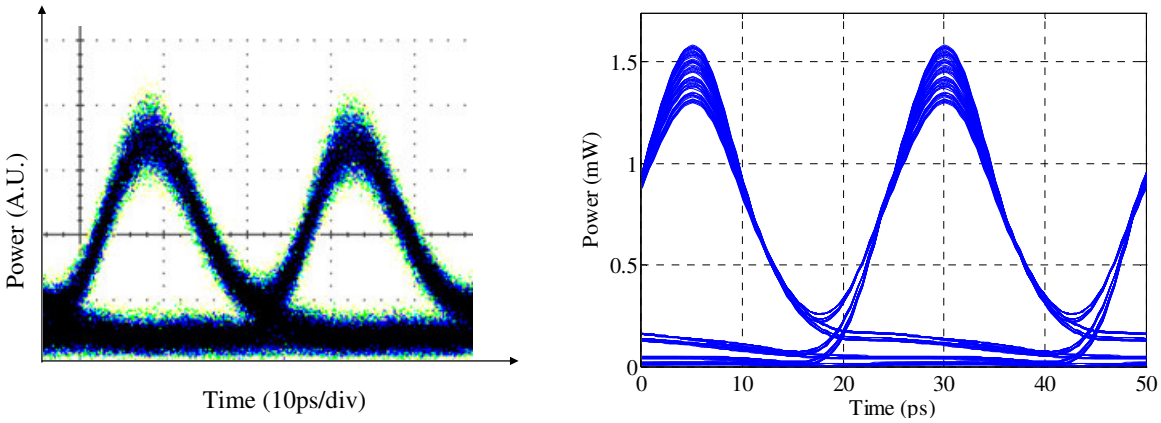

Fig. 3.14 Experimental (left) and simulated (right) eye diagrams of wavelength conversion of a 40 Gb/s RZ signal using the push-pull configuration.

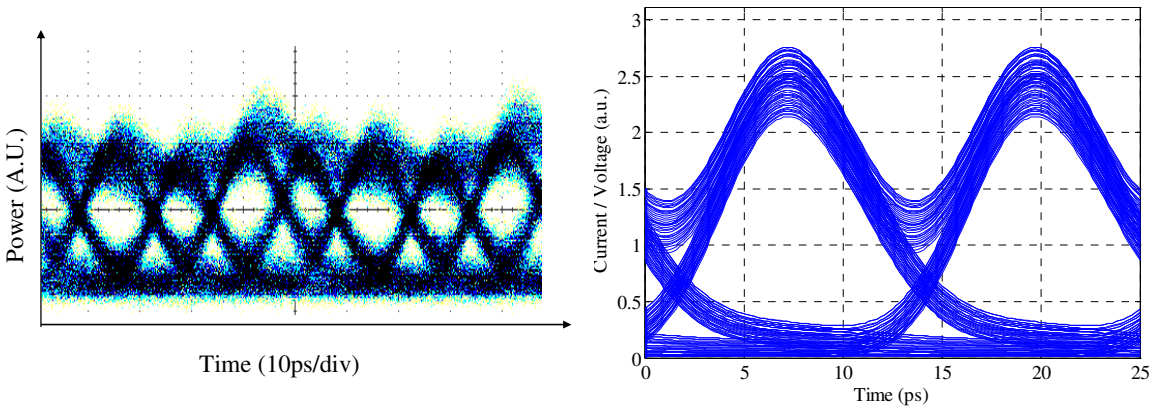

Fig. 3.15 Experimental (left) and simulated (right) eye diagrams of wavelength conversion of an 80 Gb/s NRZ signal using the push-pull configuration.

Changing the modulation format to RZ, with a duty cycle of 50%, significantly improved the performance of the wavelength conversion, which can be attested by the eye diagrams in Fig. 3.14. With an RZ pulse format, the push pull mode of operation can be

fully exploited as explained in Chapter 2. In this case, the output eye diagram shows very little bit patterning effects with double traces for bit transitions, depending on the previous bit value. Encouraged by the good performance at 40 Gb/s, 80 Gb/s operation was also tried. However, the 80 Gb/s transmitter suffered from stability problems, particularly in the bit rate multiplier (see Appendix C) and therefore the transmitter output was impaired by crosstalk between neighbouring pulses. As a consequence, the power of adjacent pulses of the transmitted signal depended on the delay and phase difference between the pulses, which explain the unevenness of the power of adjacent bits in the wavelength converted eye diagram in Fig. 3.15. Apart from that, although the MZI-SOA was capable of producing an eye diagram, very broad bit transitions and occurrences inside the eyediagram were observed due to the very significant bit patterning.

To better assess the wavelength conversion capabilities of the MZI-SOA at the different bit rates and configurations, the OSNR penalty was calculated through simulation. Since different bit rates are to be compared, a common OSNR reference would not be suitable. Therefore, for each bit rate and experimental condition (signal format and differential or non-differential configuration) the presented OSNR penalty is the difference between the required OSNR of the MZI-SOA output and input signals.

The results are plotted in Fig. 3.16 and are grouped in three curves. The first was obtained with a NRZ signal and the push-pull mode was not used. The second curve is still for a NRZ signal but now using the push pull configuration. For the last curve the pulse format is RZ and the configuration was differential. The results corroborate the conclusions drawn from the eye diagrams previously shown. Clearly, the differential mode outperforms the non differential mode and is practically unavoidable for bit rates larger than 10 Gb/s. Also, the RZ format does better than NRZ, allowing wavelength conversion at a bit rate of 40 Gb/s with a penalty of about 1.2 dB. Although an open eye diagram had been obtained at 80 Gb/s, the wavelength conversion penalty is at about 3.6 dB, which is too large for any practical application and is believed to underestimate the experimental penalty. The RZ with push-pull curve shows a floor of OSNR penalty at -1.5 dB at 15 – 20 Gb/s and for larger bit rates the penalty steadily increases. At low enough bit rates, the conversion penalty is negative, which means that the signal quality is actually improved. In this case, the input signal is not impaired, but the MZI-SOA is augmenting the extinction ratio by removing the power in the ‘0’ by reshaping the signal. Decreasing even more the

bit rate would not additionally improve the signal quality since the power in the '0' has already been removed to a great extent. However, for larger bit rates, the gain recovery speed limitation introduces ever increasing bit patterning. This result leads to the conclusion that wavelength conversion of an RZ signal in the MZI-SOA is limited to 40 Gb/s, with a penalty of 1.2 dB. The bit rate limitation of a NRZ signal is more severe, with a penalty of 1.9 dB at 20 Gb/s. The push-pull configuration is always superior to the non push-pull mode configuration and, henceforth, the differential mode will always be used.

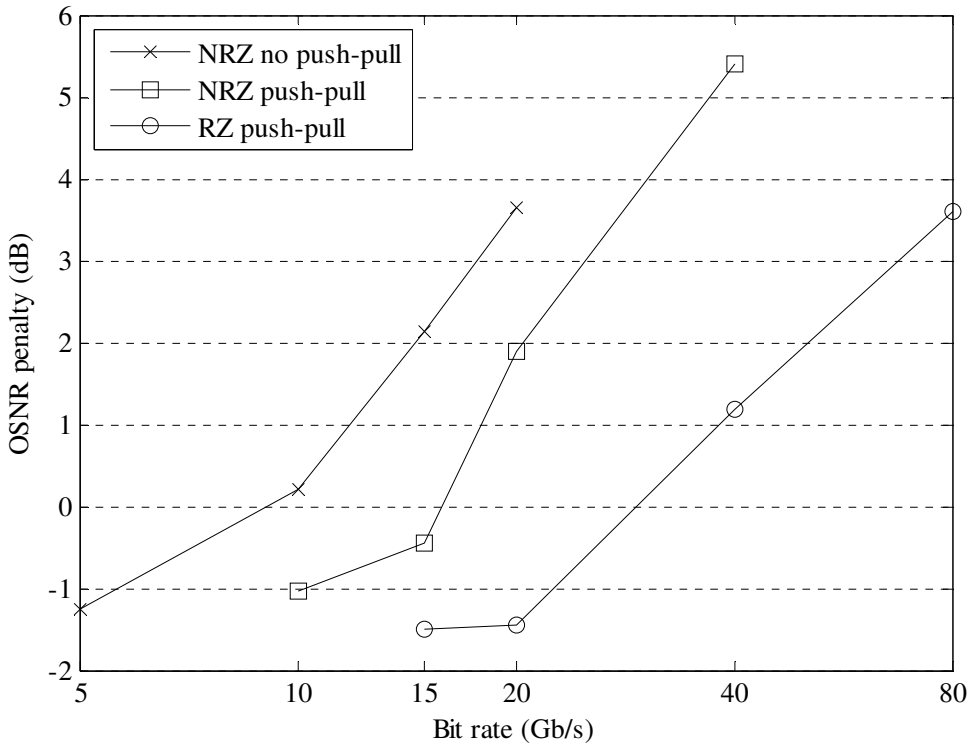

Fig. 3.16 OSNR penalty due to wavelength conversion in a MZI-SOA for NRZ input using the differential and non-differential mode and RZ input using the differential mode as a function of the signal bit rate. The lines are guides for the eyes.

3.4 Format conversion to CW beam

In the previous section, the MZI-SOA maximum operation bit rate was established to be 40 Gb/s. In this section, a more detailed study of the wavelength and format conversion will be done, using a CW beam at the interferometric input of the MZI-SOA. Format conversion is obtained when the MZI-SOA output signal does not have the same format as the input signal. The following formats will be fed to the MZI-SOA: RZ, carrier-suppressed RZ (CS-RZ) and NRZ. The powers of the input signal and CW beam strongly

determine the conversion performance and therefore this section will be dedicated to its analysis.

The dependence on the input powers will now be investigated for the RZ format, with 50% duty cycle. The OSNR has been fixed at 14.5 dB and the BER has been calculated for a wide range of interferometric and control input powers. The attenuation of the pull arm was set to 6.4 dB and the delay is 15 ps, as these are optimum values. The results are presented in Fig. 3.17 as a contour plot. It can be seen that higher power of the CW beam at the interferometric input enhances the wavelength conversion performance. This is known as the holding beam technique where the presence of a beam makes the gain recovery faster at the expense of reducing the SOA gain [11].

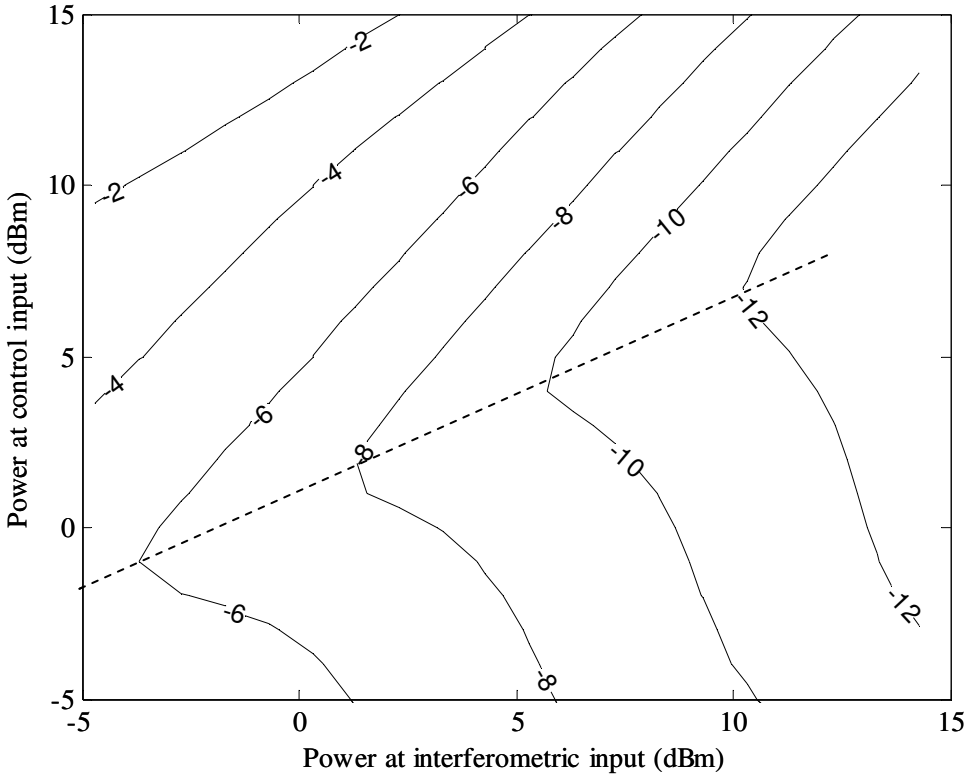

Fig. 3.17 Contour plot of $\log_{10}$(BER) of a 40 Gb/s RZ wavelength converted signal in the MZI-SOA. The abscissa and ordinate are, respectively, the powers at the control input and interferometric CW input. The dashed line is an approximation of the power at control input that minimizes the BER for a given interferometric input power.

Another conclusion to be drawn is that there is an optimum control signal power that minimizes the BER. The dependence of the optimum control signal power is approximately linear on the CW beam power and is expressed as

$$P_{cont} = a + b \times P_{int} \quad (4.1)$$

where P_{cont} and P_{int} denote the powers at the control input and interferometric inputs, respectively, in dBm, and a and b are fitting parameters. The fitting parameter values are presented in Table 3-2. Since similar fittings were performed for other modulation formats, Table 3-2 encompasses the fitting parameters of all the studied conditions. For the particular case of the RZ format, this expression means that under these simulation conditions the signal power that minimized BER should be about 60% of the power of the CW beam (in dB), plus 1 dB.

Table 3-2 Fitting parameters of the optimum control power as a function of the interferometric input power, for CW and short pulse interferometric inputs and RZ, CS-RZ and NRZ modulation formats.

Interferometric input	Modulation format	*a*	*b*
CW	RZ	1.09	0.57
	CS-RZ	1.09	0.66
	NRZ	1.87	0.62
Short pulse	RZ	2.10	0.41
	CS-RZ	2.05	0.42
	NRZ	3.27	0.49

The BER was also measured experimentally in the same OSNR and pull attenuation and delay conditions, as a function of the control signal power, for two CW beam powers. The CW beam power was set to 4.3 dBm, which was the maximum attainable value in the experiment, and then decreased 1 dB to 3.3 dBm. The experimental results are plotted in Fig. 3.18, as well as the simulation results, for comparison. Both the simulation and experimental curves show a V-shape trend. The power of the control signal at which the BER is minimum is well predicted by the simulation in comparison to the experiment, but, away from the minimum, the simulation significantly underestimates the BER. For the CW power of 4.3 dBm, the optimum control signal power is 4 and 4.5 dBm for the simulation and the experiment, respectively, whereas the practical rule found before predicts a power of 3.5 dBm. Analysing the curves for a CW power of 3.3 dBm, the optimum control signal power is 3 dBm for both the simulation and the experiment, whereas the practical rule predicts a power of 2.8 dBm. The practical rule slightly underestimates the optimum control signal power, but its precision is good enough for a starting point for a posterior finer tune of the control signal power. So as to explain the discrepancy between simulation and experimental results for the remaining regions of the V-shaped curves, the simulated

eye diagrams are shown for 4.3 dBm of CW power and the two control power extremes: 0 and 10 dBm. At these powers, the eye diagram shows bit patterning, especially for 10 dBm of control signal power. It should be noted that the match between simulation and experiment is much better for higher control signal powers than for lower powers relatively to the optimum power. The strong patterning effects due to incomplete gain recovery occurring at high power predicted by the simulation were also observed in the experiment, which corroborates the simulation prediction. However, at lower power, the simulation predicts a much better performance than the one found in the experiment. The problem at low powers is that the signal does not have enough power to open the MZI-SOA switch. In the simulation, the '0' state is biased with great precision, and a very low output power is obtained in the '0' state. Therefore, a small power is enough to alter the MZI-SOA state to a '1'. However, in the experiment, the '0' state is already transmitting a more significant amount of power and hence more control signal power is required to commute the MZI-SOA to a '1' state. One other reason could be the shape of the gain saturation curve of Fig. 3.7 and the power transfer curve of Fig. 3.8. While the simulated curve is much smoother, the experimental curve has two distinct gain saturation regions. Consequently, in the simulation, the SOA operation is less sensitive to the absolute input power, whereas in the experiment, for actual SOA saturation and switching, the power must lie beyond a given threshold, which is related to the transition between the unsaturated and saturated regimen.

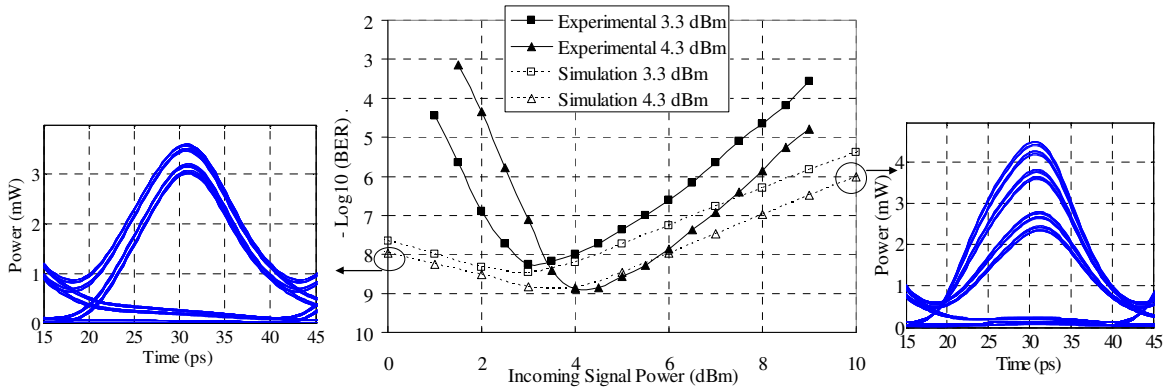

Fig. 3.18 Middle: BER of wavelength conversion of a 40 Gb/s RZ signal as a function of the control signal power, for two different interferometric powers (3.3 and 4.3 dBm). Full lines and symbols denote experimental data whereas dashed lines and empty symbols denote simulation data. The lines are guides for the eyes. Left and right: simulation eye diagrams of the wavelength conversion output for a CW power of 4.3 dBm and 0 and 10 dBm of control signal, respectively.

Note that the power required to saturate the SOA in the determination of the gain saturation curve of Fig. 3.7 is not comparable to the powers in a wavelength conversion

experiment, since in the wavelength conversion the probe beam has significant power that also saturates the SOA, acting as a holding beam.

The performance sensitivity to the control signal power has also been obtained from this data. It is defined as the power range where the BER is up to 10 times larger than the minimum BER. From the experimental data, the sensitivity to the control signal power was 2.7 and 2.9 dB for 4.3 and 3.3 dBm of CW power, respectively. The acceptable power range for 3.3 dBm is larger than for 4.3 dBm, since the minimum BER is larger and the V-shaped curve is more open. Due to the discrepancies of the V-shaped curve enounced before, the simulation completely misses the correct sensitivity to the control signal power, with calculated values between 6 and 7 dB.

The wavelength conversion OSNR penalty will now be determined, using -4.3 dBm of CW power and optimum control signal power. Instead of using the ideal noiseless receiver as was done to obtain the results of Fig. 3.18, now it is considered that the receiver has a sensitivity of -3 dBm at 40 Gb/s, for an infinite extinction ratio NRZ signal and a BER of 10^{-9}, to better match the experimental findings. This sensitivity encompasses all the noises generated by the receiver and also the subsequent noise and impairments from the parallel BER tester, such as from the demultiplexing stage and discriminator. Also, in the experiment, a very long binary sequence of 2^{31} bits was used, which give rise to temporal effects that are not modelled accurately in the simulation. These effects are accounted for in the simulation by the sensitivity of the receiver as a practical way, even though this is a rather imperfect description of these effects. The extinction ratio of the RZ input signal is 15 dB.

The BER has been both measured experimentally and calculated by simulation and is plotted in Fig. 3.19, for both the RZ input signal and the wavelength conversion output.

The comparison between the experimental and simulation curves shows good agreement, except for the input signal curve, also called back to back curve, at very low BER. The discrepancy is most likely caused by intersymbolic effects due to the long sequence used in the experiment which are not properly modelled in the simulation, as mentioned. At high BER the optical noise dominates and the simulation can describe its effect with adequate accuracy, while at high OSNR other effects start to dominate, and therefore the simulation description might lack accuracy.

Taking the required OSNR values for a BER of 10^{-10}, the back to back simulation deviates -0.6 dB from the experiment, while for the wavelength conversion output, this deviation is 0.1 dB. Considering the penalty of the wavelength conversion, i.e. the difference between the OSNR of the wavelength converted signal and the back to back signal, the experimental penalty is 3.0 dB, while the simulation predicts 3.7 dB, mainly due to the discrepancy of the back to back curve. The origin of the 3.0 dB of penalty can be seen in Fig. 3.20, where the experimental and simulated eye diagrams are shown. Bit patterning is evident both at the '0' and '1' levels, causing the observed penalty. Fig. 3.20 also shows the experimental and simulated optical spectra of the wavelength converted signal.

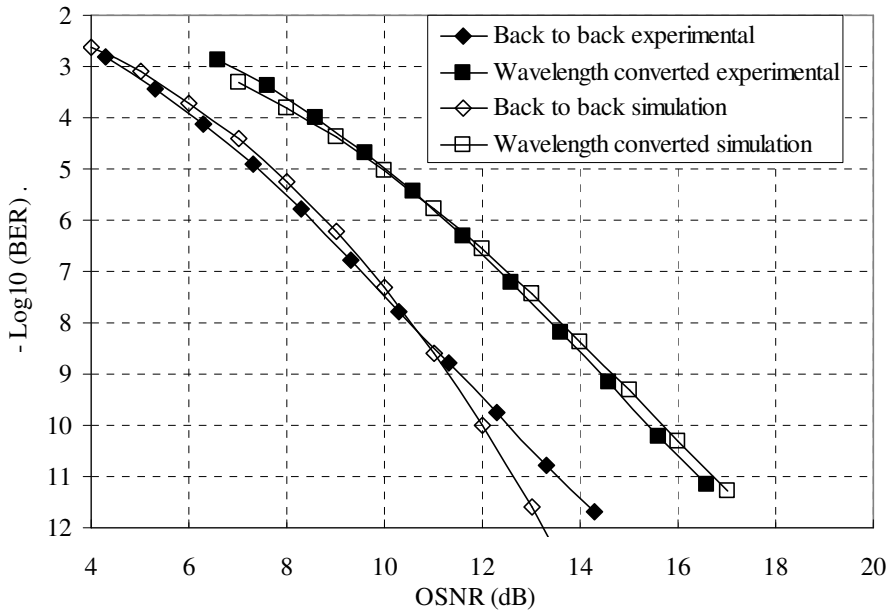

Fig. 3.19 BER experimentally measured (full symbols) and calculated by simulation (open symbols) for the RZ input signal (diamonds) and the wavelength conversion output (squares) as a function of the OSNR at the receiver. The lines are guides for the eyes.

The spectra show a typical spectrum of a RZ signal with chirp, noticeable by the asymmetry of both side lobes and sub-carriers. The experimental spectrum shows greater asymmetry than the simulated spectrum, most likely due to stronger phase-amplitude coupling in the SOA than anticipated, or improper modelling [10]. One other difference is the small undulation of the simulation spectrum that does not appear in the experimental spectrum. The reason behind this undulation is the small bit sequence size of 2^7= 128 bits, while in the experiment the sequence size is 2^{31} bits. In the simulation, due to the small sequence size, small chunks of data are repeated often and therefore there are specific

frequencies that have more power in the spectrum. Both experimental and simulated spectra were taken with a resolution of 0.01 nm.

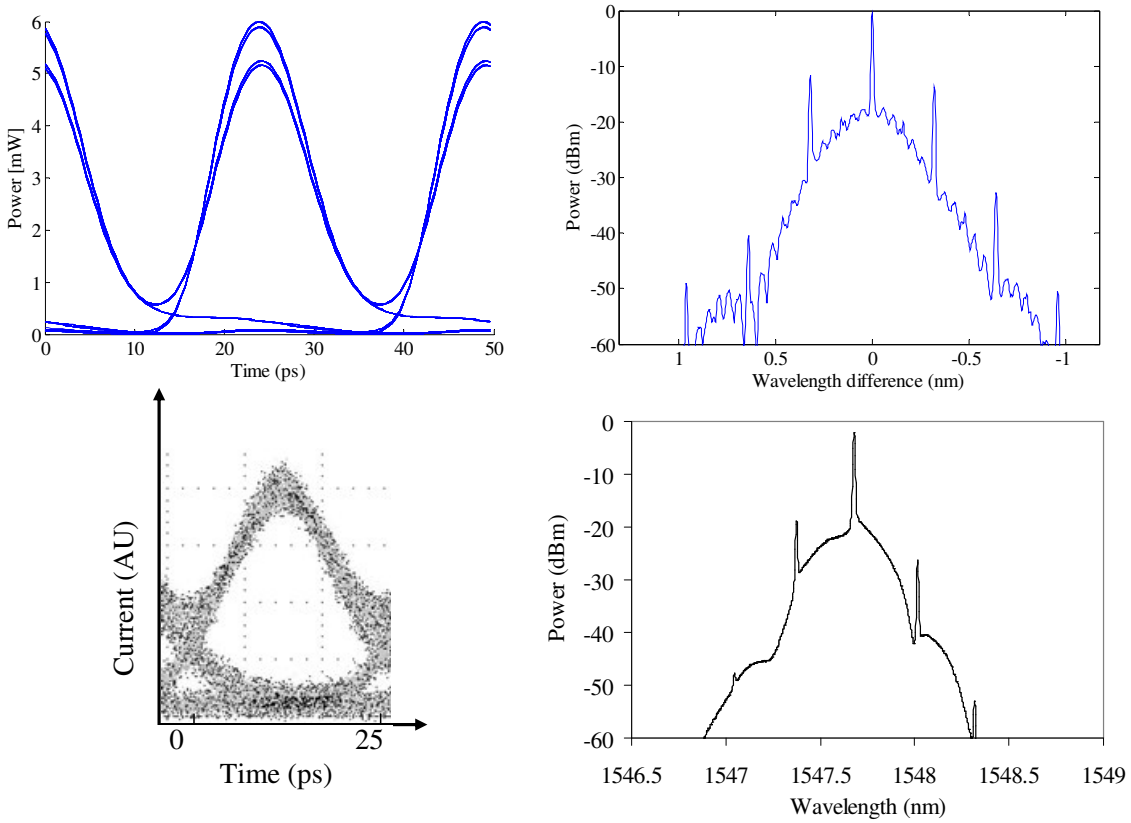

Fig. 3.20 Simulated (top) and experimental (bottom) eye diagrams (left) and optical spectra (right) of a wavelength converted RZ signal to a CW beam. The optical spectra resolution is 0.01 nm.

The same study of the BER performance of the wavelength conversion as a function of the input power was also done for a CS-RZ formatted control signal. The CS-RZ format is of great interest to long-haul optical transmission links due to its higher tolerance to nonlinear effects [12]. In the CS-RZ format, the pulse carver (see Appendix C) both suppresses the optical carrier by introducing a pi phase difference between consecutive bits and shapes the pulses to the RZ format. Hence, as the SOA gain (and therefore the MZI-SOA operation) is dependent only on the input signal power and not signal phase, it is expected that the MZI-SOA operation will be similar to the operation with the RZ format. However, the MZI-SOA modulates only the amplitude of the incoming CW laser beam with some chirp and the pi phase difference in consecutive bits is not restored. Therefore, the format of the MZI-SOA wavelength converted signal is not CS-RZ anymore, but, instead, it is RZ. So, when operated with the CS-RZ (or another

format with phase management), the optical processing operation in the MZI-SOA is effectively a wavelength and format conversion rather than a wavelength conversion alone. Nonetheless, the data is correctly imprinted on the probe wavelength, enabling optical processing at subsequent stages. Fig. 3.21 shows the simulated and experimental spectra and eye diagrams of the CS-RZ converted signal. The spectrum of the converted signal is a typical spectrum of a RZ signal and not CS-RZ anymore, as the signal now clearly has an optical carrier. The eye diagrams show some bit patterning in both the '0's and '1's. As it will be seen, these patterning effects translate into worse BER and OSNR penalty performance when compared to the RZ format.

The optimum operation powers of the CW beam and control signal will now be investigated as it was also done for the RZ format. The BER results are presented in Fig. 3.22, which were obtained in the same conditions as for the RZ signal format, at a fixed OSNR of 14.5 dB.

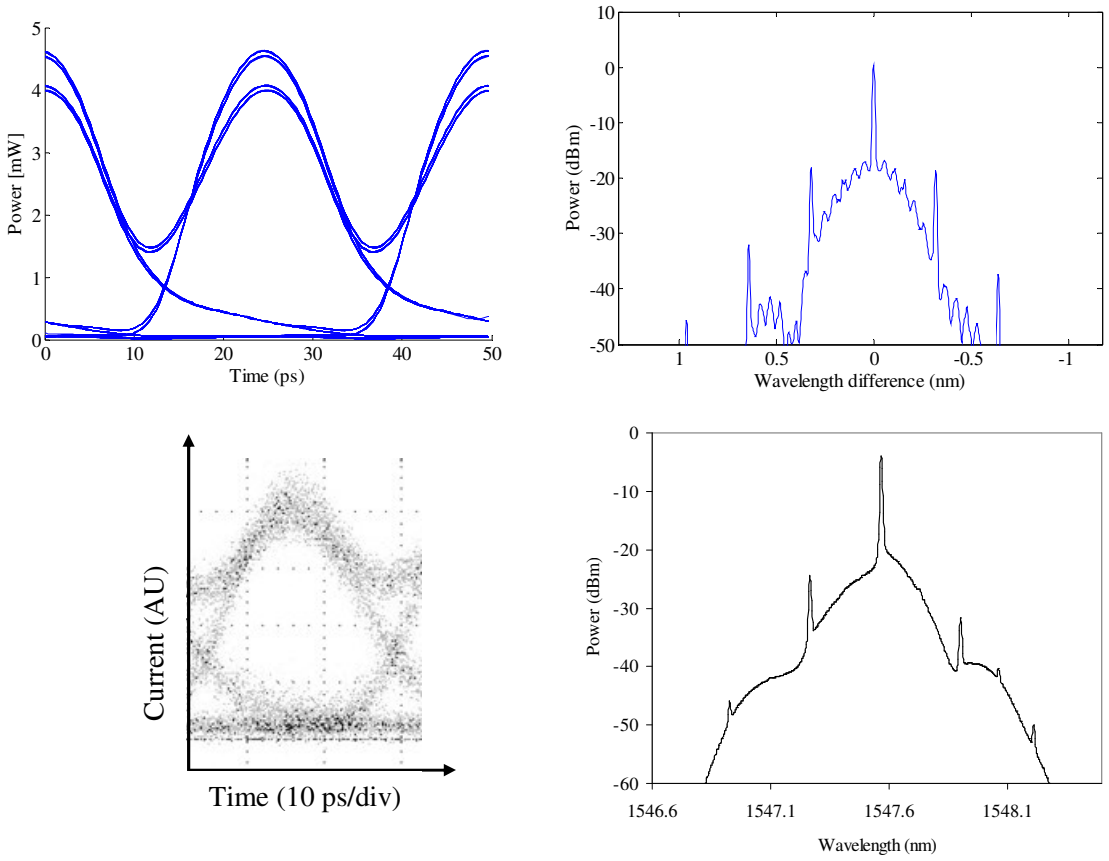

Fig. 3.21 Simulated (top) and experimental (bottom) eye diagrams (left) and optical spectra (right) of the output of the wavelength conversion of a CS-RZ signal to a CW beam. The optical spectra resolution is 0.01 nm.

It can be observed that the same general conclusion can be drawn for the CS-RZ format as for the RZ-format, which is expectable due to the similar pulse shape, although the duty cycle is different. Again, it is beneficial to increase the CW beam power according to the holding beam technique. Within the investigated range of powers it is also possible to define the region of control signal powers that minimizes the BER. Again, the optimum control signal power depends approximately linearly on the CW beam power and Eq. (4.1) can be used once more. The fitting parameters were already presented in Table 3-2. Comparing the fitting parameters relative to the CS-RZ input signal to those of the RZ input signal, only the proportionality factor increased from 0.56 to 0.66. In other words, the CS-RZ wavelength conversion requires more control signal power than the RZ wavelength for optimum performance, for the same CW beam power. It should be noted that the CS-RZ format, due its larger duty cycle, has less peak power than the tested RZ, for the same average power. Therefore, the CS-RZ format, when compared to the RZ format, needs more average power to achieve the same peak power, SOA gain saturation and MZI-SOA switching transmissivity.

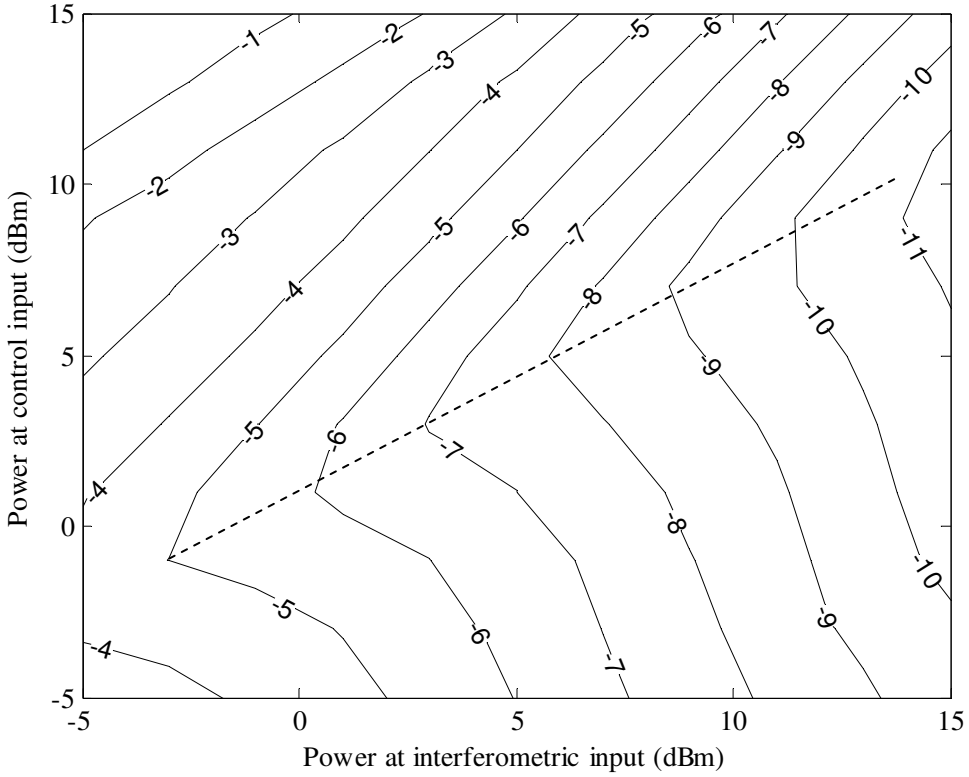

Fig. 3.22 Contour plot of $\log_{10}$(BER) of wavelength conversion of a 40 Gb/s CS-RZ signal in the MZI-SOA as a function of the powers at the control input and interferometric CW input. The dashed line is an approximation of the power at control input that minimizes the BER for a given interferometric input power.

The simulation predictions of the optimum control powers were also compared to the experiment for CW beam powers of 4.3 and 3.3 dBm and the results are plotted in Fig. 3.23. The dependence of the BER on the control signal power is the familiar V-shaped curve and again it is observed that, for powers away from the optimum control signal power, the BER is higher in the experiment than in the simulation. Naturally, the reason for this discrepancy for the CS-RZ is the same as in the case of the RZ. However, for the CS-RZ format the optimum control signal power is underestimated by 1 – 1.5 dB. Whereas the simulated optimum power are 3 dBm and 4 dBm, respectively, for the 3.3 and 4.3 dBm input powers, the experimental results indicate optimum control powers of 4.5 and 5 dBm. Furthermore, the minimum BER is overestimated in the simulation by about 1.5 and 1 orders of magnitude for the 4.3 and 3.3 dBm CW beam powers, respectively.

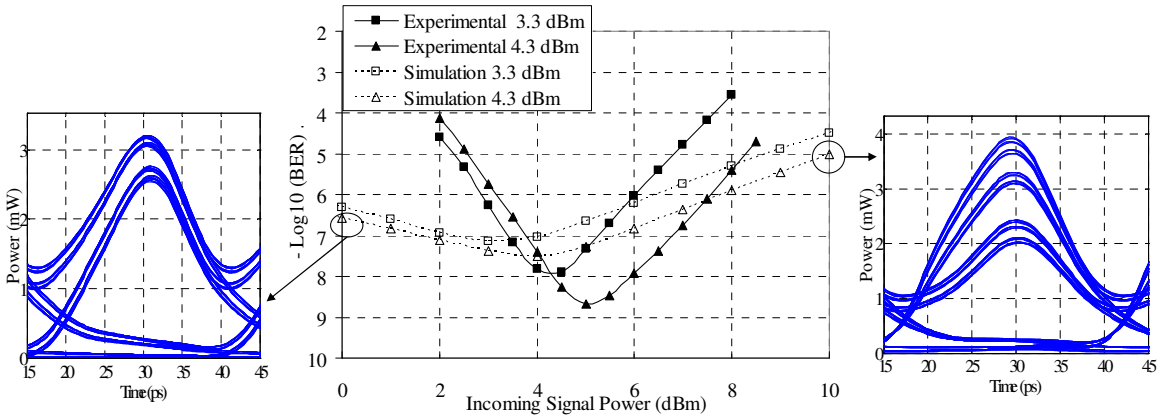

Fig. 3.23 Middle: BER of wavelength conversion of a 40 Gb/s CS-RZ signal as a function of the control signal power, for two different interferometric powers (3.3 and 4.3 dBm). Full lines and symbols denote experimental data whereas dashed lines and empty symbols denote simulation data. The lines are guides for the eyes. Left and right: simulation eye diagrams of the wavelength conversion output for a CW power of 4.3 dBm and 0 and 10 dBm of control signal, respectively.

The BER was also measured as a function of the OSNR for both the input signal and the wavelength converted output, which results are plotted in Fig. 3.24. The CW beam and control signal powers were set at 4.3 and 4.5 dBm, the same as in the RZ case. Comparing the simulation and experimental curves shows that the trends in both cases are very similar, even though the curves have some offset. For a BER of 10^{-10}, the required OSNRs for the input signal are 13.1 and 13.6 dB for the experiment and simulation, respectively, while for the converted signal they are 16.5 and 17.7 dB, respectively, for the experiment and simulation. Hence, the penalty, or difference of required OSNR, due to the

conversion is 3.4 and 3.9 dB for the experiment and simulation, respectively. The obtained values for the RZ signal were 3 and 3.7 dB in the same conditions.

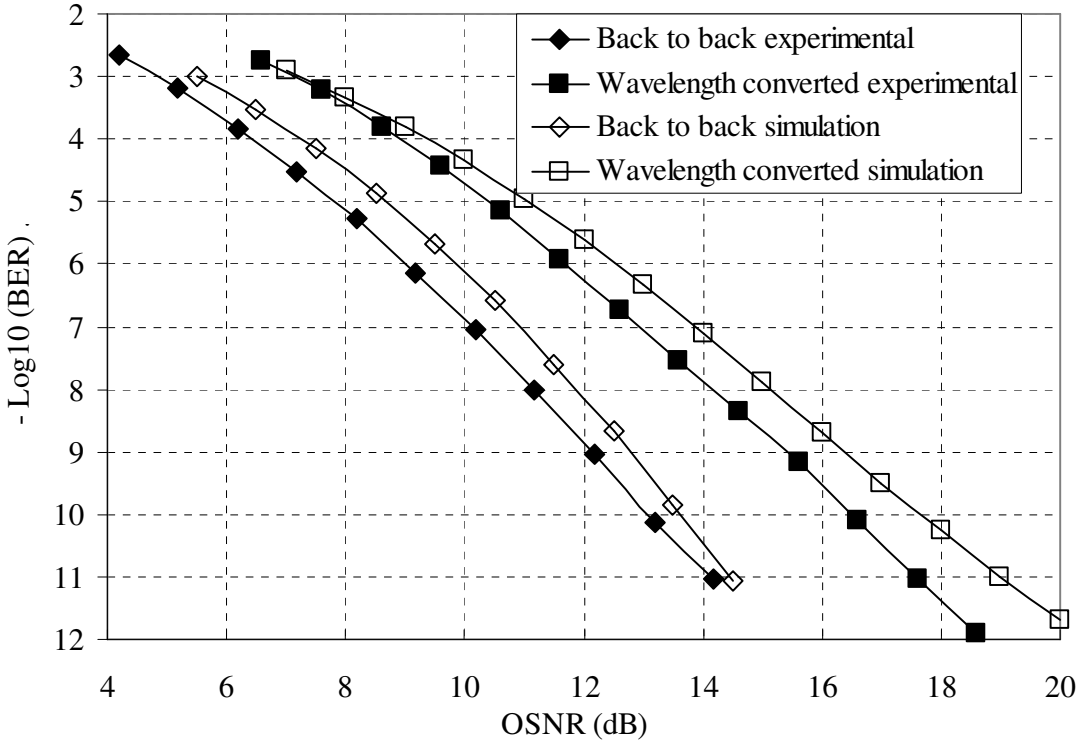

Fig. 3.24 BER experimentally measured (full symbols) and calculated by simulation (open symbols) for the CS-RZ input signal (diamonds) and the wavelength conversion output (squares) as a function of the OSNR at the receiver. The lines are guides for the eyes.

The increase of penalty and larger BER at the optimum input powers when using the CS-RZ signal relatively to the RZ is due to the larger duty cycle of the CS-RZ compared to the RZ signal. There is less time with no power between each pair of pulses for pulses with larger duty cycle. Hence, after the pulse disappears, there is less time for the SOA to recover from saturation before the next pulse arrives. Consequently, the gain experienced by the following pulse will be more influenced by the previous pulse for signals with larger duty cycle than for signal with smaller duty cycle, even though the differential mode is applied to cancel some of the slow gain recovery. The impact of the input signal duty cycle on the performance will be studied in greater detail in section 3.6.

As it was seen in the previous section, the wavelength conversion performance for the NRZ format is worse than for the RZ format. A more detailed study is now presented. The study previously done for the RZ format and CS-RZ format is presently done for the NRZ. Again, in the same conditions as the other formats, the OSNR has been fixed at 14.5

dB and the BER was calculated by simulation as a function of the input control signal and CW beam powers. The results are shown in Fig. 3.25. As expected, the BER improves for larger CW powers, and the optimum control signal power depends approximately linearly on the CW beam power.

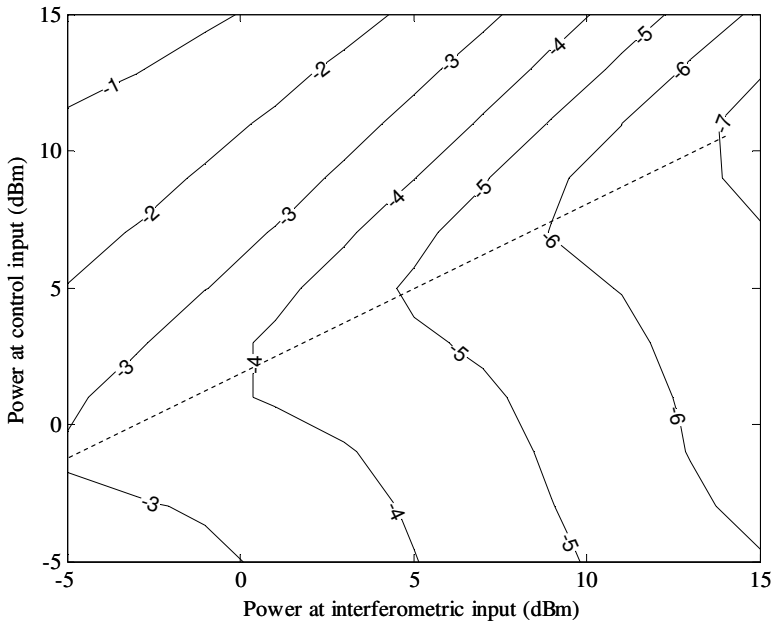

Fig. 3.25 Contour plot of $\log_{10}$(BER) of wavelength conversion of a 40 Gb/s NRZ signal in the MZI-SOA as a function of the powers at the control input and interferometric CW input. The dashed line is an approximation of the power at control input that minimizes the BER for a given interferometric input power.

The fitting parameters for Eq. (4.1) are again presented in Table 3-2. Although the fitting parameters are very similar to the parameters of the RZ and CS-RZ modulation formats, the value of the optimum BER is significantly larger for the NRZ format than for the RZ and CS-RZ formats. This agrees with the preliminary simulation study, whose results were plotted in Fig. 3.16. As a matter of fact, when the wavelength conversion was attempted experimentally, the BER tester was not able to synchronize with the signal and therefore it was not possible to obtain experimental BER measurements. Therefore, Fig. 3.26, that presents the plot of BER versus the OSNR at the receiver results, misses the experimental curve of the wavelength converted signal. It can be observed in the BER simulation curve of the wavelength converted signal that there is an error floor, which explains why the BER tester could not acquire the signal clock. Typically, the BER tester would be able to synchronize first to a good quality signal that is progressively impaired,

allowing measurements of BER up to 10^{-2}. However, when the signal is very impaired from the beginning of the test, the BER tester is not able to perform a BER measurement.

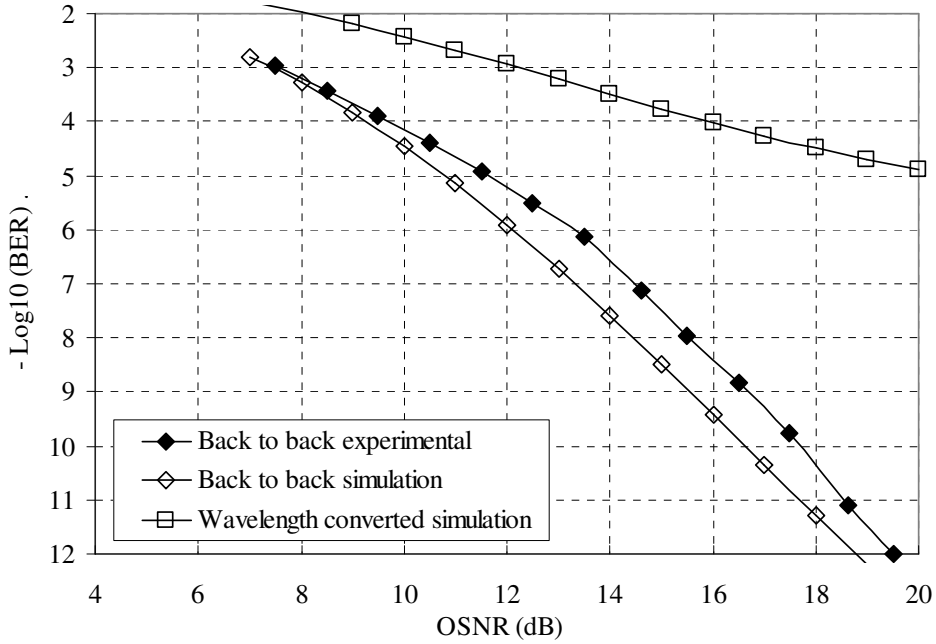

Fig. 3.26 BER experimentally measured (full symbols) and calculated by simulation (open symbols) for the NRZ input signal (diamonds) and the wavelength conversion output (squares) as a function of the OSNR at the receiver. The lines are guides for the eyes.

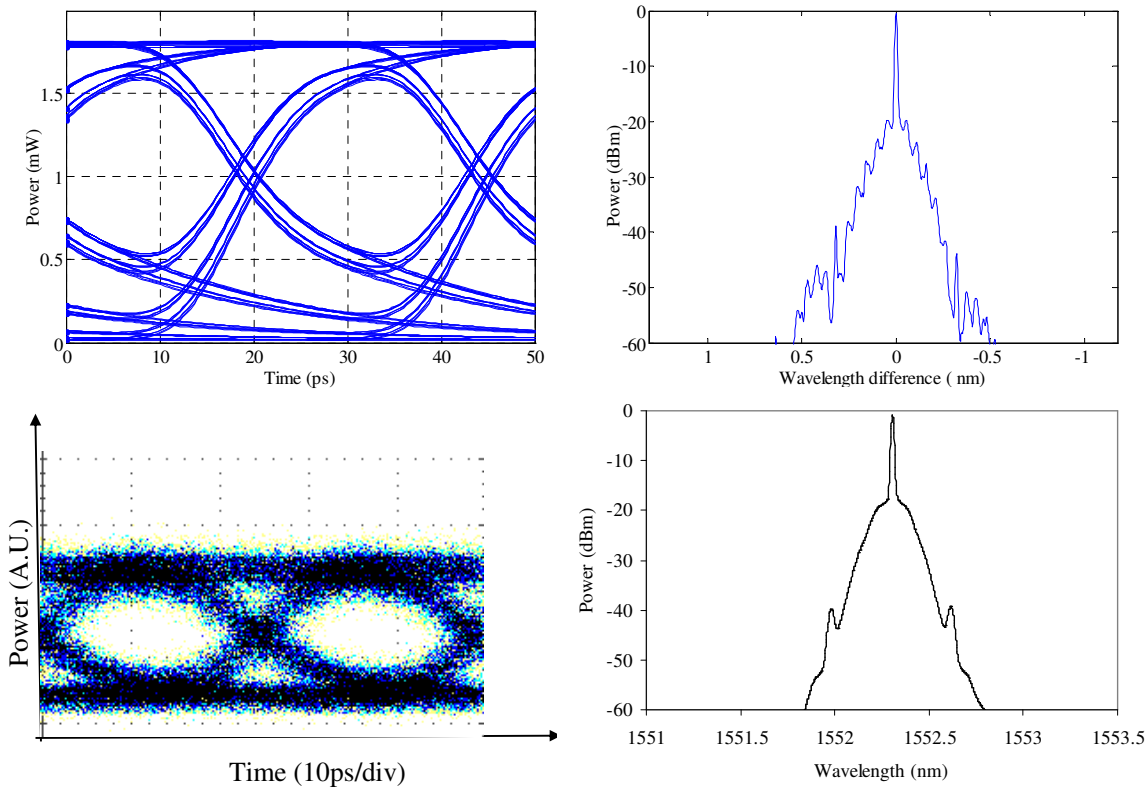

Fig. 3.27 Simulated (top) and experimental (bottom) eye diagrams (left) and optical spectra (right) of the output of the wavelength conversion of a NRZ signal to a CW beam. The optical spectra resolution is 0.01 nm.

The eye diagrams and spectra obtained in the experiment and simulation are shown in Fig. 3.27. The spectra are typical of a NRZ signal, but the eye diagrams show that the quality of the signal is very bad, with significant bit patterning and reduced extinction ratio, confirming the BER results.

3.5 Format conversion to short pulse beam

Up to this point, wavelength and format conversion has always been performed in the MZI-SOA using a CW beam at the interferometric port. However, several optical processing applications require short pulse format signals, as seen in Chapter 2. The CW beam will now be replaced by a pulsed laser beam to perform data conversion to short pulses, as depicted in Fig. 3.28. The pulsed laser beam is produced by a mode locked laser (MLL), synchronous to the input signal bit rate. The MLL output is fed to the MZI-SOA through a variable optical delay line to control the delay between the short pulses and the control signal, and additionally through a polarization controller, attenuator and isolator, as in the CW beam case. In the simulation, the short pulses were modelled as having Gaussian shape and a full width at half maximum (FWHM) of 4 ps, which match well the experimental observations. The experimental and simulation characterization of the MLL output is presented in Fig. 3.29, with the eye diagrams and spectra in both cases.

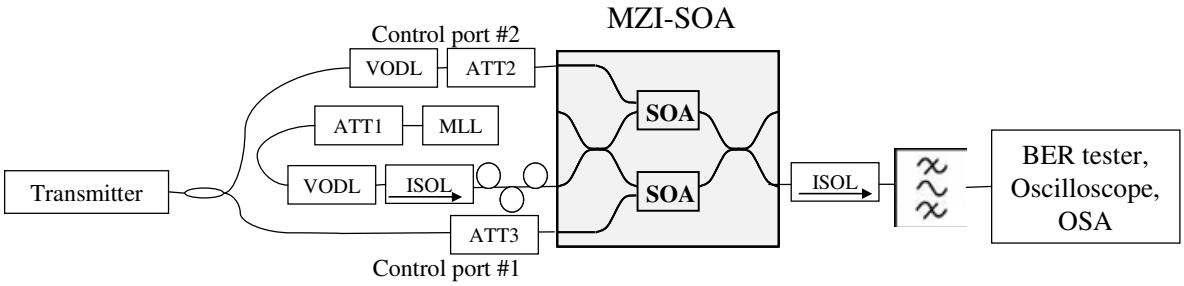

Fig. 3.28 Setup to perform wavelength and format conversion to short pulses in the MZI-SOA.

The power optimisation procedure was repeated as before for the CW beam case and a RZ signal at the control input. The eye diagrams, optical spectrum and BER curves were then acquired. For the BER evaluations, because of the good operating capabilities of the MZI-SOA with RZ format, the extinction ratio of the incoming signal was deliberately reduced to 10 dB. The power optimisation plot is presented in Fig. 3.30. Similarly to the

CW case, the optimum control signal power is linearly dependent on the interferometric input power and Eq. (4.1) can be used once again. The fitting parameters are again in Table 3-2. Comparing to the CW case, it can be seen that the fitting parameters changed, which is expectable due to the very different nature of the probe beam. In fact, it was noticed that for different delay and attenuation of the pull arm, there is an optimum probe beam power, unlike the dependence of Fig. 3.30. In this case, increasing the probe power does not always yield better performance. This phenomenon was also observed in the experiment.

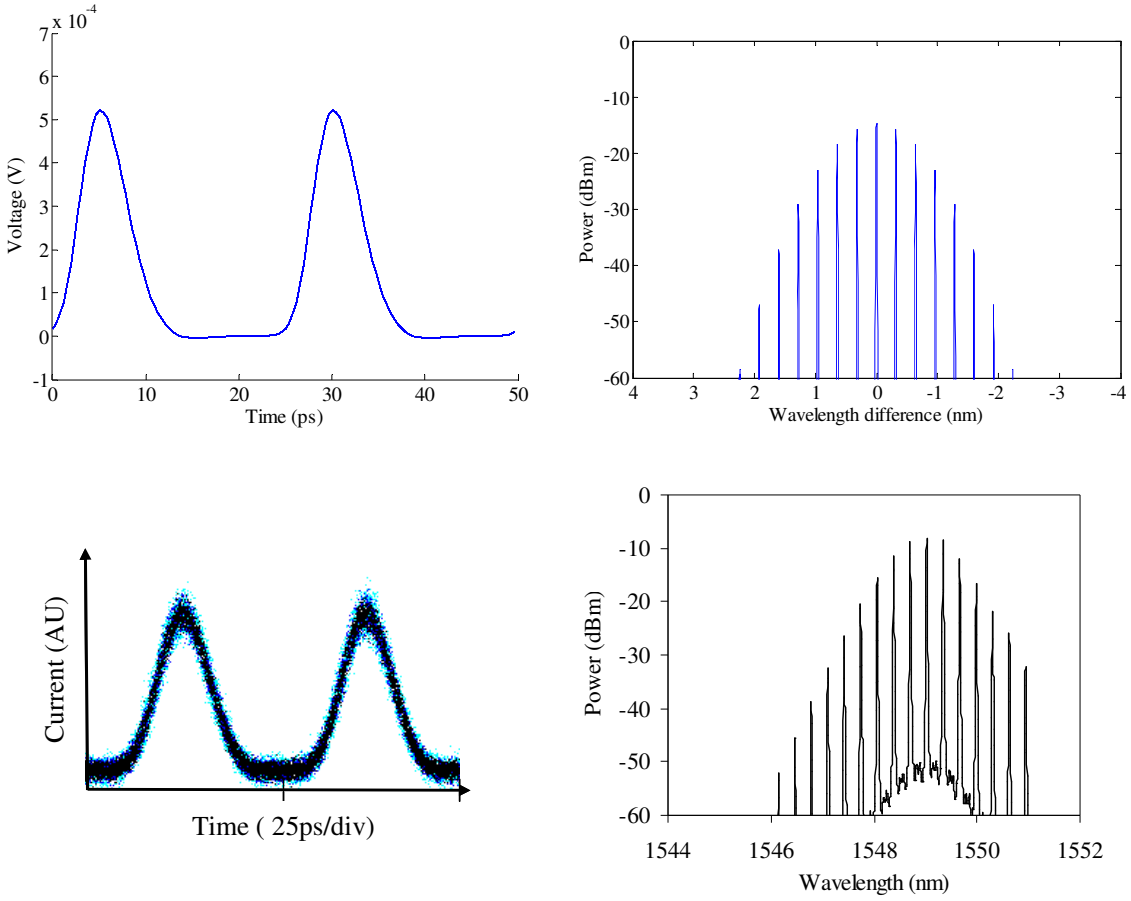

Fig. 3.29 Simulated (top) and experimental (bottom) eye diagrams (left) and optical spectra (right) of the output of the short pulse MLL output.

The eye diagrams and spectra of the MZI-SOA output are presented in Fig. 3.31. The first difference to be noted from the conversion of the RZ signal to a CW beam is that now the output pulses are much narrower, as expected, due to the use of the short pulses at the interferometric input port. Still, the eye diagrams again show bit patterning effects on the '1' level. Regarding the optical spectra, it is very broad because of the short duration of

the pulses. The experiment revealed a broader and more asymmetric spectrum than in the simulations, most likely due to the stronger chirp and self phase modulation than considered in the simulation.

The BER results from both the simulation and experiment are plotted in Fig. 3.32 as a function of the OSNR at the receiver, for the incoming RZ signal and for the short pulse output signal. Again, taking the required OSNR to attain a BER of 10^{-10}, the OSNR for the back to back, or input control signal, is 14 and 14.6 dB for the experiment and simulation, respectively. For the short pulse converted signal, the required OSNR is 13 dB for both the experiment and simulation. Hence, the short pulse conversion penalty is -1.0 and -1.6 dB, respectively, for the experiment and simulation. A negative penalty indicates that even though bit patterning is introduced, the signal is actually improved from the input to the output signal. The increase in quality of the signal is attributed solely to the very short duty cycle of the output signal. It is known that for the same average power, shorter duty cycle signals have a larger vertical eye opening at the sampling instant and therefore have better performance than larger duty cycle signals.

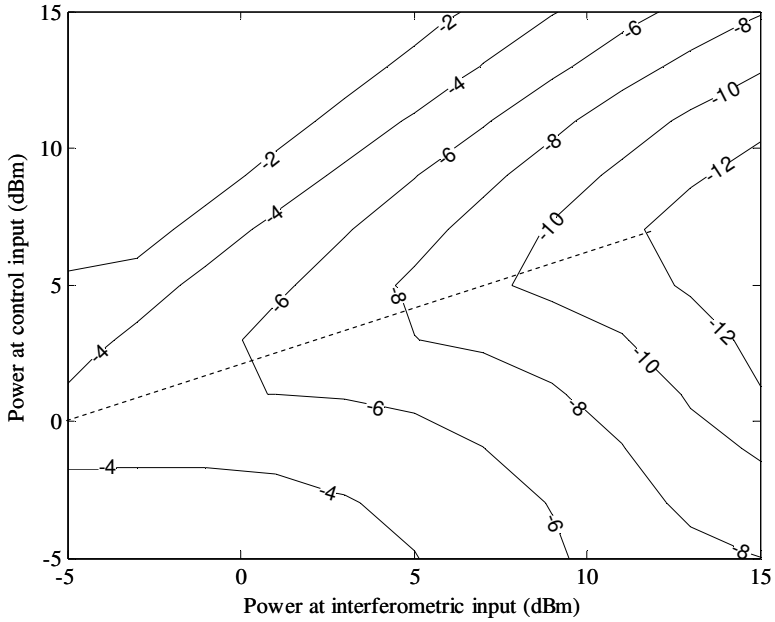

Fig. 3.30 Contour plot of $\log_{10}$(BER) of wavelength conversion of a 40 Gb/s RZ signal in the MZI-SOA as a function of the powers at the control input and interferometric pulsed input. The dashed line is an approximation of the power at control input that minimizes the BER for a given interferometric input power.

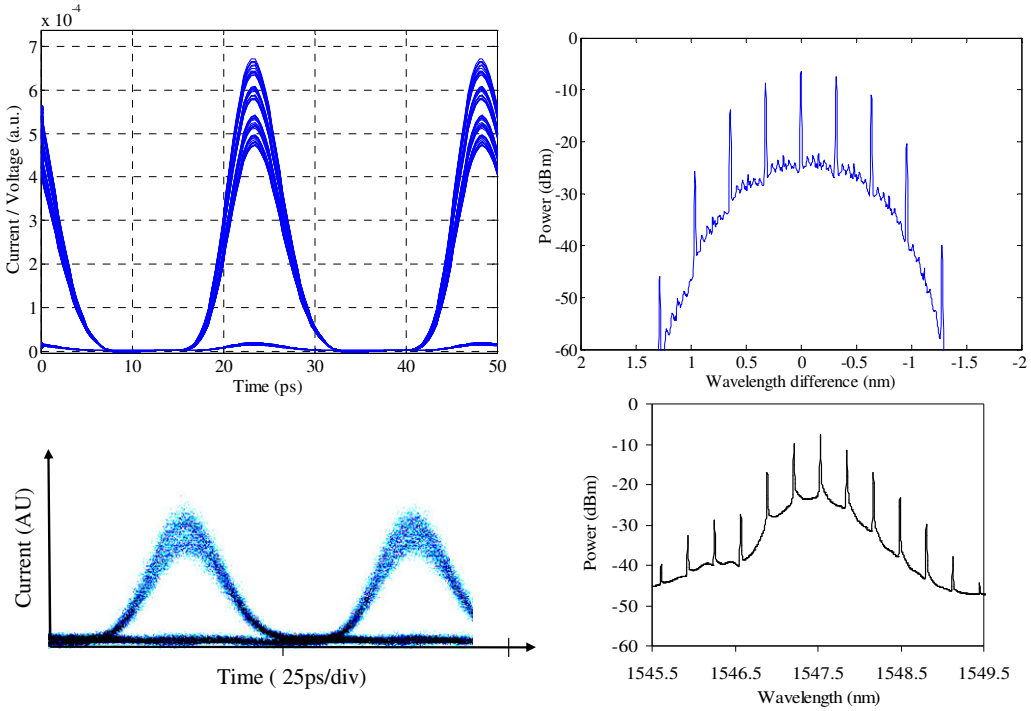

Fig. 3.31 Simulated (top) and experimental (bottom) eye diagrams (left) and optical spectra (right) of the MZI-SOA conversion output when operated with a RZ control signal and pulsed probe beam. The optical spectra resolution is 0.01 nm.

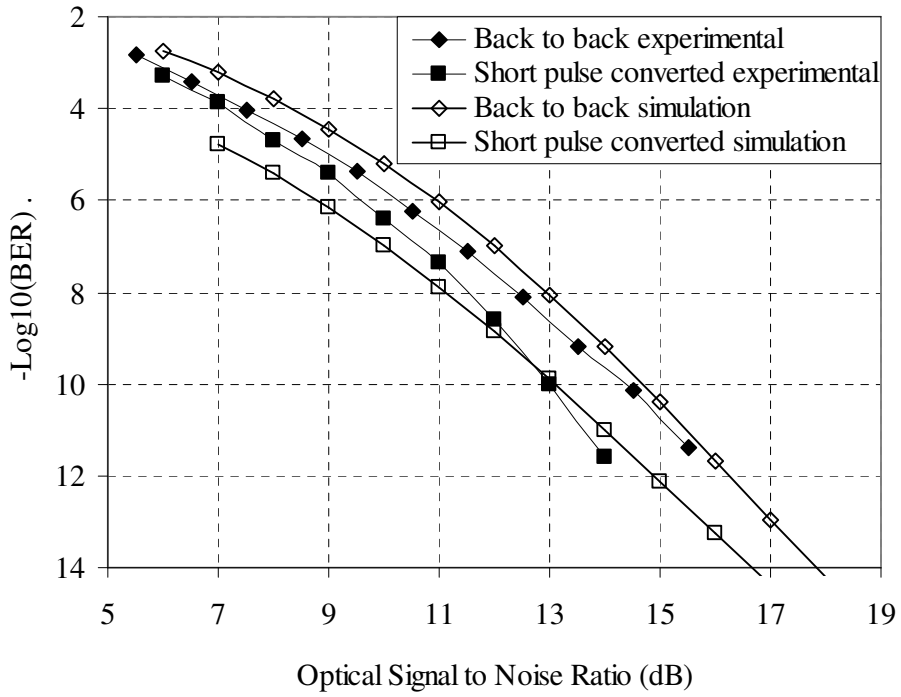

Fig. 3.32 BER experimentally measured (full symbols) and calculated by simulation (open symbols) for a RZ input signal (diamonds) and the wavelength conversion output (squares) as a function of the OSNR at the receiver. The lines are guides for the eyes.

The format of the input signal was now changed from RZ to CS-RZ format and the power optimisation and BER measurements were repeated, as well as the spectrum and eye diagram acquisitions. The extinction ratio was also set to 10 dB. Fig. 3.33 presents the simulated BER values as a function of the interferometric and control input power. The conclusions for the CS-RZ format are the same as for the RZ format. The fitting parameters of the linear dependence of Eq. (4.1) are in Table 3-2 which are very similar to the values for the RZ signal.

The eye diagrams and optical spectra are shown in Fig. 3.34, where, again, bit pattern effects are present in the '1' level, and now, also on the '0' level. Once more, the experimental optical spectrum is more asymmetric and broad than in the simulations, due to the aforementioned reasons.

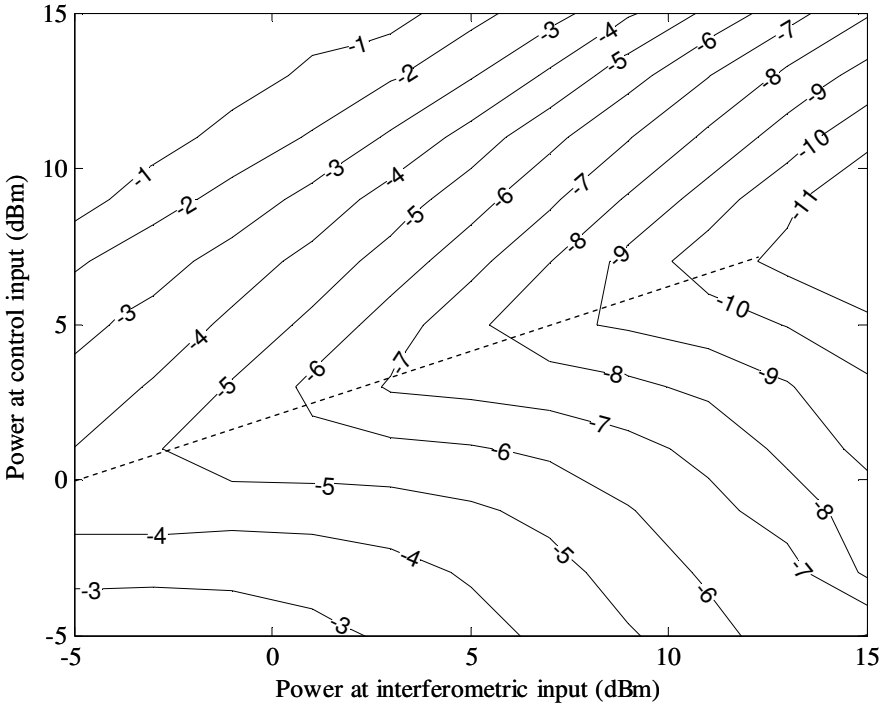

Fig. 3.33 Contour plot of $\log_{10}$(BER) of wavelength conversion of a 40 Gb/s CS-RZ signal in the MZI-SOA as a function of the powers at the control input and interferometric pulsed input. The dashed line is an approximation of the power at control input that minimizes the BER for a given interferometric input power.

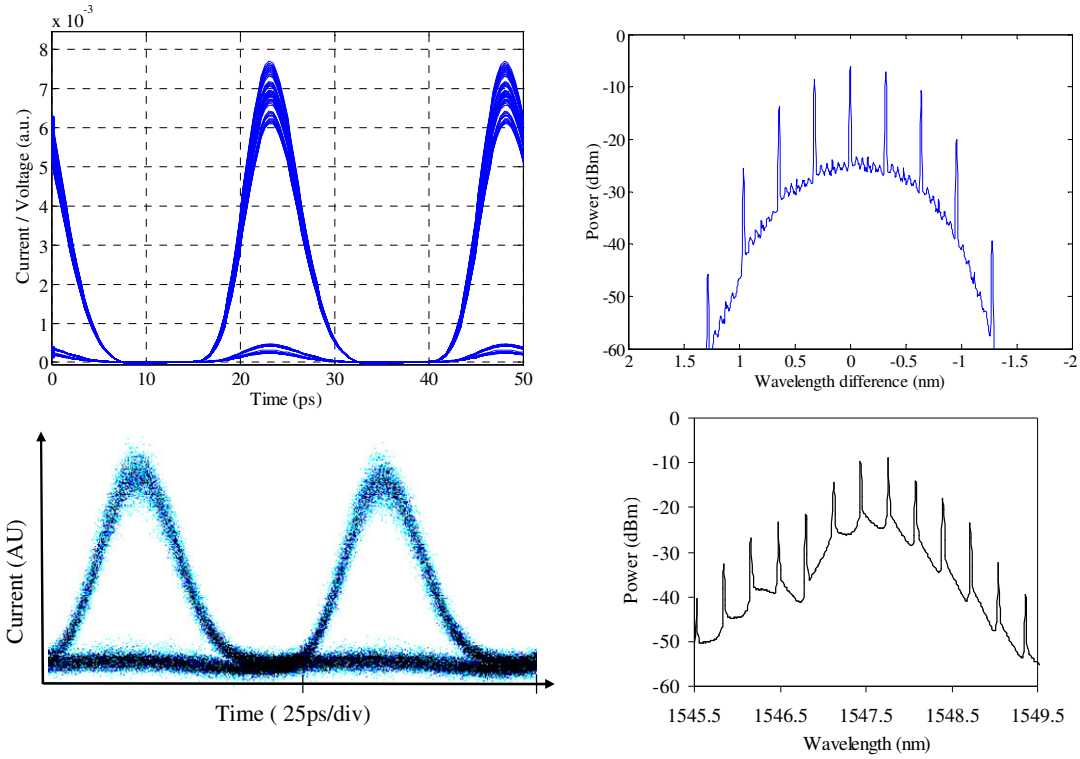

Fig. 3.34 Simulated (top) and experimental (bottom) eye diagrams (left) and optical spectra (right) of the MZI-SOA conversion output when operated with a CS-RZ control signal and pulsed probe beam. The optical spectra resolution is 0.01 nm.

As for the BER results, these are shown in Fig. 3.35, as a function of the OSNR at the receiver. The match between the experiment and simulation is quite good, with the BER agreeing within 0.5 orders of magnitude, except for the curves of the converted signal at low BER. In this region the experimental curve shows significantly worse performance. The required OSNR for a BER of 10^{-10} is 15.2 and 13.8 dB for the experiment and simulation, respectively, so there is a 1.4 dB of difference between the curves. This discrepancy is attributed to the different size of sequences used in the experiment and simulation. In the experiment, the sequence is very large and hence contains sub sequences that do not occur in the simulation, for example a long stream of '0' or '1'. These long streams, although rare, might cause severe bit patterning affecting the MZI-SOA operation and hence one occasional bit error. In the simulation, the sequence does not contain these long streams and therefore there rare events are not observed. For the back to back curve, the OSNR is 16.2 and 16.6 dB for the experiment and simulation, respectively. In this case, the difference of 0.4 dB could be explained by an extinction ratio mismatch in the experiment and simulation. The penalties due to the conversion are -1.0 and -2.8 dB for the

experiment and simulation, respectively. Since the discrepancies that have been explained before in both back to back and converted curves accumulate, the resulting difference in penalty is quite large. Still, the OSNR penalty is clearly negative, indicating an improvement in signal quality which is again related to the shorter duty cycle of the converted output signal.

Afterwards, the CS-RZ format was replaced by the NRZ format. In the experiment of the wavelength conversion using a CW beam at the interferometric port, there was an error floor and hence, for the wavelength conversion using a short pulse laser beam at the interferometric port, the extinction ratio was kept at the previous value of 15 dB.

The BER results as a function of the interferometric and control input powers of Fig. 3.36 show precisely that the BER for this format is significantly higher than that for the RZ and CS-RZ formats. Still, the linear dependence of Eq. (4.1) of the optimum control signal power on the interferometric beam power is observed. The fitting parameters (shown in Table 3-2) have changed somewhat relatively to the RZ and CS-RZ, due to the particular and significantly worse performance of the conversion of a NRZ signal.

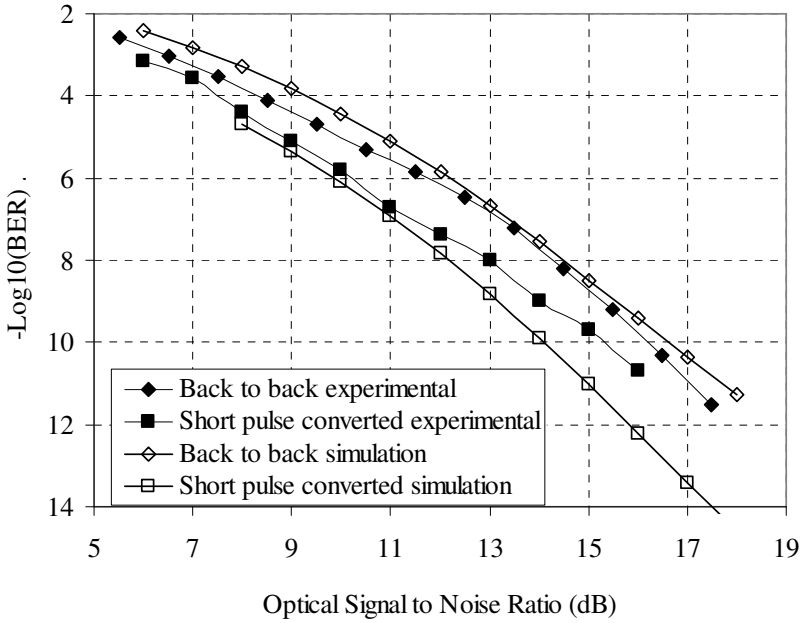

Fig. 3.35 BER experimentally measured (full symbols) and calculated by simulation (open symbols) for a CS-RZ input signal (diamonds) and the wavelength conversion output (squares) as a function of the OSNR at the receiver. The lines are guides for the eyes.

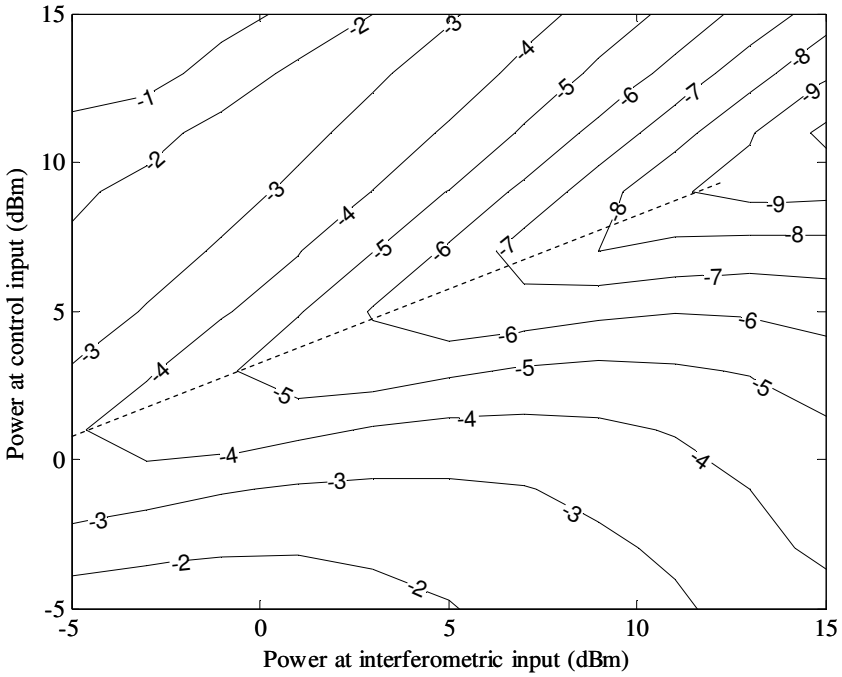

Fig. 3.36 Contour plot of $\log_{10}$(BER) of wavelength conversion of a 40 Gb/s NRZ signal in the MZI-SOA as a function of the powers at the control input and interferometric pulsed input. The dashed line is an approximation of the power at control input that minimizes the BER for a given interferometric input power.

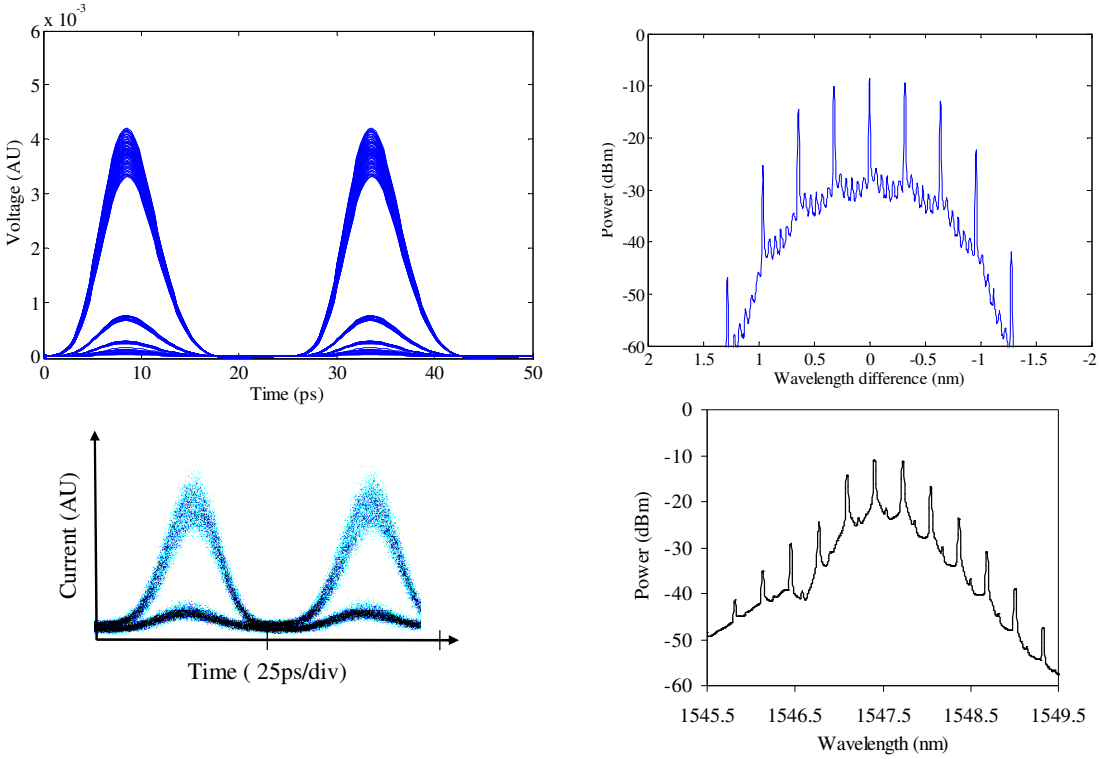

Fig. 3.37 Simulated (top) and experimental (bottom) eye diagrams (left) and optical spectra (right) of the MZI-SOA conversion output when operated with a NRZ control signal and pulsed probe beam. The optical spectra resolution is 0.01 nm.

The eye diagrams and optical spectra of the conversion output are displayed in Fig. 3.37. The bit patterning is present once more at the '1' level, and now very significantly in the simulation in the '0' level. In the experiment, the '0' level also shows some bit patterning, but more evident is the low extinction ratio, which is due to the non-idealities of the real MZI-SOA that are not modelled in the simulation, such as the polarization effects.

As for the BER measurements, they are shown in Fig. 3.38, as a function of the OSNR at the receiver, for both simulation and experiment, and for both the back to back input signal and the converted output signal. It is noteworthy that in this case of the conversion to short pulses the converted curve does not show a BER floor and a BER as low as 10^{-11} was measured. There is a good agreement on the trend of the experimental and simulation curves for the back to back signal as it had been observed for the conversion to the CW beam. At a BER of 10^{-10}, the OSNR of the back to back curves are 17.6 and 16.6 dB, while for the converted signal they are 19.9 and 16.2 dB, for the experiment and simulation, respectively. The curves for the converted signal have a poor match, with 3.7 dB of difference on the OSNR at a BER of 10^{-10}. Through simulation it is predicted that there is a slight improvement on the required OSNR when converting a NRZ signal to short pulses, while experimentally it was observed significantly worse performance. In terms of penalty, the experimental and simulated values are 2.3 and -0.4 dB. The discrepancy of these values is attributed to the over-performance predicted by the simulation. Recalling the case of conversion of the CS-RZ signal to short pulses, the very long streams of '0' and '1' caused increased experimental BER when compared to the simulation, in the low BER region. In the case of NRZ, the duty cycle is even larger that in the case of the CS-RZ and therefore the MZI-SOA copes more hardily with long streams of '1' and '0'. Moreover, the MZI-SOA will have problems even for not so long streams of '1' and '0' that are contained in the experimental sequence, but not in the simulation one. Therefore it is expectable that the experimental BER is larger than the simulated BER, even for the larger BER region.

When the conversion penalty values are compared to the NRZ conversion to a CW beam, there is still a big improvement, but when compared to the negative penalties obtained for the RZ and CS-RZ conversion to short pulses, it is again evident the unsuitableness of the MZI-SOA to convert the NRZ format at 40 Gb/s.

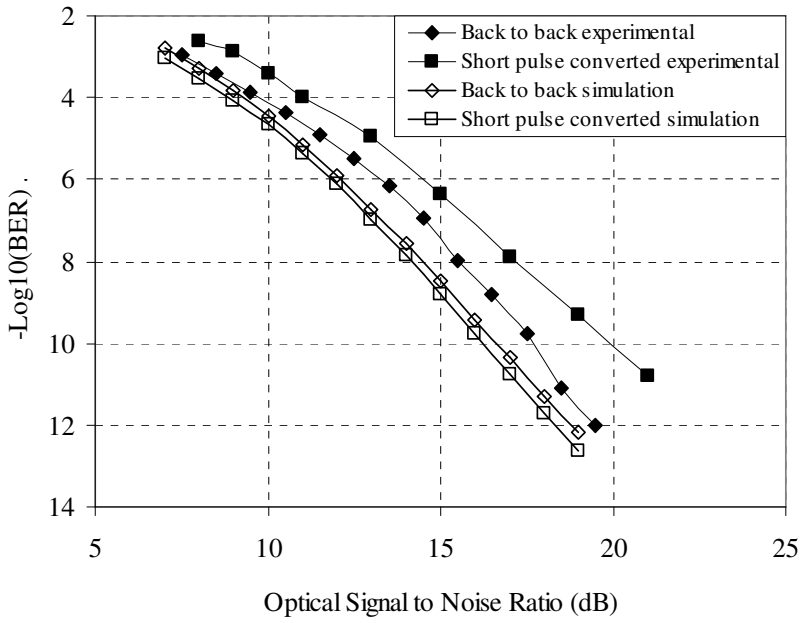

Fig. 3.38 BER experimentally measured (full symbols) and calculated by simulation (open symbols) for a NRZ input signal (diamonds) and the wavelength conversion output (squares) as a function of the OSNR at the receiver. The lines are guides for the eyes.

3.6 Performance dependence on the pulse shape

Although the simulation is not capable of providing accurate results on every condition studied, it has been capable of providing useful qualitative insight on the performance of the MZI-SOA performance as a wavelength and format converter. Therefore, in this section, the simulation will be used to investigate the effect of the pulse shape, described by the extinction ratio and the duty cycle of the input signals, on the performance of the wavelength conversion. The pulse width of the probe beam also plays a role on the conversion performance and therefore it will also be investigated in this section. The results presented in this section and in the following chapters were obtained considering a noiseless receiver, i.e. only optical noise, and not electrical noise, as opposed to the results in the two former sections.

When the extinction ratio of the incoming signal changes, the gain experienced either by the '1' and/or '0' will also change, according to the power transfer function of Fig. 3.8. More specifically, when the extinction ratio of the input signal is reduced, the powers of the '1' and '0' levels of the input signal come closer. As a result, the transmissivity for the '1' and '0' levels will also become closer and consequently, the

output extinction ratio will also diminish. As for the effect of the duty cycle, it was observed in the previous section that the larger the duty cycle, the worse is the performance. A more formal study on this matter will be pursued in this section.

The results of the impact of the extinction ratio on the quality of the output converted signal are presented in Fig. 3.39 and Fig. 3.40 for the conversion to a CW beam and to a short pulse beam, respectively.

The first remark, for both interferometric beams, is that the format with lowest required OSNR both in back to back and after wavelength conversion is the RZ format, followed by the CS-RZ and finally the NRZ. It should be kept in mind though, that the simulation overestimates the performance of the wavelength conversion of the NRZ format, as observed in the previous section.

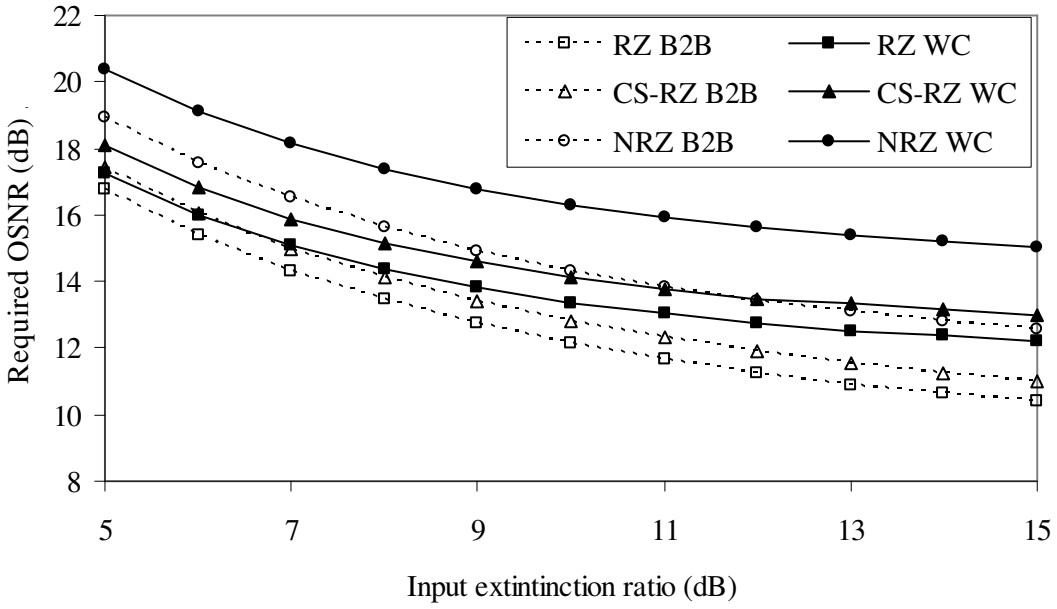

Fig. 3.39 Required OSNR for a BER of 10^{-10} as function of the extinction ratio of the signal input to the MZI-SOA for the input signal (B2B) and wavelength conversion output signal (WC) when converting to a CW beam and for the following formats at the input: RZ, CS-RZ and NRZ. The lines are guides for the eyes.

Relatively to the dependence on the extinction ratio, the required input signal OSNR (back to back) obviously increases when the extinction ratio of the input signal decreases. The results show also that the required OSNR of the wavelength converted signal (WC) also increases as the extinction ratio of the input signal decreases which means that wavelength conversion in the MZI-SOA is sensitive to the input extinction

ratio. This is a direct consequence of the fact that the power transfer curve of Fig. 3.8 is smooth and not step-like. Still, the required OSNR dependence on the input extinction ratio is stronger for the input signal than for the MZI-SOA wavelength converted output signal. The difference of the required OSNR at the extinction ratios of 10 and 15 dB will now be analysed, i.e. how much more OSNR is needed in the case of the input signal with 10 dB of extinction ratio compared to the input signal with 15 dB of extinction ratio. The difference of the OSNR is about 1.8 dB for all the back to back signals, independently of the format. However, for the wavelength converted signal, it depends on the modulation format. Considering conversion to a CW beam, the values are 1.1 dB, 1.1 dB, and 1.3 dB for RZ, CS-RZ and NRZ formats, respectively. For the conversion to a short pulse beam, the following OSNR differences were observed: 0.9 dB, 1.0 dB, and 1.3 dB for the RZ, CS-RZ and NRZ formats, respectively. The OSNR difference is always lower for the output converted signal (1.1 dB in average) comparing to the input signal (1.8 dB for all cases).

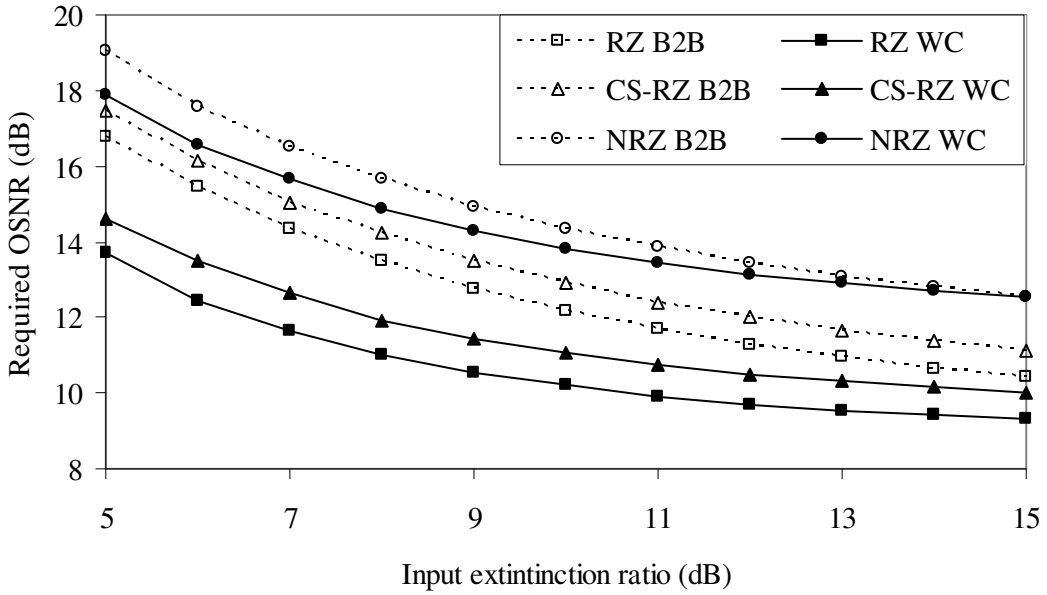

Fig. 3.40 Required OSNR to attain a BER of 10^{-10} as function of the extinction ratio of the signal input to the MZI-SOA for the input (B2B) and wavelength conversion output (WC) signals when converting to a short pulse beam and for the following formats at the input: RZ, CS-RZ and NRZ. The lines are guides for the eyes.

Consequently, furthermore to the reduced required OSNR of the wavelength converted signal relatively to the input signal in the case of the conversion to a pulsed

beam, it is beneficial to use the wavelength conversion in the MZI-SOA as a way to reduce the sensitivity to the extinction ratio.

The required OSNR values for the analysed modulation formats were sorted by the duty cycle and plotted in Fig. 3.41. It is well known that the smaller the duty cycle of a given pulse, the lower OSNR is required for a given BER. Fig. 3.41 shows precisely this behaviour for the back to back signal, but also for the converted signal. It should be remarked that these results were obtained using a short pulse beam at the interferometric input. Thus, the output pulse width is fairly constant independently of the pulse format at the control input, since the output pulse width is mainly defined by the width of the probe pulses at the interferometric input port. Hence, the required OSNR of the converted signal plotted in Fig. 3.41 isolates the effect of the duty cycle of the input signal on the conversion performance. Consequently, the observed increase of the required OSNR for the converted signal for increasing duty cycles is due to the growing bit patterning arising from the SOA slow gain recovery that has been already discussed when analysing the conversion of the CS-RZ and NRZ formats.

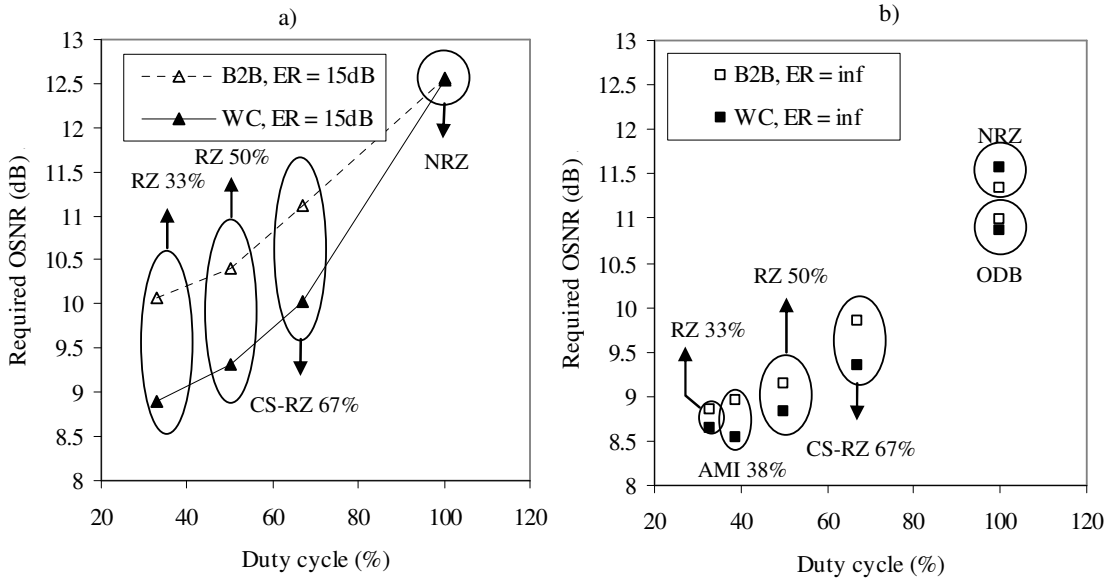

Fig. 3.41 Required OSNR for the input signals (B2B) and MZI-SOA conversion output signals (WC) as a function of the duty cycle of the input signals for a) 15 dB of extinction ratio and b) ideal (infinite) extinction ratio. The lines are guides for the eyes.

Besides the already studied formats NRZ, RZ, and CS-RZ with duty cycles of 100%, 50%, and 67%, respectively, Fig. 3.41 also presents the RZ, the alternate mark inversion with RZ pulse format (AMI-RZ) and the optical duobinary (ODB) with duty

cycles of 33%, 38% and 100%, respectively. The details of the transmitters of the AMI-RZ, ODB and RZ with 33% duty cycle are presented in Appendix C. The duty cycle values here presented are the full width at half maximum expressed as a percentage of the bit period, and were measured in the eye diagram. The eye diagrams of the input signals are shown in Fig. 3.42 for reference and comparison. It can be seen that there is a definite and clear trend of the required OSNR as a function of the signal duty cycle. In fact, the dependence of the converted signal on the duty cycle shows a very similar trend as for the input signal. The slight deviations of the main trend of the AMI-RZ and ODB formats is due to the slight skew of the AMI-RZ pulses and low crossing point of the ODB pulses. At this point, it should, however, be recalled that the simulation predicts better performance of the large duty cycle signals (NRZ) than the experimentally observed performance and this might apply also to other large duty cycle pulse formats.

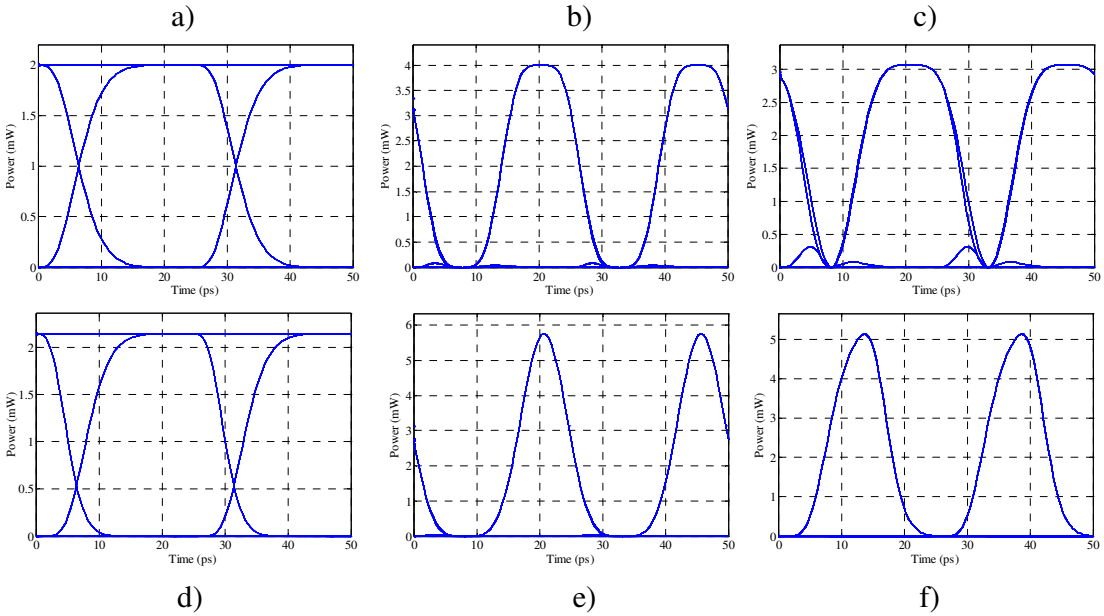

Fig. 3.42 Simulated eye diagrams of a) NRZ, b) RZ with 50% duty cycle, c) CS-RZ, d) duobinary, e) RZ with 33% duty cycle, and f) AMI-RZ formatted signals, with infinite extinction ratios.

The duty cycle and extinction ratio of the control signal have been varied with the purpose of investigating the impact of the control signal shape on the performance of the conversion. However, the shape of the light pulses fed to the interferometric input of the MZI-SOA also plays an important role on the conversion performance. The enormous difference of performance when using the CW or the pulsed beam is an extreme example.

Therefore, the width of the pulse fed to the interferometric input has been varied and the required OSNR of the converted signal has been calculated by simulation and plotted in Fig. 3.43. The required OSNR for the input signal is also shown for comparison, but, evidently, it does not depend on the pulse width of the short pulse beam.

Contrasting with the dependence of the performance on the duty cycle of the input signal, the required OSNR does not always increase for increasing pulse widths. Indeed, for very low pulse widths, the required OSNR also increases. The increase of required OSNR for larger pulse widths is easy to explain by the larger duty cycle of the converted signal, which, at the receiver, will need more power to attain the same peak power as the signals with narrower pulses. However, for very small pulse widths, this effect has smaller impact than the increasing bit patterning effects observed in the eye diagram. In fact, the operating conditions of the MZI-SOA were optimised for a pulse width of 4 ps, and when the pulse width becomes significantly smaller, carrier heating and spectral hole burning start to have a larger effect on the signal rather than the carrier depletion alone. Therefore, the optimum operating conditions change for very short pulse widths. Hence, to take best profit of very short pulse widths, input signal powers should be optimised on purpose.

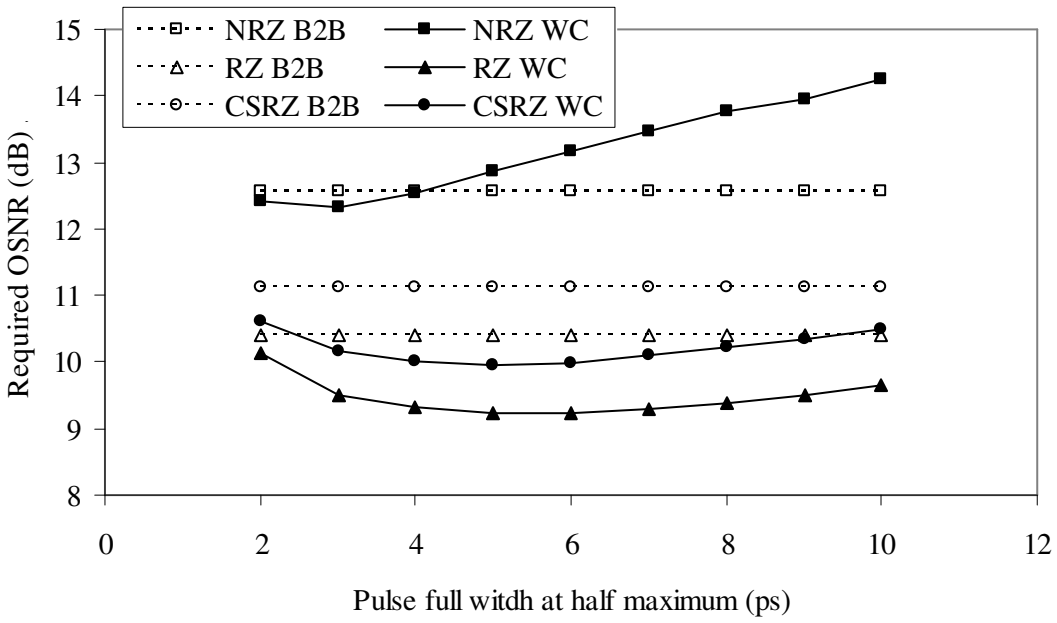

Fig. 3.43 Required OSNR for the input signals (B2B) and MZI-SOA conversion output signals (WC) as a function of the full width at half maximum of the short pulse fed to the interferometric input of the MZI-SOA. The lines are guides for the eyes.

3.7 Conclusions

The results presented in this chapter focus on the performance of the wavelength and format conversion in the MZI-SOA. Taking as a base of study the CIP MZI-SOA experimented in this work, a characterization of the SOA was done, and parameters for the simulation model were extracted.

Using the simulation model and experimental observations, the maximum wavelength conversion bit rate using the push-pull configuration at a reasonable penalty is 40 Gb/s. Without push-pull operation, the conversion performance is significantly worse, achieving a mere maximum bit rate of less than 20 Gb/s.

Comparing the conversion using a CW or a pulsed probe, the latter shows much better performance, regardless of the modulation formats (RZ, CS-RZ, and RZ) employed in the control signal. Moreover, the pulsed beam operation enabled negative penalty conversions due to the short duty cycle of the output signal. The optimum powers for wavelength conversion were investigated and an approximate rule of the optimum signal power as a function of the interferometric power was derived.

The duty cycle of the control signal has a major influence on the conversion performance, with larger duty cycles showing a worse performance. In fact, it has been observed that the duty cycle of the control signal determines, to the highest degree, the optimum conversion performance, regardless of existing phase management of the modulation format. The extinction ratio of the input signal also influences the performance of the wavelength conversion, but it was shown that the MZI-SOA converted signal reduces the performance dependence of the input signal on the extinction ratio due to the MZI-SOA reshaping capabilities. Finally, the pulse width of the probe beam also impacts the performance of the conversion. For large enough pulse widths, the performance is better for narrower pulses. However, for very narrow pulses, the balance between the phenomena contributing to the SOA saturation changes and re-optimisation of the operating powers is required.

Summarizing, having in mind next generation optical networks, which are meant to be as flexible and transparent as possible, this chapter has characterized the operating conditions of the MZI-SOA working as a wavelength and format converter with different modulation formats, which results will be useful for the next chapter.

3.8 References

[1] "Preliminary datasheet, 40G-2R-ORP, rev H," *CIP Technologies, retrieved online in 2009/05/21 from http://ciphotonics.com/PDFs_March09/40G_2R_ORP_H.pdf.*

[2] D. Cassioli, S. Scotti, and A. Mecozzi, "A time-domain computer simulator of the nonlinear response of semiconductor optical amplifiers," *IEEE Journal of Quantum Electronics*, vol. 36, no. 9, pp. 1072–1080, 2000.

[3] G. Maxwell, A. Poustie, C. Ford, M. Harlow, P. Townley, M. Nield, T. Lealman, S. Oliver, L. Rivers, and R. Waller, "Hybrid integration of monolithic semiconductor optical amplifier arrays using passive assembly," *in Proc. Electronic Components and Technology Conference*, pp. 1349–1352, 2005.

[4] G. Maxwell, B. Manning, M. Nield, M. Hadow, C. Ford, M. Clements, S. Lucas, P. Townley, R. McDougall, S. Oliver, *et al.*, "Very low coupling loss, hybrid-integrated all-optical regenerator with passive assembly," *in Proc. European Conference on Optical Communication (ECOC)*, p. PD3.5, Sept. 2002.

[5] J. Leuthold, J. Eckner, C. Holtmann, R. Hess, and H. Melchior, "All-optical 2× 2 switches with 20 dB extinction ratios," *IEE Electronics Letters*, vol. 32, no. 24, pp. 2235–2236, 1996.

[6] J. Castro, R.Meleiro, J. Pina, and P. Monteiro, "Deliverable D7.3 Network performance," *MUFINS European Union Framework Programme 6 project report*, 2006.

[7] R. Manning, D. Davies, and J. Lucek, "Recovery rates in semiconductor laser amplifiers: optical and electrical bias dependencies," *IEE Electronics Letters*, vol. 30, no. 15, pp. 1233–1235, 1994.

[8] L. Occhi, *Semiconductor Optical Amplifiers made of Ridge Waveguide Bulk InGaAsP/InP: Experimental Characterization and Numerical Modelling of Gain, Phase, and Noise*. PhD thesis, Eidgenössische Technische Hochschule Zürich, 2002.

[9] R. Manning, A. Kelly, A. Poustie, and K. Blow, "Wavelength dependence of switching contrast ratio of semiconductor optical amplifier-based nonlinear loop mirror," *IEE Electronics Letters*, vol. 34, no. 9, pp. 916–918, 1998.

[10] G. Agrawal, "Intensity dependence of the linewidth enhancement factor and its implications for semiconductor lasers," *IEEE Photonics Technology Letters*, vol. 1, no. 8, pp. 212–214, 1989.

[11] M. Hill, E. Tangdiongga, H. de Waardt, G. Khoe, and H. Dorren, "Carrier recovery time in semiconductor optical amplifiers that employ holding beams," *OSA Optics Letters*, vol. 27, no. 18, pp. 1625–1627, 2002.

[12] P. Winzer and R. Essiambre, "Advanced optical modulation formats," *Proceedings of the IEEE*, vol. 94, no. 5, pp. 952–985, 2006.

Chapter 4 Optical processing in the time and the wavelength domains

Wavelength division multiplexing (WDM) technology is key in current optical transmission systems, enabling a large number of wavelength channels to be transmitted in the same optical fibre. However, due to the large increase in data traffic demand, more transmission capacity is required. Commercial systems are now employing 40 Gb/s per channel, and a strong demand for 100 Gb/s per channel is underway [1].

In the 100 Gb/s range, the electronic bandwidth bottleneck effect becomes significant and therefore electrical time domain multiplexing becomes impractical and other forms of multiplexing must be found. A possible solution is optical time division multiplexing (OTDM) that can provide grooming of lower bit rate signals to higher bit rate signals, circumventing the electrical bandwidth problem.

OTDM can be particularly useful in the interface of different network hierarchies. While the network core operates at very high bit rates per wavelength channel, inferior network hierarchies are low bit rate. Hence, WDM to OTDM conversion might be helpful in the nodes that interface network hierarchies with different line bit rates. An example is shown in Fig. 4.1, where a core network with 120 Gb/s per channel is served by a 40 Gb/s per channel lower hierarchy network. In the edge nodes, which interface both network hierarchies, three WDM channels are aggregated to a single OTDM 120 Gb/s channel, while the reverse operation is performed in the opposite direction.

Contrasting with optical circuit switching (OCS), optical packet switching (OPS) has been proposed to increase the efficiency of the network by reducing the switching granularity. The change from OCS to OPS presents a number of technological challenges, but also the great advantage of switching on a packet granularity. In the case of OPS, the concept of OTDM can be further extended and enhanced to packet compression. Whereas in OTDM several tributaries are time interleaved on a bit-by-bit basis, in packet compression the bit and packet durations are shortened and packets are multiplexed on a packet-by-packet basis. Hence, the fundamental switching unit of the network remains

unchanged, while the bit rate is effectively increased. An example of this architecture is shown in Fig. 4.2.

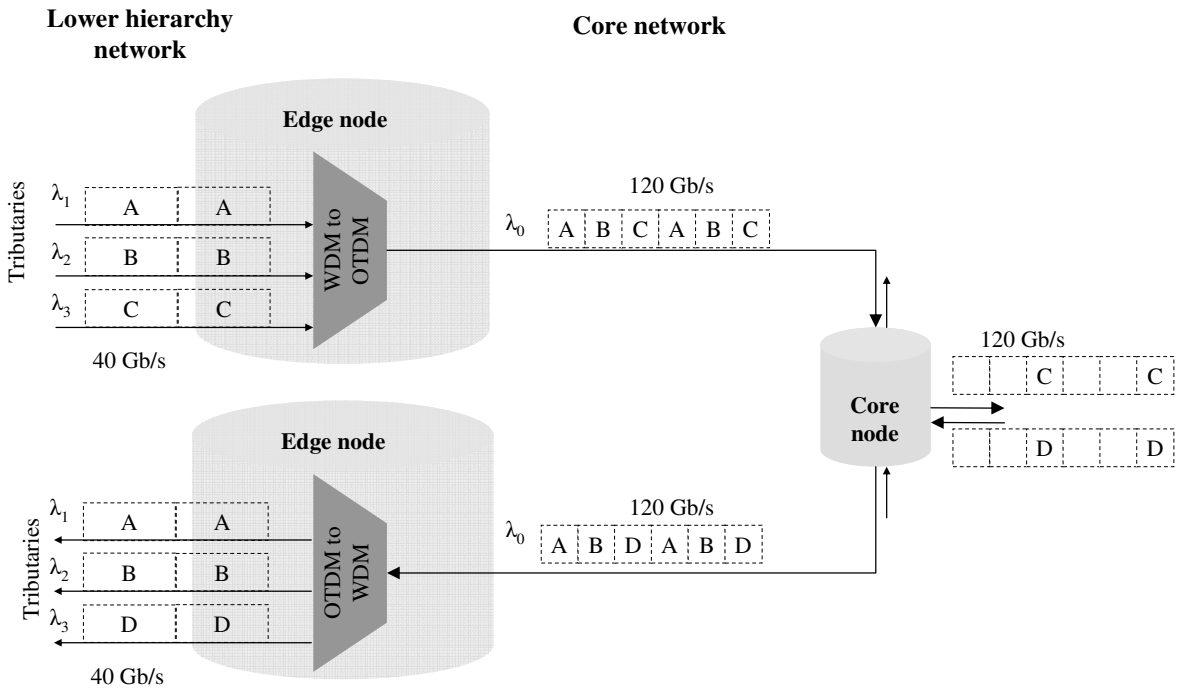

Fig. 4.1 Example of edge nodes of an optical network interfacing an OTDM core network and a lower hierarchy network using WDM. A, B, C, and D denote bits from different origins.

In order to take full advantage of the packet switching paradigm, some OPS network architectures require packet schedulers to ensure low or no packet loss [2]. This is the case of the example of Fig. 4.2. A fundamental unit of the packet scheduler is the time slot interchanger (TSI), which function is to delay a packet by a selectable amount of time. The TSI allocates a given packet to the proper time slot before being multiplexed with other packets.

The work disclosed in this chapter relates precisely to techniques that perform the functionalities just enounced. The capability of the MZI-SOA to operate as a basic block of larger circuits performing time domain processing will be assessed through experiments and simulation, making use of the investigations of the previous chapter. In particular, section 4.2 deals with the conversion of a wavelength multiplexed signals to time domain multiplexing. Next, packet compression and decompression are investigated in section 4.3. Then, in the following section, a TSI architecture is presented and its performance is

studied experimentally and by simulation. At the end, general conclusions are drawn on the presented optical circuits.

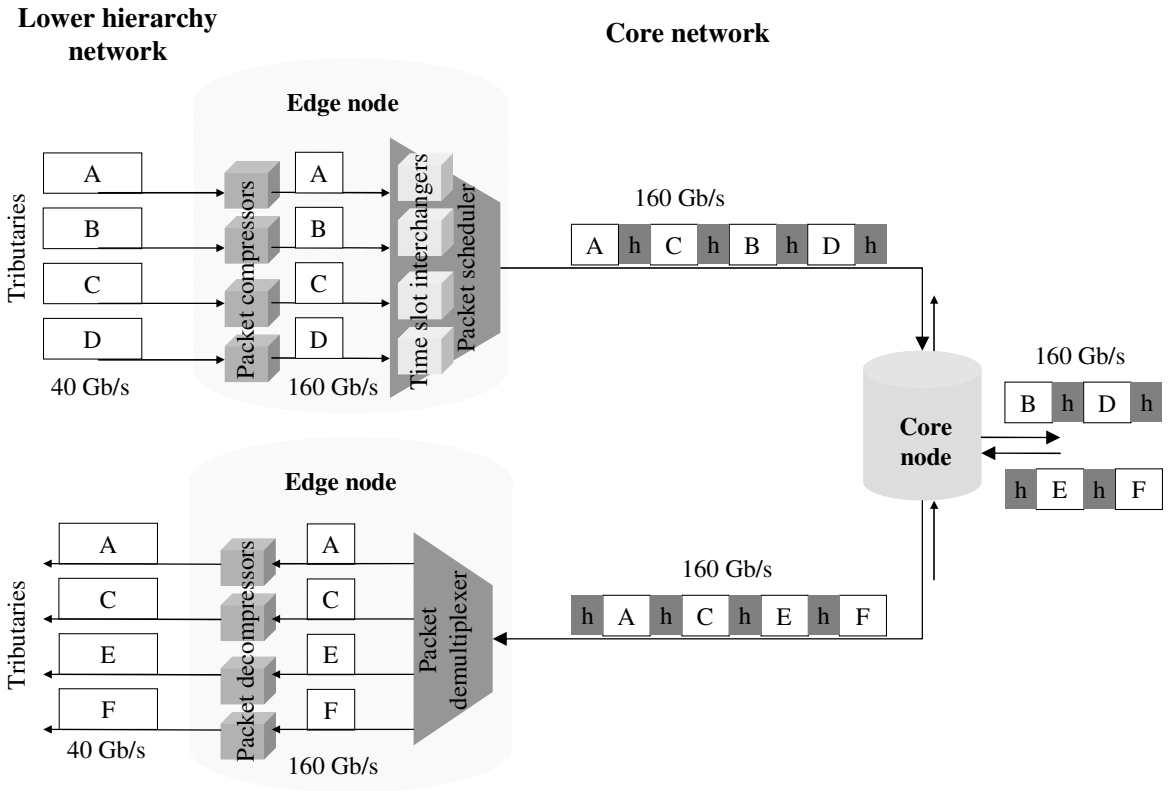

Fig. 4.2 Example of packet compression and decompression in edge nodes connecting a core network and a lower hierarchy network. A, B, C, D, E, F denote packets' payloads from different origins, whereas h is the header for each payload.

4.1 WDM to OTDM conversion

OTDM to WDM systems have been proposed at the 100 Gb/s range, mainly using non-linear fibres [3, 4]. WDM to OTDM conversion has been performed in a fibre based nonlinear optical loop mirror (NOLM) from 4×10Gb/s channels to 40 Gb/s [5] and in an electro-absorption modulator (EAM) based wavelength converter by converting 3×20Gb/s channels to 60 Gb/s [6]. At higher rates, 4×40 Gb/s to 160 Gb/s conversion has been proposed using hybrid integrated periodically poled Lithium Niobate (PPLN) [7]. When compared with the fibre based and PPLN based processing devices, the MZI-SOA has the advantage of being an integrated device which is polarization independent and with a good

output power of the OTDM signal, while not requiring very high input powers, as overviewed in chapter 2.

In this section, an all-optical scheme based on the MZI-SOA is proposed to convert three WDM channels at 40 Gb/s to an OTDM channel at 120 Gb/s. The three incoming WDM channels are wavelength converted to a local short pulse laser in three MZI-SOA gates. Each of the MZI-SOA gates is performing similarly to the work carried out in section 3.5. The MZI-SOA gates' output is then passively multiplexed to 120 Gb/s.

4.1.1 Operating principle

The operating principle is as follows and is depicted in Fig. 4.3. Each of the three incoming 40 Gb/s WDM signals is fed to the control input of one MZI-SOA. The output of the laser that produces the short pulse beam is split in three parts and fed to the interferometric inputs of the three MZI-SOAs. Hence, the incoming signals are converted to short pulses, all at the same wavelength. The delays between the outputs of the three MZI-SOAs are then adjusted so that, when they are passively combined together in an optical combiner, each signal occupies the right 120 Gb/s signal time slot.

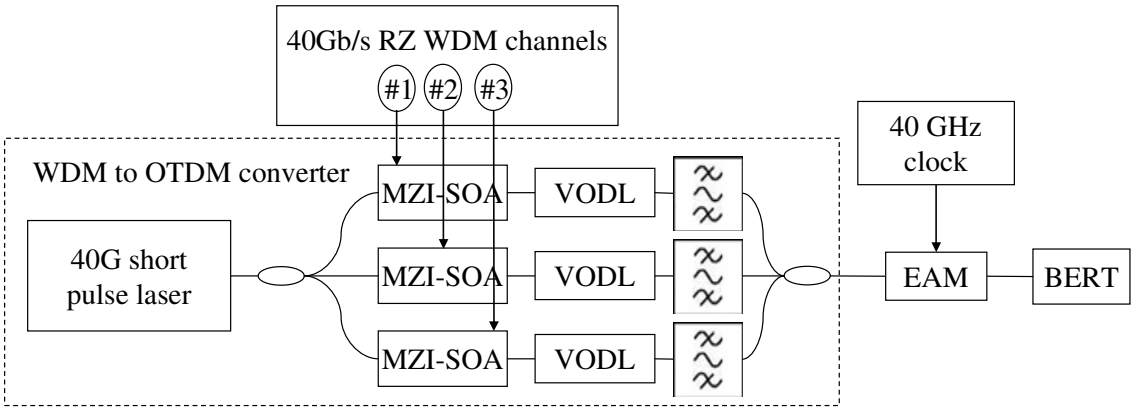

Fig. 4.3 Schematic of the MZI-SOA based WDM to OTDM converter.

The described operating principle was implemented experimentally. The input signals to the MZI-SOA were 2^{31}-1 PRBS 40 Gb/s RZ signals, with 50% duty cycle. In the outputs of the MZI-SOAs optical band-pass filters are used to transmit only the locally generated wavelength and eliminate the incoming WDM signals. The 120 Gb/s signal is demultiplexed to 40 Gb/s by an electro-absorption modulator (EAM) driven by an electrical clock signal at 40 GHz so that BER measurements could be made at 40 Gb/s.

The EAM switching window is modelled as having Gaussian shape and full width at half maximum of 6 ps.

4.1.2 Results

Both eye diagrams and optical spectra taken throughout the experiment are shown in Fig. 4.4. It can be seen that the incoming 50% duty cycle RZ WDM signal (Fig. 4.4 a)) is successfully wavelength converted to pulses with shorter duty cycle (Fig. 4.4 c)), due to the smaller duty cycle of the short pulse probe (Fig. 4.4 b)), as already described in the preceding chapter. As before, the converted signal shows some patterning effects in the "ones" level, due to the slow recovery time of the SOAs and the large duty cycle (50%) of the incoming RZ signal. The 120 Gb/s combined output of the three MZI-SOAs is shown in Fig. 4.4 d). The signals in Fig. 4.4 b), c) and d) have a bandwidth larger than the oscilloscope electrical bandwidth and therefore the eye diagrams are bandwidth limited by the oscilloscope. Recalling the results from section 3.5, the conversion OSNR penalty in this situation is -1 and -1.6 dB for the experiment and simulation, respectively. However, after combining the three outputs of MZI-SOAs, experimental BER measurements show a severe error floor at 10^{-5}.

The typical source of large BER penalties in OTDM signals is crosstalk between pulses [4], so the output signals of the MZI-SOAs were investigated by simulation. Gaussian shaped pulses with 4 ps of full width at half maximum were considered for the short pulse clock signal. In order to calculate an OSNR penalty, the simulation of interleaving the MZI-SOAs ouputs was repeated 1000 times with different phases between MZI-SOAs outputs to recreate the phase drifting observed in the experiment. It was verified that this number of simulation runs was enough to guarantee stable results, at moderate computation times. The simulated eye diagrams of the short pulse clock, the MZI-SOA wavelength converted signal and the 120 Gb/s multiplexed signal are shown in Fig. 4.5. The eye diagrams were taken without applying any electrical filtering. It is visible that the pulses of the wavelength converted output signal are broadened relatively to the short pulse probe signal fed to the MZI-SOA. This agrees with the observation that the optical spectra of the MZI-SOA output signal and 120 Gb/s multiplexed signal are narrower than the short pulse clock signal spectrum. The explanation behind this effect is

that the short pulse clock signal experiences less gain in the peaks and more gain in the tails due to self gain modulation in the SOAs. Hence, the tails are amplified relatively to the pulse peak and the pulse becomes broader. The widths of the wavelength converted optical pulses at 50% and 10% of the pulse maximum power were 5.2 and 9.4 ps, respectively, while the same widths of the input pulses were 4 and 7.4 ps, respectively. For comparison, the bit slot at 120 Gb/s spans 8.3 ps. Therefore the output signal pulse tails considerably overlap the neighbouring bit slots causing severe crosstalk and eventually the BER floor. Additionally, temporal, phase and polarization drifts between the three 40 Gb/s tributaries also contribute to an increased BER.

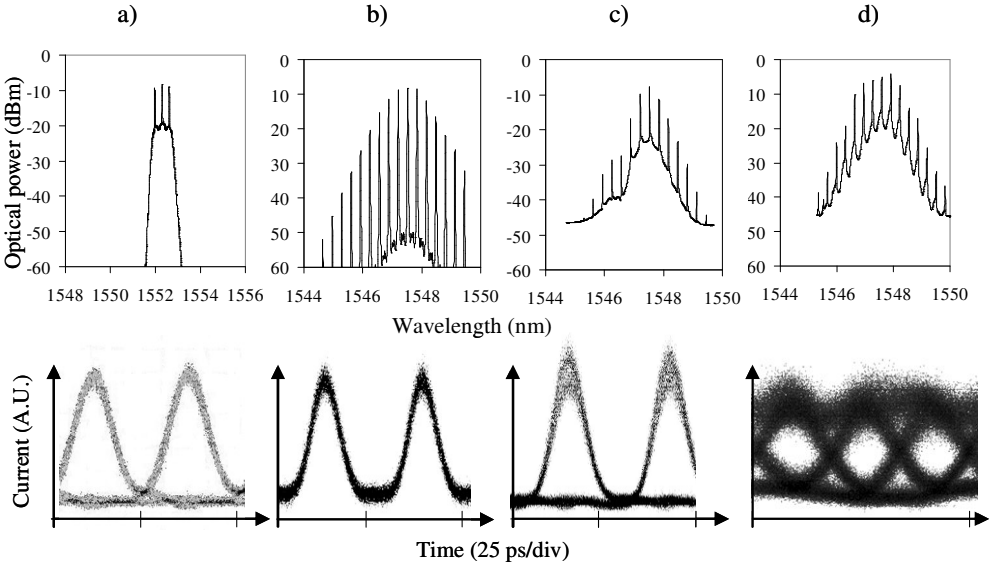

Fig. 4.4 Optical spectra (top) and eye diagrams (bottom) of a) incoming 50% RZ WDM signal, b) 40 GHz clock signal, c) RZ to short pulse wavelength converted signal and, d) 120 Gb/s OTDM multiplexed signal. The eye diagrams were obtained with a 65 GHz electrical bandwidth oscilloscope. The spectra resolution is 0.01 nm.

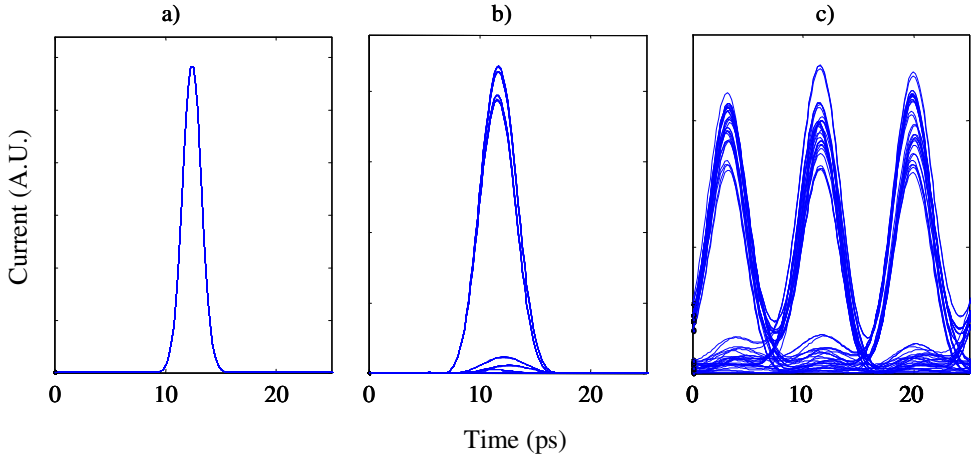

Fig. 4.5 Simulated eye-diagrams of a) short pulse optical clock, b) MZI-SOA wavelength converted output and c) 120Gb/s OTDM multiplexed output signal.

Reducing the MZI-SOA input powers, and thus the self gain modulation, does reduce the pulse broadening, but at the expense of non-optimum operation and a lower output OSNR due to the amplified spontaneous emission (ASE) noise introduced by the SOAs. This trade-off has prevented error free operation of the WDM to OTDM converter.

Clearly, the 4 ps pulses are too wide to be used in the WDM to OTDM converter, since the MZI-SOA broadens them. Fig. 4.6 shows the pulse width of the input and MZI-SOA output converted signal, measured at 10% and 50% of the maximum pulse amplitude. The input signal has a width of about 1.9 times more at 10% than at 50% of the maximum, whereas for the output signal, this value is closer to 1.75. It is readily concluded that the MZI-SOA affects the pulse shape, in addition to the pulse width. Another conclusion is that the MZI-SOA broadens the shorter pulse widths more than the larger pulses, since the slope of the output curves is smaller than that of the input curves. This is because since the average input power of the pulses was kept constant, the shorter pulses have higher peak power and hence cause more self gain modulation in the SOAs. Therefore, shorter duty cycle pulses have their peak less amplified relatively to the tails and more broadening occurs than in the case of a broader pulse. Considering the limit of the bit slot at 120 Gb/s of 8.3 ps, it can be observed that pulses broader than 3.5 ps have their output pulse width at 10% of the pulse maximum larger than 8.3 ps. This might indicate that at the eye centre, there is still significant crosstalk and, consequently, shorter pulses should be used. An OSNR study will be done later on to better assess the requirements on the pulse width.

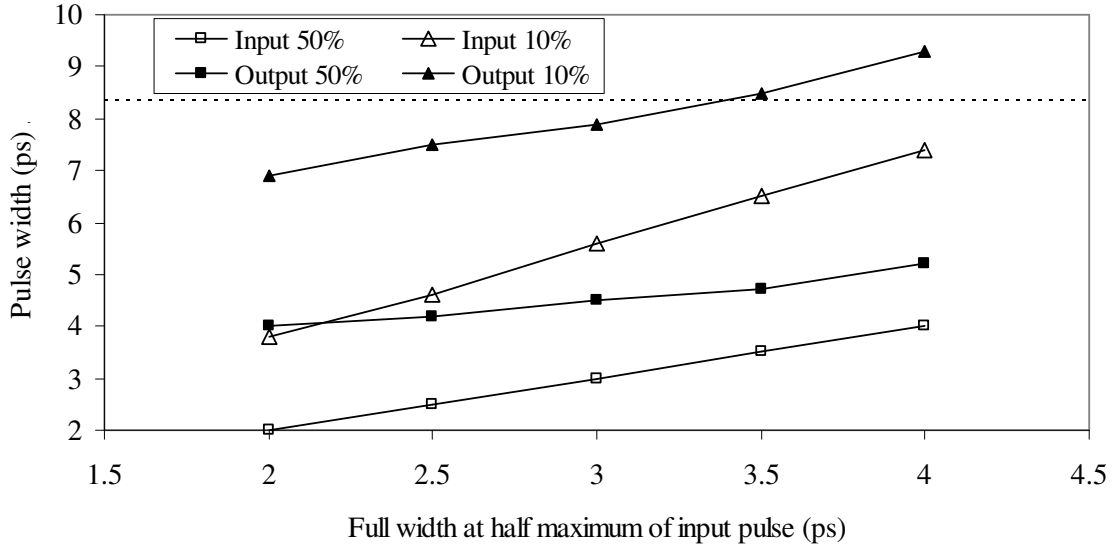

Fig. 4.6 Pulse width of the input and output converted signal, measured at 10% and 50% of the pulse maximum, as a function of the full width at half maximum of the input signal. The dashed line at 8.3 ps represents the bit period at 120 Gb/s. The lines are guides for the eyes.

The incoming data signal was modulated with other modulation formats, but the former pulse broadening conclusions still hold. The results are presented in Fig. 4.7 for the additional NRZ and CS-RZ formats. The output pulse widths for these formats agree to a maximum deviation of 0.2 ps to the RZ format. This is an indication that the phenomenon governing the pulse broadening inside the MZI-SOA is the self gain modulation of the pulsed beam and not cross gain or phase modulation from the data signal. Although the output pulse width is rather similar for the different formats, the performance is quite different depending on the control signal format due to the patterning effects, as observed in section 3.5. Fig. 4.8 presents the required OSNR at the output of the MZI-SOA and after demultiplexing to 40 Gb/s the 120 Gb/s multiplexed signal. The results for the MZI-SOA converted output were already discussed in section 3.5, where the increase of required OSNR for narrower pulses was attributed to non-optimum powers due to the fast gain compression effects. For the 120 to 40 Gb/s demultiplexed signal, the required OSNR steeply increases for pulse widths larger than 3 ps, corroborating the previous conclusions that for broad pulses, there is significant crosstalk between adjacent pulses. Whereas for an input pulse width of 2 ps the penalty from multiplexing to 120 Gb/s is 1.1 dB for the NRZ format and 1.0 dB for the RZ and CS-RZ formats, for an input pulse width of 4 ps, the penalty is 3.6, 3.0 and 2.7 dB for the NRZ, RZ and CS-RZ formats, respectively. These penalty values are already too high for any practical application, and therefore the input pulse width should be limited to a maximum value of 3 ps, or 36% of the OTDM bit period.

Since the WDM to OTDM conversion of three 40 Gb/s channels to one OTDM channel at 120 Gb/s requires very stringent pulse widths, it was attempted to multiplex two 40 Gb/s channels to 80 Gb/s OTDM channel. The simulation setup was obtained from the one depicted in Fig. 4.3 by disconnecting one of the MZI-SOA branch and adjusting the delay of the remaining MZI-SOA, so that the two tributaries occupy the proper bit slot at 80 Gb/s. All other parameters were kept fixed. The results are presented in Fig. 4.9. For short pulse widths, below 6 ps, or 46% of the bit period, the required OSNR of the demultiplexed signals is the same as of the MZI-SOA output signal, i.e. there is no penalty associated to the OTDM process. However, for pulse widths larger than 6 ps, the penalty starts to increase and for 7 ps of width, there is already a penalty of 1.4, 0.8, and 0.7 dB for the NRZ, RZ and CS-RZ formats, respectively. Again, this is due to the crosstalk between

neighbouring pulses of the OTDM signal. However, in the 80 Gb/s OTDM signal, the accepted pulse width is much larger than in the case of 120 Gb/s since the bit slot is now 12.5 ps.

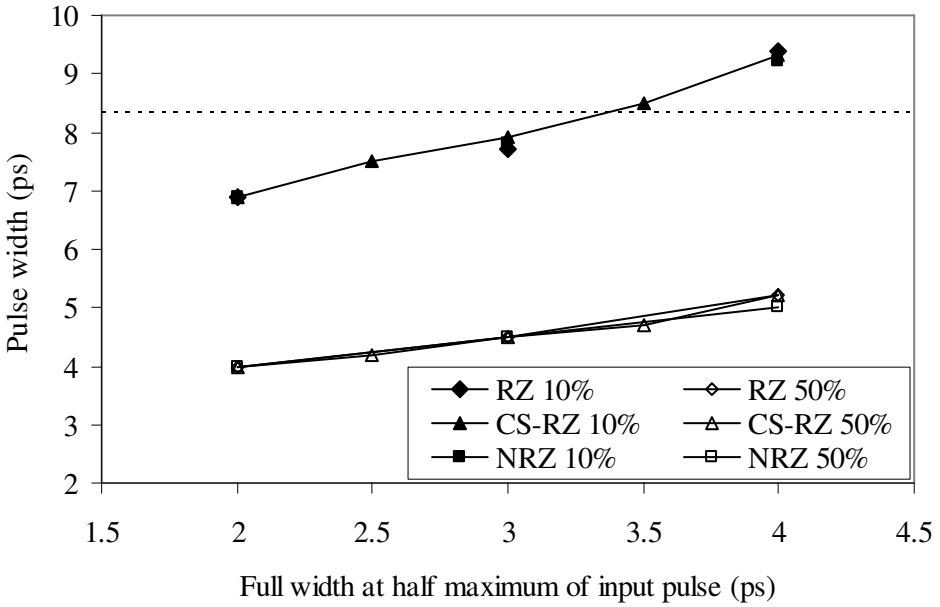

Fig. 4.7 Pulse width of the MZI-SOA output, measured at 10% and 50% of the pulse maximum, for NRZ, RZ and CS-RZ control signal formats, as a function of the probe pulse width. The dashed line at 8.3 ps represents the bit period at 120 Gb/s. The full lines are guides for the eyes.

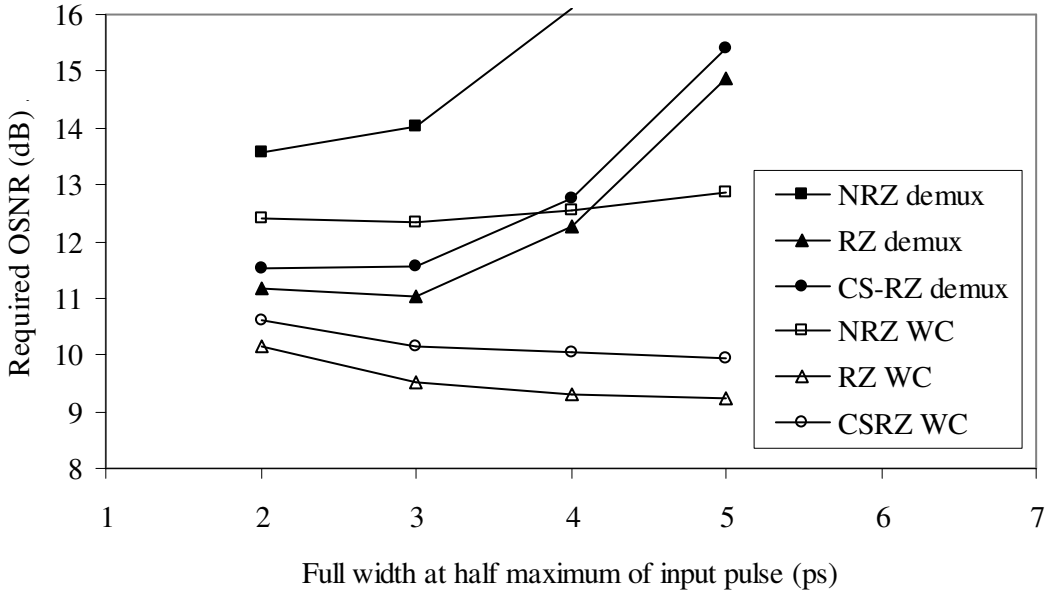

Fig. 4.8 Required OSNR for the MZI-SOA converted output (WC) and for the 120 to 40 Gb/s demultiplexed signal (demux), as a function of the probe pulse width, for the NRZ, RZ and CS-RZ formats. The lines are guides for the eyes.

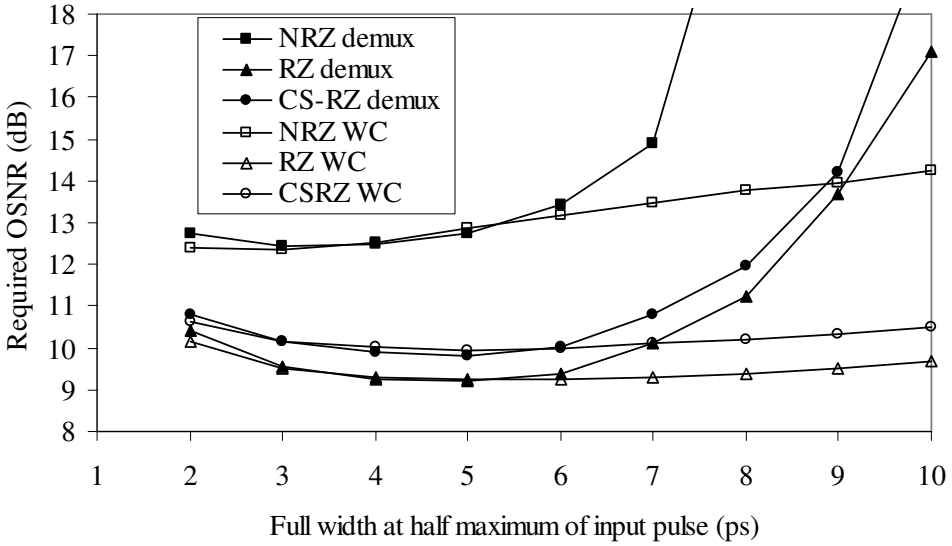

Fig. 4.9 Required OSNR for the MZI-SOA converted output (WC) and for the 80 to 40 Gb/s demultiplexed signal (demux), as a function of the probe pulse width, for the NRZ, RZ and CS-RZ formats. The lines are guides for the eyes.

4.2 Packet compression and decompression

The previous section dealt with OTDM to achieve higher bit rates in OCS networks. The present section presents a technique to achieve higher bit rate transmission in OPS networks. In OPS networks, the bit rate of each packet must be increased and therefore OTDM cannot be applied in a straightforward manner as in OCS. The optical scheme that increases the bit rate of optical packets is known as optical packet compressor, because it effectively compresses (reduces) the time duration of the packet. The optical packet decompressor performs the reverse operation.

Optical packet compression and decompression schemes have been proposed, but usually incorporate electrically driven components such as electro-optic switches and modulators [8]. Therefore, these schemes are limited by the bandwidth of the electrical components and require electrical clock recovery. Other all-optical methods have used fibre based time-to-wavelength conversion [9], or the terahertz optical add-drop (TOAD) [10], but are bulky and require high optical powers. Therefore, an architecture of packet compression and decompression based on the MZI-SOA would bring the already mentioned benefits to these circuits.

It has been observed that existing methods that use optical delay line (ODL) structures to interleave packet replicas have significant drawbacks. In a previous solution, the output of the compressor is separated in time and therefore is not a unique compressed packet [10]. In another solution, the maximum packet size in bits is 2^M, where M is the number of ODL stages in the ODL structure [8]. For a 1024 bits packet, 10 ODL stages would be necessary, which might not be feasible or practical. The ODL structure proposed here eases this problem by relating the number of ODLs to the bit rate compression ratio.

Additionally, extant packet compressor and decompressor schemes have focused on intensity modulated formats, but, in this work, PSK formats will be used, since high bit rate optical networks are likely to adopt these formats. PSK formats allied to differential detection provide an enhanced optical signal to noise ratio, when compared with the intensity modulated (IM) formats, as well as more robustness against transmission impairments [11].

In this section, novel all-optical packet compressor and decompressor schemes based on MZI-SOAs are proposed, and their functionality is demonstrated by simulation. The packet compressor and decompressor operation is shown for a base baud rate of 10 Gbaud/s and compressed baud rates of 20 and 40 Gbaud/s with quantum well SOA, and for a base baud rate of 40 Gbaud/s and a compressed baud rate of 160 Gbaud/s with quantum dot SOAs (QD-SOAs). Henceforth, MZI-SOA will denote an MZI structure with quantum well SOAs in its arms, whereas MZI-QDSOA will denote the same structure, but with QD-SOAs instead of quantum well SOAs. One advantage of the proposed schemes is transparency to the phase encoded information, which will be demonstrated by using packets modulated with BPSK and QPSK formats. The impact on the performance of the compressor and decompressor pair of the packet size and pulse width will be addressed. Additionally, the cascadability of such devices is investigated and finally fabrication tolerances of delay and phase mismatch are assessed.

4.2.1 Concept and architecture

The conceptual operation of the packet compressor will now be explained. As multi bit per symbol formats will be used, the concept of bit rate compression should be replaced by baud rate compression. An example of the packet compressor architecture, for a four

fold baud rate increase, is shown in Fig. 4.10. The main idea is to interleave packet replicas to increase the baud rate. It is assumed that the incoming packets already have a reduced baud rate in order to prevent crosstalk between interleaved replicas. However, interleaving packet replicas produces repeated symbols that must be discarded properly. This packet compressor provides a single compressed packet at the output, improving on a drawback of a previous solution [10]. The packet compressor uses an ODL structure to passively increase the baud rate B by a factor of N ($N = 4$ in Fig. 4.10). The number of ODLs in the ODL structure is M=N. ODL k ($k = 0,$ 1, 2, …, $N - 1$) introduces a delay of $k(T_p/N + T_s/N)$, where T_p and $T_s = 1/B$ are the packet and symbol duration, respectively. Hence, the ODL number is linked to the baud rate compression ratio and not the packet size, as in a previous architecture [8]. This packet compressor is suited for fixed packet duration. For a different packet length, the ODL delays must be adjusted accordingly. In Fig. 4.10, each of the four replicas is delayed by one fourth of the packet length plus one fourth of the symbol slot duration at the base baud rate. Hence, when the packet replicas overlap at the ODL structure output, the interleaved symbols are spaced according to the new symbol duration, T_s/N. After interleaving the packet, the time interval in which all packet replicas overlap must be selected and the symbols outside this interval must be discarded. This is achieved by generating a gating signal that is a clock with the duration of a packet length and frequency equal to $N \times B$. The gating signal will afterwards be used as the switching control signal in a MZI-SOA gate, to switch only the appropriate symbols in an optical switch.

With this setup, the symbol sequence in the resulting high baud rate packet is not the original one, but it is restored when the packet is decompressed back to the original baud rate. It should be remarked that no restrictions have been imposed on N. It has to be a natural number, but it is not required that N is a power of 2, as typically assumed. However, it is beneficial that $T_p/(T_sN)$, i.e. the number of symbols in the packet is a multiple of the compression ratio N so that the packet is truly compressed N-fold. If this condition is not fulfilled, the effective compression ratio is less than N. Consider, for instance, that the packet of Fig. 4.10 had 7 symbols instead of 8 symbols, or in other others, the 8th symbol is void. The compressed packet would be still be 8 symbols long, with a blank symbol in the middle. Thus, the effective compression ratio would be 7/2=3.5,

since the original packet is 7 symbols long ($7\times T_s$) and the compressed packet has the length of 8 compressed symbols ($8\times T_s/4$).

The decompressor conceptual operation is schematized in Fig. 4.11, assuming that the incoming packet was compressed by the packet compressor just described. It uses the same ODL structure as the compressor. The ODL structure produces replicas delayed by the compressed packet duration plus one symbol at the baud rate $N\times B$. To recover the original packet, it is enough to demultiplex the ODL structure output at a rate equal to the uncompressed baud rate B, starting at the N^{th} symbol. The clock signal to be used as demultiplexing signal can be obtained from an optical sub-harmonic clock recovery subsystem. The demultiplexing clock signal then acts as a control signal in an optical demultiplexer gate.

The packet compressor and decompressor circuits have, however, one drawback. They cannot operate with an uninterrupted stream of incoming packets, requiring guard bands between packets. In the case of the packet decompressor, this requirement stems from a fundamental reason. As the output baud rate is N times lower than the baud rate of the incoming packet, the output packet length is N times larger than the input packet. A direct consequence is that the packet decompressor can only receive compressed packets every T_p. Conversely, the guard time between compressed packets is $(N\text{-}1)\times T_p/N$. As for the packet compressor, as long as the packet beginning and ending are clearly delimited, there is no fundamental requirement on the required guard band, since the output baud rate is larger than the baud rate of the input packet and hence the output packets are shorter than the incoming ones. However, this particular packet compressing architecture produces packet replicas which span up to one packet duration after the incoming packet. Hence, the packet compressor can only compress packets arriving every $2\times T_p$, or, equivalently, the guard band time for the packet compressor is T_p.

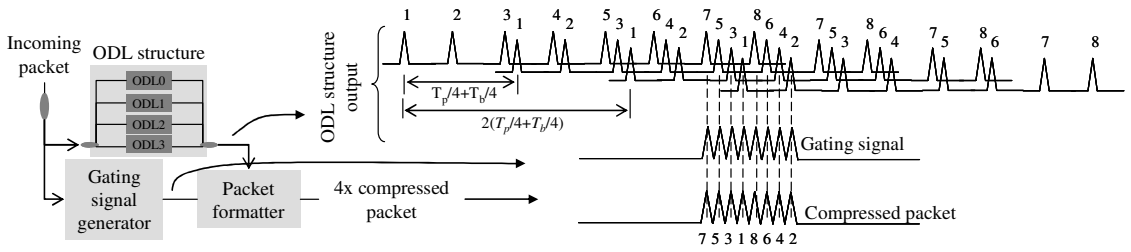

Fig. 4.10 Four-fold packet compressor operating principle.

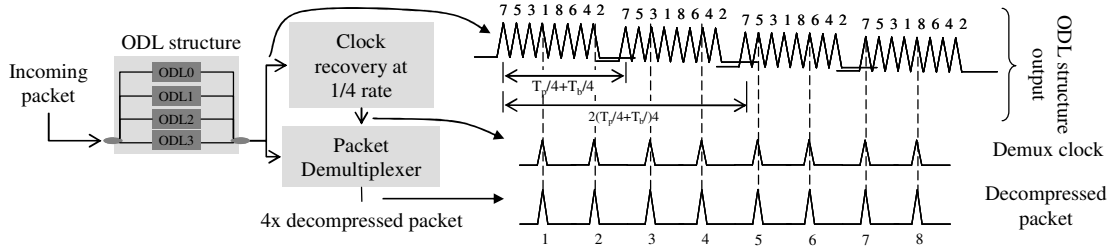

Fig. 4.11 Four-fold packet decompressor operating principle.

The implementation of the packet compressor based on the MZI-SOA will now be presented. It is depicted in Fig. 4.12, with some oscilloscope traces obtained in the simulation, using 10 Gbaud/s packets and a four-fold compression ratio. This figure replaces the generic boxes of Fig. 4.10 with MZI-SOA devices and other auxiliary components. Interconnecting EDFAs are not shown. The gating signal is obtained with the MZI-SOA in the following way. One first device operates the seemingly typical wavelength conversion of the incoming packet onto a local CW laser beam. Yet, since the packet format is PSK, the wavelength converted output is just a clock signal, without the phase information, with the same duration as the original packet. The functionality is the same the PED circuit presented in Chapter 2, for an intensity modulated RZ packet. A second MZI-SOA gate is now used to shorten the clock signal duration. The original packet is used as the control signal, which is delayed relatively to the clock signal of $T_p(1-1/N)$, so that only the last $1/N$ of the clock signal is switched to the MZI-SOA output. The shortened clock signal is then passively multiplexed N times, resulting in a clock signal with duration T_p/N and repetition rate $N \times B$. This is the desired repetition rate and duration of the future compressed packet. Only the phase encoded data is missing.

It should be emphasized that the first MZI-SOA is required in order to have a clock signal at a different wavelength from the incoming packet. The explanation follows. For the packet formatter stage, the phase information encoded in the clock signal is irrelevant and therefore a packet replica could be used instead of the clock signal as the control signal. However, the second MZI-SOA gate in the gating signal generator section and the MZI-SOA at the packet formatter require that the signals fed to the control and interferometric gates have different wavelengths. Otherwise, it would not be possible to separate at the output the desired probe signal from the pump signal.

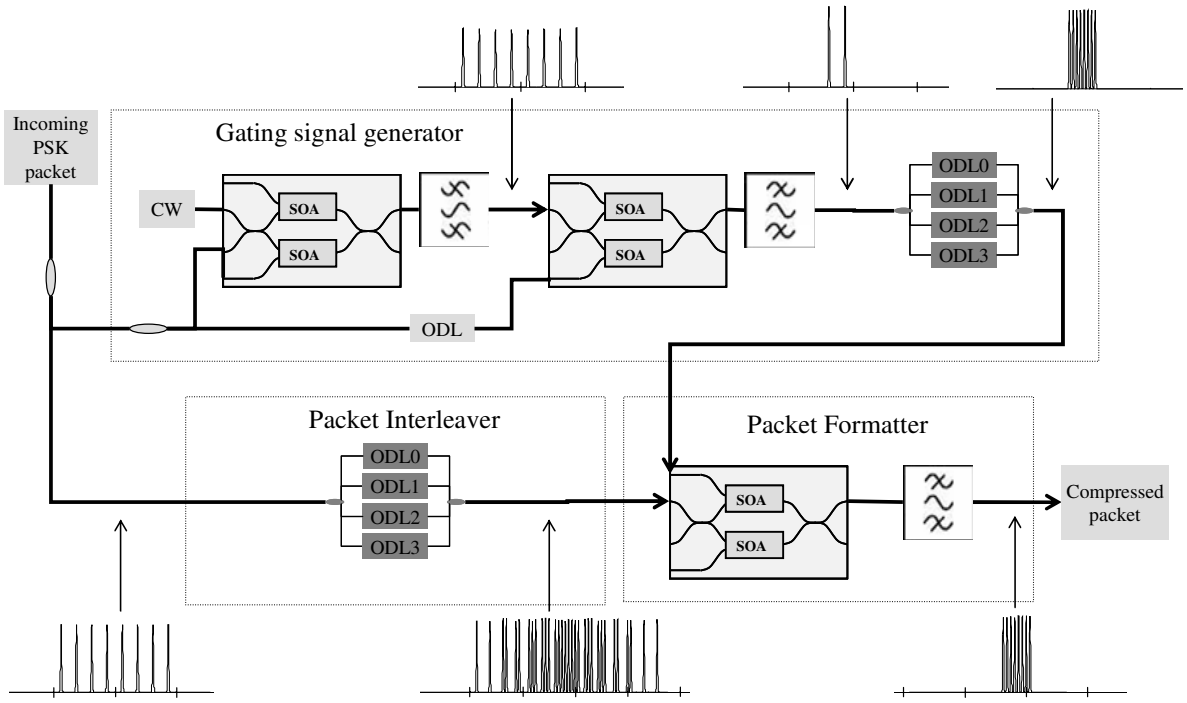

Fig. 4.12 Four fold MZI-SOA based all-optical packet compressor. The insets show simulated oscilloscope traces of the packet signal at various stages of the compressor. The incoming packet baud rate is 10 Gbaud/s and the horizontal scale is 400 ps/division.

The decompressor implementation with MZI-SOA gates is presented in Fig. 4.13. The first step is to expand the incoming packet by interleaving it in a delay line structure identical to the one previously used in the packet compressor. More details about the requirements of the ODL structures of the compressor and decompressor are discussed in Appendix E. The output of the ODL structure is then passed to the only active block in this circuit that is the packet demultiplexer. A single MZI-SOA gate, with the help of a mode-locked laser (MLL), performs this functionality. The MLL synchronizes its output to the incoming packet and a clock signal at a sub-multiple frequency of that of the incoming packet [12, 13]. The sub-multiple frequency should match the baud rate of the decompressed packet *B*. In this work, since the focus is not on clock recovery, the MLL is considered ideal, producing pulses at the desired rate with 10 ps of pulse width, no jitter and instantaneous frequency locking to the signal. The sub-multiple frequency clock signal is fed to the MZI-SOA gate as a control signal that switches every N^{th} symbol of the expanded packet. The baud rate of the packet is hence reduced by a factor of *N*, and the symbols are re-ordered according to the original packet data.

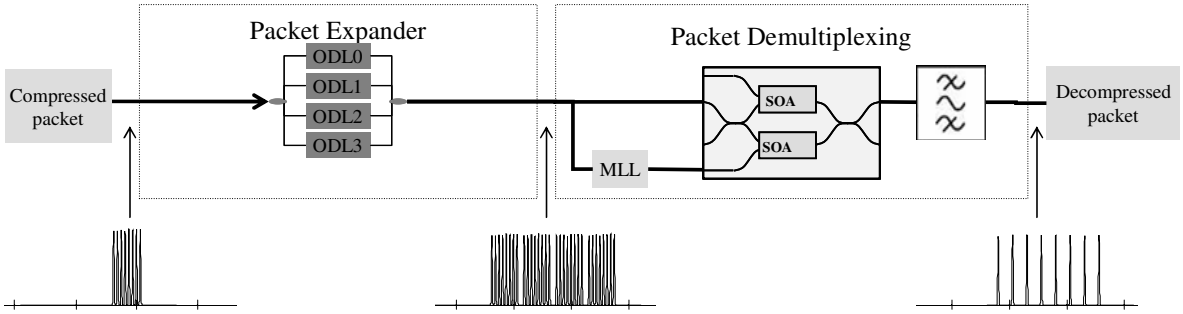

Fig. 4.13 Four-fold MZI-SOA based all-optical packet decompressor. The insets show simulated oscilloscope traces of the packet signal at various stages of the compressor. The incoming packet baud rate is 40 Gbaud/s and the horizontal scale is 400 ps/division.

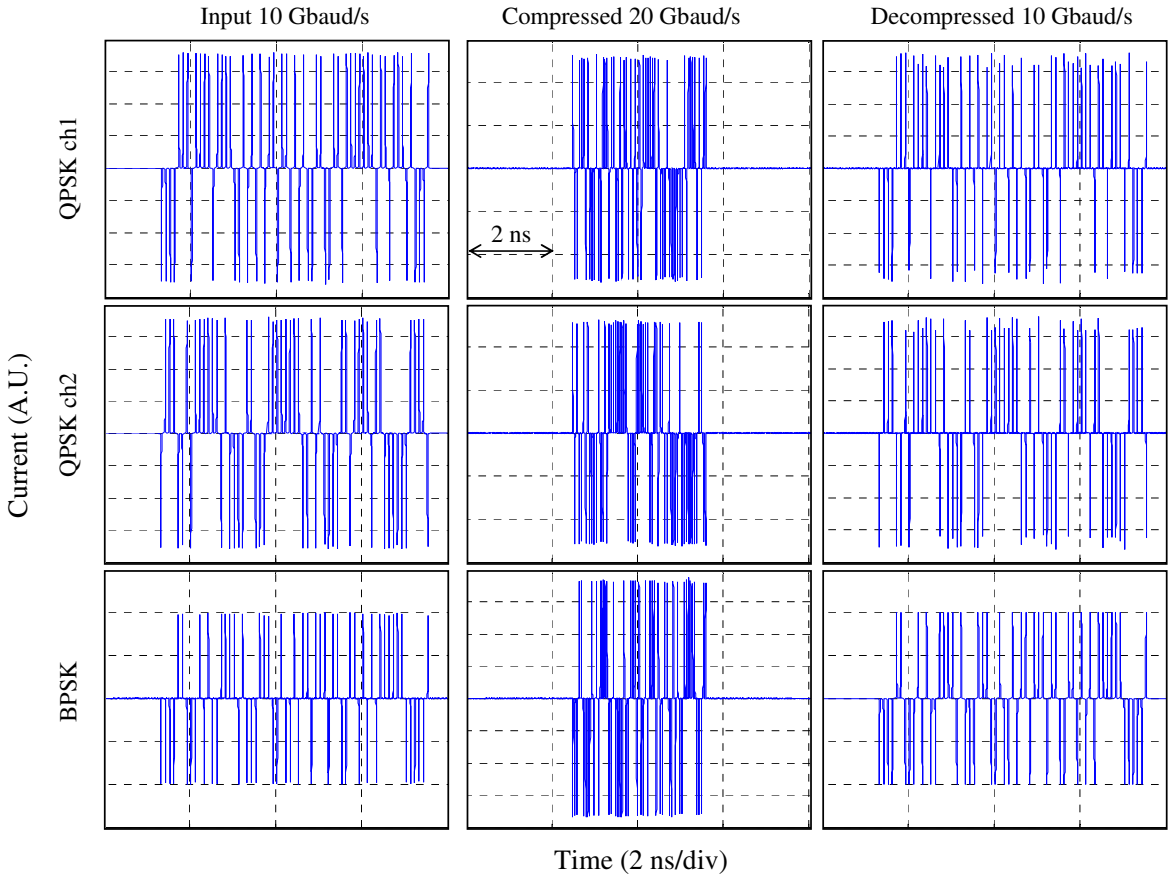

Fig. 4.14 Oscilloscope traces of differential detection of input packets (left column), compressed packets (middle column), and decompressed packets (right column). The two top rows are the two detected channels of QPSK modulated packet, whereas the bottom row is the detection of a BPSK modulated packet. The base and compressed baud rates are 10 Gbaud/s and 20 Gbaud/s, respectively. The horizontal axis is time (2 ns/div.) and the vertical axis is electrical current (arbitrary units).

The symbol and, consequently, bit re-ordering can be seen in Fig. 4.14 and Fig. 4.15 that show oscilloscope traces of the incoming, compressed and decompressed packets. The oscilloscope traces were obtained by placing differential receivers for the appropriate

modulation format and baud rate after the packet transmitter, the packet compressor and packet decompressor. The BPSK and QPSK formats have been used. The QPSK format has two bits per symbol and therefore oscilloscope traces are shown in pairs, corresponding to the outputs of the two balanced photodetectors inside the receiver. The base baud rate is 10 Gbaud/s and two compressed baud rates of 20 Gbaud/s and 40 Gbaud/s have been simulated, corresponding to a compression ratio of 2 (Fig. 4.14) and 4 (Fig. 4.15), respectively.

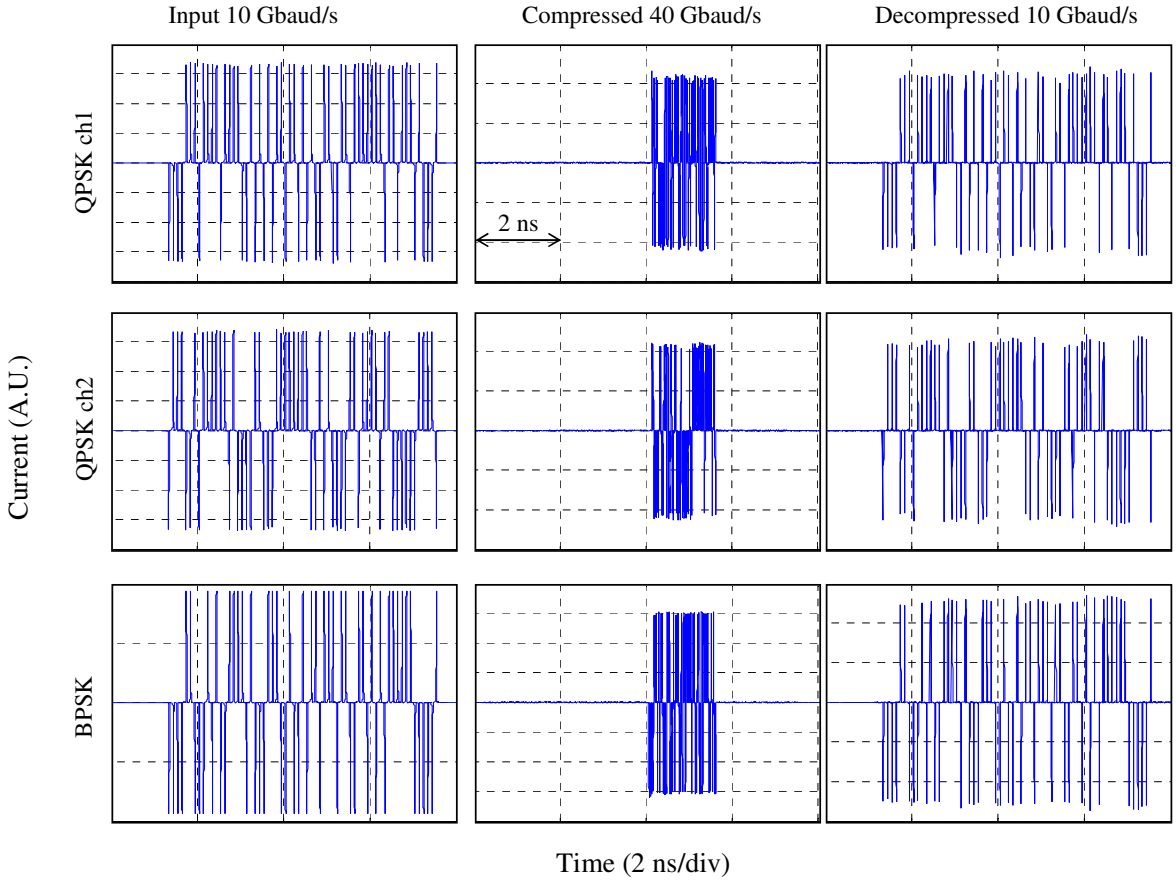

Fig. 4.15 Oscilloscope traces of differential detection of input packets (left column), compressed packets (middle column), and decompressed packets (right column). The two top rows are the two detected channels of QPSK modulated packet, whereas the bottom row is the detection of a BPSK modulated packet. The base and compressed baud rates are 10 Gbaud/s and 40 Gbaud/s, respectively. The horizontal axis is time (2 ns/div.) and the vertical axis is electrical current (arbitrary units).

As expected, it can be observed from the oscilloscope traces that the compressed data, at the compressed baud rate, is different from the original data due to the symbol re-ordering, but the decompressed data is the same as the original data. This applies to both BPSK and QPSK formats, attesting the transparency of the compressor and decompressor

scheme transparency to the phase information. It can be noted, however, that the decompressed packet presents larger peak current fluctuations than the original packet. This is mainly due to the accumulated impairments from the dynamics of the MZI-SOAs of the compressor and decompressor circuits.

In order to quantify the degradation introduced by the packet compressor and decompressor, the following eye closure penalty (ECP) was defined for the electrical signal output of a balanced receiver. Very wide band photodetectors are considered and no electrical filters are used so that the signal is not distorted by electrical filtering. Denoting by i_1 and i_0 the samples of the '1' and '0' levels at the sampling instant with largest eye opening, the ECP is defined in linear units as

$$ECP = \frac{\min(i_1) - \max(i_0)}{\overline{i_1} - \overline{i_0}}. \quad (4.1)$$

$\overline{i_1}$ and $\overline{i_0}$ represent the average of the samples i_1 and i_0, respectively. For a perfect eye diagram, where all the samples have the same value, the ECP is 1, or, in logarithmic units, 0 dB. In the case of the QPSK format, the receiver comprises a pair of balanced photodetectors and therefore the output of each balanced photodetector, called channel 1 and 2, is analysed independently. Hence, the performance of a QPSK signal is given by the ECP of both channel 1 and 2.

In a practical application where packet compression and decompression are used, the quality of the compressed packets is not critical, since what is truly important is the quality of the decompressed packet. Therefore, the performance of the proposed circuits will be always assessed considering a packet compressor and decompressor combo, where the ECP is measured after the decompressor stage.

4.2.2 Results with MZI-SOA gates

The first investigation of the performance of the packet compressor and decompressor operation was the influence of the packet size on the ECP after a compressor and decompressor stage. For each packet size, the simulation is performed twice, for two different pseudo-random binary sequences and then the average of the ECP is taken. The results are shown in Fig. 4.16 and Fig. 4.17 for the compression from 10 Gbaud/s to 40 Gbaud/s and to 20 Gbaud/s, respectively. Both figures include results considering both

BPSK and QPSK modulated packets. Additionally, the simulation time of a single simulation run is presented. The total simulation time for both binary sequences is obtained by multiplying the plotted values by 2. The pulse width of the input packets is 12 ps in all cases.

As expected, the simulation time is proportional to the packet size and hence it is desirable to simulate the smallest packet size to keep the simulation time within reasonable values. Whereas the BPSK and QPSK have the same simulation time, four-fold compression takes about 10% more time than two-fold compression simulations. This is not because of the larger ODL structure, but rather because more packet replicas are produced and hence the propagation of more pulses inside the SOAs has to be simulated.

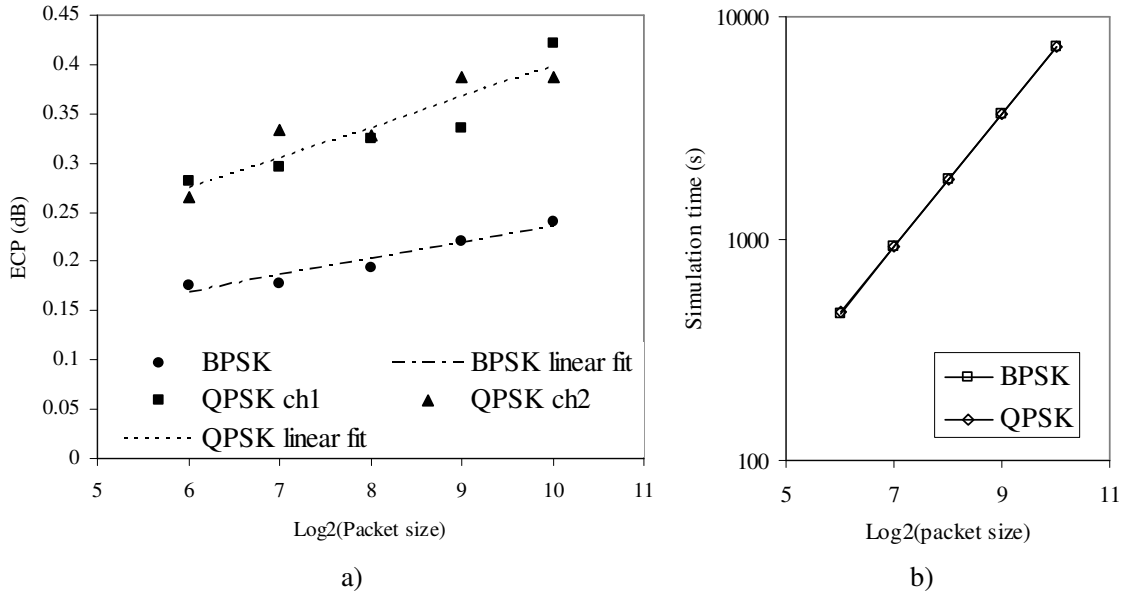

Fig. 4.16 Eye closure penalty (ECP) (a) and simulation time (b) of the compressor and decompressor pair as a function of the packet size, for the BPSK and QPSK modulation formats. The compression is performed from 10 Gbaud/s to 40 Gbaud/s.

As for the ECP, it increases approximately linearly as a function of the logarithm of the packet size for both compression ratios and for both modulation formats. A linear fit of the ECP as a function of the logarithm of base 2 of the number of symbols in the packet n_p, $ECP \approx a + b \times \log_2 n_p$, was done using the least squares method, as to obtain a quick rule of thumb of the ECP for a given packet size. The parameters a and b are presented in Table 4-1 for BPSK and QPSK for 10 Gbaud/s to 40 Gbaud/s, and for 10 Gbaud/s to 20 Gbaud/s. The same table shows the square of the correlation coefficient (r^2) for each linear fit.

Table 4-1 Fitting parameters (*a* and *b*) of the linear fit to the ECP of the packet compressor and decompressor combo as a function of the packet size, for the BPSK and QPSK modulation formats and a base baud rate of 10 Gbaud/s and compressed baud rates of 20 Gbaud/s and 40 Gbaud/s. r^2 is the square of the correlation factor.

	Mod. format	*a*	*b*	r^2
10 Gbaud/s to 40 Gbaud/s	BPSK	0.070	0.016	0.93
	QPSK	0.089	0.031	0.97
10 Gbaud/s to 20 Gbaud/s	BPSK	-0.0018	0.012	0.92
	QPSK	0.13	0.015	0.88

The ECP is larger and increases more quickly for the QPSK than for the BPSK because of the smaller phase distance between symbols in the phase constellation diagram. Any degradation of the phase or amplitude caused by the compressor and decompressor thus has a more severe impact on the QPSK than on the BPSK. As in the other MZI-SOA based sub-systems, the main impairments are the gain recovery causing inter-symbolic effects, as well as coherent crosstalk in the delay line structures, as observed in the WDM to OTDM converter. The main drivers for the increase of the ECP for larger packets are the inter-symbolic effects arising from the gain compression recovery. Still, these results confirm the phase transparency of the packet compressor and decompressor combo. The square of the correlation coefficient is between 0.88 and 0.97 for all fits, which shows the ECP linear dependence on the logarithm of the packet size is a valid assumption.

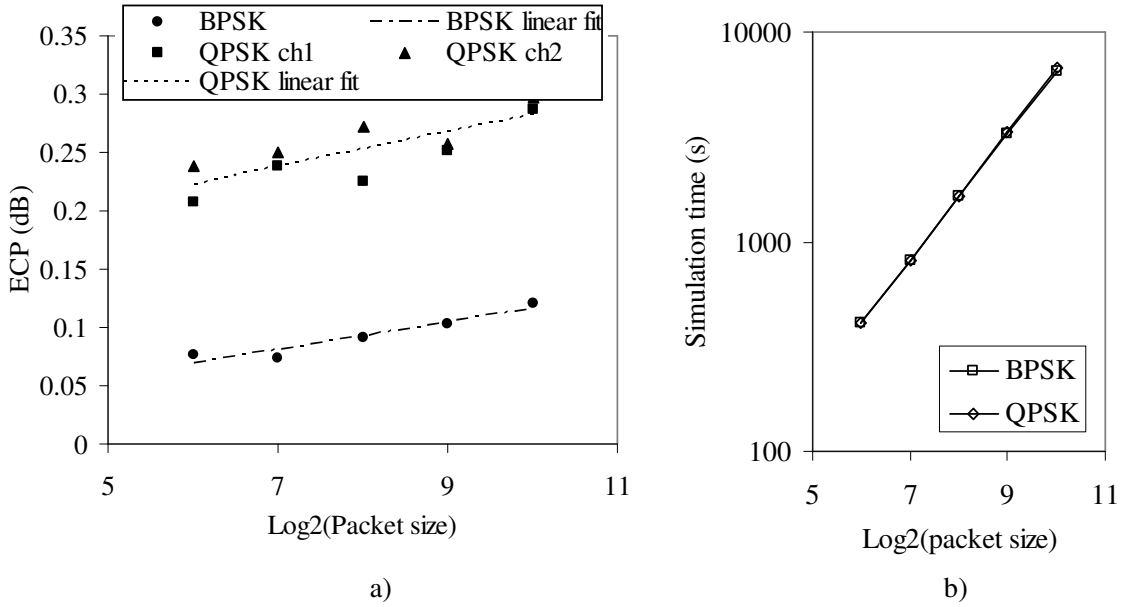

Fig. 4.17 Eye closure penalty (ECP) (a) and simulation time (b) of the compressor and decompressor pair as a function of the packet size, for the BPSK and QPSK modulation formats. The compression is performed from 10 Gbaud/s to 20 Gbaud/s.

An interesting application of the linear fit of Table 4-1 is to extrapolate the performance of the compressor and decompressor combo for Ethernet packets, which have, at most, 1518 bytes or, equivalently, 12144 bits. The smallest natural power of base 2 that is larger than this number is 2^{14}=16384, which will be used as the packet size to be used in the packet compressor and decompressor. According to the linear fit and for a compressed baud rate of 40 Gbaud/s, packets 2^{14} symbols long would have an ECP of 0.30 and 0.52 dB, for BPSK and QPSK, respectively. Considering that the QPSK has two bits per symbol, a 2^{13} symbols packet would be enough to encapsulate an Ethernet packet, resulting in an ECP of 0.49 dB. Considering a compressed baud rate of 20 Gbaud/s, the ECP of a packet of 2^{14} symbols would be 0.16 and 0.34 dB for BPSK and QPSK, respectively. For 2^{13} symbols packet modulated with QPSK, the ECP decreases slightly to 0.33 dB. If the ODL architecture proposed in prior art [8] would be used for compressing Ethernet packets, 14 ODL stages would have been required, considering 1 bit per symbol, which is rather impractical.

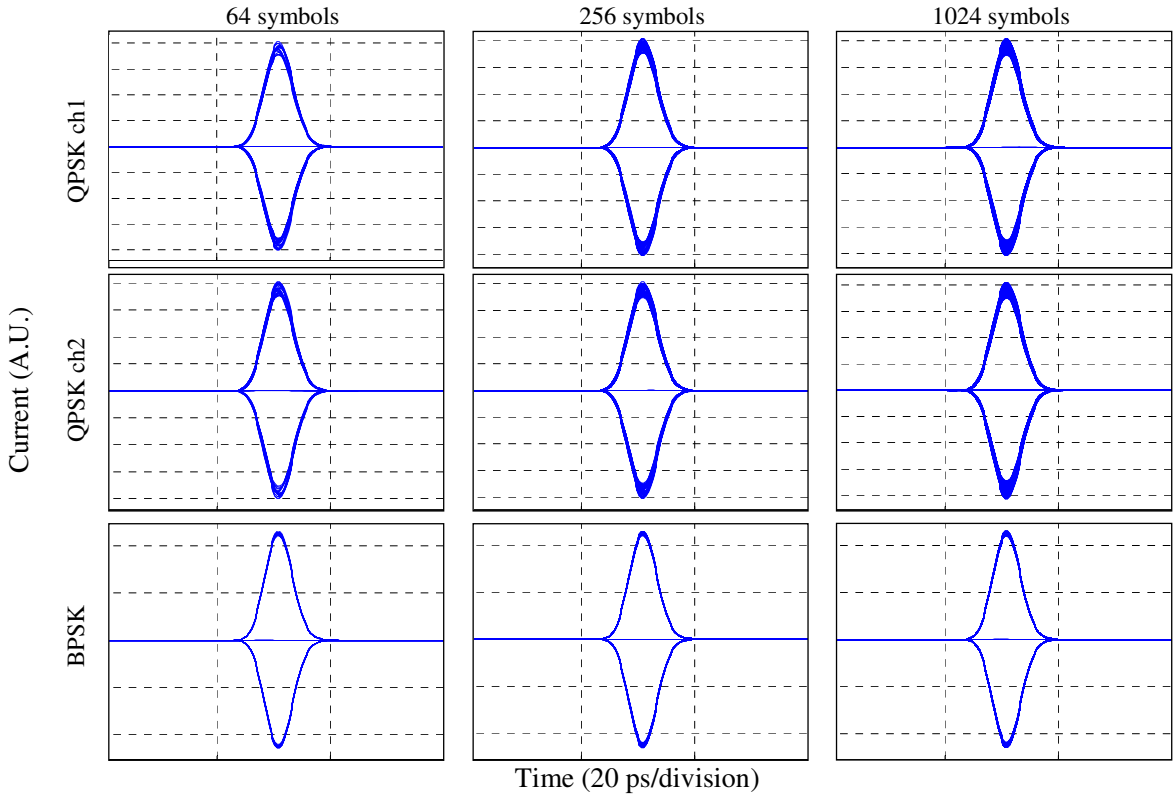

Fig. 4.18 Eye diagrams of the balanced detection of 64-symbol (left column), 256-symbol (middle column), and 1024-symbol (right column) packets after the compressor and decompressor combo. The modulation format is QPSK (channel 1 and 2 in the two top rows) and BPSK (bottom row). The base and compressed baud rates are 10 Gbaud/s and 20 Gbaud/s, respectively. The horizontal axis represents time (20 ps/div.) and the vertical axis represents electrical current (arbitrary units).

Some eye diagrams of the packets at the output of the compressor and decompressor combo for different packet sizes are presented in Fig. 4.18. The base and compressed baud rate are 10 Gbaud/s and 20 Gbaud/s, respectively, and the modulation formats are BPSK and QPSK. Three packet sizes have been used: 64, 256, and 1024 symbols. It is visible that for larger packets the amplitude jitter is larger, in agreement with the increase of ECP in the results of Fig. 4.17. In addition, it is clear that the amplitude jitter is more significant for the QPSK format than for the BPSK format, again agreeing with the quantitative results presented in Fig. 4.17.

In the WDM to OTDM circuit analysis, it was concluded that the input pulse width played a major role on the performance. Since in the packet compressor and decompressor some form of multiplexing involving delay lines is performed, the impact of the pulse width on the performance will also be studied. All pulse widths presented here are full width at half maximum.

The results are presented in Fig. 4.19 and Fig. 4.20, for compressed baud rates of 40 Gbaud/s and 20 Gbaud/s, respectively, whereas the base baud rate is 10 Gbaud/s. It can be seen that for narrow pulses, below 12 and 25 ps for the compression to 40 and 20 Gbaud/s, respectively, the ECP remains low. These values correspond to about 50% of the symbol period at the compressed baud rate. However, for larger pulse widths, the performance quickly degrades and reaches untenable penalties. The large penalties arise once again from inter-pulse crosstalk, as in the case of the WDM to OTDM converter. In order to have less than 1 dB of ECP, the pulse width should be inferior to 16 ps in the case of the 10 to 20 Gbaud/s compression, corresponding to 64% of the compressed symbol period. For the 10 to 40 Gbaud/s compression, the maximum pulse width should be 32 and 34 ps for the BPSK and QPSK formats, respectively, corresponding to 64 – 68% of the symbol period at 40 Gbaud/s. It was observed that the pulse width of the output pulses of the compressor and decompressor combo did not significantly depended on the input pulse width, within the region of operation below 1dB of ECP. This is due to the re-shaping properties of the all-optical circuit, and, in particular, of the MZI-SOA. Whereas for the 6 ps input pulses the output pulse width was 5.2 ps, for 32 ps input pulses the width of the output pulses was 7.5 ps.

It is noticeable that, for both compression ratios, and for pulse widths smaller than 50% of the compressed symbol period, there is an increase of the ECP for the QPSK

format, whereas for the BPSK there is not. This could be due to second order nonlinear effects inside the SOA, e.g. cross phase modulation from four wave mixing products. For very short pulse widths, these effects become stronger and affect more severely the QPSK due to the smaller phase difference between symbols.

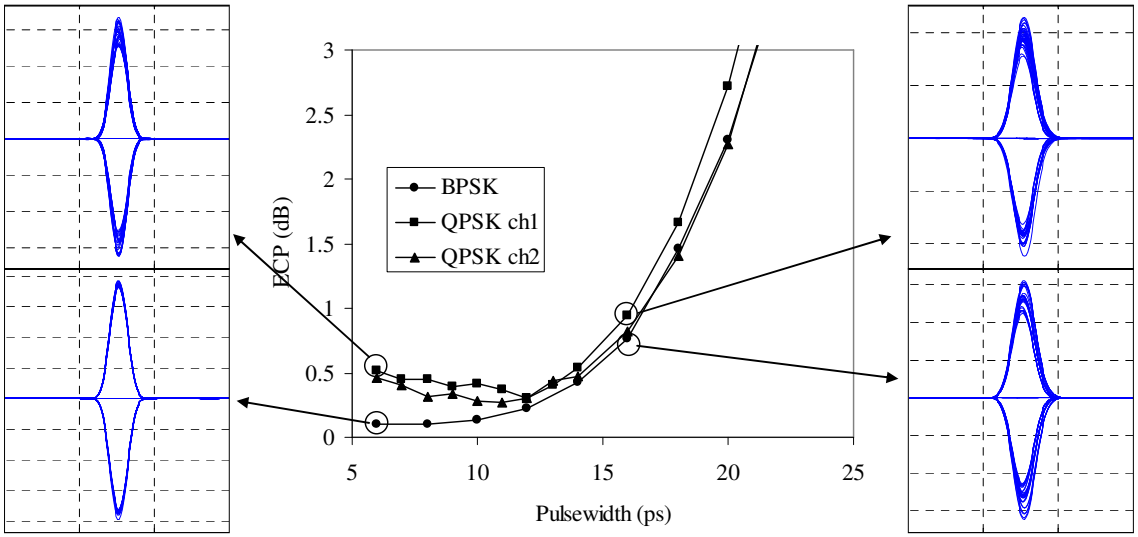

Fig. 4.19 Eye closure penalty (ECP) as a function of the packet pulse width fed to the compressor and decompressor pair, for the BPSK and QPSK modulation formats. The compression is performed from 10 Gbaud/s to 40 Gbaud/s. The lines are guides for the eyes. Eye diagrams of the packets after differential detection are also shown for 6 ps and 16 ps of pulse width. The horizontal axis of the eye diagrams represents time (20 ps/division) and the vertical axis represents electrical current (arbitrary units).

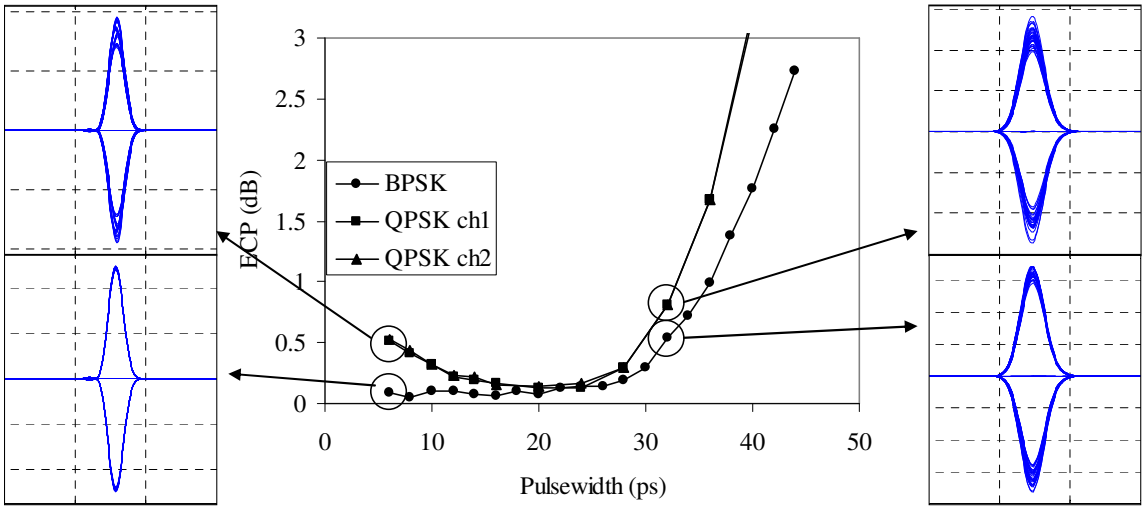

Fig. 4.20 Eye closure penalty (ECP) as a function of the packet pulse width fed to the compressor and decompressor pair, for the BPSK and QPSK modulation formats. The compression is performed from 10 Gbaud/s to 20 Gbaud/s. The lines are guides for the eyes. Eye diagrams of the packets after differential detection are also shown for 6 ps and 32 ps of pulse width. The horizontal axis of the eye diagrams represents time (20 ps/division) and the vertical axis represents electrical current (arbitrary units).

In an optical packet switched network, it might be possible for an optical packet to cross several optical network nodes before reaching its final destination. Possibly, in each of these network nodes, the packet is decompressed for processing and routing and is again compressed before being transmitted through a fibre link to the next destination. Hence, the cascadability of the packet compressor and decompressor combo is important and it will now be assessed. Through simulation, the same packet will be compressed and decompressed a number of times and its ECP will be calculated at each stage to quantify the degradation. The results are presented in Fig. 4.21 and Fig. 4.22 for a base baud rate of 10 Gbaud/s and compressed baud rates of 40 Gbaud/s and 20 Gbaud/s, respectively. In fact, the ECP increases rather steeply, and for all the studied cases only two cascades are possible in order to have an ECP below 1 dB. Between the two modulation formats, BPSK shows better performance than QPSK, as before. Facing these results, it is recommended to have regeneration between packet compressor and decompressor pairs to enable cascading more of these devices.

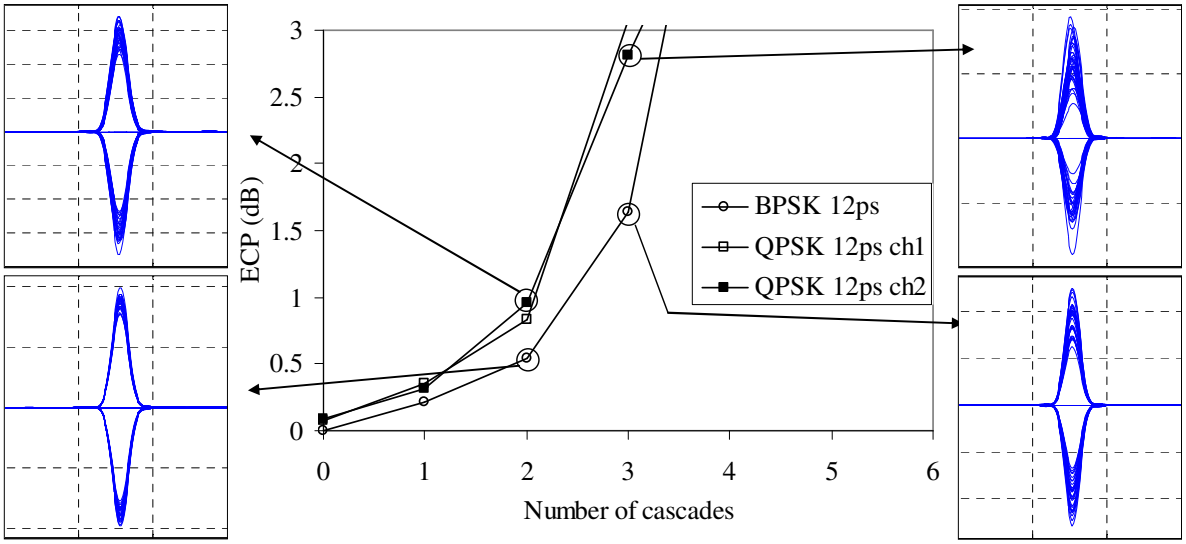

Fig. 4.21 ECP versus the number of cascaded compressor and decompressor pairs (10 Gbaud/s to 40Gbaud/s) for packets modulated with BPSK and QPSK formats, and 12 of pulse width. The lines are guides for the eyes. Eye diagrams of the packets after differential detection are also shown after 2 (left) and 3 (right) cascaded pairs. The horizontal axis of the eye diagrams represents time (20 ps/division) and the vertical axis represents electrical current (arbitrary units).

For a compressed baud rate of 40 Gbaud/s only 12 ps pulses are simulated, whereas for the compressed baud rate of 20 Gbaud/s both 12 and 24 ps are simulated. These two pulse widths were chosen since 12 ps is the largest acceptable pulse width before the ECP starts to increase significantly. Additionally, 12 ps pulses were also used to investigate if a

narrower pulse width would improve the cascading performance. Nevertheless, as seen before, the combo output pulse width does not depend significantly on the input pulse width. As corroboration, from these results one concludes that the cascading performance depends only very slightly on the pulse width, considering the two investigated pulse widths.

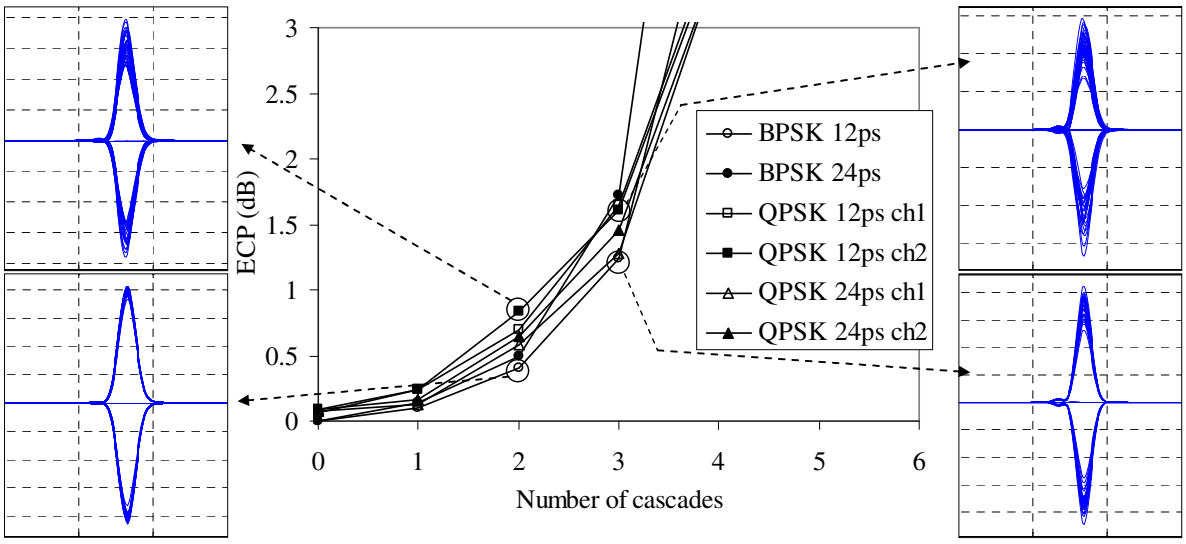

Fig. 4.22 ECP versus the number of cascaded compressor and decompressor pairs (10 Gbaud/s to 20Gbaud/s) for packets modulated with BPSK and QPSK formats, and 12 and 24 ps of pulse width. The lines are guides for the eyes. Eye diagrams of the packets after differential detection are also shown after 2 (left) and 3 (right) cascaded pairs. The horizontal axis of the eye diagrams represents time (20 ps/division) and the vertical axis represents electrical current (arbitrary units).

Up to now, the SOA devices have been modelled according to the experimental observations and the remaining passive devices are considered ideal in the sense that their specifications are exactly the desired ones. At this time, the effect of mismatches in the ODL structures will be considered. The ODL structure has the purpose of creating packet replicas at desired delays. These delays will now be altered from the ideal value and the impact on the ECP will be assessed.

ECP results as a function of the delay mismatch in each of the ODL composing the ODL structure are presented in Fig. 4.23 and Fig. 4.24, for a base baud rate of 10 Gbaud/s and a compressed baud rate of 40 Gbaud/s and 20 Gbaud/s, respectively. To facilitate the interpretation of the plots of the QPSK results, the maximum ECP of both channels is presented, instead of the ECP results of both channels. Anyhow, it was verified that both channels yielded similar ECP values and the maximum penalty represents well the performance of both channels. The incoming packet pulse width is 12 ps.

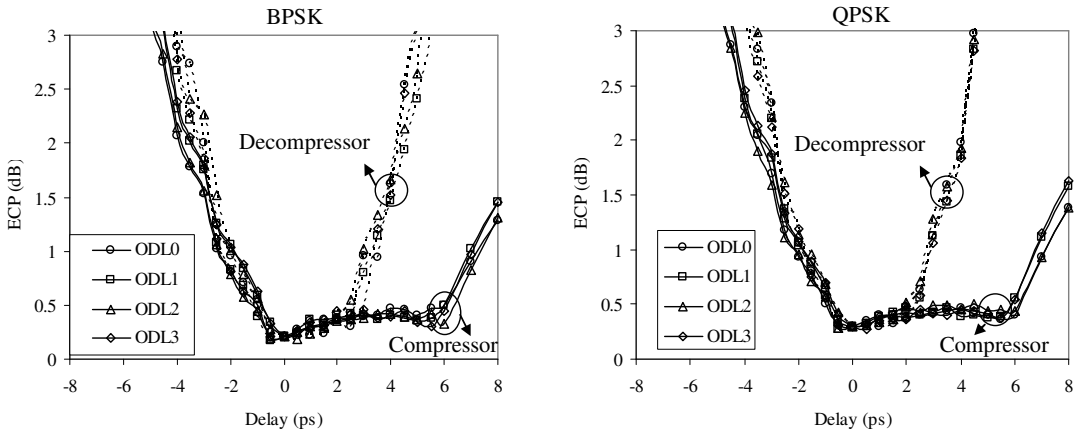

Fig. 4.23 Eye closure penalty (ECP) of the packet compressor and decompressor pair, as a function of the delay mismatch in ODL0 (circles), ODL1 (squares), ODL2 (triangles), and ODL3 (diamonds) in the compressor (full line) and in the decompressor (dashed line). The lines are guides for the eyes only. The base baud rate is 10 Gbaud/s and the compressed baud rate is 40 Gbaud/s. The plot on the left is for BPSK and the plot on the right is for QPSK.

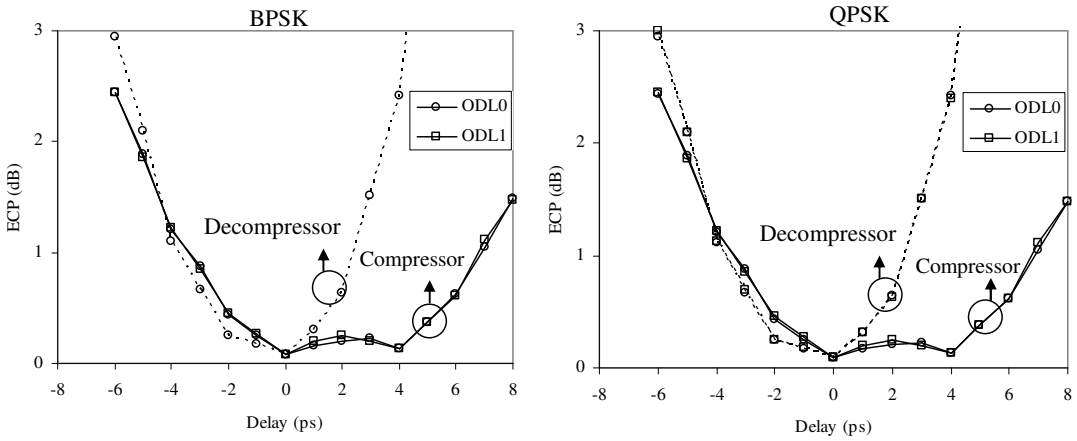

Fig. 4.24 Eye closure penalty (ECP) of the packet compressor and decompressor pair, as a function of the delay mismatch in ODL0 (circles) and ODL1 (squares) in the compressor (full line) and in the decompressor (dashed line). The lines are guides for the eyes only. The base baud rate is 10 Gbaud/s and the compressed baud rate is 20 Gbaud/s. The left plot is for BPSK and the right plot is for QPSK.

It is readily concluded that the mismatch in every ODL of the compressor or of the decompressor has the same practical effect on the ECP. Furthermore, BPSK and QPSK yield similar ECP results, for both compressed baud rates of 20 and 40 Gbaud/s. Thus, the ECP is not arising from phase distortions, but rather from amplitude distortions. If not, BPSK and QPSK would have different performances due to the smaller phase distance of the QPSK format. When there is a delay mismatch in one of the ODLs in the ODL structure, one packet replica is offset in time relatively to the other packet replicas. The consequences are two-fold. First, the pulse is not in its optimum position relatively to the subsequent MZI-SOA switching window. At the output of that MZI-SOA gate, the pulse

shape can be partially restored due to the reshaping and retiming properties of the MZI-SOA, but only up to a given maximum delay mismatch. So, a delay mismatch will degrade the MZI-SOA operation. Second, if the ODL mismatch is significant, it causes crosstalk on the neighbouring pulses and thus amplitude jitter. Depending on the particular operating conditions, each effect might dominate. Either way, the signal acquires amplitude jitter and penalties arise.

ODL delay mismatches are more tolerated in the packet compressor comparing to the packet decompressor, mainly because if the mismatches occur in the compressor, i.e. earlier in the compressor and decompressor combo, the degraded signal will cross more MZI-SOA gates before the decompressor output, which progressively improve the signal quality. For a maximum ECP of 1 dB, a mismatch interval of [-2 ps, 3 ps] is acceptable in the decompressor, whereas for mismatches in the compressor a larger interval of [-2 ps, 7 ps] is tolerated, for the 40 Gbaud/s compressed baud rate. For the 20 Gbaud/s compressed baud rate and the same tolerated ECP, the decompressor and compressor delay mismatch range is [-3.5 ps, 2 ps] and [-4 ps, 6.5 ps], respectively. There is little crosstalk between pulses since the interval span for a compressed baud rate of 40 Gbaud/s is only slightly narrower than that for a compressed baud rate of 20 Gbaud/s. Hence, the main origin of the limitation is the pulse position relatively to the MZI-SOA switching window, which is also corroborated by the fact that the curve for the delay mismatch in the compressor is asymmetrical around 0 ps, because so is the switching window, which does not happen with the crosstalk effect.

As a rule of thumb, it will be considered that the maximum delay deviation in the ODLs should be 10% of the symbol period.

The study of the ODL delay mismatch was repeated for different delays between the demultiplexing clock signal and the packet replicas in the decompressor, hereafter called signal-replicas delay. The underlying idea is to understand if shifting the MZI-SOA switching window can compensate for the ODL delay mismatch. The modulation format is QPSK and the compressed baud rate is 20 Gbaud/s. The results are plotted in Fig. 4.25, where 0 ps of clock-replicas delay is the optimised reference value used before. It can be noticed that it has the lowest ECP for zero ODL delay mismatch. Still, the other clock-replicas delays have similar penalty for no ODL delay mismatch, which indicates that, within the investigated range, the replicas' pulses are inside the MZI-SOA switching

window. However, excluding the -3 ps clock-replicas delay, which shows comparable performance to the reference, all other clock-replicas delay have very narrow tolerance to ODL delay mismatches. This is because the replicas' pulses are too close to the MZI-SOA switching window edges where the switching window has rising or declining amplitude. Therefore, a relative delay between replicas induced by an ODL delay mismatch is translated to an amplitude difference between replicas and consequently an increased ECP.

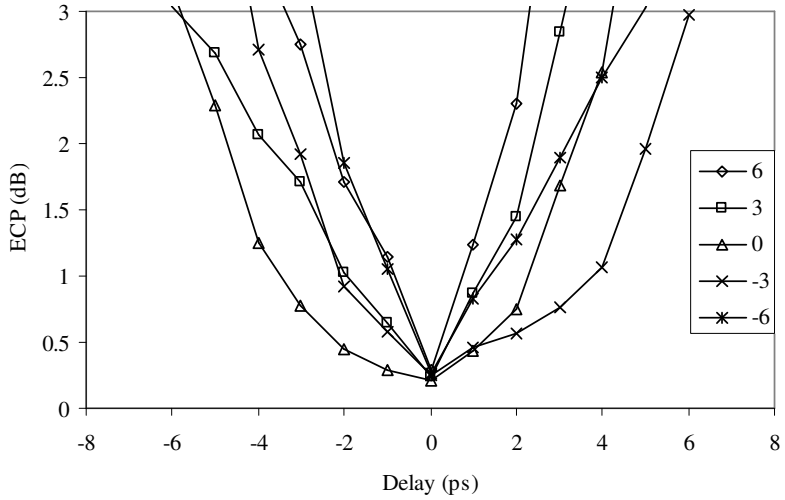

Fig. 4.25 Eye closure penalty (ECP) of the packet compressor and decompressor pair, as a function of the delay mismatch of ODL1 in the decompressor. Each curve was obtained for a different delay (from -6 ps to 6 ps) between the signal replicas and the demultiplexing clock in the decompressor. The lines are guides for the eyes.

The next investigation will be incident on the effect of phase mismatches of the ODL structures on the compressor and decompressor pair performance. As the packets are phase modulated, all the ODLs must be phase aligned with each other so that the packet replicas have no phase difference between them, which is a rather strict requirment. If packet replicas have phase differences between them, that phase difference will be converted to an amplitude variation after differential detection of symbols coming from different packet replicas, and consequently an impaired performance and possibly bit errors. This effect is not limited to this particular architecture, but, instead, it is valid for all architectures based on interleaving packet replicas and serving phase modulated packets. The situation of a phase mismatch in the decompressor ODL structure causing an undesired phase difference between symbols is illustrated in Fig. 4.26 for a two-fold decompression ratio and an 8 symbol packet. The effect of such spurious phase difference after packet detection in a differential receiver is shown in Fig. 4.27.

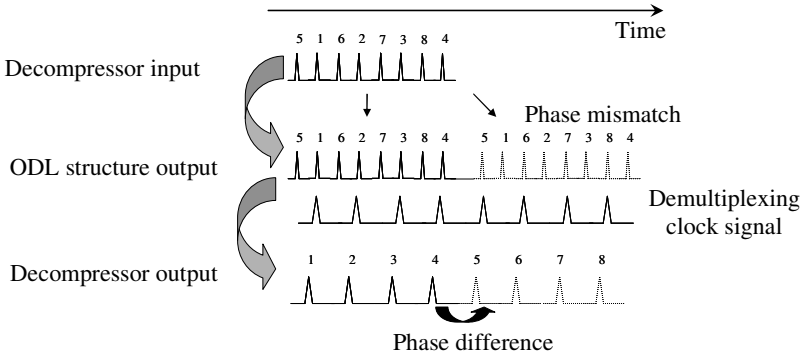

Fig. 4.26 Schematics depicting how a phase mismatch in one ODL of the decompressor ODL structure causes a phase difference inside the packet output by the decompressor.

It is visible that some bits are strongly impaired in terms of amplitude due to the phase difference introduced by the ODL structure. The impaired bits occur only in times corresponding to the different packet replicas produced in the ODL structure. Therefore, for larger baud rate compression ratios, there are also more ODLs in the ODL structures, more packet replicas, and consequently more impaired bits. In Fig. 4.27 a), two-fold compression of a BPSK packet was performed and hence only one bit corresponding to the phase difference between the two packet replicas is impaired. However, four-fold compression of a BPSK packet was performed in Fig. 4.27 b) and there two bits are impaired. Those bits correspond to the phase difference between replica number 1 and replica number 2, and between replica number 2 and replica number 3, since the phase mismatch was in ODL1, which affects replica number 2. Fig. 4.27 c) and d) show the two channels of a QPSK differential detection of a two compressed and decompressed packet. It is interesting to see that two bits, one in each detection channel, are impaired from one phase difference between symbols. This is because each symbol in the QPSK carries two bits. However, if the one of the bits is degraded in the sense that it closes the eye diagram, the electric current level of the other one is moved away from the eye diagram centre. This mirrors what happens in the phase constellation. If one symbol is rotated through a phase shift, it will get closer to one of the neighbouring symbols, but it will also be further apart from the other neighbour.

The impairment arising from phase mismatches is fundamentally different from the origin of the impairment of ODL delay mismatches, where all pulses of a given packet replica are shifted in time and therefore all symbols are affected in subsequent MZI-SOA stages.

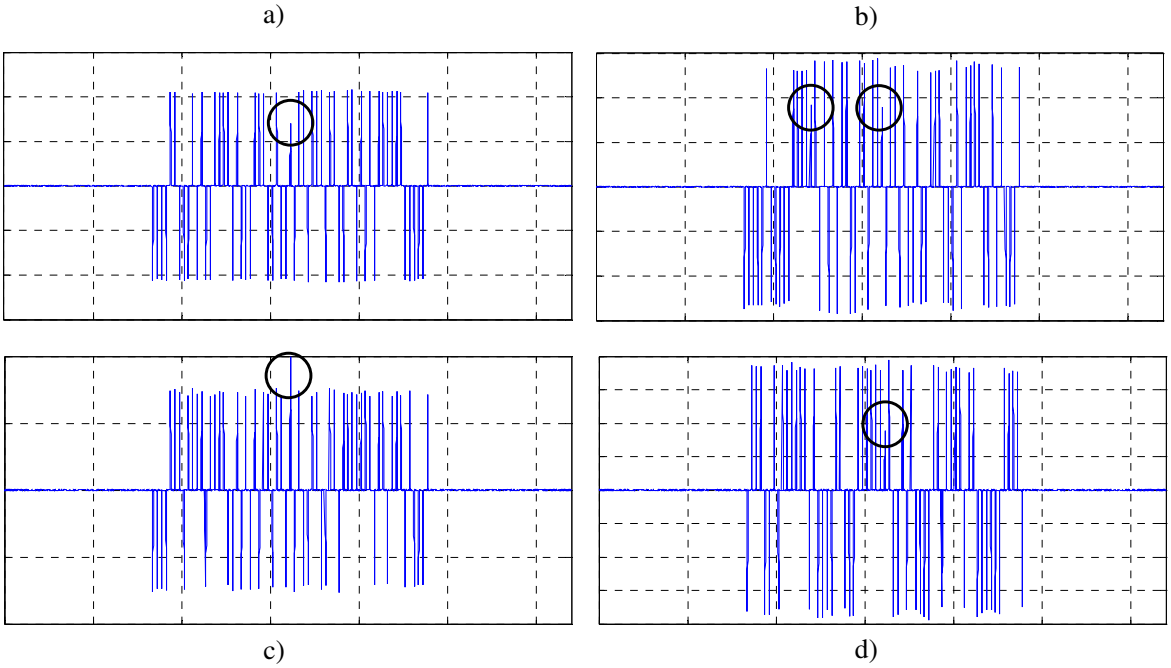

Fig. 4.27 Oscilloscope traces of differentially detected packets after compression and decompression, where ODL1 in the decompressor is phase mismatched. The circles mark the bits that are impaired. a) and b) were obtained from a BPSK packet that was compressed from 10 Gbaud/s to 20 Gbaud/s (a) or to 40 Gbaud/s (b) with a phase mismatch of 50º. c) and d) were obtained from both detection channels of a QPSK packet that was compressed from 10 Gbaud/s to 20 Gbaud/s with a phase mismatch of 25º. The horizontal axis is time (2 ns/division) and the vertical axis is current (arbitrary units).

Some quantitative ECP results will now be presented for different phase mismatches in the compressor and decompressor ODLs. The base baud rate is 10 Gbaud/s in the forthcoming results. Fig. 4.28 and Fig. 4.29 show the results for BPSK and QPSK modulation formats, respectively, and a compressed baud rate of 20 Gbaud/s. As before, for the QPSK format, the plots show only the maximum of the ECP of the two detection channels. The ECP results are plotted in contour plots, where the phase of two different ODLs is simultaneously varied. Appendix E further explores the phase requirements of the ODL structures.

Analysing the plots, a definite trend can be observed. The penalty is minimum in the region where the phase mismatch of one ODL is either identical or symmetrical to the phase mismatch of the other inspected ODL. The case of a compression ratio of two is the easiest to investigate because there are only two ODLs in each ODL structure. If there is a phase mismatch in ODL0 of the compressor, there should be a similar mismatch in ODL1 of the compressor so that both packet replicas have null phase difference. At this point, it should be recalled that the symbols after compression and decompression have passed

through complementary delays in the ODL structures of the compressor and decompressor so that the total delay is the same for each symbol. Thus, a phase mismatch of ODL0 in the compressor can also be compensated by an opposite phase mismatch of ODL1 in the decompressor because the delay and phase of ODL0 in the compressor is compensated by the delay and phase of ODL1 in the decompressor. In other words, at the end of the compressor and decompressor pair, the symbols that have passed in ODLk, k=0, 1, .., N-1 of the compressor will pass in ODL(N-1-k) of the decompressor, and therefore the phase mismatch of ODLk of the compressor can be compensated by a symmetrical phase mismatch of ODL(N-1-k) of the decompressor.

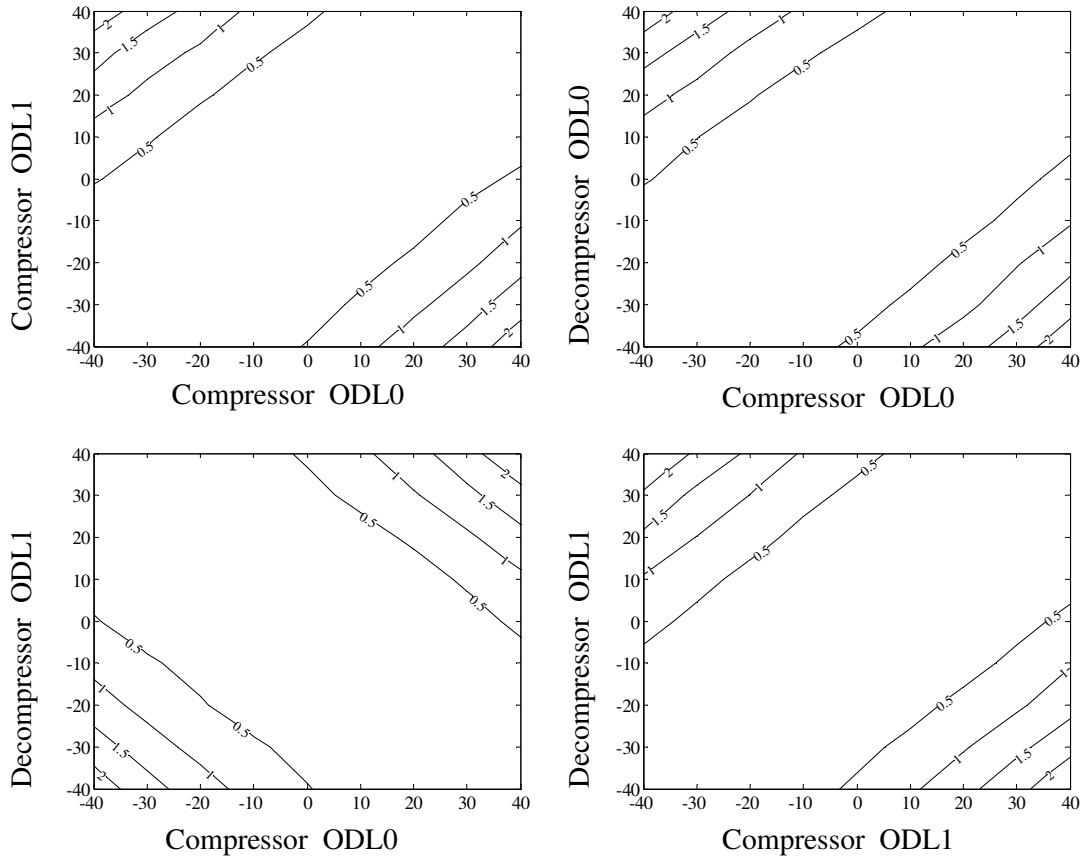

Fig. 4.28 Contour plot of the ECP in dB after a packet compressor and decompressor pair as a function of the phase delay mismatch (in degrees) in different ODLs. The base baud rate is 10 Gbaud/s and the compressed baud rate is 20 Gbaud/s and the modulation format is BPSK.

This reasoning applies for both the BPSK modulation format and the QPSK format, as can be seen comparing Fig. 4.28 and Fig. 4.29. However, due to the closer symbols of the QPSK in the phase constellation, the allowed phase mismatch is smaller than that for

the BPSK. Whereas for the BPSK case, a performance rule for the phase mismatch can be written as $|\Delta\varphi_A-\Delta\varphi_B|<50º$, for the QPSK the rule becomes $|\Delta\varphi_A-\Delta\varphi_B|<17º$, for a maximum ECP of 1 dB. $\Delta\varphi_A$ and $\Delta\varphi_B$ are the phase mismatch of ODLs that are not complementary in the sense explained in the previous paragraph. For complementary ODLs, the minus sign in the rules is replaced by a plus sign. Areas of very close contour lines in the edges of the plots are due to numerical artifacts in the ECP calculation.

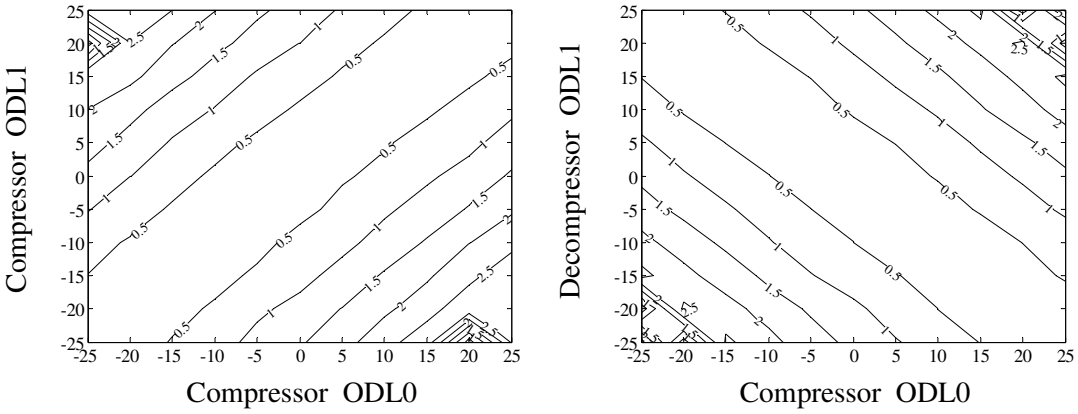

Fig. 4.29 Contour plot of the ECP in dB after the packet compressor and decompressor pair as a function of the phase delay mismatch (in degrees) in different ODLs. The base baud rate is 10 Gbaud/s and the compressed baud rate is 20 Gbaud/s and the modulation format is QPSK.

The analysed case of two-fold baud rate compression is the simplest. For a four-fold compression ratio, the analysis is slightly different since only the complementary ODLs can compensate each other's phase mismatch. Mismatches in all other ODLs will contribute with a phase error and consequently an impaired bit after differential detection. An example of phase mismatches in complementary ODLs and non-complementary ODLs for a four-fold compression ratio is shown in Fig. 4.30 and Fig. 4.31, for the BPSK and QPSK modulation formats, respectively. For the complementary ODLs case, the penalty is completely analogous to that of the two-fold compression ratio, since the same type of phase error and compensation is happening. However, for non-complementary ODLs, the contour plots show a different behaviour. As mentioned before, the phase mismatches never compensate each other. In this case, the rule can be approximately written as $|\Delta\varphi_A|<50º \wedge |\Delta\varphi_B|<50º$ and $|\Delta\varphi_A|<17º \wedge |\Delta\varphi_B|<17º$ for the BPSK and QPSK case, respectively, for ECP smaller than 1 dB. The symbol $\wedge$ represents the set intersection operation. The ECP rule contains two parts, one for each phase mismatch, that are independent of each other. This is because each phase mismatch is affecting different bit

transitions and causing eye closure after differential detection at distinct bits. The ECP performance metric considers only the worst bit and not all of the sequence, and hence only the largest phase mismatch matters for the ECP. Consequently, there can be separate rules establishing bounds for each phase mismatch.

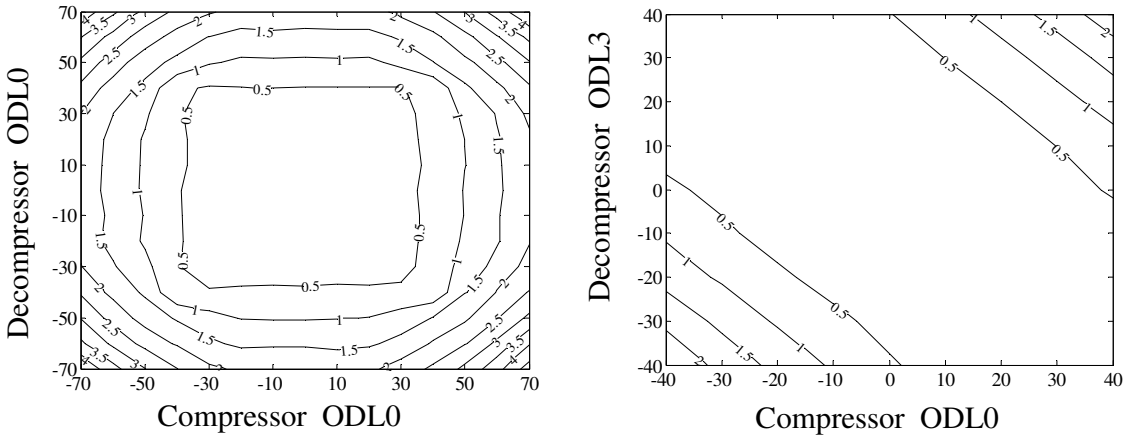

Fig. 4.30 Contour plot of the packet compressor and decompressor pair ECP (dB) as a function of the phase delay mismatch (in degrees) in different ODLs. The base baud rate is 10 Gbaud/s and the compressed baud rate is 40 Gbaud/s and the modulation format is BPSK.

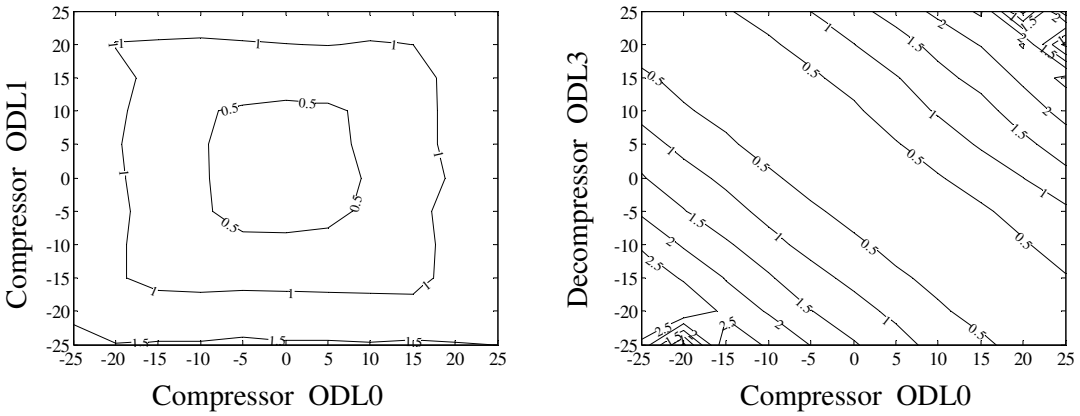

Fig. 4.31 Contour plot of the packet compressor and decompressor pair ECP (dB) as a function of the phase delay mismatch (in degrees) in different ODLs. The base baud rate is 10 Gbaud/s and the compressed baud rate is 40 Gbaud/s and the modulation format is QPSK.

4.2.3 Results with MZI-QDSOA gates

The MZI-SOA has shown good processing capabilities up to bit rates of 40 Gb/s, and in some functionalities at even larger bit rates. However, to accomplish all-optical processing at larger bit-rates, the SOAs inside the MZI structure must have shorter gain

recovery times. For this reason, it has been proposed that the MZI-SOA is equipped with quantum-dot SOAs (QDSOAs), instead of quantum well SOAs [14]. QDSOAs were expected to achieve operation bit rates above 160 Gb/s [15], and recently 160 Gb/s wavelength conversion has been demonstrated experimentally [16]. Additionally, it is expected that QDSOAs have the possibility of multi-wavelength operation [17]. Earlier studies about the QDSOA based Mach-Zehnder Interferometer (MZI-QDSOA) have shown enhanced processing capabilities, namely high output extinction ratio and regenerative characteristics [14, 18]. For this reason, this section presents the packet compressor and decompressor implemented with the MZI-QDSOA, in order to achieve compression to higher bit-rates.

Although in the QD-SOAs the phase shift arising from the gain compression (alpha factor) is very low (~0.1) [14], the MZI-QDSOA structure operates nonetheless. While in the MZI-SOA the output signal is produced from XPM causing a phase shift in one SOA, in the MZI-QDSOA the output signal is produced from the power unbalancing caused by XGM in the QDSOA. Even though a different transmission versus input power curve results, the switching window opening is totally analogous and the same functionalities of the MZI-SOA are promptly achieved. Therefore, to obtain the packet compressor and decompressor functionalities, the MZI-SOA is simply replaced by the MZI-QDSOA.

Simulation results were obtained using the QDSOA model described in [19] with the parameter set presented in [20]. A brief explanation of the model follows. The QDSOA is considered to be well approximated by a system of three equations describing the carrier densities of the wetting layer and of the ground and excited quantum dot states. The wetting layer acts as a reservoir for the two quantum dot states and it is where the carriers are electrically pumped to. The excited state acts as an intermediary state between the wetting layer and the ground state. The latter state provides gain to the optical field. During pulse amplification, as the carriers in the ground quantum dot state are depleted, carriers transit from the excited state to the ground state in a femtosecond time scale. As the carrier density in the excited state reduces, carriers from the wetting layer fill the excited state in the picosecond time scale. The capability of the QDSOA to operate in the 100 Gb/s range arises from this fast dynamics.

All QDSOAs were considered to have the dimensions $4000\times3\times0.2$ μm^3 and to be pumped with a current density of 5 kA/cm^2, corresponding to a current of 600 mA. The

simulated optical pulses have a Gaussian profile and 2 ps of full width at half maximum, which is 32% of the bit period at 160 Gb/s to minimize crosstalk. The MZI-QDSOAs input powers were optimised to ensure negligible pulse broadening and also to prevent patterning effects caused by wetting layer depletion. The results presented here were obtained using the BPSK modulation format, so that one symbol carries only one bit.

First, an analysis of the influence of the packet size on the ECP was performed, similarly to the study for the MZI-SOA. The base bit rate is 40 Gb/s and the compressed bit rate is 160 Gb/s. The results are plotted in Fig. 4.32, which also shows eye diagrams of the differential detection of the decompressed packets. The ECP increase with the packet size is approximately linear within the investigated range, which motivates a linear fit using the least squares method, as in the case of the MZI-SOA. The resulting fit parameters a and b of the expression $ECP \approx a + b \times \log_2 n_p$ are -0.1 and 0.04, respectively. Although the ECP values are quite low, the increase of the ECP with packet size is larger for the MZI-QDSOA than for the MZI-SOA. This is, on one side, due to the larger bit rates and thus more stringent inter-symbolic effects requirements, and, on the other side, due to the slow wetting layer depletion acting on the scale of nanoseconds. Retaking the example of the Ethernet packets, the extrapolated ECP is 0.53 dB for a 2^{14} packet, which is significantly larger than the 0.28 dB for MZI-SOA compression and decompression for a 10 Gbaud/s base baud rate and a 40 Gbaud/s compressed baud rate, due to the reasons just mentioned.

Setting the packet size at 64 bits, the cascadability performance of the compressor and decompressor combo was also studied. The results are shown in Fig. 4.33, accompanied with eye diagrams of the differential detection of the output packet after 2, 4 and 6 compression and decompression pairs. The MZI-QDSOA based compressor and decompressor shows much better cascadability than the MZI-SOA based one, since four pairs can be cascaded, against the previous two pairs, for a maximum ECP of 1 dB. One reason of the better performance of the MZI-QDSOA is that the fast gain recovery mechanisms (excluding therefore the wetting layer depletion) are faster than those of the MZI-SOA. Additionally, the power transfer curve is different in the MZI-QDSOA and the amplitude reshaping might be more effective in the MZI-QDSOA than in the MZI-SOA. Moreover, the MZI-SOA introduces chirp, which accumulates over the cascades and further degrades the signal, while the MZI-QDSOA does not.

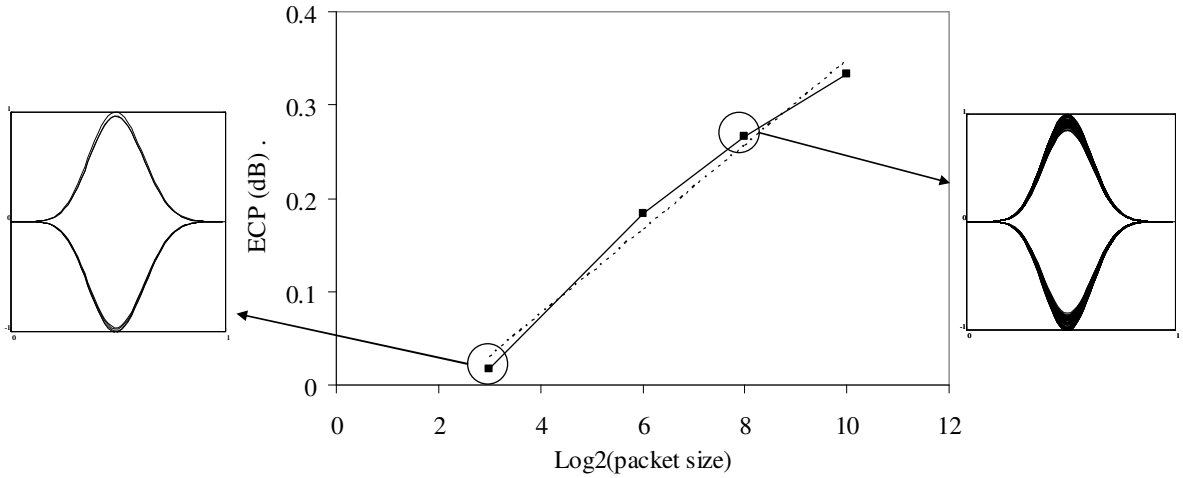

Fig. 4.32 Eye closure penalty (ECP) of the MZI-QDSOA based packet compressor and decompressor pair as a function of the packet size. The full line is a guide for the eyes. The dashed line is a linear fit using the least squares method. Eye diagrams of the differential detection of the decompressed packets are shown for a packet size of 8 bits (left) and 256 bits (right). The horizontal scale is normalized to the bit period and the vertical axis is current (arbitrary units).

The tolerance of the compressor and decompressor pair based on the MZI-QDSOA on the phase mismatches of the ODLs was also investigated and the results are plotted in Fig. 4.34. Because of the phase transparency of the compressor and decompressor architecture, this implementation presents the same tolerance as that of the implementation with MZI-SOA gates. For a maximum ECP of 1 dB, up to 50º of phase mismatch are tolerated in the ODLs.

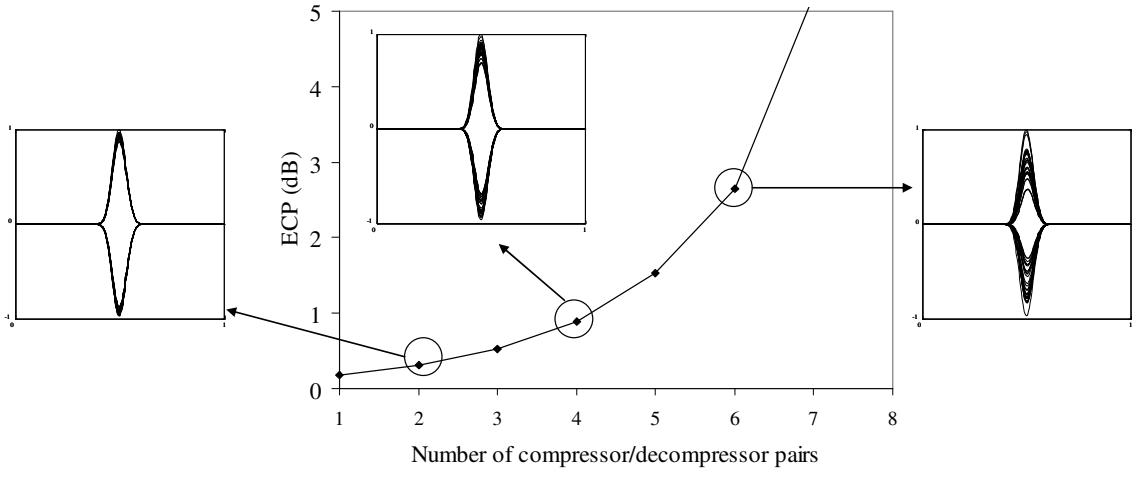

Fig. 4.33 Eye closure penalty (ECP) of the MZI-QDSOA based packet compressor and decompressor as a function of the number of compressor and decompressor pairs. The lines are guides for the eyes only. Eye diagrams of the differential detection of the decompressed packets are shown after 2 pairs (left), 4 pair (inset) and 6 pairs (right). The horizontal scale is normalized to the bit period of the base bit rate and the vertical axis is current (arbitrary units).

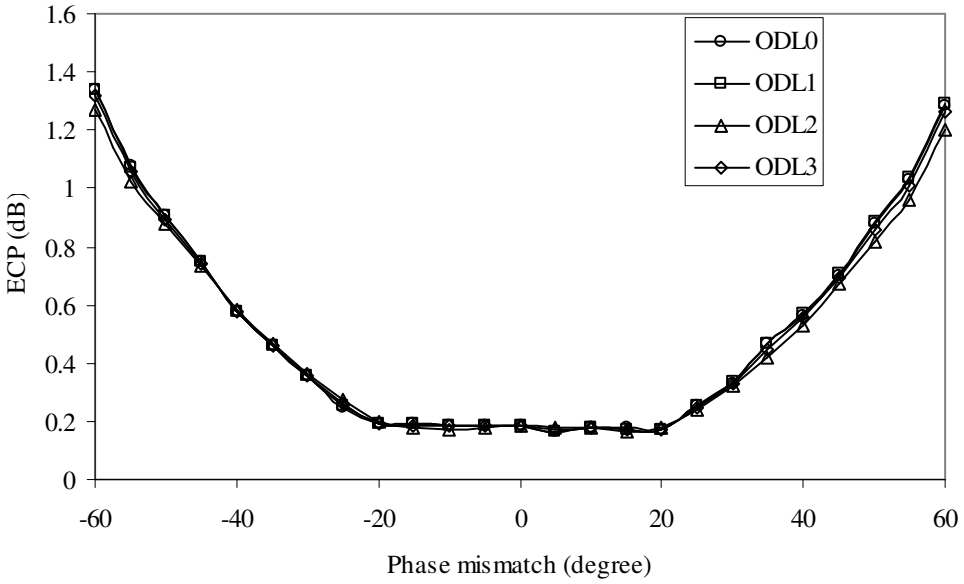

Fig. 4.34 Eye closure penalty (ECP) of the MZI-QDSOA based compressor and decompressor pair, as a function of the phase mismatch of the compressor ODLs.

4.3 Slot interchanging

Time slot interchangers (TSI) have been proposed before based on feed-forward delay lines [21]. That previous work used cross gain modulation in SOAs to convert the wavelength of incoming packets and route them to the appropriate delays. However, wavelength conversion through cross gain modulation is known to have low extinction ratio at the output, which limits the scalability of such technique. More recently, an integrated 2×2 switching matrix was used to build a feedback time slot interchanger [22]. The switching matrix contains current-controlled SOAs that transmit or block each input-output pair. Compared to the feed-forward architecture, the feedback architecture has the advantage of theoretically infinite delay possibility, but, in practice, it is limited by the synchronization in the feedback path. In fact, if a small delay mismatch exists, it will accumulate over successive re-circulations. Moreover, it is expected that with appropriate traffic engineering, a limited number of delay possibilities will be required [23]. Thus, a feed forward time slot interchanger based on wavelength conversion in the MZI-SOA will be presented in this section. In the next chapter, a time slot interchanger based on space switching in the MZI-SOA will also be investigated. The time slot interchanger based on

wavelength conversion in the MZI-SOA is now investigated by simulation and then experimentally, using the first quad-integrated MZI-SOA device ever fabricated.

In the adopted architecture, the MZI-SOA converts the wavelength of an incoming packet to a suitable wavelength. The wavelength converted packet is then delayed by in an appropriate ODL in an ODL bank, according to its wavelength. Fig. 4.35 shows such operation. A single TSI stage has limited delay possibilities, which are the number of available wavelengths (three in the example of Fig. 4.35). In order to obtain a large number of delay possibilities, the same number of lasers as the delay possibilities, or a wide-range tuneable laser, and an ODL bank of the same size must be employed. This might not be practical or even feasible for a large number of wavelengths and the SOA wavelength conversion may be limited for large wavelength differences. Alternatively, cascading several TSI stages can overcome this limitation, and a large TSI structure can be obtained with the capacity of delaying each packet by an increased number of delay possibilities.

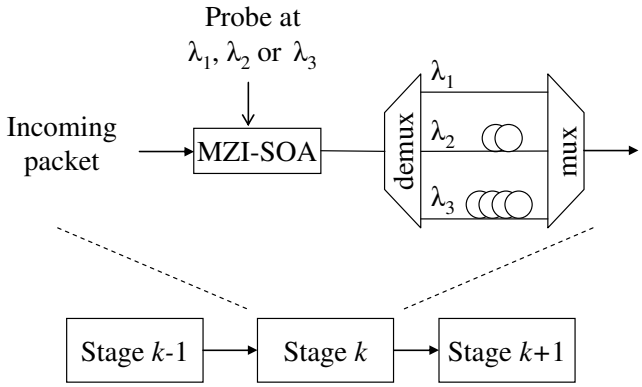

Fig. 4.35 Multi-stage time slot interchanger based on wavelength conversion in the MZI-SOA.

This way, one can avoid using so many different wavelengths, although, at the expense that not only more MZI-SOA gates are required, but also the penalties will accumulate. Thus, it is a compromise between feasibility and acceptable performance penalty. For a given number of timeslots to interchange, the required number of wavelengths and TSI stages is presented in reference [24]. In order to exchange four time slots, three wavelengths and three stages are required. In the forthcoming investigations, the number of wavelengths will be set to three, and the penalty at the output of each cascade will be assessed.

The probe signal, which sets the wavelength of the output packet, is assumed to be properly chosen at the electronic control level, which is not modelled, to ensure the correct delay for each packet.

4.3.1 Simulation results

The TSI operation will be modelled first for a bit rate of 10 Gb/s using the non-differential mode, and then at 40 Gb/s using the differential mode.

The combined response of the multiplexer and demultiplexer filters of the ODL bank is modelled as second order Gaussian filters. For the 10 Gb/s and 40 Gb/s cases, respectively, the combined full width at half maximum of the multiplexer and demultiplexer are 35 GHz and 130 GHz and the wavelength spacings are 50 GHz and 200 GHz. These filter bandwidths are typical values for these multiplexer and demultiplexer wavelength spacings. The TSI output signal contains packets at different wavelengths, according to the desired delay. Hence, in order to assess the performance of all the packets, a narrow optical filter to reject ASE cannot be used at the receiver input. Hence, the OSNR is calculated assuming a rectangular-shaped optical filter at the receiver input, with bandwidth equal to the simulation bandwidth. At 64 samples per bit, the simulation window width is 640 GHz and 2.56 THz for the 10 Gb/s and 40 Gb/s cases, respectively. The OSNR penalty is calculated as the difference of the required OSNR for a BER of 10^{-10} of the signal under analysis and of the signal at the TSI input.

The simulation time span is divided into four slots. Before the first TSI stage, each of the first three slots is occupied by one packet, whereas the last slot is empty. Each slot has the extent of two packets, and the packet is centred in the middle of the slot. The remaining time without data acts as guard bands, although this TSI architecture does not intrinsically require guard bands. The three packets are three different de Bruijn sequences. The delays of the ODLs in each TSI stage are shown in Table 4-2. In the simulation, negative delays are used, so that time just expresses the change of the slots' relative position in the simulation window.

Unless counter-propagating control signals are fed to the MZI-SOA, the wavelengths in the TSI must be adequately planned. At the first TSI stage output, the packets will have wavelengths λ_1, λ_2 and λ_3. However, in the next TSI stage, the wavelengths of the probe are the same as the wavelengths of the control signal, which are

the packets. If the beams are counter-propagating, no interference occurs and probe and control signals can have the same wavelength. However, the counter-propagating configuration is impaired in terms of maximum conversion bit rate. A solution is to allocate different wavelength bands for odd and even TSI stages. If at the second TSI stage the wavelengths of the probe signal to be used are λ_4, λ_5 and λ_6, there is no wavelength collision at the MZI-SOA inputs, and the co-propagating scheme can be used again. This alternative, however, has the disadvantage of requiring more available wavelengths, for example, a tuneable laser source with a larger wavelength range. The simulation will be performed using the co-propagating scheme with alternate wavelength bands between TSI stages.

Table 4-2 Delay of the ODLs in the ODL bank, for each wavelength and TSI stage.

TSI stage	Delay (in units of slot duration)		
	λ_1/λ_4	λ_2/λ_5	λ_3/λ_6
1	-1	0	1
2	-2	0	2
3	-1	0	1
4	-2	0	2

The eye diagrams and oscilloscope traces of the TSI output are presented in Fig. 4.36, for from one up to four TSI stages. Packets are 32 bits long, the bit rate is 10 Gb/s and the data format is NRZ. From the oscilloscope traces, it can be concluded that packets effectively change their relative positions according to the delays (and wavelengths) of Table 4-2. It is clear, however, that the signal is progressively more degraded as the number of stages increases. Accordingly, the OSNR penalty simulation results increase for increasing TSI size, as shown in the curve labelled ‘regular TSI’ of Fig. 4.37. About 0.4 – 0.45 dB of OSNR penalty is introduced per TSI stage. For a maximum OSNR penalty of 1 dB, two TSI stages are allowed.

Each packet at the TSI output has a different wavelength, which might not be suitable for the next processing steps, or, for example, for WDM transmission. Hence, the simulation was repeated but now with an additional MZI-SOA gate at the TSI output to convert the wavelength of all packets to the same wavelength. This set of results was also plotted in Fig. 4.37. It shows that the OSNR penalty of the final MZI-SOA wavelength conversion stage approximately matches that of an additional TSI stage. In fact, both

processing units, the TSI stage and the wavelength conversion, are similar except for the different wavelengths and filter structure of the TSI stage. Thus, the penalties are similar. Consequently, for a given maximum allowed OSNR penalty, if a wavelength conversion stage is required at the TSI output, one TSI stage must be sacrificed to keep the same penalty.

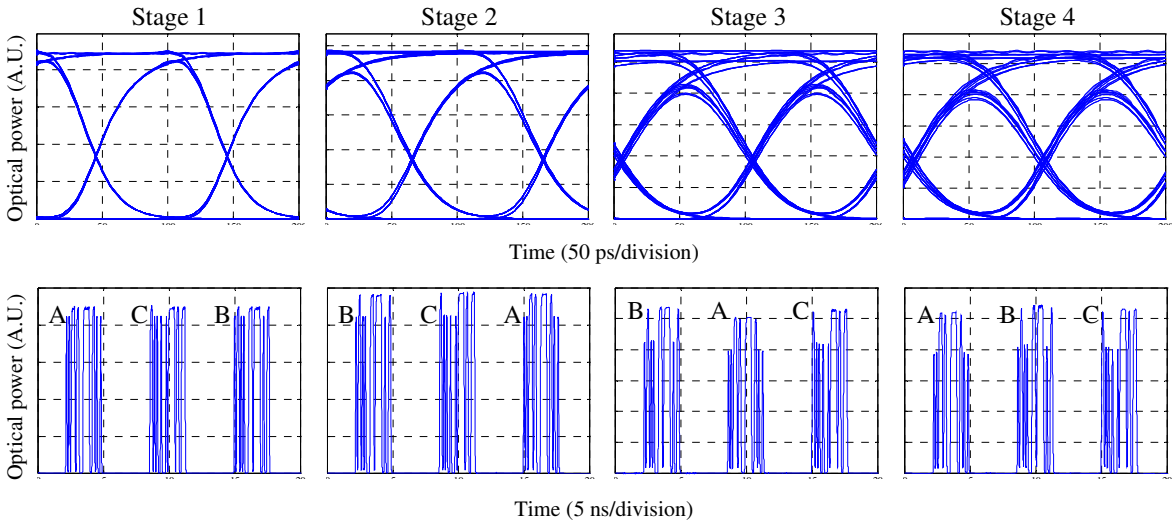

Fig. 4.36 Eye diagram (top row) and oscilloscope traces (bottom row) of the output of the 10 Gb/s TSI stages 1 to 4. A, B and C denote the three different packets being reordered.

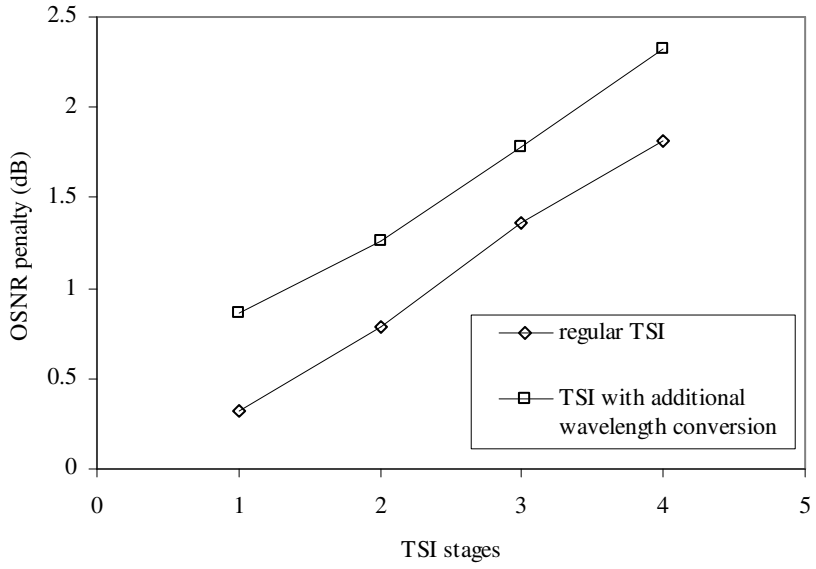

Fig. 4.37 OSNR penalty of the TSI output as a function of the number of the TSI stages, with and without an additional wavelength conversion stage, at 10 Gb/s. The lines connecting the data points are guides for the eyes.

The last results were obtained for quite small packets of 32 bits and so the simulation was performed for larger packets. The results are shown in Fig. 4.38, for packet sizes of 32 to 512 bits. The penalty is approximately constant for all the investigated packet sizes. The maximum penalty difference is about 0.05 dB between the 32 and the 512 bits packets, for the fourth TSI stage.

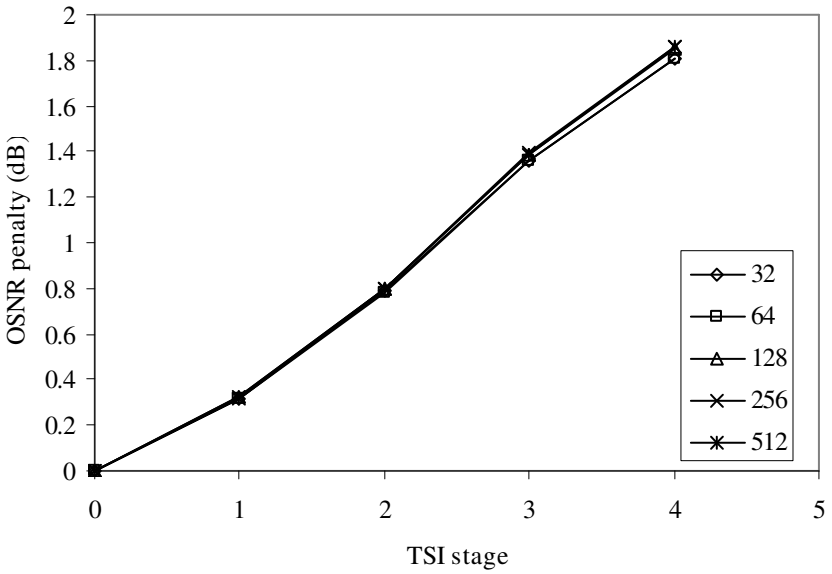

Fig. 4.38 OSNR penalty of the TSI output as a function of the number of TSI stages, for packet lengths from 32 to 512 bits. The bit rate is 10 Gb/s.

The OSNR penalty as a function of the TSI and packet size was also studied for 40 Gb/s 50% duty cycle RZ packets in the push-pull configuration, and the results are plotted in Fig. 4.39. The penalty at 40 Gb/s is about 1 – 1.1 dB per TSI stage, which is more than the double at 10 Gb/s, due to the larger bit rate and more influential gain compression recovery time. The eye diagrams and oscilloscope traces are shown in Fig. 4.40, which corroborate the numerical results of the OSNR penalty. The ‘0’ level increases at each TSI stage, corresponding to extinction ratio degradation, and the ‘1’ level becomes broader due to the gain recovery time of the SOA. Particularly, consecutive ‘1’s are the worst pattern, with low optical level at the bit centre and the RZ characteristic of null power between bits is almost lost.

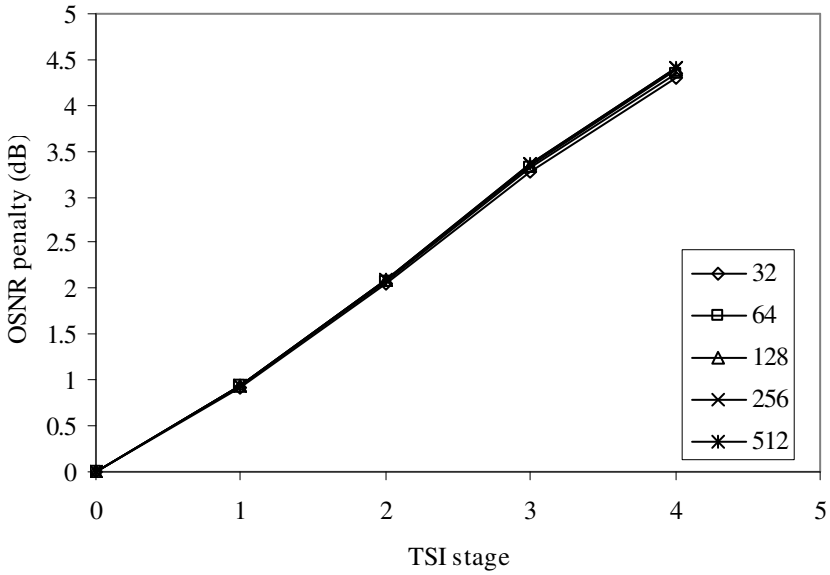

Fig. 4.39 OSNR penalty of the TSI output as a function of the number of TSI stages, for packet lengths from 32 to 512 bits. The bit rate is 40 Gb/s.

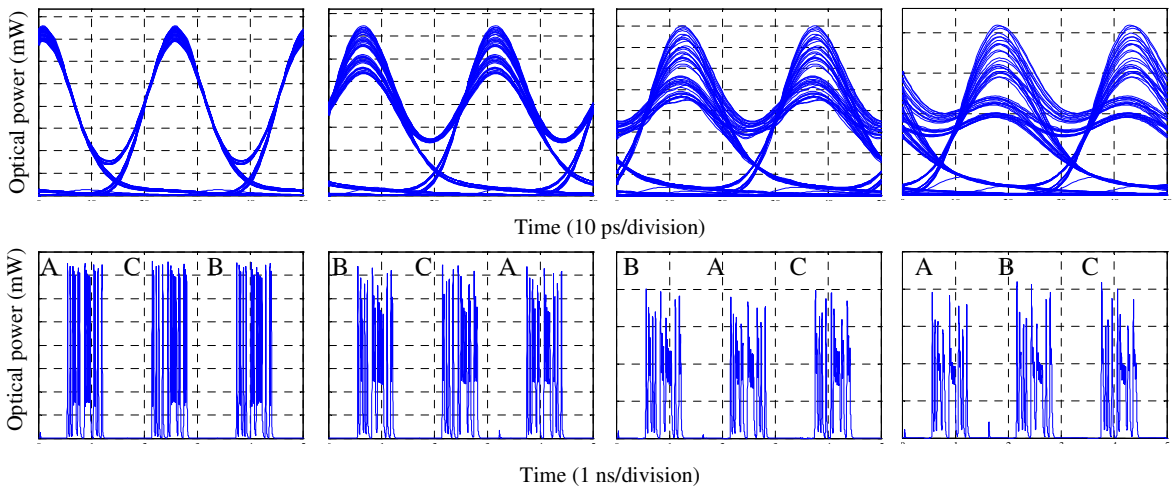

Fig. 4.40 Eye diagram (top row) and oscilloscope traces (bottom row) of the output of the 40 Gb/s TSI stages 1 to 4. A, B and C denote the three different packets being reordered.

4.3.2 Experimental results

The time slot interchanger architecture was experimentally evaluated in a world-first quad integrated MZI-SOA device. The quad device contains two twin MZI-SOA chips mounted on a motherboard, thus totalling four devices in the same package. A picture of the device is presented in Fig. 4.41. Although these devices offer increased compactness

relatively to the twin device, cooling requirements are more stringent, and thermal crosstalk is more significant. Thus, the Peltier cell and heat dissipation becomes more critical in this device, which justifies the oversized heatsink used in the experiment. The package dimensions of the quad MZI-SOA are 90×32×12 mm^3, while those of the twin MZI-SOA are 65×30×14 mm^3.

In the experiment, 10 Gb/s NRZ packets were used and hence the counter-propagating control scheme could be used, due to the relaxed gain recovery requirements. This enabled to reduce the number of laser sources required for the experiment. A schematic of the three stages TSI experimental setup is presented in Fig. 4.42. The wavelengths of the CW sources and multiplexer and demultiplexer filters are 1546.6 nm, 1548.2 nm and 1559.8 nm, whereas the wavelength of the incoming packet signal is 1553 nm. The binary sequence loaded to the sequence generator and error analyser is composed of four 40 bits long slots, thus totalling 160 bits. Each of the first three slots contains a data packet of 25 bits, and 15 empty bits behaving as a guard band. The last slot is empty. The relative delays of the ODL bank are the same as in the simulation, as given in Table 4-2. Thus, packet reordering at each stage is performed similarly to the simulation. To illustrate the packet reordering, the oscilloscope traces of the TSI input signal and outputs at each TSI stage are shown in Fig. 4.43.

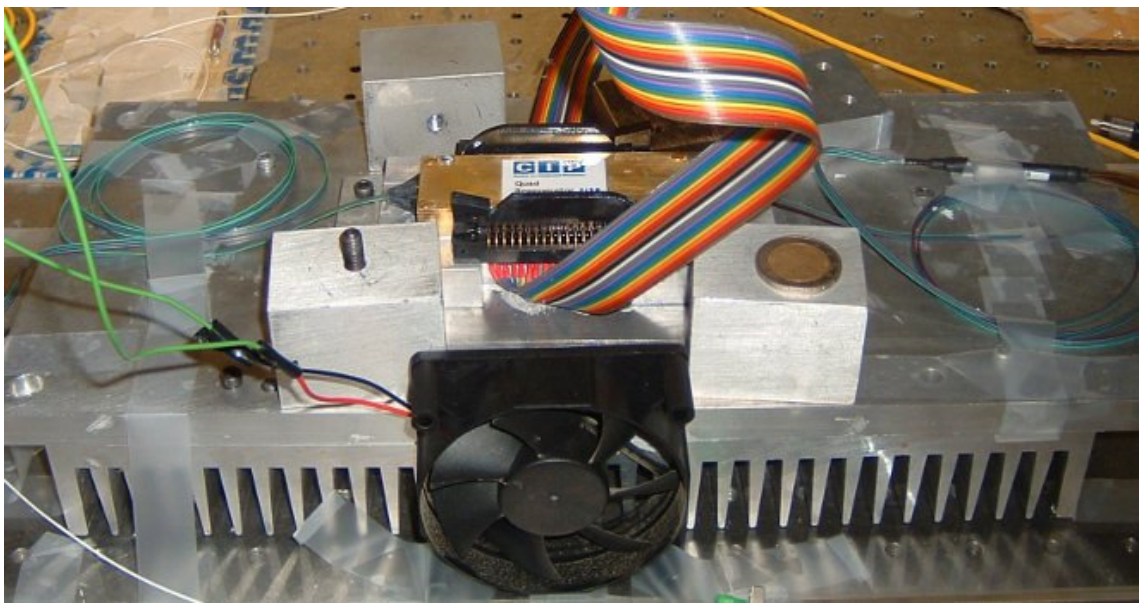

Fig. 4.41 Picture of integrated hybrid quad MZI-SOA. A 2 Euro coin is also shown for size comparison.

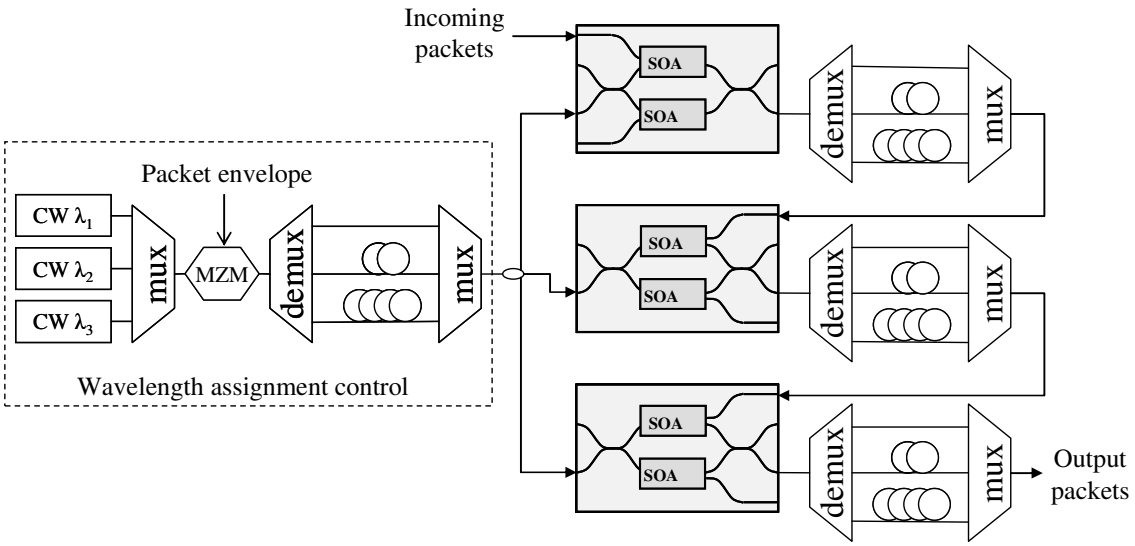

Fig. 4.42 Experimental setup of the three stages TSI.

In order to measure the OSNR penalty, a flat spectrum ASE source with very large spectral bandwidth (in excess of 13 nm) and with high output power would be required to cause bit errors. Such equipment was not available and therefore the performance was experimentally assessed by measuring the power penalty instead of the OSNR penalty. The power penalty is the difference between the required optical power at the receiver input to attain a BER of 10^{-10} of the signal under study and the reference, which is the TSI input signal. The BER results are shown in Fig. 4.44, as a function of the receiver input power. No error floors are observed for any of the data sets. Fig. 4.45 depicts the power penalties measured in the experiment and also simulation results for the various TSI stages. The simulation results correspond to the ones presented in the previous section, but instead of calculating an OSNR penalty, a power penalty was calculated, to enable comparison to the experiment. The agreement between the experimental results and those from the simulation is not satisfactory at all. The experimental penalties are about 3.5 – 4.6 times larger than the simulated penalties. This discrepancy is attributed to sub-optimum operation of the MZI-SOA wavelength conversion in the experiment. Posterior improved experimental results [24] have shown smaller experimental penalties of 0.2, 0.78 and 1.43 dB which compare well to the simulation results of 0.30, 0.77 and 1.35 dB, for the first, second and third TSI stages, respectively. The penalty improvements were mainly obtained optimising the polarization stability of the probe signals. Additionally, a holding beam was also employed to reduce the ASE and improve the SOA recovery speed.

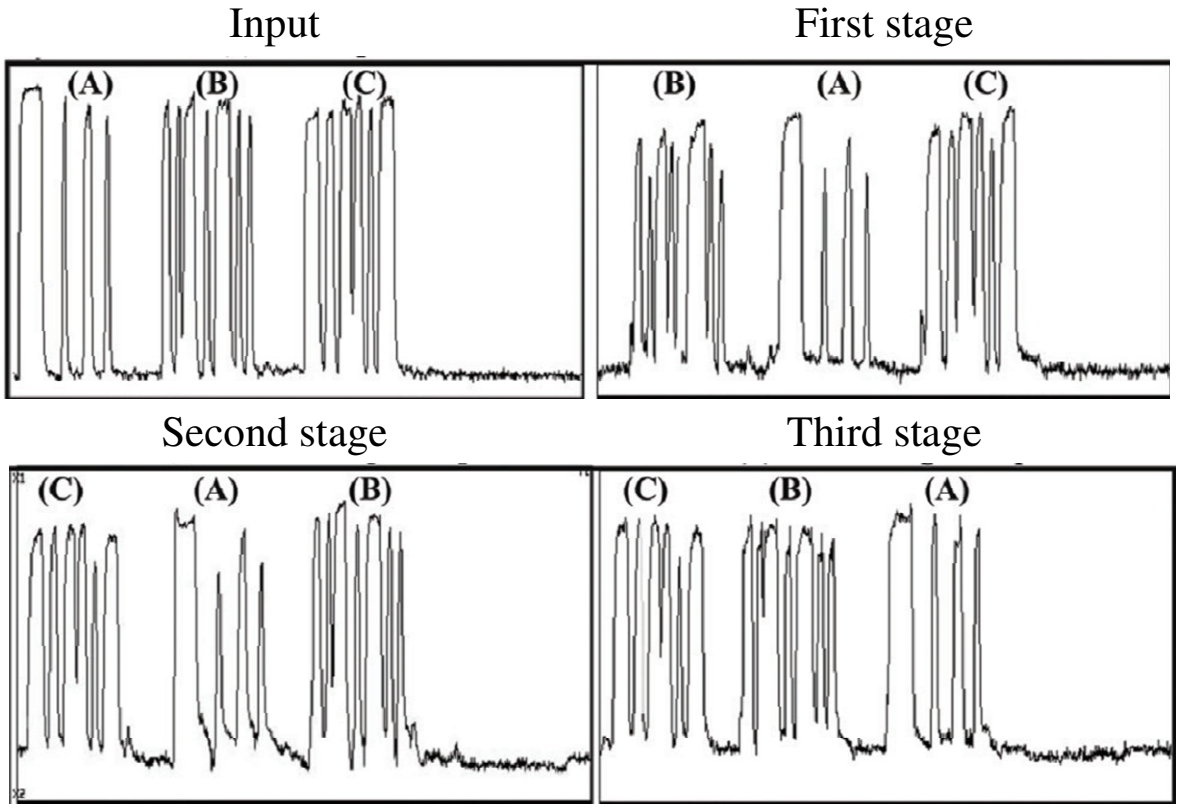

Fig. 4.43 Experimental oscilloscope traces of the TSI input and outputs at each stage. The horizontal axis is time with a full span of 160 ns, and the vertical axis is current (arbitrary units).

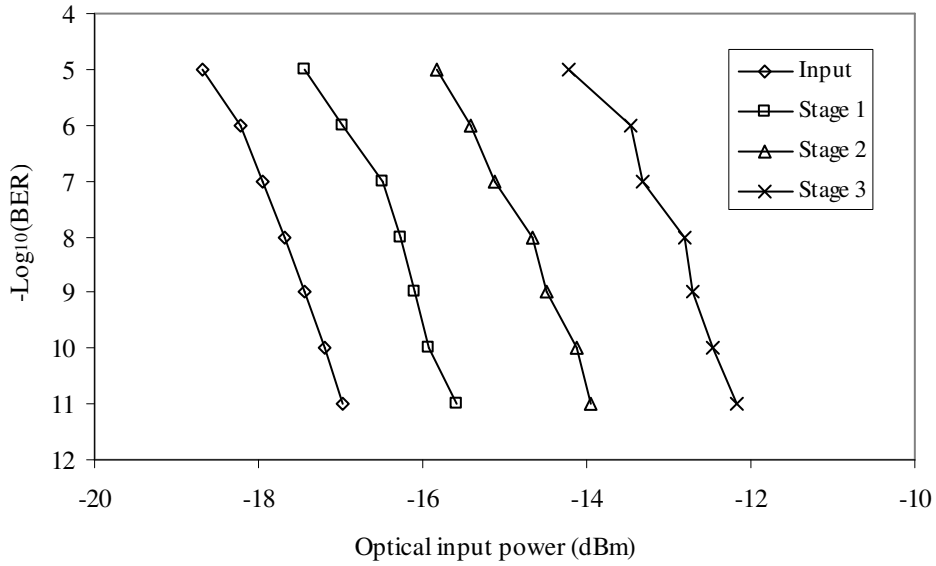

Fig. 4.44 Experimental BER results of the TSI output at each stage, as a function of the received power. The lines connecting the data points are guides for the eyes.

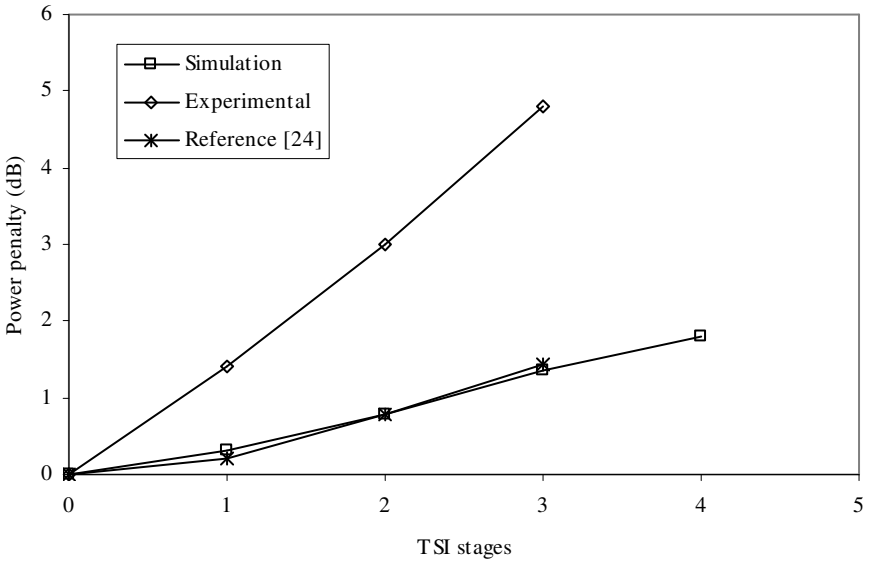

Fig. 4.45 Power penalty of the TSI as a function of the number of stages obtained experimentally and by simulation. The lines connecting the data points are guides for the eyes.

Comparing to the scalability studies of the previous section which investigated the optical packet compressor and decompressor with the TSI scalability, the latter shows better performance. Since each packet compressor and decompressor is composed of a significant larger number of MZI-SOA gates, this result is expectable. It is also for this reason that penalty introduced by the compressor and decompressor is super-linear on the number of cascaded pairs, whereas the TSI shows approximately linear dependence.

4.4 Conclusions

This chapter has presented three optical processing functions that were performed using a set of MZI-SOA gates. These functionalities have in common bit or packet displacement in time and arise in the context of next generation optical networks, either circuit or packet switched.

The first functionality was WDM to OTDM conversion. A number of WDM channels are converted in the MZI-SOA to the same wavelength and to shorter width pulses. Then, the MZI-SOA outputs are time interleaved to produce an OTDM signal. Experimental and simulation evidence has shown that pulse broadening in the MZI-SOA causes inter-pulse crosstalk which prevented error free conversion of three WDM 40 Gb/s

to one 120 Gb/s OTDM channel. This effect was analysed through simulation and requirements on the pulse widths were established for the NRZ, CS-RZ and RZ input modulation formats.

Then, to serve the demands of OPS networks, an architecture and implementation with MZI-SOA gates was proposed to perform compression and decompression of packets by all-optical means. The operation concept is based on producing replicas of the original packet at appropriate delays, choosing only the desired output symbols, and discarding the remaining. The presented architecture is transparent to the phase of the incoming symbols and hence is adequate for multi-level phase modulated packets. The performance of the packet compressor and decompressor was investigated for both BPSK and QPSK packets by simulation. An implementation with MZI-SOAs was studied for a base baud rate of 10 Gbaud/s and compressed baud rates of 20 and 40 Gbaud/s. Again, the pulse width requirements of the input signal were investigated and a minimum value was established to be around 50% of the symbol period before the penalty rises steeply. Regarding the impact of the packet size, it was found that OSNR penalty is linear on the logarithm of the packet size. The OSNR penalty for a compressed baud rate of 20 Gbaud/s and 2^{10} symbols packets was 0.1 and 0.3 dB for BPSK and QPSK formats, respectively. For the same packet size, but a compressed baud rate of 40 Gbaud/s, the penalties rise to 0.2 and 0.4 dB for BPSK and QPSK formats, respectively. The cascadability of the packet compressor and decompressor combo was then studied. Only two compressor and decompressor pairs are accepted for an OSNR penalty below 1 dB. The rather limited cascadability is due to the accumulation of impairments from the insufficient SOA response time in the several MZI-SOA gates that compose the packet compressor and decompressor. In a real device, the ODLs will have phase and delay mismatches relatively to the ideal values and thus requirements on these quantities were evaluated. As a rule of thumb, the maximum delay deviation in the ODLs should be 10% of the bit period, while the phase deviation should be below 50º and 17º for the BPSK and QPSK formats, respectively.

Results with the same architecture, but with MZI-QDSOAs instead of MZI-SOAs were also obtained through simulation. The MZI-QDSOAs allows optical processing at higher bit rates and although the results were obtained at a base bit rate of 40 Gb/s and a compressed bit rate of 160 Gb/s, the same qualitative conclusions as for the MZI-SOA hold true. The OSNR penalty for the compression and decompression is again

approximately linear on the logarithm of the packet size, and for a BPSK 2^{10} bits packet, the penalty is 0.35 dB. Although this penalty is larger than for the corresponding case of the MZI-SOA, the packet compressor and decompressor based on the MZI-QDSOA shows better cascadability. Four pairs can be cascaded for an OSNR penalty below 1 dB.

Finally, a feed forward wavelength-driven time slot interchanger based on wavelength conversion on the MZI-SOA was investigated. The performance of such system was simulated with three wavelengths per stage and at 10 Gb/s and 40 Gb/s using the non-differential and differential scheme, respectively. It was observed that the simulated penalty depended linearly on the number of cascaded stages. For a TSI with three stages, the simulated OSNR penalties are 1.4 dB and 4.5 dB for 10 Gb/s and 40 Gb/s, respectively. The higher bit rate operation suffered from increased intersymbolic effects due to the limited SOA gain recovery speed. If an additional MZI-SOA is required to convert the wavelength of all packets to the same wavelength, the arising penalty is similar to an additional TSI stage.

The TSI was also implemented experimentally using a world-first integrated quad MZI-SOA. No error floors were observed, for a three stages MZI-SOA, and the measured power penalty was 4.8 dB. The simulation has predicted a much lower penalty of 1.35 dB, which was found to be comparable to a posterior experimental assessment of the three stages TSI where a penalty of 1.45 dB was measured.

Overall, the MZI-SOA performance has been studied for three different applications for time domain processing. The capability to perform such varied processing functions attests the MZI-SOA versatility, but the cascadability of these devices, depending on the application, can be inadequate, requiring intermediate regeneration stages.

4.5 References

[1] "P802.3ba 40Gb/s and 100Gb/s Ethernet Task Force, Institute of Electrical and Electronics Engineers, available online at http://www.ieee802.org/3/ba/."

[2] E. Varvarigos, "The "packing" and the "scheduling packet" switch architectures for almost all-optical lossless networks," *IEEE/OSA Journal of Lightwave Technology*, vol. 16, no. 10, pp. 1757–1767, 1998.

[3] R. Morais, R. Meleiro, P. Monteiro, and P. Marques, "OTDM-to-WDM conversion based on wavelength conversion and time gating in a single optical gate," *in Proc. Optical Fiber Communication Conference (OFC)*, vol. OTuD5, 2008.

[4] Y. Awaji, T. Miyazaki, and F. Kubota, "160/4x40 Gb/s OTDM/WDM conversion using FWM fibre," *in Proc. European Conference on Optical Communication (ECOC)*, vol. We1.5.6, 2004.

[5] P. Almeida, P. Petropoulos, F. Parmigiani, M. Ibsen, and D. Richardson, "OTDM Add-Drop Multiplexer Based on Time-Frequency Signal Processing," *IEEE/OSA Journal of Lightwave Technology*, vol. 24, no. 7, pp. 2720–2732, 2006.

[6] M. Hayashi, H. Tanaka, K. Ohara, T. Otani, and M. Suzuki, "OTDM transmitter using WDM-TDM conversion with an electroabsorption wavelength converter," *IEEE/OSA Journal of Lightwave Technology*, vol. 20, no. 2, pp. 236–242, 2002.

[7] T. Ohara, H. Takara, I. Shake, K. Mori, K. Sato, S. Kawanishi, S. Mino, T. Yamada, M. Ishii, I. Ogawa, *et al.*, "160-Gb/s OTDM transmission using integrated all-optical MUX/DEMUX with all-channel modulation and demultiplexing," *IEEE Photonics Technology Letters*, vol. 16, no. 2, pp. 650–652, 2004.

[8] P. Toliver, K. Deng, I. Glesk, and P. Prucnal, "Simultaneous optical compression and decompression of 100-Gb/s OTDM packets using a single bidirectional optical delay line lattice," *IEEE Photonics Technology Letters*, vol. 11, no. 9, pp. 1183–1185, 1999.

[9] P. Almeida, P. Petropoulos, B. Thomsen, M. Ibsen, and D. Richardson, "All-optical packet compression based on time-to-wavelength conversion," *IEEE Photonics Technology Letters*, vol. 16, no. 7, pp. 1688–1690, 2004.

[10] W. Hui, W. Jian, and L. Jintong, "Packet compression decompression for 100 Gbit/s OTDM networks," *Journal of Optical Communications*, vol. 28, pp. 255–259, 2007.

[11] P. Winzer and R. Essiambre, "Advanced optical modulation formats," *Proceedings of the IEEE*, vol. 94, no. 5, pp. 952–985, 2006.

[12] V. Roncin, A. O'Hare, S. Lobo, E. Jacquette, L. Bramerie, P. Rochard, Q. Le, M. Gay, J. Simon, A. Shen, *et al.*, "Multi-Data-Rate System Performance of a 40-GHz All-Optical Clock Recovery Based on a Quantum-Dot Fabry–Pérot Laser," *IEEE Photonics Technology Letters*, vol. 19, no. 19, pp. 1409–1411, 2007.

[13] B. Sartorius, "All-optical clock recovery for 3R optical regeneration," *in Proc. Optical Fiber Communication Conference (OFC)*, p. MG7, 2001.

[14] J. Pina, H. J. A. da Silva, P. N. Monteiro, J. Wang, W. Freude, and J. Leuthold, "Cross-Gain Modulation-based 2R Regenerator Using Quantum-Dot Semiconductor Optical Amplifiers at 160 Gbit/s," *in Proc. International Conference on Transparent Optical Networks (ICTON)*, p. Tu.A1.8, 2007.

[15] T. Akiyama, N. Hatori, Y. Nakata, H. Ebe, and M. Sugawara, "Wavelength Conversion Based on Ultrafast (< 3 ps) Cross-Gain Modulation in Quantum-Dot Optical Amplifiers," *in Proc. European Conference on Optical Communication (ECOC)*, vol. 2, 2002.

[16] G. Contestabile, A. Maruta, S. Sekiguchi, K. M. M. Sugawara, and K. Kitayama, "160 Gb/s Cross Gain Modulation in Quantum Dot SOA at 1550 nm," *in Proc. Optical Fiber Communication Conference (OFC)*, p. PD1.4, 2009.

[17] M. Spyropoulou, S. Sygletos, and I. Tomkos, "Simulation of Multiwavelength Regeneration Based on QD Semiconductor Optical Amplifiers," *IEEE Photonics Technology Letters*, vol. 119, no. 20, pp. 1577–1579, 2007.

[18] J. Wang, Y. Jiao, R. Bonk, W. Freude, and J. Leuthold, "Regenerative Properties of Bulk and Quantum Dot SOA Based All-Optical Mach-Zehnder Interferometer DPSK Wavelength Converters," *in Proc. Photonics in Switching, Herakleion, Greece*, vol. O4.5, 2006.

[19] T. Berg, S. Bischoff, I. Magnusdottir, and J. Mork, "Ultrafast gain recovery and modulation limitations in self-assembled quantum-dot devices," *IEEE Photonics Technology Letters*, vol. 13, no. 6, pp. 541–543, 2001.

[20] T. Berg, J. Moerk, and J. Hvam, "Gain dynamics and saturation in semiconductor quantum dot amplifiers," *New Journal of Physics*, vol. 6, no. 1, p. 178, 2004.

[21] Z. Pan, J. Cao, Y. Bansal, V. Tsui, S. Fong, Y. Zhang, J. Taylor, H. Lee, M. Jeon, V. Akella, S. Yoo, K. Okamoto, and S. Kamei, "All-optical programmable time-slot-interchanger using optical-label switching with tunable wavelength conversion and n by n arrayed waveguide grating routers," *in Proc. Optical Fiber Communication Conference (OFC)*, pp. 267–268, Mar 2002.

[22] E. Burmeister and J. Bowers, "Integrated gate matrix switch for optical packet buffering," *IEEE Photonics Technology Letters*, vol. 18, no. 1/4, p. 103, 2006.

[23] N. Beheshti, Y. Ganjali, R. Rajaduray, D. Blumenthal, and N. McKeown, "Buffer sizing in all-optical packet switches," *in Proc. Optical Fiber Communication Conference (OFC)*, p. OThF8, 2006.

[24] O. Zouraraki, K. Yiannopoulos, P. Zakynthinos, D. Petrantonakis, E. Varvarigos, A. Poustie, G. Maxwell, and H. Avramopoulos, "Implementation of an All-Optical Time-Slot-Interchanger Architecture," *IEEE Photonics Technology Letters*, vol. 19, no. 17, pp. 1307–1309, 2007.

Chapter 5 Optical crosstalk modelling and its effects in optical WDM networks

Crosstalk is a major impairment in optical networks causing large power penalties and bit error rate (BER) floors [1]. It is due to reflections from splices or connectors, or to other signals leaking from optical cross-connects, add-drop multiplexers, or wavelength routers [1]-[4] and interfering with the signal.

The optical amplifier is a key component of modern optical networks, which amplifies the optical signals while generating amplified spontaneous emission (ASE) noise. At the receiver, the signal beats with the ASE noise thereby further degrading the BER.

Optical networks employing both crosstalk inducing components [1] and optical amplifiers, or SOA based switches [5], [6] have their performance impaired by both crosstalk and ASE. Particularly, sub-systems that employ MZI-SOA performing as space switches will have their performance impaired by these effects. One example is the time slot interchanger based on space switching, which can have its scalability limited by the accumulating crosstalk. Simple models for estimating the BER due to both crosstalk and ASE are therefore extremely useful.

In this chapter, in section 5.1, the calculation method that will be used throughout the chapter to draw conclusions in the crosstalk impact on network performance is presented. The method is based on the Modified Chernoff Bound (MCB) and it will be used to calculate the BER in the presence of crosstalk considering a signal distorted by narrow optical and electrical filters. It presents an extension of previous literature to include the effects of the distorted signals on the crosstalk penalties. The results of the MCB method are compared to semi-analytical and Monte Carlo simulation and to experimental results.

Afterwards, in section 5.2, the crosstalk induced penalty is evaluated by the MCB method for an optical system with narrow optical filtering, detuned optical filtering, and narrow electrical filtering. It is shown that the crosstalk penalty can be higher than expected for such conditions. A practical network scenario is considered, where cascaded

filtering is considered and it is demonstrated that the maximum number of cascaded filters is reduced when the combined crosstalk and filtering penalty is taken into account, when compared to the sum of the expected crosstalk penalty and the filtering penalty.

Section 5.3 is dedicated to the analysis of a time slot interchanger based on MZI-SOA space switches. In each TSI stage crosstalk and ASE accumulate, which limit the maximum number of TSI stages. An improved TSI structure is proposed, that alleviates the crosstalk requirements of the individual space switch.

In section 5.4 of this chapter, the transmission effects as chromatic dispersion and self phase modulation are taken into account in the crosstalk signal. It is observed that when the crosstalk signal contains strong over-shoots from self-phase modulation, the crosstalk penalty is higher than expected.

Finally, conclusions about this topic are drawn in section 5.5.

5.1 BER calculation method for crosstalk impaired networks with intersymbolic effects

A number of techniques exist for evaluating the BER in an optical network impaired by crosstalk (see [7] for an extensive list of references). The simplest techniques assume that the crosstalk beatings have Gaussian statistics [1]. Whilst this approach is analytically tractable, it does not give accurate results when the number of interfering crosstalk channels is small [1], [8]-[11]. Alternative, more accurate techniques, like the Gram-Charlier series approximation [12], or the Gaussian Quadrature Rule, [13] require a heavy computational effort. For estimating the effects of crosstalk, the Modified Chernoff Bound (MCB) approximation [14] stands out for its computational simplicity, while providing reasonably accurate BER uppers bounds [10], [13]. Additionally, a considerable number of methods exist for calculating the BER due to ASE noise. The simplest assume a Gaussian approximation [15], [16], whereas the most complex use more accurate noise statistics [17]-[19]. The calculation method described in [16], which has been already used in the preceding chapters, has proven to be accurate, while modelling arbitrary optical and electrical filter shapes [16], [20], [21].

Analytical models were also developed for calculating the BER of signals impaired by both ASE and crosstalk. An all Gaussian approximation for both crosstalk and ASE has

been used [2], which again does not yield accurate results when the number of crosstalk channels is small [1]. More accurate methods of calculation resorted to numerical averaging of the crosstalk optical carrier phases, while dealing analytically with the ASE using a Gaussian approximation [22], [23]. However, the computational effort required by this method grows exponentially with the number of crosstalk channels, due to a series of time consuming numerical integrations. Other alternative methods have derived a Moment Generating Function (MGF) for the received signal in the presence of ASE, and used it together with one [24], infinite [25], and even an arbitrary number [26] of crosstalk interfering channels MGFs. However, this ASE-ASE and ASE-signal beatings MGF is only valid for both a rectangular optical filter with a bandwidth multiple of the signal bit rate, and an integrate-and-dump electrical filter. A more elaborate MGF could also be used for arbitrary optical and electrical filter shapes [18]. Although accurate, this method is computationally expensive and time consuming.

Despite all the above efforts there is arguably still a need for a method of calculation which is accurate and does not require lengthy calculations. An accurate and computationally simple method, for calculating the BER of a received signal impaired by both crosstalk and ASE, with arbitrarily shaped optical and electrical filters will now be described. The tractability of this approach is ensured by neglecting the contribution of the second order magnitude crosstalk-ASE beatings, without compromising the accuracy of the results. The omission of the crosstalk-ASE beatings terms enables both handling the crosstalk-signal beating terms with adequate accuracy, and modelling the signal-ASE beatings separately, assuming a Gaussian approximation which has been experimentally shown to give accurate results [27]. The separate treatment of the noise beating terms also enables capturing the effect of optical and electrical filters with arbitrary shapes. Conversely, simulation of the optical signal through the system under study provides the best signal description. Thus, a quick signal simulation will be done to extract signal data, which is then fed to the BER calculation method.

In the next sub-section (5.1.1) it will be shown that this simplification leads to an analytical MGF suitable for applying the MCB, and provides a method for calculating the BER in the presence of both crosstalk and ASE, which is both accurate and requires little computational effort, when compared with other extant methods. In the sub-section 5.1.2, the results obtained with this method are both discussed and compared to the results

obtained with semi-analytical and Monte Carlo simulation methods, and also to experimental results, demonstrating the accuracy of the method.

5.1.1 Theory

The studied system model is shown in Fig. 5.1. The receiver consists of an optical band-pass filter and a square law detector, followed by an electrical filter with an arbitrary shape. The current is then fed to a decision circuit.

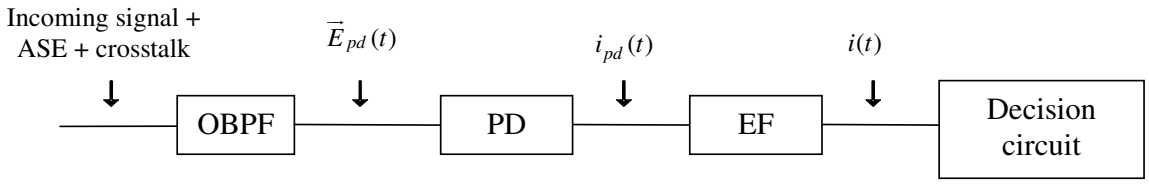

Fig. 5.1 Receiver schematics: optical band pass filter (OBPF); square law photodetector (PD); electrical filter (EF).

The electrical field of the optical signal at the photodetector input can be, generally, given by

$$\vec{E}_{pd}(t) = h_o(t) \otimes \left\{ \vec{E}_s(t) + \sum_{k=1}^{N} \vec{E}_k(t) + \vec{n}_{in}(t) \right\} \tag{5.1}$$

where $\vec{E}_s(t)$ and $\vec{E}_k(t)$ represent the electric field of the signal and of the k^{th} crosstalk interferer, respectively, N is the number of crosstalk channels, and $\vec{n}_{in}(t)$ represents the incoming ASE electric field. In the expression (5.1), $h_o(t)$ is the impulse response of the optical filter. For the time being, it is assumed that the optical filter bandwidth is large enough to only filter the ASE noise without affecting the signal and crosstalk pulse shapes. In this case, the optical field at the photodetector input can be given by

$$\vec{E}_{pd}(t) = \vec{E}_s(t) + \sum_{k=1}^{N} \vec{E}_k(t) + \vec{n}(t) \tag{5.2}$$

where $\vec{n}(t)$ denotes the optically filtered ASE electric field. Assuming unitary photodetector responsivity, the detector current is

$$i_{pd}(t) = \left| \vec{E}_{pd}(t) \right|^2 + n_{el}(t) = \vec{E}_{pd}(t) \cdot \vec{E^*}_{pd}(t) + n_{el}(t) \tag{5.3}$$

where $n_{el}(t)$ is the post-detection generated electrical Gaussian noise. The electric field of the signal and the crosstalk can be given, respectively, by

$$\vec{E}_s = \vec{p}_s A_s(t)\exp\left(j\omega_s t + j\varphi_s(t)\right) \tag{5.4}$$

$$\vec{E}_k = \vec{p}_k A_k(t)\exp\left(j\omega_k t + j\varphi_k(t)\right) \tag{5.5}$$

where $A_s(t)$ and $A_k(t)$, $\phi_s(t)$ and $\phi_k(t)$, $\vec{p}_s$ and $\vec{p}_k$, and ω_s and ω_k are the signal and crosstalk field envelope amplitudes, phases, polarisations, and optical frequencies, respectively. The electrical filter output current can be given by $i(t) = i_{pd}(t) \otimes h_e(t)$ where $h_e(t)$ is the electric filter impulse response. Hence, the received electrical current can be written in the following way:

$$i(t) = \left\{ A_s{}^2 + \sum_{k=1}^{N} A_k{}^2 + i_{s-x} + i_{x-x} + i_{s-ASE} + i_{x-ASE} + \left|\vec{n}\right|^2 + n_{el} \right\} \otimes h_e(t) \tag{5.6}$$

where

$$i_{s-x}(t) = 2\sum_{k=1}^{N} \vec{p}_s \cdot \vec{p}_k A_s A_k \cos\left(\Delta\theta_{sk}\right) \tag{5.7}$$

$$i_{x-x}(t) = 2\sum_{k=1}^{N} \sum_{l>k}^{N} \vec{p}_k \cdot \vec{p}_l A_k A_l \cos\left((\omega_k - \omega_l)t + \phi_k - \phi_l\right) \tag{5.8}$$

$$i_{s-ASE}(t) = \vec{E}_s \cdot \vec{n}^* + c.c. \tag{5.9}$$

$$i_{x-ASE}(t) = \sum_{k=1}^{N} \vec{E}_k \cdot \vec{n}^* + c.c. \tag{5.10}$$

where the explicit time dependence *(t)* has been dropped off to keep the notation simple. The phase difference between signal and crosstalk is denoted by $\Delta\theta_{sk} = \omega_s t - \omega_k t + \phi_s - \phi_k$, and *c.c.* designates the complex conjugate of the preceding term.

The first and second right hand side terms of (5.6) are the signal and crosstalk powers, respectively. The second term represents additive crosstalk power, which is always present regardless of other conditions. Again, for now, it is assumed that the electrical filter bandwidth is large enough not to cause signal or crosstalk pulse distortion, thus simplifying the calculations. However, the effect of noise filtering is modelled by using the appropriate noise variance [16].

The signal-crosstalk beating, $i_{s\text{-}x}(t)$, is responsible for the interferometric noise. The nominal laser frequencies of each crosstalk laser source are assumed to be identical to the signal laser frequency, i.e., in-band crosstalk noise is assumed. In this case, the cosine argument $\Delta\theta_{sk} = \omega_s t - \omega_k t + \phi_s - \phi_k$ in $i_{s\text{-}x}(t)$ simply gives $\Delta\theta_{sk} = \phi_s - \phi_k$, which depends

only on the phase difference between the signal and crosstalk. The magnitude of $i_{s\text{-}x}(t)$ is maximum for co-polarized signal and crosstalk, and vanishes for orthogonal signal and crosstalk polarizations. Here, the signal and crosstalk are assumed to be co-polarized, i.e., $\vec{p}_s.\vec{p}_k = 1$, which is a worst case. Additionally, it is assumed that the signal and crosstalk pulses overlap in time.

The crosstalk-crosstalk beatings, $i_{x\text{-}x}(t)$, represent interferometric noise caused by the various crosstalk channels, and are similar to the signal-crosstalk beatings, as far as the polarization and frequency difference between crosstalk channels are concerned.

The signal-ASE beating, $i_{s\text{-}ASE}(t)$, is usually the dominant noise term in pre-amplified systems. Both the optical and the electrical filters significantly affect the BER, by filtering the ASE noise beatings. The $|n|^2$ term in (5.6) encompasses both the ASE-ASE beating, and the ASE power. The exact signal–ASE and ASE–ASE beatings variances, σ^2_{s-ASE} and $\sigma^2_{ASE-ASE}$, respectively, assuming arbitrary filter shapes and constant signal power, can be given by [16], [28]

$$\sigma^2_{s-ASE} = 2S_{ASE}\left|A_s\right|^2 \int_{-\infty}^{+\infty} \left|H_e(f)\right|^2 \left|H_o(f)\right|^2 df \tag{5.11}$$

$$\sigma^2_{ASE-ASE} = {S_{ASE}}^2 \int_{-\infty}^{+\infty} \left|H_e(f)\right|^2 \left[\left|H_o(f)\right|^2 * \left|H_e(f)\right|^2\right] df \tag{5.12}$$

where $H_e(f)$ and $H_o(f)$ are the electric and optical filters frequency responses, respectively, and S_{ASE} is the ASE noise spectral power density. This approach enables modelling arbitrary filter shapes with accurate results [16], [20], [21].

Finally, n_{el} in (5.6) represents all the electrical noise generated after photodetection, and is assumed to be Gaussian distributed. Its variance after electrical filtering is given by ${\sigma_{el}}^2$.

When both the crosstalk and ASE noise powers are much smaller than the signal power, both the crosstalk-crosstalk beatings $i_{x\text{-}x}(t)$, and the crosstalk-ASE beatings $i_{x\text{-}ASE}(t)$, are only of a second order magnitude compared to the other first order beating terms, and, hence, can be safely neglected without compromising the accuracy, as will be verified. With these simplifications, the electric current can be given by

$$i(t) = {A_s}^2 + \sum_{k=1}^{N} {A_k}^2 + 2\sum_{k=1}^{N} A_s A_k \cos\left(\phi_s - \phi_k\right) + \left(\vec{E}_s.\overrightarrow{n^*} + c.c. + \left|\vec{n}\right|^2 + n_{el}\right) \otimes h_e(t) \tag{5.13}$$

.

Neglecting the crosstalk-ASE beatings, results in a current, *i(t)*, where the remaining crosstalk and ASE beating terms are all statistically independent. Therefore, the moment generating function (MGF) of the sum of independent current terms can be given by the product of the MGFs of the signal-crosstalk beatings and the MGF of the signal-ASE beatings [29].

The assumption that the phases ϕ_k are uniformly distributed in [0, 2π[leads to an arcsine probability density function (PDF) for the signal–crosstalk beating [30]. The resulting signal–crosstalk beating MGF $M_X(z)$ can be expressed by

$$M_X(z) = \prod_{k=1}^{N} I_0(2A_s A_k z) \tag{5.14}$$

where I_0 is the zero order modified Bessel function of the first kind [30]. z has been used instead of the typical s parameter of the MGFs, to prevent confusion with the subscript s representing the signal.

Using the Gaussian approximation and neglecting crosstalk-ASE beatings, the MGF of the ASE beatings is [29]

$$M_{ASE}(z) = \exp\left((\sigma_{s-ASE}^2 + \sigma_{ASE-ASE}^2) z^2 / 2\right). \tag{5.15}$$

Finally, the MGF of the electrical Gaussian noise can be given by

$$M_{el}(z) = \exp\left(\sigma_{el}{}^2 z^2 / 2\right). \tag{5.16}$$

Therefore, the MGF, $M_i(z)$, of the photodetector current *i(t)* is equal to the product of the individual MGFs:

$$M_i(z) = M_{el}(z) M_{ASE}(z) M_X(z) = \exp\left(\sigma_{el}{}^2 z^2 / 2\right) \exp\left((\sigma_{s-ASE}^2 + \sigma_{ASE-ASE}^2) z^2 / 2\right) \prod_{k=1}^{N} I_0(2A_s A_k z). \tag{5.17}$$

It should be emphasised that an analytical and exact MGF for the first order received current could only be obtained by neglecting all second order current terms. This MGF is now used to derive theoretical expressions for the BER, which are accurate provided the crosstalk and ASE noise powers are relatively small compared to the signal power.

The BER for "0" and "1" bits can be calculated by applying the MCB to the MGF of *i(t)* [31], which is given, respectively, by

$$BER_0 < MCB^{(0)}(z_0, D) = \frac{1}{z_0 \sigma_{tot}^{(0)} \sqrt{2\pi}} M_i^{(0)}(z_0) \exp\left[-z_0 \left((A_s^{(0)})^2 - D\right)\right] \tag{5.18}$$

$$BER_1 < MCB^{(1)}(z_1, D) = \frac{1}{z_1 \sigma_{tot}^{(1)} \sqrt{2\pi}} M_i^{(1)}(z_1) \exp\left[-z_1 \left((A_s^{(1)})^2 - D \right) \right] \tag{5.19}$$

where D represents the decision threshold, the total variance is $\sigma_{tot}^2 = \sigma_{s-ASE}^2 + \sigma_{ASE-ASE}^2 + \sigma_{el}^2$, and where the superscripts (1) and (0) in the variables denote a conditioning on the signal to be a "1" bit or a "0" bit, respectively. To obtain a tight BER bound, the expressions (5.18) and (5.19) are minimized with respect to z_1, for "1" bits, and, z_0, for "0" bits [31]. For a sequence of $2L$ bits, with equal number of "0" and "1" bits, the BER upper bound, MCB_{seq}, can be given by

$$BER < MCB_{seq} = \frac{1}{2L} \left[\sum_{l=1}^{L} MCB_l^{(0)}(z_0, D) + \sum_{l=1}^{L} MCB_l^{(1)}(z_1, D) \right] \tag{5.20}$$

which, by bringing out D into evidence, gives

$$BER < MCB_{seq} = \frac{1}{2L} \left[m_o(z_0) e^{-z_0 D} + m_1(z_1) e^{z_1 D} \right] \tag{5.21}$$

where, m_0 and m_1 are

$$m_0(z_0) = \sum_{l=1}^{L} M_{i,l}^{(0)}(z_0) \frac{\exp\left[z_0 \left((A_{s,l}^{(0)})^2 + \sum_k A_k{}^2 \right) \right]}{z_0 \sigma_{tot,l}^{(0)} \sqrt{2\pi}} \tag{5.22}$$

$$m_1(z_1) = \sum_{l=1}^{L} M_{i,l}^{(1)}(z_1) \frac{\exp\left[z_1 \left((A_{s,l}^{(1)})^2 + \sum_k A_k{}^2 \right) \right]}{z_1 \sigma_{tot,l}^{(1)} \sqrt{2\pi}} . \tag{5.23}$$

The subscript l refers to a specific bit of the bit sequence. The last expression is valid for fixed crosstalk amplitudes. When all the crosstalk channels have equal power and extinction ratio, i.e., $A_k^{(1)} = A_x^{(1)}$ and $A_k^{(0)} = A_x^{(0)}$, $k = 1, \ldots, N$, the variables $m_0(z_0)$ and $m_1(z_1)$, can be averaged over all the possible signal and crosstalk bit combinations, giving

$$m_0(z_0) = \sum_{l=1}^{L} \frac{1}{2^N} \sum_{k=1}^{N} C_k^N I_0(2A_{s,l}^{(0)} A_x^{(1)} z_0)^k \times I_0(2A_{s,l}^{(0)} A_x^{(0)} z_0)^{N-k} \frac{\exp\left[(\sigma_{tot}^{(0)})^2 z_0^2 / 2 + z_0 \left((A_{s,l}^{(0)})^2 + k (A_x^{(1)})^2 \right) \right]}{z_0 \sigma_{tot}^{(0)} \sqrt{2\pi}} \tag{5.24}$$

$$m_1(z_1) = \sum_{l=1}^{L} \frac{1}{2^N} \sum_{k=1}^{N} C_k^N I_0(2A_{s,l}^{(1)} A_x^{(1)} z_1)^k \times I_0(2A_{s,l}^{(1)} A_x^{(0)} z_1)^{N-k} \frac{\exp\left[(\sigma_{tot}^{(1)})^2 z_1^2 / 2 + z_1 \left((A_{s,l}^{(1)})^2 + k (A_x^{(1)})^2 \right) \right]}{z_1 \sigma_{tot}^{(1)} \sqrt{2\pi}} \tag{5.25}$$

where the crosstalk power for "0"s has been neglected inside the exponential.

The minimum BER can be analytically derived from (5.21), by optimising the decision threshold D. The optimum decision threshold D_{opt}, can be found by solving the

equation that results from setting the derivative of (5.21) with respect to D to zero, which gives

$$D_{opt} = \frac{1}{z_1 + z_0} \ln\left[\frac{z_0 m_0(z_0)}{z_1 m_1(z_1)}\right]. \tag{5.26}$$

The optimum MCB_{seq} is obtained by substituting D_{opt} in (5.21), which gives

$$MCB_{seq,Dopt} = \frac{1}{2L}\left[\left(\frac{z_1}{z_0}\right)^{\frac{z_0}{z_0+z_1}} + \left(\frac{z_1}{z_0}\right)^{\frac{z_1}{z_0+z_1}}\right] \times m_1(z_1)^{\frac{z_0}{z_0+z_1}} m_0(z_0)^{\frac{z_1}{z_0+z_1}}. \tag{5.27}$$

Note that (5.27) is a general result that is valid for any MGF, regardless of the statistical properties of the noise and crosstalk, as long as the MCB can be given by (5.21).

Finally, the minimum BER is obtained by minimizing the optimum MCB in (5.27), with respect to both z_1 and z_0,

$$BER_{Dopt} \approx \min_{z_0, z_1}\left\{\frac{1}{2L}\left[\left(\frac{z_1}{z_0}\right)^{\frac{z_0}{z_0+z_1}} + \left(\frac{z_1}{z_0}\right)^{\frac{z_1}{z_0+z_1}}\right] \times m_1(z_1)^{\frac{z_0}{z_0+z_1}} m_0(z_0)^{\frac{z_1}{z_0+z_1}}\right\} \tag{5.28}$$

Expression (5.28) , together with (5.22) and (5.23), or (5.24) and (5.25) enable the calculation of a BER approximation, where the effects of crosstalk and of ASE noise filtering by both the optical and electrical receiver filters are captured, respectively, by the MGF for "0" and "1" bits, given by $m_0(z_0)$ and $m_1(z_1)$, and by the filtered variances given by (5.11) and (5.12). The model computational simplicity is due to the relatively small effort required to minimize (5.27), where both $m_0(z_0)$ and $m_1(z_1)$ are given analytically, with all bit combinations implicitly considered. Consequently, this method requires much less computational effort compared to the Monte Carlo, and even to other semi-analytical simulation methods.

However, the MCB, as is, does not take into account the ISI effect caused either by optical or electric filtering. In order to account for the distortion in the signal, the optical and electrical filters effect on the signal and crosstalk should not have been neglected in equation (5.1) and (5.6), respectively. In that case, the final current would have been

$$i(t) = i_s + \sum_{k=1}^{N} i_k + 2\sum_{k=1}^{N}\left[\left(A_s \otimes h_o(t)\right)\left(A_k \otimes h_o(t)\right)\cos\left(\phi_s - \phi_k\right)\right] \otimes h_e(t) + \left(\vec{E}_s.\overrightarrow{n^*} + c.c. + \left|\vec{n}\right|^2 + n_{el}\right) \otimes h_e(t) \tag{5.29}$$

where i_s and i_k are the signal and crosstalk currents in the absence of other optical fields, given by $i_s(t) = \left|A_s \otimes h_o(t)\right|^2 \otimes h_e(t)$ and $i_k(t) = \left|A_k \otimes h_o(t)\right|^2 \otimes h_e(t)$, which capture the effect of

optical and electrical filtering. The signal - crosstalk beating term is more complex, and cannot be written in a simple way in terms of the detected currents i_s and i_k. Therefore, for this particular factor, it will still be assumed that the filters do not affect the signal and crosstalk signal shapes significantly. Hence, the final expression of the current is

$$i(t) = i_s + \sum_{k=1}^{N} i_k + 2\sum_{k=1}^{N} A_s A_k \cos(\phi_s - \phi_k) + \left(\vec{E}_s . \overrightarrow{n^*} + c.c. + \left|\vec{n}\right|^2 + n_{el} \right) \otimes h_e(t) . \quad (5.30)$$

By comparison with the previously derived current and respective MGF, the new MGFs are

$$m_0(z_0) = \sum_{l=1}^{L} \frac{1}{2^N} \sum_{k=1}^{N} C_k^N I_0(2A_{s,l}^{(0)} A_x^{(1)} z_0)^k \times I_0(2A_{s,l}^{(0)} A_x^{(0)} z_0)^{N-k} \frac{\exp\left[(\sigma_{tot}^{(0)})^2 z_0^2 / 2 + z_0 \left(i_{s,l}^{(0)} + k i_x^{(1)} \right) \right]}{z_0 \sigma_{tot}^{(0)} \sqrt{2\pi}} \quad (5.31)$$

$$m_1(z_1) = \sum_{l=1}^{L} \frac{1}{2^N} \sum_{k=1}^{N} C_k^N I_0(2A_{s,l}^{(1)} A_x^{(1)} z_1)^k \times I_0(2A_{s,l}^{(1)} A_x^{(0)} z_1)^{N-k} \frac{\exp\left[(\sigma_{tot}^{(1)})^2 z_1^2 / 2 + z_1 \left(i_{s,l}^{(1)} + k i_x^{(1)} \right) \right]}{z_1 \sigma_{tot}^{(1)} \sqrt{2\pi}} . \quad (5.32)$$

The latter MGFs are no longer exact up to the first terms of the current as the former MGFs, since the former were derived from the properties of A_s and A_k and not of i_s and i_k. More details of the implementation of the MCB method with the eye diagram simulation are given in Appendix F. However, it will be seen by the results that the approximate MGFs do capture the effect of both intersymbolic interference and crosstalk at the same time with proper accuracy. It should also be added that, from the point of view of the signal shape, the distortion can be caused not only by optical and electrical filters, but also from dispersion or non-linear effects. On the other hand, the noise variances assume white Gaussian ASE noise filtered by the considered filters, which might not be the case for a system with non-linear effects.

One limitation of this method is that, due to the approximation that the signal - crosstalk beating term is not affected by the filters, the method is not able to correctly model the case when the crosstalk signal is itself distorted. Whereas for the signal the most important term is i_s, and it captures the filter effects, for the crosstalk, the most significant term is the signal - crosstalk beating term and it does not capture the filter effects. In section 5.4 a similar situation, where the crosstalk signal is distorted, will be considered. A brief test of the method in this situation is done in Appendix G. Future work could include the improvement of this aspect of the derived method.

Now, with the complete theoretical model, i_s and i_x must be determined. In order to calculate the i_s and i_k, a noiseless and crosstalk-free simulation of the signal is performed,

considering the optical filter cascade in the optical path and the electrical post-detection filter to produce an ISI impaired eye diagram. A histogram of the signal is then obtained from the eye diagram at the desired sampling time, e.g. at the point of maximum eye aperture, to obtain the filter induced ISI effect. Each of the histogram power values are then used in the MCB, instead of the steady state mark and space power levels. The final MCB result is the weighted averaged of all the bounds obtained from each power level, where the weights are the occurrences of each power level of the signal histogram. Hence, a BER estimate for a crosstalk and ISI impaired signal is obtained without the need of a large number of simulation runs. Naturally, when the filtering effects do not affect the signal at the sampling instant, the MGFs given by equations (5.31) and (5.32) are equivalent to those given by (5.24) and (5.25), and the simulation is not required.

The probability density function associated to the obtained MGF will now be analysed. It had been previously shown that both the crosstalk-ASE and the ASE noise beating terms result in an asymmetric current PDF, leading to a complex and hardly tractable MGF [32]. However, in this derivation of the photocurrent PDF, we assumed Gaussian ASE beatings and neglected the crosstalk-ASE beatings, which results in a symmetric photocurrent PDF, and leads to an analytically tractable MGF. Moreover, when both the crosstalk and the ASE power are much smaller than the signal power, the exact PDF tends to the symmetrical PDF, which justifies the previous approximations in this region. Therefore, although the expressions for calculating the BER were derived assuming a first order current PDF approximation, the accuracy of the results is not expected to be significantly hampered, provided that both crosstalk and ASE power are relatively small. Both the simulation and the experimental results presented in the next section confirm this view.

Fig. 5.2 plots both the exact and the approximate PDFs, for an optical signal impaired by one crosstalk channel with SXR = 14 dB and ASE noise with OSNR= 34.3 dB measured over a 0.1 nm bandwidth. The optical and electrical filter bandwidths at -3 dB are 50 GHz and 10 GHz, respectively, which do not introduce patterning effects at the eye diagram centre.

A comparison of the two PDFs, shows that the approximate PDF overvalues the leftmost part of the exact PDF of the “1” bit, which overestimates the BER for “1” bits. On the other hand, the approximate PDF undervalues the rightmost part of the exact PDF of

the “0” bit, which underestimates the BER for “0” bits. Incidentally, when an optimum threshold level is used, the overestimation of the BER for the “1” bits is partially compensated by the underestimation of the BER for the “0” bits [21]. Consequently, although the MCB usually gives a tight BER upper bound, the derived method gives only close approximate BER results.

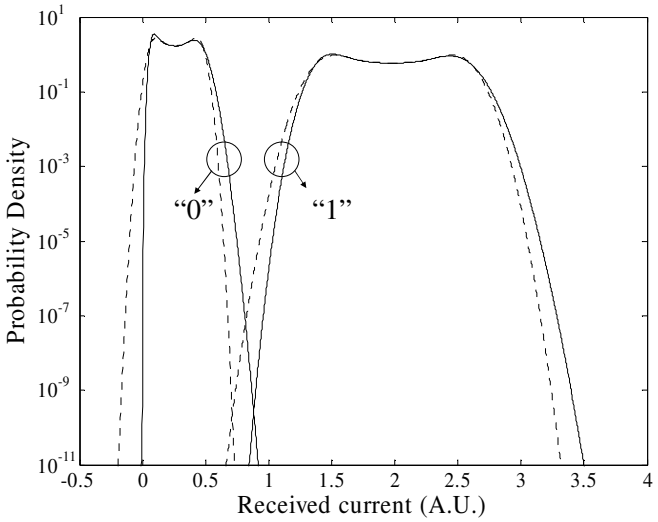

Fig. 5.2 Asymmetric exact (full line) [32], and approximate symmetric (dashed) current probability density function of a “0” and a “1” bit impaired by both a “1” crosstalk bit, and ASE noise.

5.1.2 Results and discussion

In the following, the numerical results obtained with the previously presented BER calculation method are presented and validated both by simulation and experimentally using identical test setups.

The experimental setup for measuring the BER is depicted in Fig. 5.3. There are two independent, but synchronized, 2^{31}-1 pseudorandom bit sequence data generators at 10 Gb/s (PRBSG1 and PRBSG2), for generating the signal and up to three crosstalk channels. The ASE noise is added to both the signal and crosstalk before optical filtering and photodetection by a p-i-n photodiode. The BER is measured from the photodiode output signal, by comparing it with an optimum data threshold level, at optimum sampling instant. The in-band incoherent crosstalk is generated by splitting the output power of one of the data generators into three separate optical fibre paths, of different lengths (2 metres, 760 metres, and 1000 metres) of standard single mode fibre, for decorrelating the laser phase among the three paths. Two of the three crosstalk paths can be disabled for measuring the BER with only one crosstalk channel. The OSNR is measured over a 0.1 nm bandwidth.

The semi-analytical simulation [16] is performed by simulating several 2^{12}-1 pseudorandom bit sequences for both signal and crosstalk with random phase differences and random sequence delay, while the ASE noise is accounted for analytically using the Gaussian approximation. Each simulation is run 1000 times throught the results of this chapter, which is a large enough number of simulations to have good accuracy at a reasonable computation time. The semi-analytical simulation method has been shown to give accurate results when compared to those obtained with more sophisticated and theoretically exact methods [16], [20], [21], as already mentioned. Moreover, its results can be justifiably compared with the results of the BER calculated through the MCB method presented in the previous section, because both methods return the BER corresponding to the same random optical electromagnetic field variable at the optical receiver input.

The BER results calculated with the MCB method are compared with similar results obtained both with the semi-analytical method and in the experiment, using the experimental set up depicted in Fig. 5.3.

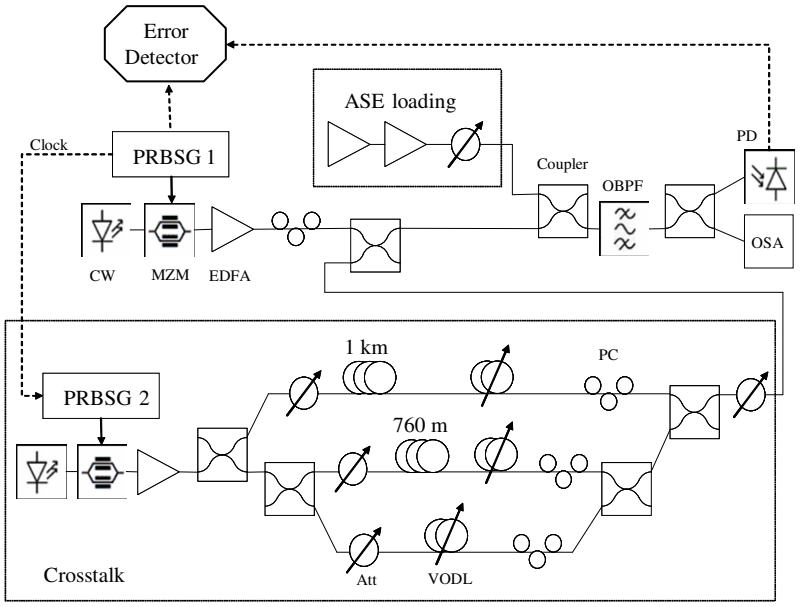

Fig. 5.3 Experimental setup for measuring the BER of a signal impaired by three crosstalk channels and ASE. CW – Continuous wave laser; MZM – Mach-Zehnder modulator; OBPF – Optical band pass filter; PD – Photodiode with electrical filter; PC – polarization controller; VODL – Variable optical delay line; Att – Attenuator, PRBSG - Pseudorandom Bit Sequence Generator.

The BER has been plotted in Fig. 5.4 as a function of the signal to crosstalk ratio (SXR), defined as the signal power divided by the total crosstalk power, for 22.7 dB OSNR and a 50 GHz optical filter bandwidth. Two separate sets of plots are shown in the figure,

corresponding to three crosstalk data channels (N=3) and one crosstalk data channel (N=1). Both the BER test signal and the crosstalk signals have 11 dB extinction ratios. Each set of plots compares the results obtained with the MCB calculation method, both with the results obtained with the semi-analytical simulation method, and with experimental results.

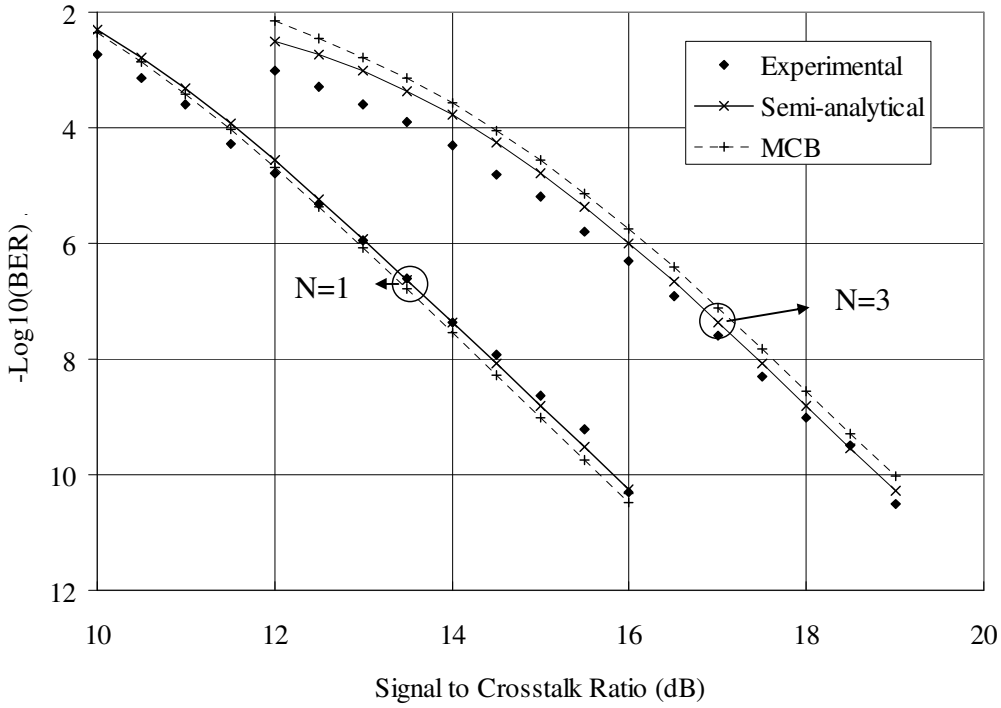

Fig. 5.4 Experimental, semi-analytical simulation, and MCB BER results for N=1 and N=3 crosstalk channels as a function of the signal to crosstalk ratio. The OSNR is 22.7 dB and the optical filter bandwidth is 50GHz. The lines connecting the data points are guides for the eyes.

The set of plots, corresponding to N=1, are practically in full agreement, with a maximum discrepancy of 0.5 in units of $\log_{10}$(BER) between the experimental and numerical results. Hence, the MCB method is validated both by the semi-analytical simulation results, and by experimental results, even for large BER caused by crosstalk. For the set of plots corresponding to N=3, i.e., with three independent crosstalk data channels, the agreement between the MCB calculation method and the simulation is still very good, although there is a slight discrepancy for very high BER ($>10^{-3}$) of 0.5 in units of $\log_{10}$(BER), corresponding to large SXR. The discrepancy could be due to the second order approximation, or to the inherent approximative nature of the MCB. Nevertheless, remarkably, the MCB method only deviates from the simulation results for very large values of BER. Therefore, the MCB calculation method can still be applied to systems employing Forward Error Correction, which typically operate at a BER of around 10^{-4}.

There is also a good agreement with the experimental results, which show the same trend as the MCB results, although with a larger discrepancy of 1 in units of $\log_{10}$(BER). The lower measured BER in the experiment compared to simulation and MCB is likely to be explained by the difficulty in maintaining the polarization alignment between the three crosstalk channels, which is a worst case. The use of polarization maintaining components would have improved the results.

In order to better assess the match between the experimental and numeric (either semi-analytical or MCB), the reduced chi-squared has been calculated according to the following expression:

$$\chi^2 = \frac{1}{K}\sum_{k=1}^{K}\frac{(e_k - s_k)^2}{{\sigma_k}^2} \tag{5.33}$$

where e_k and s_k are the experimental and simulated $\log_{10}$(BER) results, respectively, σ_k is the standard deviation of the experimental result, and K is the number of measured or simulated results. The experimental standard deviation is considered to be 5% of the $|\log_{10}(\text{BER})|$ value, plus 0.05. The percentage factor represents the higher uncertainty that measurements at lower BER results have, due to the fewer bit errors that are observed, whereas the additional 0.05 factor prevents that for high BER the uncertainty is too low.

The chi-squared values for the one channel results are 0.97 and 0.80 for the semi-analytical and MCB results, respectively. Since these values are below 1, the observed discrepancies can be explained by the errors, therefore demonstrating a good agreement between results. However, for the three channel results, the chi-squared values are 3.4 and 8.7, for the semi-analytical and MCB results, respectively. The standard deviations cannot explain such larger deviations, but it has already been discussed that there is a systematic error. Experimental results systematically undervalue those of MCB and semi-analytical simulation, most likely due to polarization fluctuations of the four involved signals, leading to lower than expected crosstalk effects, thus justifying such high chi-squared values.

Additional simulation results shown in Fig. 5.5, with an extinction ratio of 10 dB, demonstrate that the MCB method results also agree well with simulation results for five crosstalk channels for BER $<10^{-3}$. Again, at large BER ($>10^{-3}$) the MCB overestimates the semi-analytical simulation due to the 2nd order approximation and the non-exact nature of the MCB, as in the results of Fig. 5.4.

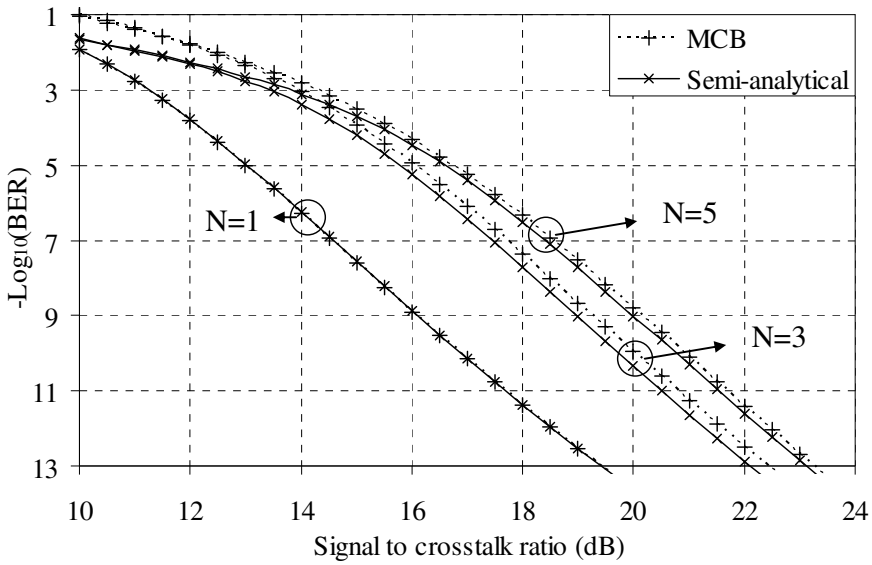

Fig. 5.5 Semi-analytical simulation and MCB BER results for N =1, 3 and 5 crosstalk channels as a function of the signal to crosstalk ratio. The OSNR is 22.7 dB and the optical filter bandwidth is 50GHz. The lines connecting the data points are guides for the eyes.

Fig. 5.6 plots three sets of BER plots as a function of the OSNR for a 30GHz optical filter bandwidth and N=3 independent crosstalk channels. Each set of plots, from the left to the right of Fig. 5.6, corresponds to a different SXR value of 30 dB, 25 dB and 20 dB, respectively. Both the signal and crosstalk pulses have an 11 dB extinction ratio. To double check, additional BER results were calculated with Monte Carlo simulations, albeit only for BER larger than 10^{-8}, and are plotted in Fig. 5.6 alongside the results of the other methods.

The agreement between the theoretical results obtained with the MCB method and both the semi-analytical and the Monte Carlo simulation methods, on the one hand, and between all the theoretical and experimental results, on the other hand, is again excellent over a broad range of values, with a maximum discrepancy between all methods of 0.5 in units of $\log_{10}$(BER), and low chi-squared values. The chi-squared values for the semi-analytical simulation are 0.09, 0.28, and 0.53, respectively, for SXRs of 30, 25, and 20 dB. Similarly, for the MCB method, the chi-squared values for the same SXR values are, respectively, 0.10, 0.34, and 0.68. Again, whenever the crosstalk impacts more severely the signal, the deviations between the experiment and semi-analytical simulation or MCB are also larger. Still, in this set of results, the discrepancies between semi-analytical simulation

and the MCB are small because the crosstalk power is low and the second order terms are not significant.

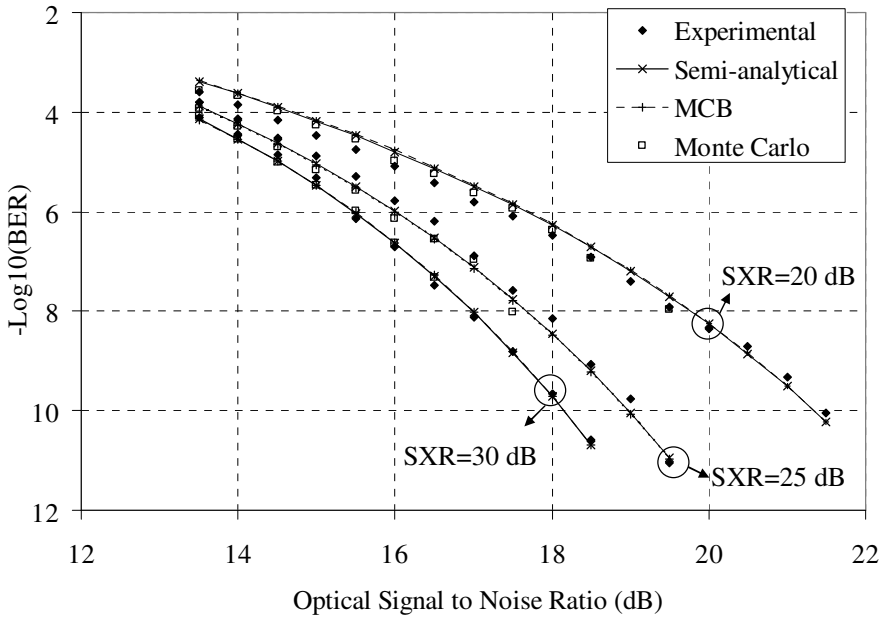

Fig. 5.6 Experimental, semi-analytical, MCB and Monte Carlo BER results as a function of the optical signal to noise ratio, for SXR = 20, 25, 30 dB and an optical filter bandwidth of 30GHz. The lines connecting the data points are guides for the eyes.

The validity of the MCB calculation method has been established over a wide range of OSNR and SXR values. In the following, it will be shown that the MCB method also captures the effect of processing of noise by specific optical and electrical filter shapes on the system BER, which is essential in WDM systems. This makes the MCB method a most useful tool to analyse these systems, especially as earlier BER calculation methods have not modelled computationally efficiently the combined effects of crosstalk and system noise when modified by the properties of the optical and electrical filters.

The behaviour of the MCB method is now studied for different optical filter bandwidths. Fig. 5.7 and Fig. 5.8 plot MCB and semi-analytical, and MCB and experimental BER results, respectively, as a function of SXR (N=3 crosstalk channels) for three different optical filter bandwidths while assuming a constant ASE power spectral density (corresponding to 19.5 dB OSNR). Both the signal and crosstalk pulses have a 10 dB extinction ratio and the electrical bandwidth is 10 GHz. The agreement between the MCB and semi-analytical and experimental results is again verified to be good, with the maximum discrepancy between the methods to be 0.5 in units of $\log_{10}$(BER). In Fig. 5.4 it had been observed that for large BER (>10^{-4}) the agreement between the MCB and other

methods degraded due to high crosstalk powers involved. In Fig. 5.7 and Fig. 5.8 this effect is not noticeable since lower crosstalk powers have been used (SXR>15dB).

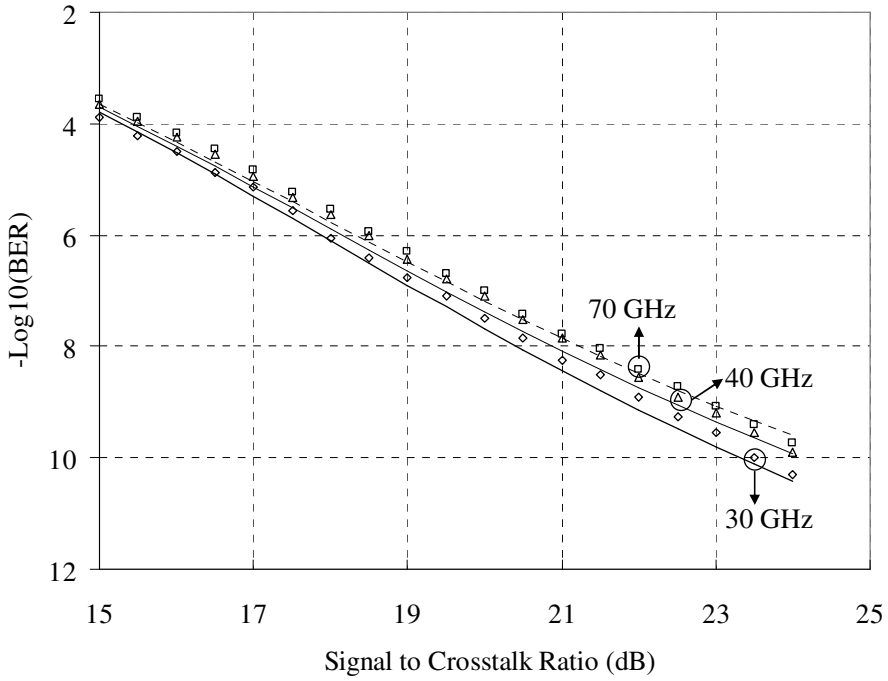

Fig. 5.7 Semi-analytical (marks) and MCB (lines) bit error ratio results for three different optical bandwidths (30, 40, and 70 GHz), versus the signal to crosstalk ratio.

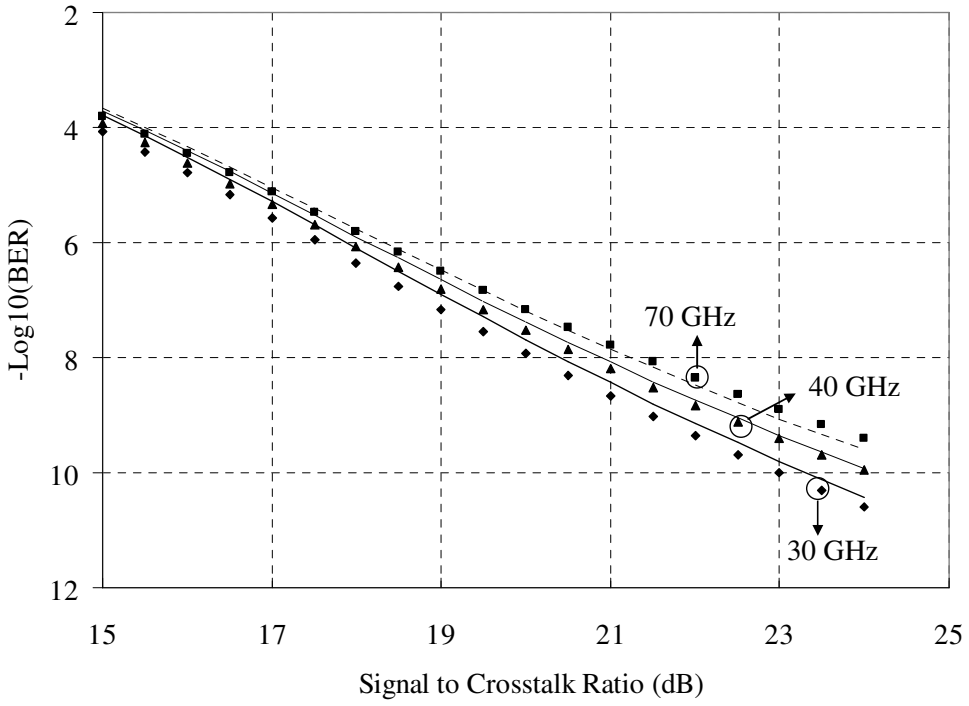

Fig. 5.8 Experimental (marks) and MCB (lines) bit error ratio results for three different optical bandwidths (30, 40, and 70 GHz), versus the signal to crosstalk ratio.

The reduced chi-squared has also been calculated in this case for the MCB results, giving 0.16, 0.32, and 0.23 for the optical bandwidths of 30, 40 and 70 GHz, respectively, demonstrating a good agreement. However, for the semi-analytical simulation results, the chi-squared is 1.0, 1.1, and 0.50, respectively, for bandwidths of 30, 40 and 70 GHz. The agreement is not as good as in the previous case, but the chi-squared values are still around 1, which means that the discrepancies can be just explained by the random errors quantified by the standard deviation. It is observed that the experimental results are lower than those of the simulation, which can be again justified by the polarization fluctuations.

Since the studied bandwidths are quite larger than the spectrum bandwidth of the optical signal, the optical filter does not filter the signal and therefore no intersymbolic effects are introduced. Hence, it is observed that the larger the bandwidth of the filter, the larger BER is obtained. However, if the filter bandwidth is sufficiently narrow, intersymbolic effects will appear which will increase the BER. Consequently, there will be an optimum filter bandwidth which produces the lowest BER, representing the trade-off between noise filtering and intersymbolic effects. This effect is studied next by simulation.

Fig. 5.9 plots the BER results obtained with both the MCB and the semi-analytical simulation methods as a function of the electrical filter bandwidth (normalized to the bit rate), for three different optical filter bandwidths. The electrical filter is a 3rd order Bessel filter and the optical filter is a 2^{nd} order super-Gaussian filter. The OSNR is 17.5 dB and the SXR is 25 dB with three crosstalk channels.

Since the standard MCB calculation method, without signal simulation, does not account for inter-symbolic interference (ISI), it is expected that for very narrow electrical bandwidths the MCB will give too optimistic, unrealistic results. The semi-analytical simulation is able to determine an optimum electrical bandwidth compromising between noise filtering and ISI, while the MCB always predicts a lower BER for narrower bandwidths. Nevertheless, the MCB gives good BER estimates for bandwidths as low as 70% of the bit rate, which are the typical filter bandwidths.

However, if narrower filters are employed, a short simulation for determining the eye closure is performed for accounting for the ISI before applying the MCB calculation method with the partially closed eye, as explained in section 5.1.1. The results obtained using this technique are also shown in Fig. 5.9 where it is clear that using the eye aperture data in the MCB (MCB-EA in Fig. 5.9) returns the correct trend even for narrow electrical

bandwidths. The optimum electrical bandwidth found by the MCB-EA, and by semi-analytical simulation differs by about 5% of the the bit rate, and the absolute optimum BER value differs at most by about half an order of magnitude (0.6 in units of $\log_{10}$(BER)). In conclusion, the MCB method with eye aperture data (MCB-EA) is capable of calculating the BER in WDM systems with arbitrary optical and electrical filtering impaired by ASE and crosstalk, in a computationally inexpensive manner and reasonable accuracy.

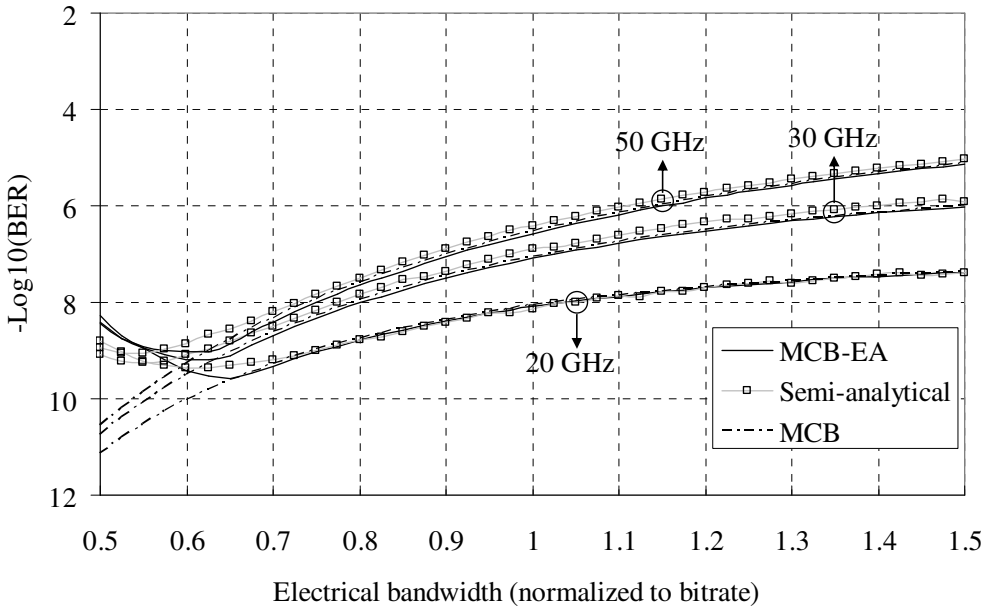

Fig. 5.9 Error probability by semi-analytical simulation and modified Chernoff bound without (MCB) and with (MCB-EA) eye aperture data versus the electrical bandwidth of a 3rd order Bessel filter, and a 2nd order Gaussian optical filter with the displayed optical bandwidths (20, 30, and 50 GHz) for three crosstalk channels. The SXR is 25 dB and the OSNR is 17.5 dB. The grey lines (semi-analytical simulation) are guides for the eyes.

The BER accuracy of the MCB method with the eye aperture data as a function of the optical bandwidth has also been investigated, and the results are reported in Fig. 5.10. The receiver electrical filter is a 3rd order Bessel filter with a bandwidth of 10 GHz, and a uniform Bragg grating is used as optical filter, with 1.3 $k_{Gr}L_{Gr}$ parameter, where k_{Gr} is the coupling coefficient and L_{Gr} is the grating length. Again, for very narrow optical bandwidths, less than 1.5 times the bit rate, the optical filter introduces severe intersymbolic effects, which are appropriately modelled by the semi-analytical method and the MCB-EA, but not by the MCB. As such, the MCB always predicts a decreasing BER for decreasing bandwidths, whereas the MCB-EA predicts an optimum optical filter

bandwidth of 1.3 times the bit rate. The largest discrepancy between the MCB-EA and the semi-analytical simulation is 0.3, in units of $\log_{10}$(BER).

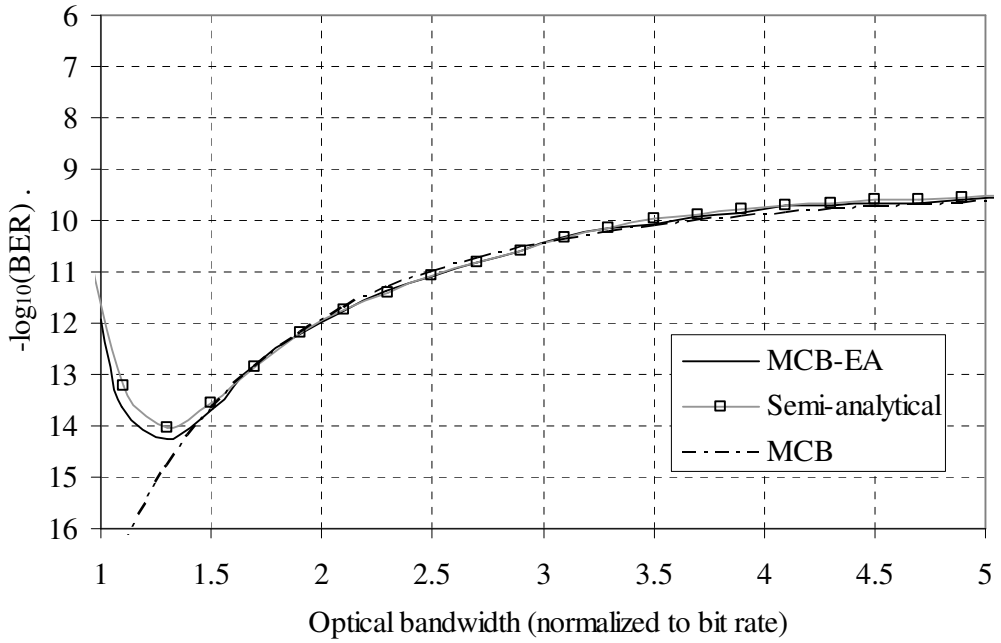

Fig. 5.10 Error probability by semi-analytical simulation and modified Chernoff bound without (MCB) and with (MCB-EA) eye aperture data versus the optical bandwidth of a 3rd order Bessel filter (10 GHz bandwidth), and a uniform Bragg grating optical filter with $k_{Gr}L_{Gr}$ parameter of 1.3, for three crosstalk channels. The SXR is 25 dB and the OSNR is 18 dB. The grey line (semi-analytical simulation) is a guide for the eyes.

5.2 Filtering effects in crosstalk penalties

The MCB method presented before has proved to be accurate, while computationally inexpensive. In this section, the MCB method with eye aperture data will be used for calculating the impact of narrow or detuned optical filtering and narrow electrical filtering in a network scenario. Whenever the MCB method is evocated, its variant with eye aperture is assumed, unless otherwise stated.

The optical cross-connect (OXC) is being adopted in optical networks, enabling the traffic to be routed in the optical domain. It provides flexibility, while avoiding the costly optical-electrical-optical (OEO) conversions. However, the OXC introduces in-band crosstalk [33] and filters the optical signal [34]. At the end of the transmission link, the optical signal accumulates a number of crosstalk interferers and can be also severely filtered, which will result in a degraded signal bit error rate (BER) performance [1], [2].

With the introduction of forward error correction (FEC) in optical networks, more signal degradation is allowed, but more precise knowledge of the impairments is needed due to the sharp FEC threshold [35]. Therefore, it is important to accurately assess the impact of the impairments on the signal performance so that the maximum number of cascaded OXC is correctly predicted.

The impact of crosstalk on the signal performance has been extensively studied [36], as well as the impact of optical and electrical filtering, namely on systems affected by ASE [37]. The crosstalk studies usually consider an ideal shape of both signal and crosstalk signal, while the studies on the impact of narrow optical and electrical filtering do not consider crosstalk. The combined effect of various impairments should be studied, since larger penalties than expected can arise when compared to a separate assessment of impairments' effects.

Because both inter-symbolic interference (ISI) due to filtering and crosstalk are generated at OXC, it is now presented a study on the combined impact of narrow filtering on the optical signal and on the crosstalk signal, where it is shown that the crosstalk induced penalties are higher than expected when the signal is narrowly filtered. The effect arises from the eye closure of the signal, which penalty adds super-linearly to the crosstalk penalty. The same effect has also been observed for small post-detection electrical bandwidths.

5.2.1 Optical network equivalent system

In an optical meshed network, an optical signal can cross several OXCs. In each OXC, the signal is filtered and, possibly, an amount of crosstalk is introduced. Considering that the signal and crosstalk signal have different origins, their path will be different and therefore they are filtered by different filters. Therefore, different optical filters with tuneable bandwidth will be used for the signal and for the crosstalk signal.

A single crosstalk signal will be considered, for a better understanding of the phenomenon, but the results should be extensible to a larger number of crosstalk interferers.

The experimental setup is depicted in Fig. 5.11. An optical transmitter (Tx) produces a 10 Gb/s, 2^{31}-1 PRBS signal that is split into the signal part and the crosstalk signal part. The signal and the crosstalk signal are each filtered by a different optical filter,

OBPF1 and OBPF2, respectively, so that the filter bandwidth can be independently selected. The crosstalk signal phase is decorrelated from the signal phase by travelling over 4 km of standard single mode fibre (SSMF) and the delay between signal and crosstalk signal is controlled by a variable optical delay line (VODL) so that the bit transitions occur at the same time in both signal and crosstalk signal, when they are added later on an optical coupler. Some results about the impact of delay between signal and the crosstalk signal are given in Appendix H. The impact of dispersion of 4 km of SSMF on the crosstalk signal shape is negligible at 10 Gb/s. A polarization controller (PC) sets the crosstalk signal state of polarization to match that of the signal and an attenuator (Att.) controls the signal to crosstalk ratio (SXR). The crosstalk signal is then coupled to the signal and also to ASE noise. An attenuator after the ASE noise source sets the OSNR. A large bandwidth optical filter (OBPF3) filters the ASE noise before the impaired signal is fed to the square-law bandwidth limited photo-receiver. The electrical signal is then fed to the BER tester.

The BER is measured with optimum decision threshold and sampling instant. The OSNR penalty is given by the difference of the OSNR required to achieve a BER of 10^{-4} (FEC threshold) between the signal with and without crosstalk, for the same filter conditions.

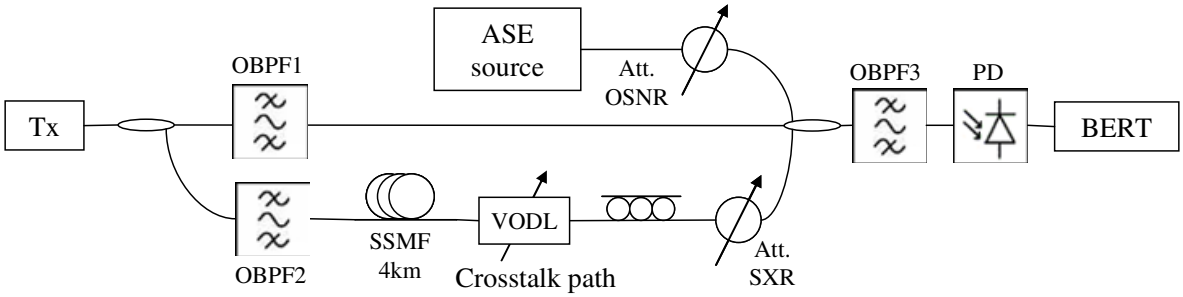

Fig. 5.11 Experimental and simulation setup.

The simulation setup is identical to the experimental setup, where the random phase fluctuations between the signal and crosstalk signal due the different paths are simulated by a random phase walk between both signals. The ASE noise is accounted for analytically according to the semi-analytical simulation description in sub-section 5.1.2, simulating 1000 times a 2^{10}-1 de Bruijn sequence padded with a zero at the end. The bandwidth-limited photodiode electrical frequency response is modelled as a third order Bessel low pass filter with bandwidth of 10 GHz at -3 dB. The optical filter is modelled as super

Gaussian band pass filter with the best order and bandwidth that match the experimental characteristics. The MCB method is employed, as explained in the previous section.

5.2.2 Results

The dependence of the crosstalk-induced OSNR penalty has been studied as a function of the optical filter bandwidth in the signal path. The results are presented in Fig. 5.12, for 20 dB of SXR. The experimental optical filter is simulated as a super-Gaussian optical filter with order 1.5, which best fits the amplitude response of the experimental filter. The agreement between the experimental, simulation and MCB results is within 0.2 dB. The OSNR penalty is constant (and equal to 0.9 dB) for bandwidths above 15 GHz, which is the classical crosstalk-induced OSNR penalty. However, for bandwidths below 15 GHz, a steep rise in the OSNR penalty is observed due to ISI. To support this, Fig. 5.12 also shows the experimental eye diagrams of the crosstalk-free signal. It is noticeable that 15 GHz is precisely the bandwidth of the optical filter that starts to cause eye closure due to ISI.

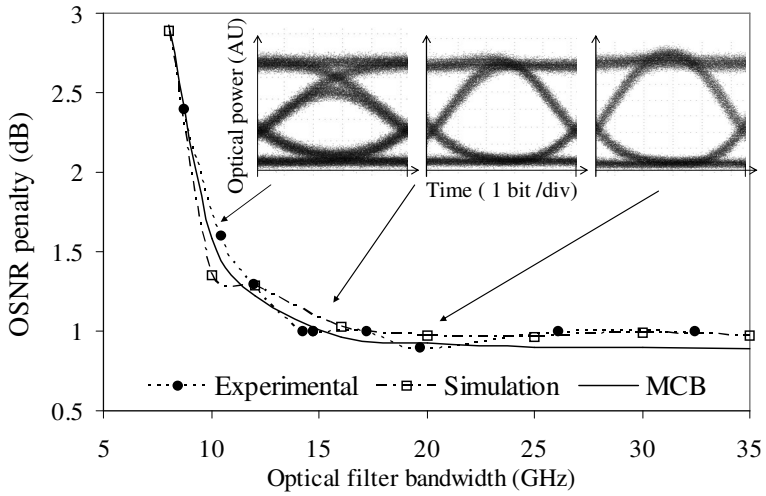

Fig. 5.12 Experimental, simulation and MCB results for the crosstalk induced OSNR penalty as a function of the bandwidth of the optical filter in the signal path. Insets: experimental eye diagrams of the crosstalk-free signal for optical bandwidths of 10, 15 and 20 GHz. The dashed lines are guides for the eyes.

The explanation for the crosstalk induced penalty increase for narrow optical filtering lies on the shape of the filtered signal. When the optical filter is very narrow, it causes ISI on the signal. In these measurements, the impact of filtering on the signal is removed from the penalty since the crosstalk penalty is measured relatively to the ISI impaired signal. However, the ISI and crosstalk impairments do not add linearly. To

visualize the origin of this effect, consider two cases. In the first case, the signal is very slightly impaired by ISI. When crosstalk is added to the signal, the BER increases and the OSNR must be improved by a small amount to recover the previous BER value. On the second case, however, the signal is significantly impaired by ISI. When the same amount of crosstalk as before is added to the signal, the BER increases more than in the previous scenario because the signal is already significantly impaired. Hence, to recover pre-crosstalk BER values, a larger OSNR improvement than before is required. In an extreme case, if the ISI or the crosstalk is too large, the eye diagram may close when the crosstalk is added, and a very high BER floor occurs. In such situation, the required is OSNR for the pre-crosstalk BER is infinite, and so is the OSNR penalty. As a conclusion, the impact of crosstalk on the signal performance depends on the shape of the signal without crosstalk. Therefore, it is not possible to calculate the OSNR penalty of a signal impaired by both crosstalk and ISI by just calculating the OSNR penalties for a signal impaired by ISI only and for a signal impaired by crosstalk only and then add them together. Instead, their effect must be accounted for simultaneously.

The effect of the optical filter bandwidth in the crosstalk signal path was also investigated. It has been observed that the bandwidth of that optical filter does not influence significantly the crosstalk penalty. The crosstalk has most impact when a "1" occurs in the crosstalk signal. Since optical filtering in the crosstalk signal path does not change the stationary "1" level, but mainly the bit transitions, the crosstalk induced penalty is also maintained, as in the case of the effect of dispersion on the crosstalk signal, which does not increase the crosstalk penalty. This result agrees with previous investigations of filtered crosstalk signals, which concluded that, when the crosstalk signal is filtered, its penalty is uniquely determined by the SXR [38].

The effect of the detuning of the optical filter in the signal path has also been studied. The results are presented in Fig. 5.13, for an optical filter bandwidth of 15 GHz (super-Gaussian shape with order 1.5). The results show that the OSNR penalty increases as the detuning of the filter increases. As the detuning increases, ISI and some eye closure is introduced, and as in the case of narrow filtering this causes a larger crosstalk penalty. The insets of Fig. 5.13, which show the crosstalk unimpaired eye diagrams, again support this conclusion. The eye diagram where the crosstalk penalty is higher is slightly closed in the "1" level due to the filter detuning. The agreement between experimental, simulation

and MCB results is within 0.1 dB, except for a detuning of 6 GHz, where the discrepancy is 0.3 dB. From 0 to 6 GHz of detuning, the crosstalk-induced OSNR penalty shows, respectively, an increase from about 1 dB to 1.5 dB in the case of the experimental results and from 1 to 1.8 dB for the simulation and MCB results. The optical filter characteristic in the simulation is not so well matched to the experimental shape at the cut-off frequency, and therefore, for a detuning of 6 GHz, the simulated ISI impaired eye diagram is not so well characterized relatively to the experiment. As a consequence, the calculated and experimentally measured OSNR penalties are slightly different for 6 GHz of detuning.

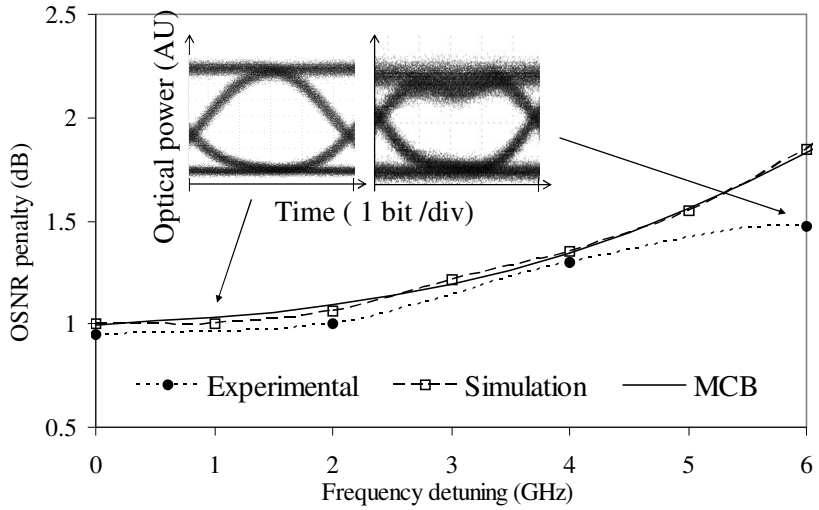

Fig. 5.13 Experimental, simulation and MCB results for the crosstalk induced OSNR penalty as a function of the detuning of the optical filter in the signal path. Insets: experimental eye diagrams of the crosstalk-free signal for a filter detuning of 0.5 and 7 GHz. The dashed lines are guides for the eyes.

The impact of the ISI caused by the electrical filter on the crosstalk induced penalties has also been investigated. The electrical filters used in an optical network are well known and fixed, unlike the equivalent optical filter, which is dependent on the signal path. Still, the same effect of penalty increase has been observed for narrow electrical bandwidths. The simulation and MCB results are shown in Fig. 5.14, for a third order Bessel electrical filter. The optical filter has second order super Gaussian shape and 30 GHz bandwidth. Once again, the agreement between the simulation and MCB is very good. As in the case of narrow optical filtering, the crosstalk induced penalty increases for small filter bandwidths. The penalty increase happens when the electrical filter starts to close the eye diagram at the sampling instant, which for this filter is at around 6 GHz. For

other filter shapes, the same conclusions hold, but the penalty increase and the bandwidth at which penalty the increases are different.

In the results of this section the MCB BER estimate was, in average, 240 times faster to compute than the simulation.

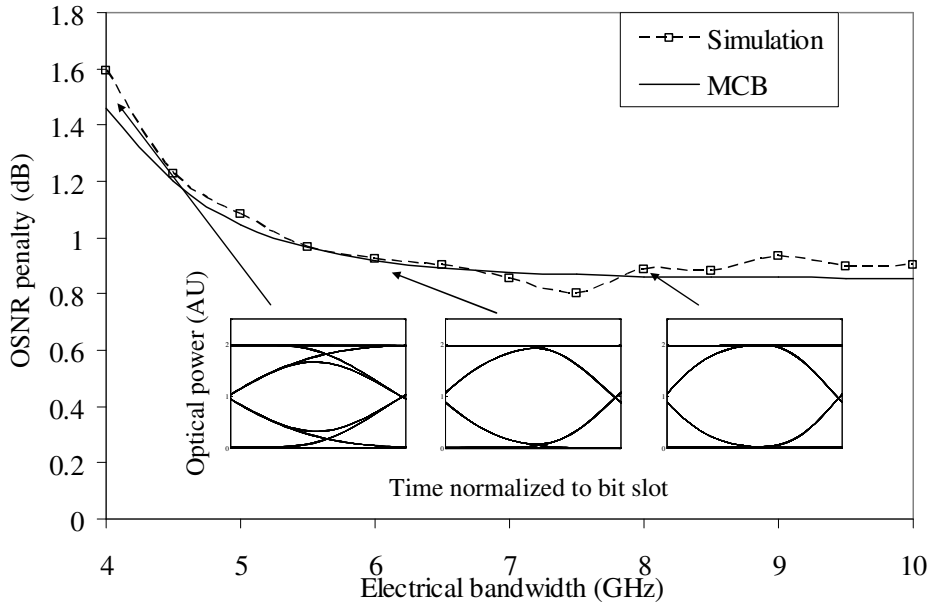

Fig. 5.14 Simulation and MCB OSNR penalty results due to crosstalk as a function of the electrical bandwidth of the electrical receiver. Insets: simulated eye diagrams of the crosstalk-free signal for a filter bandwidths of 4, 6 and 8 GHz. The dashed line is a guide for the eyes.

5.2.3 Network impact

The previous section has shown that higher crosstalk induced OSNR penalties arise when the signal is itself already ISI impaired. This section will provide the results of crosstalk penalty in a network scenario with cascaded OXC, where each OXC filters the signal.

The signal in the network crosses several OXC, which are modelled as a cascade of two second order super-Gaussian optical filters with 25 GHz of bandwidth at -3 dB tuned to the signal frequency. Transmission effects between OXC are not considered. After crossing a number of OXC, the signal is finally filtered by a second order super Gaussian optical filter of 40 GHz bandwidth, before being fed to the photo-receiver and a 7GHz bandwidth third order Bessel shaped electrical filter. The signal is affected by one crosstalk interferer with SXR = 20 dB. Both simulation and MCB results are shown in Fig. 5.15.

The OSNR penalties are measured relatively to zero OXC, i.e., only the receiver filter is considered in the signal path. The penalty due to filtering increases steadily and becomes 1 and 2 dB after 15 and 26 OXCs, respectively. The expected crosstalk penalty, i.e. considering an ISI unimpaired signal, is constant at about 0.7 dB. However, according to simulation results, the crosstalk penalty increases for more OXCs due to the ISI, as explained before. It reaches 1 and 1.5 dB at 15 and 27 OXCs, respectively. Both the expected and simulated total penalties are also shown in Fig. 5.15. Whereas the expected total penalty does not account for the increase of the crosstalk penalty due to the filtering ISI, the simulated total penalty accounts for this effect and therefore increases more steeply. For a total penalty of 1.5 and 2 dB the expected maximum number of cascaded OXC by simulation are 13 and 18, while considering the increased crosstalk penalty due to signal ISI the maximum number of OXC are 10 and 15. The MCB prediction is within ±1 OXC relatively to the simulation. Considering the results, the increase of the crosstalk penalty when the signal is impaired by optical filtering can have a significant impact on the network performance and should be considered when planning a network.

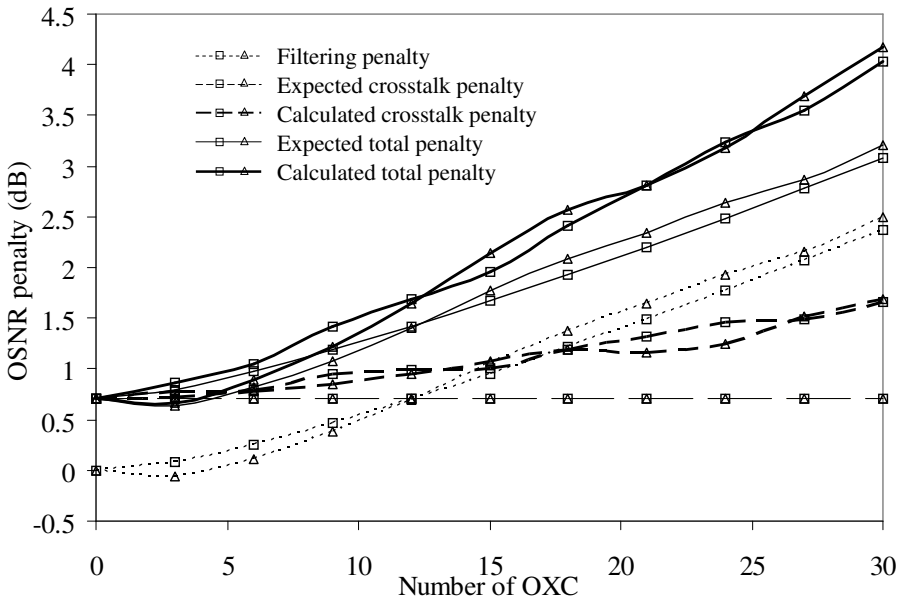

Fig. 5.15 Accurate (calculated) and expected crosstalk and total (crosstalk and filtering) OSNR penalties as a function of the number of OXC in the network, for one crosstalk channel with 20 dB of SXR. The calculated (expected) total penalty is the sum of the filtering penalty and the calculated (expected) crosstalk penalty. The squares and triangles stand for simulation and MCB results, respectively. The lines connecting the data points are guides for the eyes.

5.3 Crosstalk in time slot interchanger

Crosstalk also arises in optical processing sub-systems with space switch fabrics. In the previous chapter, in section 4.3, a time slot interchanger (TSI) was presented, based on wavelength conversion on the MZI-SOA. The role of the TSI is to delay a packet by a selectable amount of delay. The TSIs can either be built with wavelength converters that select the amount of delay according to the output wavelength, as done in chapter 4, or by fast space switches that select the delay according to the switch output. In this section, a TSI is investigated that exploits the MZI-SOA operation as a switch, which requires fewer components, such as lasers and multiplexer and demultiplexer filters. The downside is that crosstalk is introduced between inputs and therefore the performance is hampered. Moreover, due to the amplifying nature of the SOA, ASE noise is also added to the signal, resulting in a lower OSNR at the switch output. The method to calculate the performance of signals impaired by crosstalk and ASE presented in the beginning of this chapter is then perfectly suited to assess the performance of the switch-based TSI.

The interest in the MZI-SOA for a space switched TSI lies on the capability of steering the signal at the input port to any of the two output ports. The output port is chosen according to the presence or absence of the control signal. The output ports of the MZI-SOA are commonly called switched and unswitched ports depending whether the control signal was applied or not. However, the MZI-SOA will not completely transmit the power from the input to a single output port. The MZI-SOA switches the input signal between outputs depending on the phase shift caused by the control signal on the probe signal that is induced through cross phase modulation (XPM) in the SOA. Since the XPM in SOAs is accompanied by cross gain modulation (XGM), the switch becomes unbalanced because one SOA will have lower gain than the other. Consequently, there will be some power leaking at the blocked output port, which will cause crosstalk. The contrast ratio of the switch outputs is defined as the ratio of the power levels between the ‘on’ and ‘off’ state for each port. This is the quantity of interest to simulate the MZI-SOA operation since it determines the amount of crosstalk produced in the MZI-SOA.

Since the focus now is on the crosstalk and ASE that the MZI-SOA switches introduce, and not on the time evolution of the signal like in the previous chapter, the MZI-

SOA will be analytically modelled. To fully describe the MZI-SOA operation, the model must take into account the contrast ratios of the MZI-SOA switch outputs and the ASE accumulation over the MZI-SOA.

With identical SOAs in each arm of the MZI-SOA and 50:50 couplers, optimum operation is obtained with unequally current bias in each SOA to compensate for the switch unbalancing due to XGM. In these conditions, the same contrast ratio *X* is achieved for both switched and unswitched states and is given by [5]:

$$X = \coth^2(\pi/4\alpha) \tag{5.34}$$

where α denotes the SOA alpha-factor, which is basically the ratio of gain and phase modulation in the SOAs. The contrast ratio determines the amount of crosstalk that each switch introduces in the switched off output. It is important that the contrast ratios of both outputs and switch states are identical. If not, improving the contrast ratio of one output port would impair the contrast ratio of the other output. The overall performance would be limited by the worst output, and therefore the performance would be worse than in the case that both outputs have the same contrast ratio.

The contrast ratio of the MZI-SOA for equal contrast ratio in both states and output ports is plotted as a function of the alpha factor in Fig. 5.16. For an alpha factor of 5, the contrast ratio is about 16 dB, which is quite low for typical space switch applications. In order to attain a contrast ratio of 20 dB, an alpha factor of 7.8 is required. Hence, for the typical alpha factor values, the contrast ratio is between 15 dB to 25 dB, which will be the range used hereafter. The SOAs used in chapter 3 was modelled with an alpha factor from carrier depletion of 3.5, which corresponds to a contrast ratio of about 14 dB, which is rather low for switching applications.

The second aspect of the MZI-SOA that is modelled is the introduction of the ASE noise from the SOAs. The method typically used for EDFA cascading is employed for the SOAs in a straightforward way. Each SOA amplifies the incoming ASE from previous stages and adds the ASE power spectral density S_{ASE}, that can be calculated from the SOAs gain *G* and spontaneous-emission factor n_{sp} [39]:

$$S_{ASE} = (G-1)n_{sp}h\nu \tag{5.35}$$

where *h* is the Planck constant and υ is the frequency of the optical field. It is assumed that the gain of the SOAs in the MZI-SOA matches the losses between MZI-SOAs in the TSI. It is also assumed that the Mach-Zehnder structure of the MZI-SOA does not affect the

ASE noise properties of generated by previous SOAs, although the power of incoming noise is amplified by the SOAs.

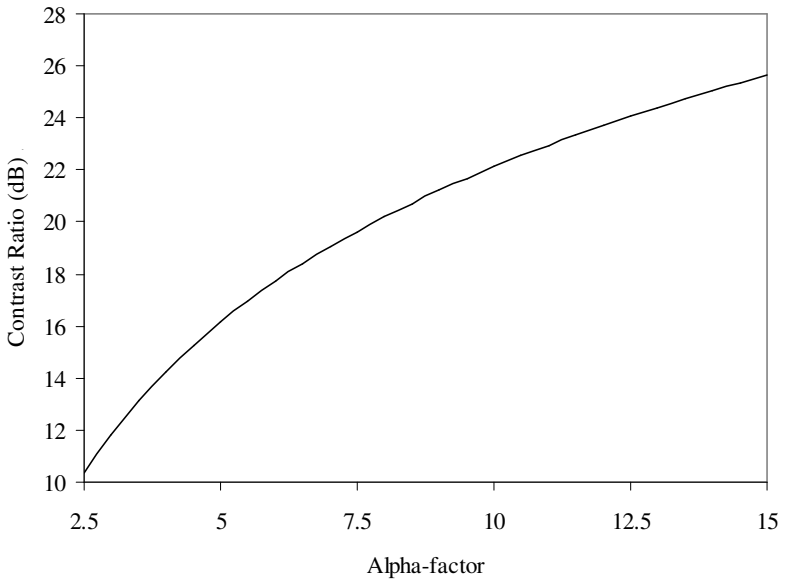

Fig. 5.16 Contrast ratio of the MZI-SOA switch as a function of the SOA alpha factor, for asymmetrical SOA bias given by [5].

The space switch based TSI is depicted in Fig. 5.17 with two stages. This configuration will be called the standard configuration. Each TSI stage comprises a MZI-SOA space switch with an ODL at one of its outputs, and no ODL at the other output. The MZI-SOA switch at the k^{th} stage selects if the packet is delayed, or not, by an amount $T_p \times (2^k\text{-}1)$, where T_p is the packet duration. At the end, a coupler combines the two outputs of the last stage MZI-SOA switch. Hence, the n stages TSI is capable of producing a delay between 0 and $T_p \times (2^n\text{-}1)$, with granularity T_p. In the example of Fig. 5.17, the first packet is delayed by T_p, while the second packet is delayed by $2T_p$.

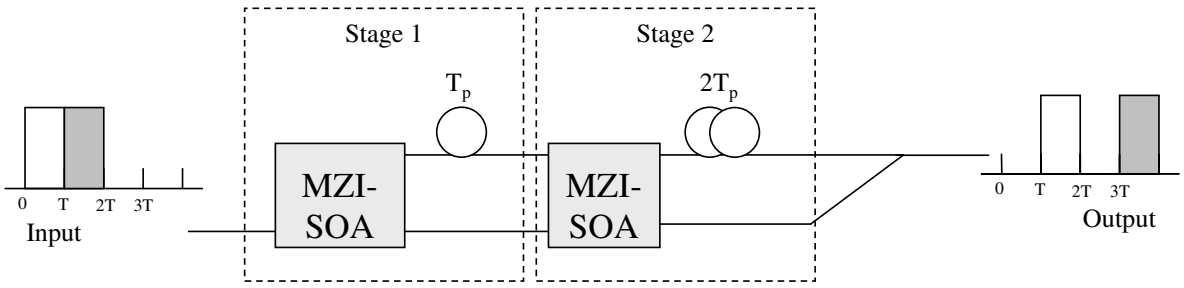

Fig. 5.17 Standard time slot interchanger with two stages.

The less then ideal contrast ratio of the MZI-SOA will produce delayed or early replicas of the signal, which will interfere with other packets incoming to the TSI. This situation is depicted in Fig. 5.18. For simplicity, only one packet is assumed to arrive at the TSI, and it is chosen that the packet is not delayed. Due to non ideal contrast ratio (an exaggeratedly low value of 3 dB was used in Fig. 5.18), an unwanted packet replica is produced at the first MZI-SOA and is delayed by T_p. The packet and its replica are propagated to the next MZI-SOA, which, in turn, produces another unwanted packet replica, and one additional spurious replica of the packet replica. Thus, the two stages TSI produces three undesired packet replicas at different delays. This reasoning has allowed determining not only the delay of the replicas, but, more importantly, the power of the replicas. The power of the replicas that are produced directly from the signal is the power of the signal divided by the contrast ratio. The power of replicas of replicas is the signal power divided by the square of the contrast ratio, and so on for replicas of replicas of replicas. Although it was assumed that the packet had no delay in each TSI stage, the same conclusions hold for other delays. Also, in this situation, only one packet was assumed to be fed to the TSI. However, the worst case is when all slots contain packets, and each packet will receive replicas from all neighbouring packets, within the delay range of the TSI. For TSIs with more stages, the same reasoning can be applied, resulting that more crosstalk interfering packets are added to the main signal. Table 5-1 presents the crosstalk replicas that arise at the output of the TSI, for one up to four stages. The order of the replicas is denoted by the exponent of the contrast ratio *X*. When the replicas are directly obtained from the signal they are said to be first order, and their power is the signal power divided by the contrast ratio with exponent 1. When the replicas are originated from other replicas they are second order and the exponent is 2, and so forth for higher order replicas and crosstalk. The data of Table 5-1 is an input of the model to calculate the crosstalk induced power penalty.

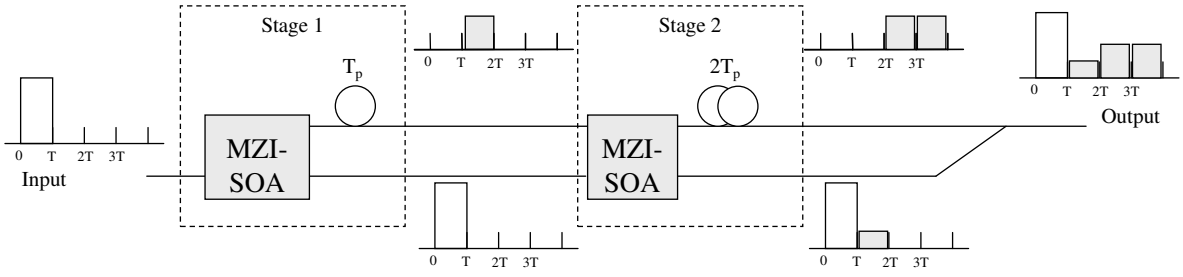

Fig. 5.18 Schematics of crosstalk accumulation in the standard TSI. The greyed out packets are crosstalk.

Table 5-1 Number of crosstalk terms at the TSI output, as a function of the number of TSI stages and of the contrast ratio order.

Standard TSI					Improved TSI			
X	X^2	X^3	X^4	Stages	X	X^2	X^3	X^4
1				1		1		
2	1			2		3		
3	3	1		3		6		1
4	6	4	1	4		10		5

It will be assumed that the crosstalk between packets is in-band, since one TSI will typically serve the same wavelength at a network node input. Also, it will be assumed that the optical phases of the signal and crosstalk signals are decorrelated, since packets are arrive from different origins and are produced from different optical sources.

In the forthcoming results, the extinction ratio of the incoming signals is 15 dB, the SOA gain is 26 dB and the spontaneous-emission factor is 1, which is the theoretical minimum. The interstage losses are exactly compensated by the MZI-SOA chip gain. For now, the impact of the ASE is reduced to keep the focus on the crosstalk, but, at a later stage, the impact of n_{sp} on the performance will also be investigated. The MCB BER calculation method will be used to evaluate the performance of the MZI-SOA based TSI in the switch configuration in terms of power penalties, to include also the effect of the accumulating ASE. The power penalty is determined by the required power at the receiver input to attain a BER of 10^{-10} of the signal under analysis subtracted by the same quantity but calculated for the input signal. This definition is the same as in the analysis of the wavelength converter based TSI so that both results can be compared.

Fig. 5.19 plots the power penalty of the TSI as a function of the contrast ratio, for one, two and three stages. The one stage TSI has 2.6 dB and 1.5 dB power penalties, respectively, for a contrast ratio of 16 dB and 20 dB, corresponding to alpha factors of 5 and 7.8, respectively. The reasonable performance is because only one crosstalk interferer is present, and ASE noise is only added from one pair of SOAs. However, the two stages TSI shows a BER floor above 10^{-10} and therefore an infinite power penalty is obtained for a contrast ratio below about 17 dB. Obviously, the performance of the three stages TSI is even worse, with BER floor at about 21 dB of contrast ratio. Clearly, the crosstalk is too large in these situations and consequently this TSI architecture is not useful.

The standard TSI configuration shown in Fig. 5.17 can be improved for better scalability by replacing the coupler at the TSI output by an additional MZI-SOA switch, as

depicted in Fig. 5.20. The additional MZI-SOA selects the correct output of the previous MZI-SOA to be transmitted to the TSI output, while the other MZI-SOA output is discarded. Hence, the crosstalk exiting from the unwanted port of the last-but-one switch is avoided and thus the performance is enhanced, as shown in Fig. 5.21.

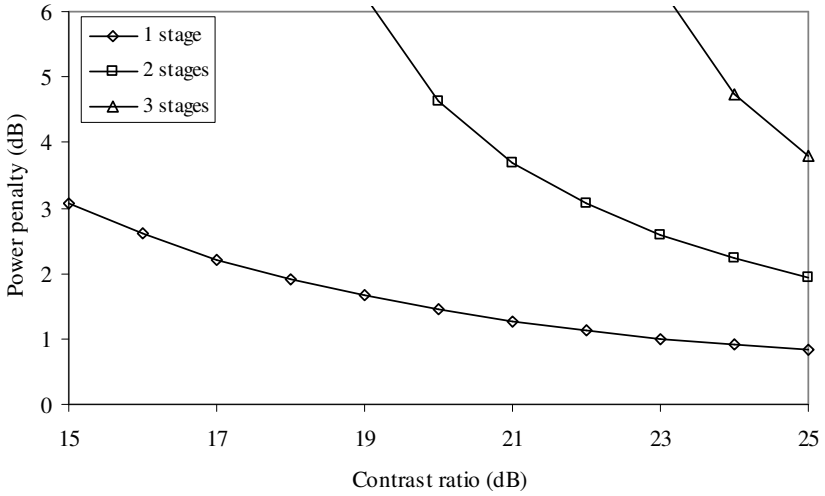

Fig. 5.19 Power penalty introduced by the standard TSI, as a function of the contrast ratio of the individual MZI-SOA switch. The lines are guides for the eyes.

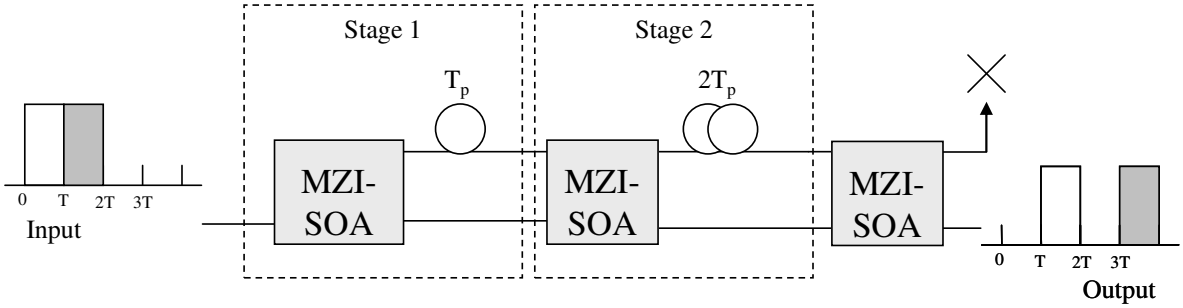

Fig. 5.20 Improved time slot interchanger with two stages.

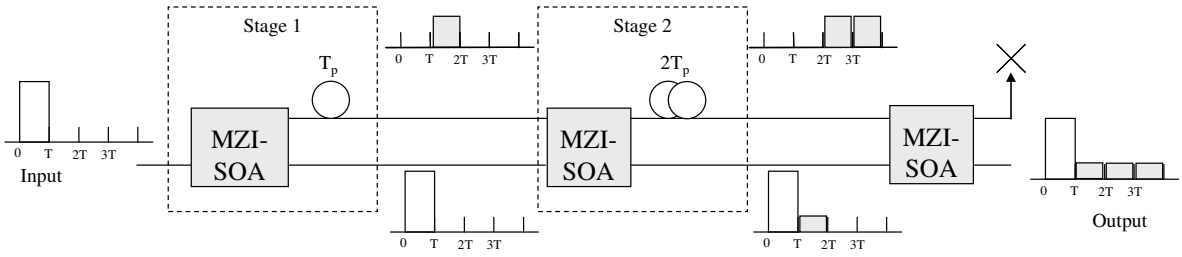

Fig. 5.21 Schematics of crosstalk accumulation in the improved TSI. The greyed out packets are crosstalk.

The results for the improved TSI are presented in Fig. 5.22. The first impression is that the power penalties are much smaller than in the case of the standard TSI. For a contrast ratio of 15 dB and one TSI stage, the penalty is now 0.93 dB, whereas it is 3.1 dB for the standard TSI. The three stages improved TSI does not show an error floor, which is a great improvement compared to the standard TSI. Only the four stages TSI shows an error floor at about 15 dB of contrast ratio, and a penalty of 2.5 dB for a contrast ratio of 20 dB. It is also noticeable that the performance is not as strongly dependent on the contrast ratio, and hence on the alpha factor, as in the standard TSI, which leaves more tolerance on the alpha-factor when fabricating these devices. In fact, for increasing contrast ratios, the power penalty becomes almost constant, due to the lower crosstalk impact. Since in the improved TSI only crosstalk terms on the second order of the contrast ratio appear, the crosstalk effect is quite low. For example, a contrast ratio of 15 and 25 dB will cause crosstalk terms at an SXR of 30 and 50 dB, respectively. When the SXR is 50 dB, the crosstalk typically has negligible effects on the performance. In the region where the power penalty is constant on the contrast ratio, the predominant effect limiting the performance is the ASE noise.

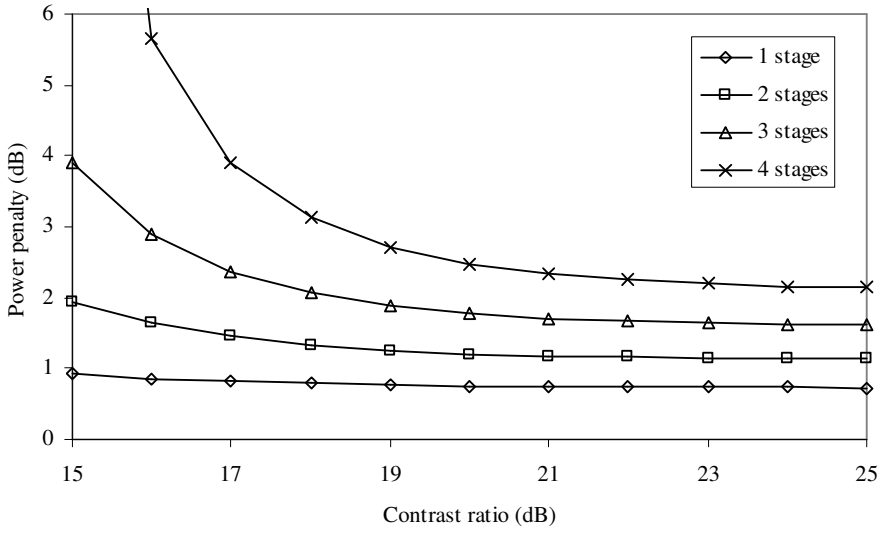

Fig. 5.22 Power penalty introduced by the improved TSI, as a function of the contrast ratio of the individual switch. The lines are guides for the eyes.

Since it was observed that the ASE noise was the main limiting factor, the spontaneous-emission factor n_{sp} was varied from zero, which corresponds to no ASE generation, up to three, corresponding to an approximate amplifier noise figure of 7.8 dB.

The results are plotted in Fig. 5.23, considering a two stages improved TSI. For no ASE generation (n_{sp} = 0), only the crosstalk effect is considered. The results show that, in this situation, the penalty is very low, which corroborates the effective crosstalk mitigation of the improved TSI architecture. As the spontaneous emission factor increases, the penalty also increases and reaches 2.8 dB for a contrast ratio of 20 dB and a spontaneous emission factor of 3. It is not uncommon that SOAs optimised for non-linear processing have such high spontaneous emission factors and thus the performance of the improved TSI can be limited by ASE noise accumulation.

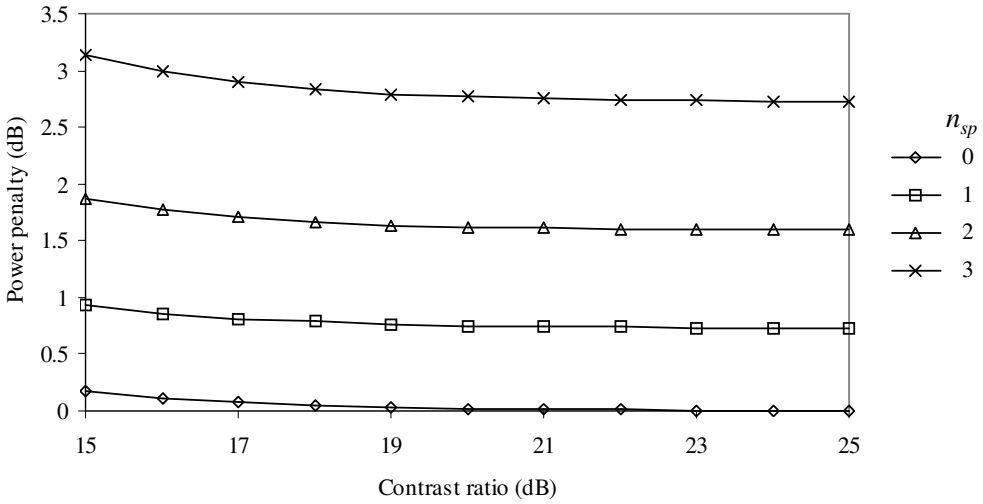

Fig. 5.23 Power penalty introduced by the two stages improved TSI for various spontaneous-emission factors n_{sp}. The lines are guides for the eyes.

In general, in the improved TSI configuration, the crosstalk is successfully mitigated by the additional MZI-SOA at the TSI output and although more ASE is added to the signal, the overall performance is improved, comparing to the standard TSI. Therefore, it is highly recommendable that the improved configuration of Fig. 5.20 is used instead the standard configuration of Fig. 5.17.

These results of the improved TSI can be compared with the results of the wavelength conversion based TSI of section 4.4 in chapter 4. The power penalty of the three stages wavelength converter based TSI was 1.35 dB, whereas for the improved TSI it is 1.77 dB, for a contrast ratio of 25 dB. Although the penalties do not differ much, it should be emphasized that the wavelength converter based TSI has more delay possibilities per TSI stage and therefore it is advantageous relatively to the switch based TSI.

Additionally, for the same number of TSI stages, the space switch based TSI requires one more MZI-SOA device than the wavelength converter based TSI.

5.4 Effect of fibre transmission effects in crosstalk penalties

It has already been mentioned that, although OXCs provide a flexible, simple and transparent way of routing the traffic in the optical domain, optical impairments such as amplified spontaneous emission (ASE) noise and crosstalk accumulate over the network. Additionally, group velocity dispersion (GVD), and self phase modulation (SPM), are also accumulated [40], especially when there is no regeneration. As it was already seen in section 5.2, when crosstalk affects signals that are already distorted, in that case by narrow filtering, penalties larger than expected may occur. Therefore, appropriate network planning is required to assess the number of cascaded OXC before a prescribed penalty is obtained.

In an optical network with long transmission links, the signals that cause crosstalk are also impaired by transmission effects such as dispersion and nonlinear propagation. Since the crosstalk signal is eventually distorted during transmission, a crosstalk induced penalty different to that given in extant methods may arise.

In this section, it is shown both experimentally and by simulation that the crosstalk penalty resulting from signals impaired by SPM and GVD is larger in some cases than the crosstalk induced penalty assuming an undistorted crosstalk signal, i.e. without distortion from SPM/GVD. Furthermore, the crosstalk induced penalty depends on the accumulated dispersion of the considered dispersion map of the impaired crosstalk signal. Finally, some considerations are made regarding the operating parameters of the network, taking the correct crosstalk penalty into account.

In this section, the MCB method is not used to evaluate the network performance since it does not properly model the effect of distorted crosstalk signals, as mentioned in the derivation of the method, in section 5.1.1.

5.4.1 Experimental and simulation setups

The experimental setup is depicted in Fig. 5.24 and consists of a 2^{12}-1 PRBS, 10 Gb/s optical intensity modulated non-return to zero (NRZ) transmitter (Tx) which output is split into the signal and the crosstalk signal. The signal is directly connected to an optical combiner and does not suffer any transmission. The crosstalk signal passes through a nonlinear transmission link, which consists of three 80 km spans of standard single mode fibre (SSMF), where the first two spans are fully dispersion compensated by dispersion compensation modules (DCM), and the third span is optionally under or over compensated. No pre-compensation has been used, according to the usually called fully inline and optimised post-compensation scheme (FOCS) dispersion map [41]. This dispersion map allows the compensation of some self phase modulation through dispersion in the pseudo-linear transmission regime, and therefore larger transmission distances are achieved. An erbium doped fibre amplifier (EDFA) boosts the crosstalk signal power before each transmission fibre span. A three span transmission link has been used, but the results are extensible in a straightforward way to more realistic transmission links, with a larger number of spans (N_{spans}) and less fibre input power (P_{fibre}), as long as $P_{fibre} \times N_{spans}$ remains constant [41]. After the transmission link, a polarization controller (PC) ensures that both the signal and crosstalk signal have the same polarization state when they are added together in the optical combiner, which is a worst case of signal performance. Due to changes in environmental conditions, the relative signal to crosstalk delay changes randomly, and their bit alignment wanders, as in a realistic network situation. When, for comparison purposes, negligible impact from SPM on the crosstalk signal is desired, the nonlinear transmission link may be replaced by a linear transmission link consisting of a single SSMF span with full dispersion compensation and a low optical power is used at the fibre input. A one span link is used instead of a few meters of fibre to have drifts in the phase and delay of the crosstalk signal, similar to the three spans link case. An attenuator on the crosstalk path is used to adjust the signal to crosstalk ratio (SXR). ASE noise is added to the crosstalk impaired signal, before being fed to an optically filtered receiver. The BER is then measured with optimum decision threshold as a function of the optical signal to noise ratio (OSNR). The OSNR penalty is given by the difference of the OSNR required to achieve a BER of 10^{-9} between the signal with and without crosstalk.

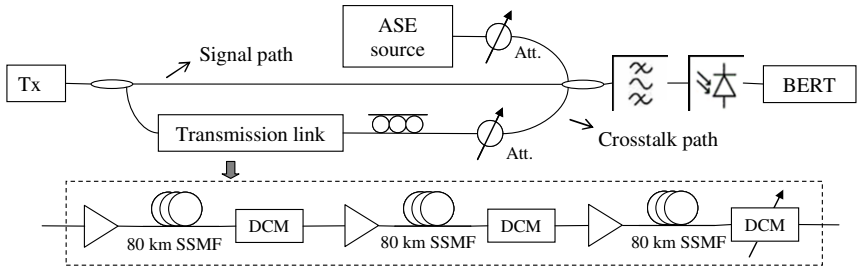

Fig. 5.24 Experimental and simulation setup layout.

The simulation setup is similar to the experimental setup. To simulate the drift of the delay and phase of the crosstalk signal, uniformly distributed random delay and phase [32] between the crosstalk and the signal are introduced. The BER results are obtained from 1000 simulation runs of a signal produced from a 2^{10} de Bruijn sequence, each having different crosstalk phase and delay, and by analytically accounting for the ASE noise [16], as before. The optical filter and the electrical post-detection filter are modelled as second order super-Gaussian filter with -3 dB bandwidth of 50 GHz and third order Bessel filter with -3 dB cut-off frequency of 10 GHz, respectively, which match well the characteristics of the experimental equipment.

The OSNR penalty assuming a crosstalk signal impaired by SPM and GVD has been both calculated by simulation and measured experimentally, for different accumulated dispersion values as a function of the SXR.

5.4.2 Results

The results are presented in Fig. 5.25, for 11 dBm of fibre input power. The OSNR penalty assuming an undistorted crosstalk signal is also presented for comparison purposes. Three accumulated dispersion values have been used for the SPM impaired crosstalk signal: 850 ps/nm, which is close to the optimum accumulated dispersion for achieving the best eye opening [41]; -170 and 1700 ps/nm which are, respectively, extreme under and over compensation values for a signal strongly affected by SPM. It can be seen that both the simulation and the experimental results exhibit the same trend. Comparing the OSNR penalty obtained for the crosstalk signal impaired by SPM and GVD to the case of undistorted crosstalk, shows that the accumulated dispersion values of 850 and 1700 ps/nm yield a higher OSNR penalty, whereas -170 ps/nm yields a lower OSNR penalty. Considering 20 dB of SXR, the penalty for the SPM impaired crosstalk signal with accumulated dispersion 1700 ps/nm is 0.5 dB higher than the penalty of 1.75 dB for the

undistorted crosstalk. On the other hand, for -170 ps/nm, the penalty is 0.1 lower than that for the unimpaired crosstalk.

These differences in the OSNR penalties can be explained by the eye patterns in Fig. 5.26, which plots both the simulated and experimental eye diagrams of the crosstalk signal, for different accumulated dispersions of the crosstalk signal, and the simulated eye patterns of the signal impaired by crosstalk. The simulated eye patterns were obtained with no ASE noise, for a better visualization of the effect of the distortion due to SPM. When the crosstalk signal is impaired by SPM and GVD for 850 and 1700 ps/nm of accumulated dispersion, it contains strong overshoots which cause significant eye closure of the crosstalk impaired signal. On the other hand, due to the different phase to intensity conversion at the tuneable DCM, for -170 ps/nm, the crosstalk signal does not have overshoots and the obtained eye opening and crosstalk induced OSNR penalty are comparable to the case of the undistorted crosstalk signal.

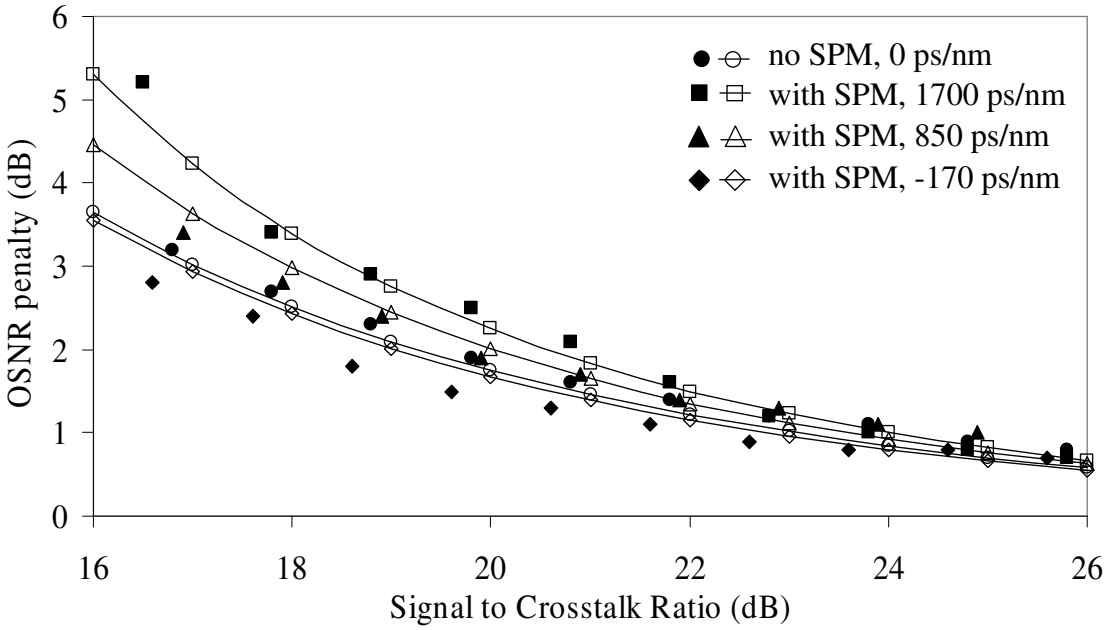

Fig. 5.25 Simulation (open symbols) and experimental (full symbols) results of the OSNR penalty versus the SXR, for a crosstalk signal without SPM, and with SPM, for accumulated dispersions of -170, 850 and 1700 ps/nm. The lines connecting the data points are guides for the eyes.

The results of the crosstalk induced OSNR penalty as a function of the delay between the signal and crosstalk signal are presented in Fig. 5.27. Comparing the crosstalk signal eye diagrams of Fig. 5.26 and the results of Fig. 5.27, it has been verified that the worst case of delay between signal and crosstalk signal is when the overshoots in the

crosstalk signal occur at the point of largest aperture of the signal eye diagram. A similar effect happens when there is crosstalk from an RZ formatted signal to an NRZ signal. Although it is less likely for an optical network to have NRZ and RZ signal in the same nodes, this case has also been investigated and some results are shown in Appendix G. The crosstalk impaired eye diagrams in Fig. 5.26 are worst cases and the delays are 0 ps for a) and c), and 50 ps for b) and d).

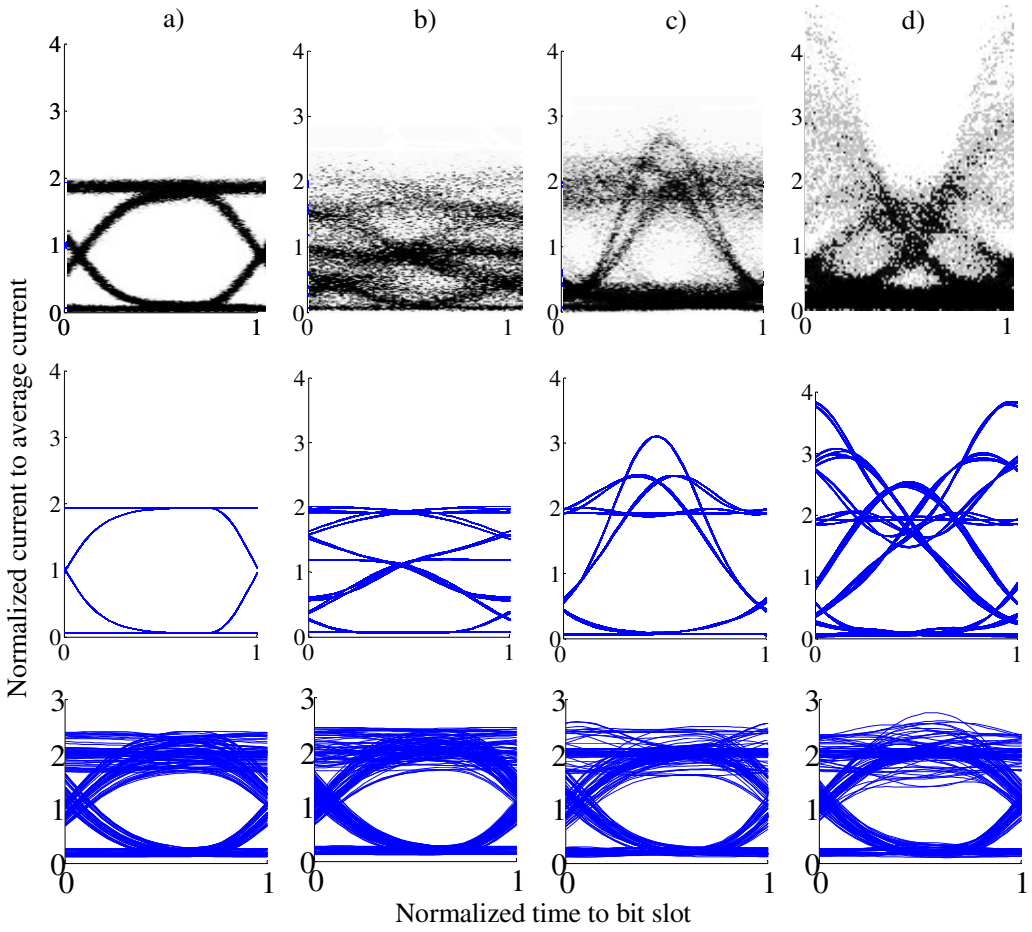

Fig. 5.26 Experimental (top row) and simulated (middle row) eye diagrams at a) the transmitter output, and at the transmission link output for accumulated dispersions of b) -170, c) 850 and d) 1700 ps/nm. The bottom row shows the eye diagrams of one simulation run of the signal impaired by the crosstalk signals of the rows above, for SXR=20 dB.

The crosstalk induced OSNR penalty results as a function of the accumulated dispersion of the crosstalk signal are shown in Fig. 5.28. Both linear and nonlinear transmission were considered, as well as two different optical filter bandwidths, 50 and 30 GHz, to investigate the effect of optical filtering. The insets of Fig. 5.28 show the optical spectra of the crosstalk signal without and with SPM at the output of the last SSMF.

Identical optical spectra are obtained at the output of the tuneable DCM independently of the accumulated dispersion since only linear transmission is considered along the tuneable DCM. The results show that, for linear transmission, the OSNR penalty is almost constant in the studied range of accumulated dispersion, which covers the acceptable region for a 10 Gb/s signal. GVD does not produce significant overshoots in the crosstalk signal and therefore the penalty does not increase. Additionally, for linear transmission the effect of the optical filter bandwidth is negligible.

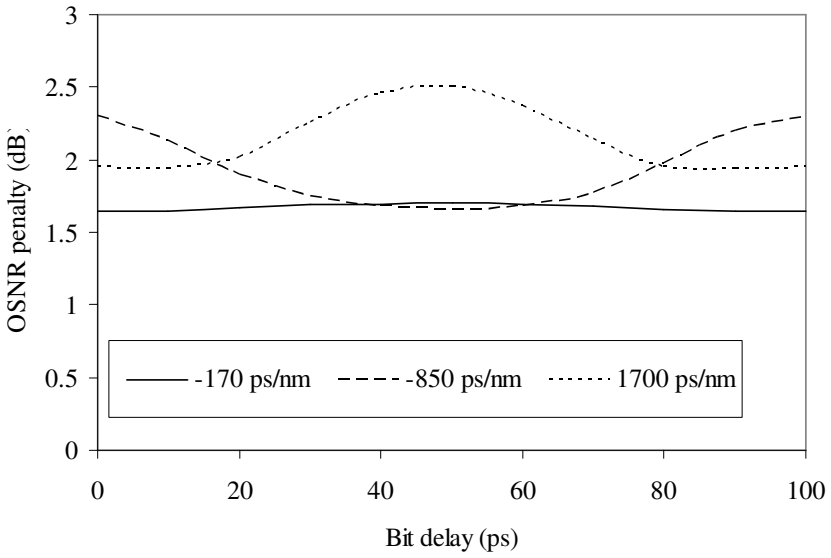

Fig. 5.27 OSNR penalty as a function of the bit delay between signal and crosstalk signal. The crosstalk signal had a fibre launch power of 11 dBm, and the accumulated dispersion values are -170, 850 and 1700 ps/nm.

Regarding the nonlinear transmission results, especially for 14 dBm, the 30 GHz results show a slightly lower penalty, when comparing to 50 GHz, since the SPM-broadened crosstalk signal optical spectrum is partially filtered, but the crosstalk signal still retains the overshoots seen in Fig. 5.26. For 14 dBm, the OSNR penalty is constant for negative accumulated dispersion and strongly increases for positive dispersion values. For 7 dBm, the OSNR penalty curve has a less pronounced increase comparing to the 14 dBm case. For both the considered input powers in nonlinear transmission the penalty is constant for negative accumulated dispersion and increases for positive accumulated dispersion.

Further results, presented in Fig. 5.29, have shown that, for post-detection electrical bandwidths down to 6 GHz (for which there is already signal eye closure due to filtering),

the same qualitative conclusions hold, but the increase in the crosstalk induced penalty due to SPM is less significant due to filtering of the crosstalk signal overshoots.

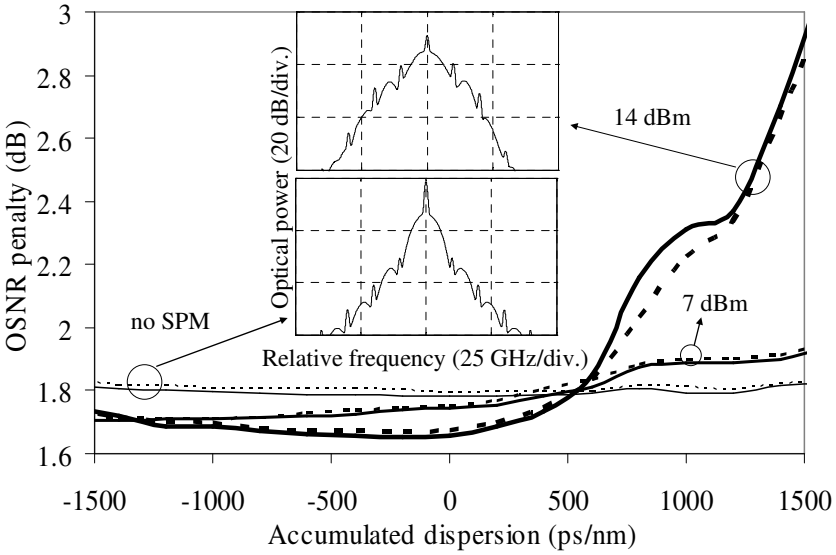

Fig. 5.28 Simulated crosstalk induced OSNR penalty as a function of the accumulated dispersion of the crosstalk signal (SXR=20dB), for linear (no SPM) and non-linear transmission (7 and 14 dBm input power), and for an optical filter bandwidth of 30 (dashed line) and 50 GHz (solid line). Insets: crosstalk signal optical spectra without and with SPM (14 dBm). The optical spectra resolution is 0.01 nm.

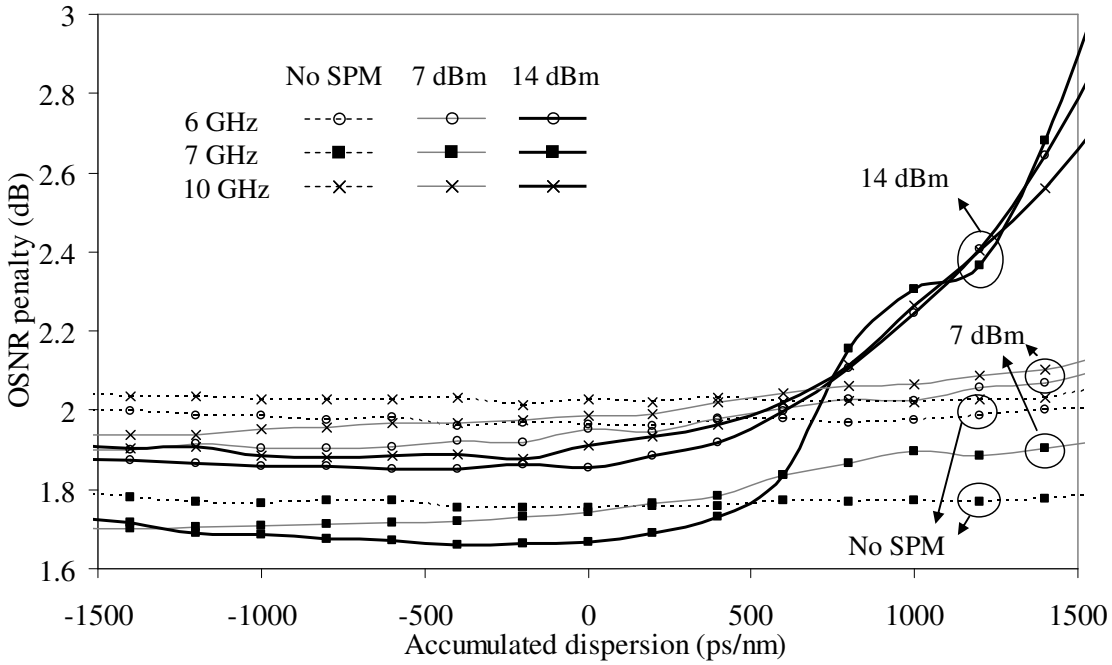

Fig. 5.29 Simulated crosstalk induced OSNR penalty as a function of the accumulated dispersion of the crosstalk signal (SXR=20dB), for linear (dotted line) and non-linear transmission (7 and 14 dBm input power, grey and black line, respectively), and for an electrical filter bandwidth of 6 (crosses), 7 (circles), and 10 GHz (squares). The lines connecting the data points are guides for the eyes.

Finally, Fig. 5.30 presents the crosstalk induced OSNR penalty as a function of the fibre input power and the accumulated dispersion of the crosstalk signal. Fig. 5.30 also presents the eye opening penalty (EOP) of the crosstalk signal at the transmission link output, using as reference the optical transmitter output. The eye opening is defined as the ratio between the minimum level of the 'ones' and the maximum level of the 'zeros', considering a 20% bit width rectangle [41]. This definition is different than the previously defined ECP for phase modulated signals used in chapter 4. An EOP less than 1 dB is acceptable [41]. The results show that if an optimum accumulated dispersion is adopted for the crosstalk signal, i.e. where the EOP is minimum, the crosstalk induced OSNR penalty is higher than in the case of undistorted crosstalk. As an example, for 11 dBm, the optimum accumulated dispersion for the crosstalk signal is about 800 ps/nm. In this case, the crosstalk induced OSNR penalty is 2.0 dB instead of 1.75 dB, as expected for an undistorted crosstalk signal. Hence, for proper network planning, the correct crosstalk induced OSNR penalties should take into account the dispersion map and input powers of the crosstalk signal. It can also be seen from Fig. 5.30 that lower accumulated dispersion values should be used for the crosstalk signal whenever it is possible, to minimize the crosstalk induced penalty.

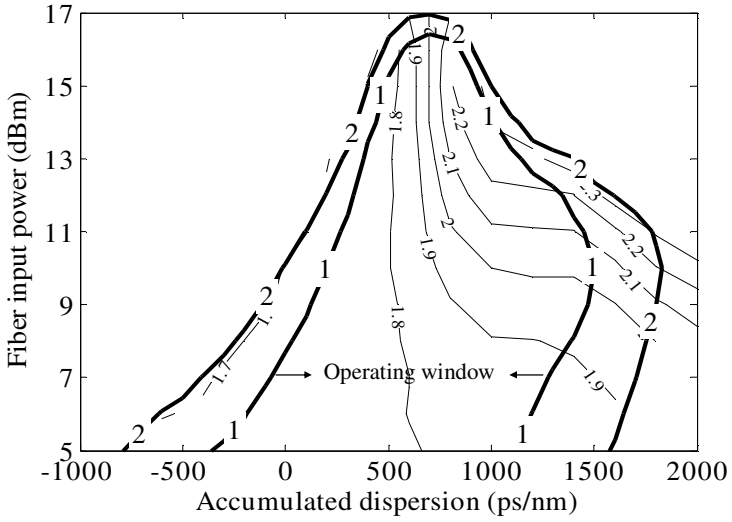

Fig. 5.30 Crosstalk signal eye opening penalty (bold line) and OSNR penalty of the signal due to crosstalk (thin line) for SXR = 20dB, as a function of the fibre input power and accumulated dispersion of the crosstalk signal.

5.5 Conclusions

In this chapter, a method based on the MCB to calculate the impact of crosstalk in optical systems impaired by intersymbolic effects was presented. However, unlike the standard MCB method, for the first time, this method combines signal simulation to account for intersymbolic effects and the computation simplicity of the MCB to account for the crosstalk and ASE noise impact.

With the standard MCB method, BER results in agreement with experimental values can be obtained for systems employing arbitrary optical and electrical filter shapes, with electrical bandwidths larger than 70% of the bit rate. The novel method enables to calculate the BER accurately for narrower electrical filter bandwidths, by calculating through simulation the eye closure caused by the reduced filter bandwidth. Considering both the experimental and simulation evidence, the novel BER calculation method is both computationally simple, efficient and accurate, and is believed to be a useful tool for designing WDM optical networks impaired both by crosstalk and ASE, employing arbitrary optical and electrical filter shapes.

The MCB method was then employed to calculate the combined impact of crosstalk and narrow and detuned optical filtering, and narrow electrical filtering. It has been shown that combined effect of crosstalk and optical filtering causes OSNR penalties that higher than the sum of the OSNR penalties of both effects taken separately. The penalty increase happens when the filtering causes signal eye closure. Although the electrical filter can be chosen to be wide enough to prevent this effect, the crosstalk penalty can significantly increase in networks with a large number of cascaded OXC. As a practical example, it has been shown that for a maximum acceptable total OSNR penalty of 2 dB the number of admissible cascaded OXC reduces from 18, considering separately the effect of filtering and crosstalk, to 15, considering both effects together, which corresponds to a decrease of 17% in the number of OXCs.

Then, a time slot interchanger (TSI) based on MZI-SOA space switches was evaluated in terms of crosstalk. It was shown that the standard TSI architecture is severely limited by crosstalk accumulation and therefore its scalability is not adequate for practical application. For a contrast ratio of the individual MZI-SOA space switch of 20 dB, the one stage standard TSI has a power penalty of 1.5 dB, whereas for two stages the penalty rises

unacceptably to 4.6 dB. Thus, an improved TSI architecture has been presented, which features an additional MZI-SOA space switch at the TSI output that rejects some of the crosstalk introduced in precedent MZI-SOA space switched. Although more ASE noise is introduced, the crosstalk is significantly mitigated, resulting in an overall improved performance. The power penalties introduced by the improved TSI are 0.75, 1.21, and 1.77 dB for one, two and three stages, respectively, and a contrast ratio of 20 dB.

Finally, the scenario where the crosstalk signal is impaired by chromatic dispersion and SPM was studied. Results have shown that the overshoots caused by SPM in the crosstalk signal can cause higher than expected crosstalk penalties. Moreover, the increase of the crosstalk penalty due to SPM is dependent on the dispersion map of the crosstalk signal and increases for positive accumulated dispersions. Therefore, if crosstalk is an issue in the network, in order to minimize the impact of crosstalk, the dispersion map of the network should be regarded as a whole, bearing in mind that the dispersion map of one signal can affect another signal performance through crosstalk. In fact, if the accumulated dispersion of the crosstalk signal affected by SPM and GVD is optimised to give the best eye opening, the crosstalk induced OSNR penalty of the signal is higher than in the case of an undistorted crosstalk.

As a rule of thumb, lower accumulated dispersions in the crosstalk signal should be used to minimize the magnitude of the crosstalk induced penalties.

5.6 References

[1] J. L. Gimlett and N. K. Cheung, "Effects of phase to intensity noise conversion by multiple reflections on Gigabit-per-Second DFB laser transmission systems," *IEEE/OSA Journal of Lightwave Technology*, vol. 7, pp. 888-895, 1989.

[2] S. M. Gemelos, D. Wonglumsom, and L. G. Kazovsky, "Impact of Crosstalk in an Arrayed-Waveguide Router on an Optical Add/Drop Multiplexer," *IEEE Photonics Technology Letters*, vol. 11, pp. 349-351, 1999.

[3] E. L. Goldstein, L. Eskilden, and A. F. Elrefaie, "Performance Implications of Component Crosstalk in Transparent Lightwave Networks," *IEEE Photonics Technology Letters*, vol. 6, pp. 657-660, 1994.

[4] H. Takahashi, K. Oda, and H. Toba, "Impact of Crosstalk in an Arrayed-Waveguide Multiplexer on N×N Optical Interconnection," *IEEE/OSA Journal of Lightwave Technology*, vol. 14, pp. 1097-1105, 1996.

[5] J. Leuthold, P. A. Besse, J. Eckner, E. Gamper, M. Dülk, and H. Melchior, "All-Optical Space Switches with Gain and Principally Ideal Extinction Ratios," *IEEE Journal of Quantum Electronics*, vol. 34, pp. 622-634, 1998.

[6] H. Wang, A. Wonfor, K. Williams, R. Penty and I. White, "Demonstration of a Lossless Monolithic 16x16 QW SOA Switch," *in Proc. Optical Fibre Communication Conference (OFC)*, pp. P1.7, 2009.

[7] J. C. Attard, J. E. Mitchell, and C. J. Rasmussen, "Performance Analysis of Interferometric Noise Due to Unequally Powered Interferers in Optical Networks," *IEEE/OSA Journal of Lightwave Technology*, vol. 23, pp. 1692-1703, 2005.

[8] M. Tur and E. L. Goldstein, "Dependence of Error Rate on Signal-to-Noise Ratio in Fibre-optic Communication Systems with Phase-Induced Intensity Noise," *IEEE/OSA Journal of Lightwave Technology*, vol. 7, pp. 2055-2058, 1989.

[9] J. E. Mitchell, P. M. Lane, and J. J. O'Reilly, "Evaluation of extinction ratio induced performance penalty due to interferometric noise," *Electronics Letters*, vol. 35, pp. 964-965, 1999.

[10] S. L. Danielsen, C. Joergensen, B. Mikkelsen, and K. E. Stubkjaer, "Analysis of Interferometric Crosstalk in Optical Switch Blocks Using Moment Generating Functions," *IEEE Photonics Technology Letters*, vol. 10, pp. 1635-1637, 1998.

[11] L. Moura, N. Karafolas, P. Lane, A. Hillt, and J. O'Reilly, "Modelling of interferometric crosstalk in optical networks," *in proc. of IEEE GLOBECOM'96*, 1996.

[12] K.-P. Ho, "Analysis of Homodyne Crosstalk in Optical Networks Using Gram-Charlier Series," *IEEE/OSA Journal of Lightwave Technology*, vol. 17, pp. 149-154, 1999.

[13] L. G. C. Cancela and J. J. O. Pires, "Rigorous Evaluation of Crosstalk Requirements for Large Optical Space Switches Based on Directional Couplers," *in proc. of Conference on Telecommunications 2001*, Figueira da Foz, Portugal, 2001.

[14] V. K. Prahbu, "Modified Chernoff Bounds for PAM Systems with Noise and Interference," *IEEE Transactions on Information Theory*, vol. IT-28, pp. 95-100, 1982.

[15] N. A. Olsson, "Lightwave Systems With Optical Amplifiers," *IEEE/OSA Journal of Lightwave Technology*, vol. 7, pp. 1071-1082, 1989.

[16] J. L. Rebola and A. V. T. Cartaxo, "Gaussian Approach for Performance Evaluation of Optically Preamplified Receivers with Arbitrary Optical and Electrical Filters," *IEE Proceedings Optoelectronics*, vol. 146, pp. 135-142, 2001.

[17] D. Marcuse, "Derivation of Analytical Expressions for the Bit-Error Probability in Lightwave Systems with Optical Amplfiers," *IEEE/OSA Journal of Lightwave Technology*, vol. 8, pp. 1816-1823, 1990.

[18] E. Forestieri, "Evaluating the Error Probability in Lightwave Systems with Chromatic Dispersion, Arbitrary Pulse Shape and Pre- and Postdetection Filtering," *IEEE/OSA Journal of Lightwave Technology*, vol. 18, pp. 1493-1503, 2000.

[19] L. F. B. Ribeiro, J. R. F. d. Rocha, and J. L. Pinto, "Performance Evaluation of EDFA Preamplified Receivers Taking into Account Intersymbol Interference," *IEEE/OSA Journal of Lightwave Technology*, vol. 13, pp. 225-231, 1995.

[20] M. Leiria, J. L. Rebola, and A. V. T. Cartaxo, "Gaussian approach to the performance assessment of optical multiplexer-demultiplexer concatenation in transparent optical networks," *IEE Proceedings Optoelectronics*, vol. 151, pp. 157-165, 2004.

[21] J. L. Rebola and A. V. T. Cartaxo, "Probability Density Function of the Output Current of Cascaded Multiplexer/Demultiplexers in Transparent Optical Networks," *Fibre and Integrated Optics*, vol. 24, pp. 55-72, 2005.

[22] L. Eskildsen and P. B. Hansen, "Interferometric Noise in Lightwave Systems with Optical Preamplifiers," *IEEE Photonics Technology Letters*, vol. 9, pp. 1538-1540, 1997.

[23] M. Leiria and A. Cartaxo, "Evaluation of Transparent Optical Network Performance in Presence of Incoherent Homodyne Crosstalk," *Fibre and Integrated Optics*, pp. 315-330, 2005.

[24] T. Monroy, E. Tangdiongga, and H. d. Waardt, "Performance of Optically Preamplified Receivers in WDM Systems Disturbed by Interferometric Crosstalk," *Photonic Network Communications*, vol. 1, pp. 313-322, 1999.

[25] T. Kamalakis and T. Sphicopoulos, "Asymptotic Behavior of In-Band Crosstalk Noise in WDM Networks," *IEEE Photonics Technology Letters*, vol. 15, pp. 476-478, 2003.

[26] T. Kamalakis, T. Sphicopoulos, and M. Sagriotis, "Accurate Estimation of the Error Probability in the Presence of In-Band Crosstalk Noise in WDM Networks," *IEEE/OSA Journal of Lightwave Technology*, vol. 21, 2003.

[27] M. Pfennigbauer, M. M. Strasser, M. Pauer, and P. J. Winzer, "Dependence of optically preamplified receiver sensitivity on optical and electrical filter bandwidths-measurement and simulation," *IEEE Photonics Technology Letters*, vol. 14, pp. 831-833, 2002.

[28] J. L. Rebola and A. V. T. Cartaxo, "Power Penalty Assessment in Optically Preamplified Receivers With Arbitrary Optical Filtering and Signal-Dependent Noise Dominance," *IEEE/OSA Journal of Lightwave Technology*, vol. 20, pp. 401-408, 2002.

[29] A. Papoulis, *Probability, Random Variables, and Stochastic Processes*, 2nd ed: McGraw-Hill, 1984.

[30] I. T. Monroy and E. Tangdiongga, *Crosstalk in WDM Communication Networks*: Kluwer Academic Publishers, 2002.

[31] J. J. O'Reilly and J. R. F. d. Rocha, "Improved error probability evaluation methods for direct detection optical communication systems," *IEEE Transactions on Information Theory*, vol. 33, pp. 839-848, 1987.

[32] X. Jiang and I. Roudas, "Asymmetric Probability Density Function of a Signal with Interferometric Crosstalk," *IEEE Photonics Technology Letters*, vol. 13, pp. 160-162, 2001.

[33] J. Zhou, R. Cadeddu, E. Casaccia, and J. O'Mahony, "Crosstalk in Multiwavelength Optical Cross-Connect Networks," *IEEE/OSA Journal of Lightwave Technology* vol. 14, no.6, pp. 1423, 1996.

[34] I. Roudas, N. Antoniades, T. Otani, T. Stern, R. Wagner, and D. Chowdhury, "Accurate modeling of optical multiplexer/demultiplexer concatenation in transparent multiwavelength optical networks," *IEEE/OSA Journal of Lightwave Technology*, vol. 20, no. 6, pp. 921–936, 2002.

[35] T. Mizuochi, "Recent progress in forward error correction and its interplay with transmission impairments," *IEEE Journal of Selected Topics in Quantum Electronics*, vol. 12, no. 4, pp. 544–554, 2006.

[36] J. Attard, J. Mitchell, and C. Rasmussen, "Performance Analysis of Interferometric Noise Due to Unequally Powered Interferers in Optical Networks," *IEEE/OSA Journal of Lightwave Technology*, vol. 23, no. 4, pp. 1692–1703, 2005.

[37] M. Pfennigbauer, M. M. Strasser, M. Pauer, and P. J. Winzer, "Dependence of optically preamplified receiver sensitivity on optical and electrical filter bandwidths-measurement and simulation," *IEEE Photonics Technology Letters*, vol. 14, no. 6, pp. 831–833, 2002.

[38] T. Zami, B. Lavigne and E. Balmefrezol, "Crosstalk analysis applied to wavelength selective switches," *in Proc. Optical Fibre Communication Conference (OFC)*, pp. OFP4, 2006.

[39] A. Yariv, "Signal-to-noise considerations in fiber links with periodic or distributed optical amplification" *OSA Optics Letters*, vol. 15, pp. 1064-1066, 1990.

[40] D. Kilper, et al., "Optical Performance Monitoring", *IEEE/OSA Journal of Lightwave Technology*, vol. 22, pp. 294–304, January 2004.

[41] J. Elbers, et al., "Reduced model to describe SPM-limited fibre transmission in dispersion-managed lightwave systems", *IEEE Journal of Selected Topics in Quantum Electronics*, vol. 6, pp. 276–281, March 2000.

Chapter 6 Final conclusions

6.1 Conclusions

This section overviews the work presented in this Thesis and summarises its main conclusions. The motivation for the work was presented in chapter 1, which arises from the wish to avoid the electronic bottleneck affecting opaque optical network nodes. A possible vehicle for solving this problem is the MZI-SOA, a compact semiconductor device capable of performing many different optical processing functions. The work presented in this Thesis starts off by studying promising single components, analyses its sub-system applications, and goes up to a network level performance analysis of the physical impact and limitations of the device.

First, in chapter 2, the state of the art of semiconductor optical processing devices was reviewed and a simulation model for such devices is presented, with a view to analyse the device performance in system applications in the most effective way.

In chapter 3, an MZI-SOA sample was experimentally evaluated, and numerical parameters were extracted and fed to the simulation model. This has enabled a comparison of the simulation predictions with the experimental observations of the MZI-SOA operating as a wavelength and format converter. The MZI-SOA maximum rate of operation as a wavelength converter was found to be 40 Gb/s, and its performance was studied in different conditions. Operational rules were derived for ensuring optimum performance of the MZI-SOA. The NRZ, RZ, CS-RZ formatted pulses at 40 Gb/s were fed to the MZI-SOA and it was found experimentally and by simulation that the performance of the wavelength conversion improves for smaller duty cycles. The same study was also performed with other intensity modulation formats with phase management, ODB and AMI, and the same conclusions apply. The MZI-SOA showed good tolerance to the input signal extinction ratio variations. Regardless of the input modulation format, a pulsed beam at the input interferometric input always provides better performance than that obtained with a CW beam. Rules have been derived in order to guarantee that the MZI-SOA is operated in optimum conditions, paving the way to system applications.

Chapter 4 presents a study of the MZI-SOA as a building block of larger sub-systems for time domain processing. First, a MZI-SOA based optical WDM to OTDM converter is proposed. Operating margins were obtained for the conversion of both two 40 Gb/s channels to 80 Gb/s and three 40 Gb/s channels to 120 Gb/s. The limiting factor is found to be the pulse broadening occurring at the MZI-SOA, and the resulting crosstalk between adjacent pulses. Then, a packet compressor and decompressor architecture, suitable for phase modulated packets, was proposed, where the number of ODLs depends only on the compression ratio and not on the number of packet bits, as in an earlier proposed architecture. The packet compressor and decompressor operation was investigated through simulation with both BPSK and QPSK modulated packets, for a base bit rate of 10 Gb/s and compressed bit rates of both 20 Gb/s and 40 Gb/s, using quantum well MZI-SOA gates. The incurred penalty depends linearly on the logarithm of the packet size and it was found that only two compressor and decompressor pairs can be cascaded for a maximum ECP of 1 dB. A similar study was carried out with a quantum dot MZI-SOA, for a base bit rate of 40 Gb/s, and a compressed bit rate of 160 Gb/s. The penalty dependence on the logarithm of the packet size is again linear, but four compressor and decompressor pairs can now be cascaded for an ECP below 1 dB. It was shown that the ODL structure has stringent requirements on both the delay and phase of each ODL, which depend on the bit rates and the modulation formats used. A three-stage time slot interchanger was experimentally demonstrated at 10 Gb/s. In each stage the incoming packet is wavelength converted in the MZI-SOA and then routed to an appropriate delay block according to the newly assigned wavelength. An average 1.6 dB power penalty per stage was measured.

Chapter 5 presents a study of the impact of crosstalk in several different situations. A method to calculate the impact of crosstalk from distorted signals is developed, which makes use of both an analytical model based on the MGF formalism suited for ideal (non-distorted) signals and a short simulation of the signal distortion. The method's results were validated by comparison with experimental results, and both semi-analytical and Monte Carlo simulations. The scalability of a time slot interchanger architecture using MZI-SOA space switches was addressed with this method. The combined impact of filtering and crosstalk was also investigated. It was found that signals impaired by both filtering and crosstalk have crosstalk penalties higher than the signals that are simply impaired by

crosstalk. Consequently, for correct network planning, both effects should be analysed simultaneously. As an example, the maximum number of OXC was determined considering a single crosstalk channel with a SXR of 20 dB. For a maximum OSNR penalty of 2 dB, a maximum number of 18 cascaded OXC is predicted using traditional methods, whereas only 15 cascaded OXC are effectively acceptable using the more accurate method developed in this work. Finally, it was observed that the shape of the signals causing crosstalk also influences the crosstalk-induced penalty. When the signal causing crosstalk travels through a long fibre link, the signal can be affected by non-linear effects which can, in turn, cause strong power peaks in the signal. In this case, the crosstalk-induced penalty may get even larger, depending on the dispersion map. For a maximum EOP of 1 dB of the crosstalk signal resulting from non-linear effects, the crosstalk-induced penalty can increase from 1.75 dB to 2.2 dB, depending on the accumulated dispersion of the signal causing the crosstalk.

6.2 Suggestions for future work

The work presented in this Thesis leaves some unanswered questions, and raises additional ones. Some future research topics suggested by those still unanswered questions are now enumerated.

- Experimental evaluation of MZI-QDSOA devices as optical processing gates for system applications.
- A limitation of the MZI-SOA is its relatively smooth power transfer function, which could be offset by complementing it with a bistable device, such as the semiconductor ring lasers under development in the European IOLOS IST-FP6 project.
- Apply the method for calculating the performance of distorted signals impaired by crosstalk to other impairments, such as dispersion, non-linear effects, and polarization mode dispersion, and derive new crosstalk operating margins for these conditions.
- Modify the method for calculating the performance of distorted signals impaired by crosstalk, to model also phase modulated formats, e.g., DPSK, and investigate the impact of combined impairments, such as crosstalk and filtering, non-linear effects, dispersion.

- Modify the method for calculating the performance of distorted signals impaired by crosstalk to include also distorted crosstalk signals.
- Research other effects, other than non-linear effects, that cause peaks in the signal that may result in increased crosstalk penalties.

Appendix A. SOA amplifier equations

In this appendix, tractable equations of amplification and phase modulation of a signal in the SOA are derived from the wave equation. The wave equation for the electrical field $\vec{E}$ is

$$\vec{\nabla}^2\vec{E}+\varepsilon k_0^2\frac{\partial^2\vec{E}}{\partial t^2}=0, \tag{A.1}$$

where $\varepsilon=1+\chi$, χ is the susceptibility, and k_0 is the wave number. The susceptibility χ contains the physical interaction of light and matter. In order to obtain an accurate SOA model, χ, which will be replaced by the SOA gain and respective phase modulation coupling later on, is modelled as being non-linearly dependent on the electrical field traversing the SOA in the past times.

From the wave equation, the practical SOA amplification and phase modulation equations can be derived by separating variables in $\vec{E}$ according to

$$\vec{E}(x,y,z,t)=A(z,t)F(x,y)\hat{k} \tag{A.2}$$

where z is chosen as the propagation direction of the optical wave envelope *A(z,t)*, *x* and *y* are the perpendicular directions which give the wave spatial mode profile *F(x,y)*, and $\hat{k}$ represents a generic polarization direction.

Introducing the above description of $\vec{E}$ in the propagation equation gives two coupled differential equations, one for the mode profile, and another for the envelope propagation. Solving the mode profile equation gives the spatial distribution of the beam in the directions of *x* and *y*, while the envelope equation describes the evolution of the optical wave inside the SOA over the longitudinal direction *z* and over time. The equation is

$$\frac{\partial A}{\partial z}+\frac{1}{v_g}\frac{\partial A}{\partial t}=\frac{1-i\alpha}{2}gA \tag{A.3}$$

where *g* is the SOA local gain, α is the linewidth enhancement factor, which related the amplitude and phase modulation in the SOA, and v_g is the group velocity in the SOA.

Equation (A.3) can be simplified adopting a time reference frame moving with the pulse, through the following time variable transformation

$$t=t'-z/v_g \tag{A.4}$$

where t' is the time (previously it was t). Moreover, by separating the amplitude and phase parts,

$$A(z,t) = \sqrt{P}e^{i\phi} \tag{A.5}$$

and substituting in Eq. (A.3) produces two equations, one for the pulse power and another one for the phase. This set of three equations describes the pulse propagation along the SOA:

$$\frac{\partial P(t,z)}{\partial z} = g(t,z)P(t,z) \tag{A.6}$$

$$\frac{\partial \phi}{\partial z} = -\frac{1}{2}\alpha g \tag{A.7}$$

Although it was not written explicitly, the SOA gain g depends on the power of the optical pulse travelling inside the SOA, $P(t,z)$. The description of the dependence of the SOA gain on the input power is where the SOA gain saturation behaviour is contained, and hence where the optical processing capabilities are described.

The latter equations can be made even more useful if they are integrated over space. The formal solution of the equation is

$$P(t,z) = G(t)P(t,0) \tag{A.8}$$

where

$$G(t,z) = e^{h(t,z)} \tag{A.9}$$

Is the amplifier gain taken as the relation of the output and input powers when $z=L$, L being the amplifier length and

$$h(t,z) = \int_0^z g(t,z)dz \,. \tag{A.10}$$

For the phase, a similar equation is obtained, which states the phase rotation inside the SOA depending on the amplifier gain.

$$\phi(t,L) = -\frac{\alpha}{2}\ln[G(t)] + \phi(t,0)\,. \tag{A.11}$$

Appendix B. Initial conditions of the SOA differential equations

The SOA model used for simulating the operation of a quantum well SOA was exposed in Chapter 2, where a set of differential equations was presented in order to calculate the SOA gain. The equations are here reproduced:

$$\frac{\partial h_N}{\partial t} = -\frac{h_N}{\tau_s} - \frac{1}{P_s \tau_s}\left[G(t)-1\right]P_{in}(t) + \frac{h_0}{\tau_s} \tag{B.1}$$

$$\frac{dh_{SHB}}{dt} = -\frac{h_{SHB}}{\tau_{SHB}} - \frac{\varepsilon_{SHB}}{\tau_{SHB}}\left[G(t)-1\right]P_{in}(t) - \frac{dh_{CH}}{dt} - \frac{dh_N}{dt} \tag{B.2}$$

$$\frac{\partial h_{CH}}{\partial t} = -\frac{h_{CH}}{\tau_H} - \frac{\varepsilon_{CH}}{\tau_H}\left[G(t)-1\right]P_{in}(t) \tag{B.3}$$

$$G(t) = e^{h(t)} \tag{B.4}$$

$$h = h_N + h_{CH} + h_{SHB}\,. \tag{B.5}$$

In order to solve this set of differential equations, initial conditions must be given, which consists of three values, the same as the number of the differential equations. Since at the beginning of time, t_0, the precise values of h_N, h_{CH} and h_{SHB} are not known, it is assumed that these time functions are stationary at t_0. So, setting the time derivatives of h_N, h_{CH} and h_{SHB} of equations (B.1) – (B.3) to zero, results in a system of three non-differential equations. An equation for $G(t_0)$ is found by solving the three equations in order to h_N, h_{CH} and h_{SHB}, and adding them:

$$h_0 = -(\varepsilon_{CH} + \varepsilon_{SHB} + 1/P_s)\left[G(t_0)-1\right]P_{in}(t_0) + h_0/\tau_s \tag{B.3}$$

Solving this nonlinear equation in order to $h_0=h(t_0)$ allows to determine $h_N(t_0)$, $h_{CH}(t_0)$ and $h_{SHB}(t_0)$ afterwards, opening the way to solve the set (B.1) – (B.3) for all time values.

The solution of the set of differential equations describes the behaviour of the SOAs in the MZI-SOA and can be used to perform optical processing functions like wavelength conversion. Fig. B.1 shows an example of an oscilloscope trace after 40 Gb/s RZ wavelength conversion in the MZI-SOA. The first bits of the binary sequence are seven '0'. It can be observed that the SOA output is not stationary at all, which violates the validity of the initial conditions assumption. The reason for this is that the SOAs are fed

with two optical beams, the CW probe and the pump signal. The SOA is sensitive to the input power, which has the fast oscillating beating terms of the probe and pump signals. The SOA gain responds to these oscillations and hence is not steady. The consequence of these oscillations is that at the first simulation time points the SOA gain is fluctuating due to a numerical issue and not from a physical cause. Therefore, the first simulation bits should be discarded when evaluating the performance of such signals. Furthermore, as shown in Fig. B.1 b), the last simulated bit is also affected by the spurious oscillations of the first bits. This is due to the optical filtering at the MZI-SOA output to eliminate all of the signals except the desired wavelength converted signal. On one hand, the fast Fourier transform is used to calculate the filter effect. This transform considers that the signal is an endless repetition of the time-limited simulation vector of the signal. On the other one hand, the use of non-causal filter transfer functions (e.g. Gaussian) leads to the non-physical influence of future times on past times. Consequently, filtering the optical signal leads to the influence of the first simulated bits on the last ones. So, the last simulated bit should be also discarded when analysing the performance of a given signal.

Facing these results, the first three and last bits are discarded when analysing performance and observing eye-diagrams. An eye-diagram is presented in Fig. B.2 to illustrate the removal of these bits. The signal represented in Fig. B.2 is the same of Fig. B.1.

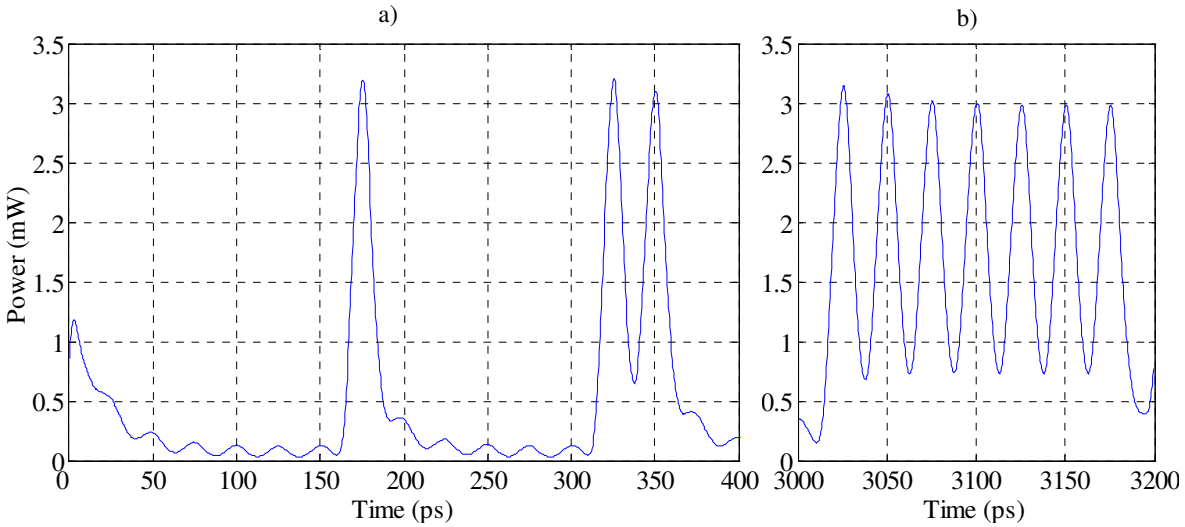

Fig. B.1 Oscilloscope trace of the initial (a) and final (b) bits of 40 Gb/s wavelength conversion in the MZI-SOA.

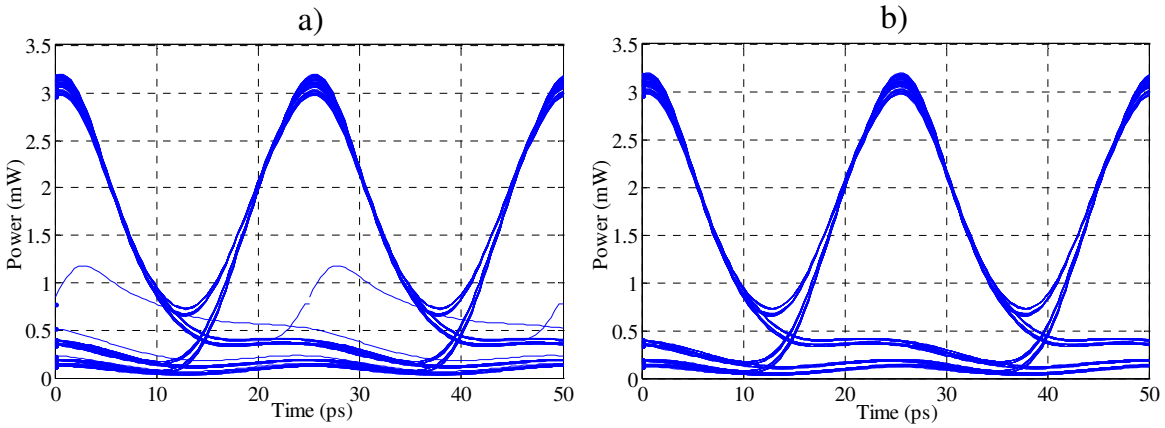

Fig. B.2 Eye diagrams of 40 Gb/s wavelength conversion in the MZI-SOA showing a) all the simulated bits and b) all simulated bits except the first three and the last simulated bits.

The situation just exposed considered a continuous data stream where there is data throughout the time vector. However, for packet switched networks, there are idle times between packets without any data and, potentially, very low optical power. The simulation of optical processing functions should include these idle times between packets, but these could be exploited in the simulation to accommodate the transitory effects of the initial conditions so that they not impact the data. Nevertheless, it was observed that the transitory effects cause peaks at the initial time of the simulation. If the signal is analysed at this stage, there is no problem, since the transitory peak is at the idle time that precedes/follows the packet. Though, if the output signal of the MZI-SOA, containing the transitory peak, is fed to another MZI-SOA, the peak will be amplified. By further cascading the MZI-SOA gates, the transitory peak can get so large that it affects the average power of the simulated signal. To prevent this issue, the power of the first three and last simulated bits of the MZI-SOA filtered output signal is set to zero. The oscilloscope traces and eye diagrams of a packet before and after this stratagem are shown in Fig. B.3.

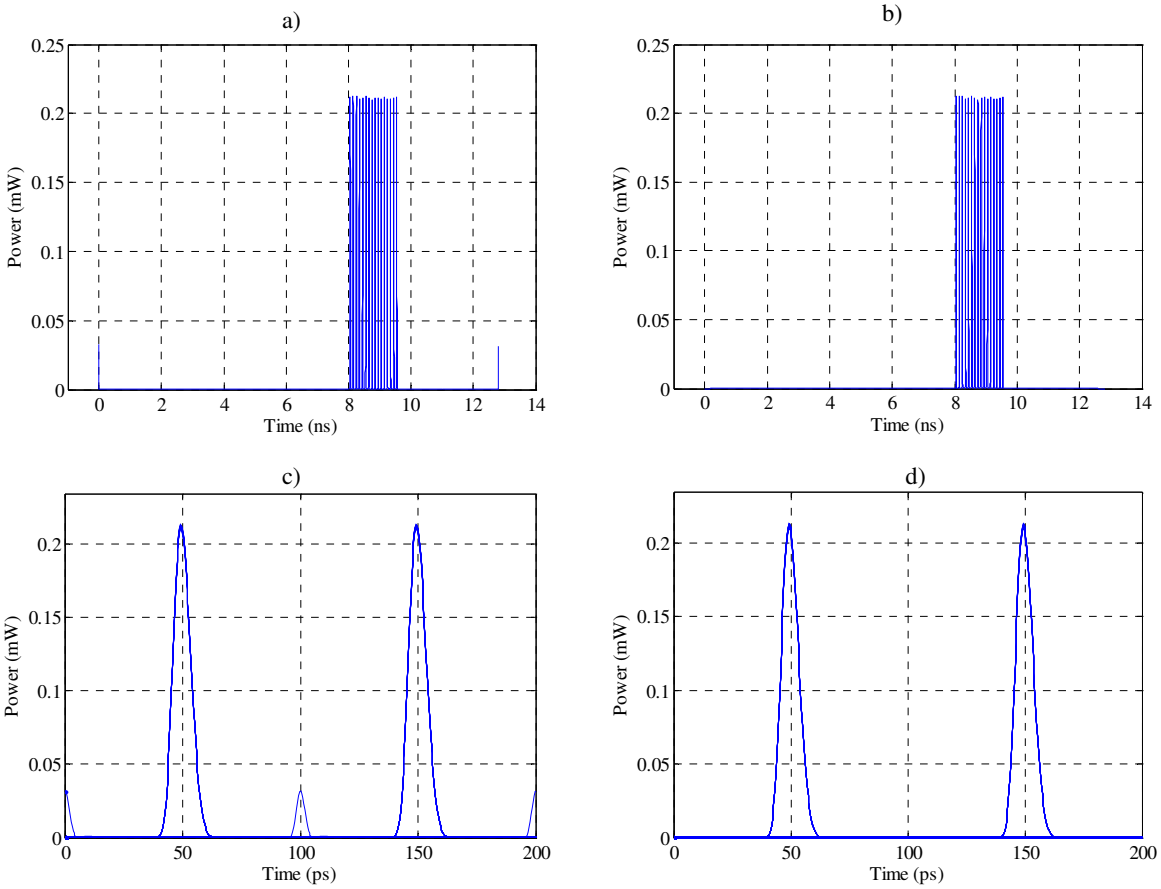

Fig. B.3 Oscilloscope traces (top row) and eye diagrams (bottom row) of 10 Gb/s packet processing in the MZI-SOA. The left column shows the signal directly from the MZI-SOA output filter, whereas the right column shows the signal without the first three and last bits.

Appendix C. Transmitter details for different formats and bit rates

This appendix presents the setups of the optical transmitters used to produce the different signals used in chapter 3. For bit rates up to 40 Gb/s, a multi-bit rate pattern generator is used at the desired signal bit rate which drives a Mach-Zehnder modulator (MZM) which, in turn, modulates a CW laser beam. Depending on the modulation format, other components may follow. Fig. C.1 depicts the different transmitter setups, which apply to both the simulation and experiment. All MZMs are operated in the push-pull mode.

For the NRZ format, no additional components are needed, as shown in Fig. C.1 a). The MZM is polarized at mid-transmission point so that the AC-coupled electrical signal is translated into a pure intensity modulated signal. The RZ and CS-RZ transmitters make use of the NRZ transmitter setup, but a subsequent MZM is used to carve the NRZ signal, according to Fig. C.1 b). RZ with 50% duty cycle is achieved by driving the carver MZM by an electrical clock signal with frequency identical to the bit rate and by polarizing the carver MZM at mid transmission point. If the frequency of the electrical clock signal is half of the bit rate, RZ with 33% duty cycle or CS-RZ with 67% duty cycle format is obtained depending if the carver MZM is polarized in the maximum or minimum transmission point, respectively. Regarding the optical duobinary (ODB) and AMI-RZ formats, they are produced with a single MZM followed by an optical delay interferometer, as presented in Fig. C.1 c). However, unlike the NRZ case, the MZM is polarized at the minimum transmission point, so that the differentially pre-coded signal data is modulated in the phase. The purpose of the delay interferometer is then to interfere one bit with the following one to convert the phase modulation to amplitude modulation. The constructive output port of the delay interferometer produces an ODB, whereas the destructive port produces an AMI-RZ. The delay between the interferometer arms is half of the bit period (12.5 ps at 40 Gb/s) which turns out into a duty cycle of 38% for the AMI-RZ.

The pattern generator and MZM used in the experiment operated at bit rates up to 40 Gb/s. To achieve 80 Gb/s, a MLL with a repetition rate of 40 GHz was used instead of the CW laser, which output was modulated by a MZM at 40 Gb/s. The short pulse 40 Gb/s

signal was then passively interleaved in an optical bit rate multiplier resulting in a 80 Gb/s optical time domain interleaved (OTDM) signal. This setup is depicted in Fig. C.1 d).

The simulation setup mimicked the experimental conditions in order to obtain simulated eye diagrams in the same conditions as the experiment.

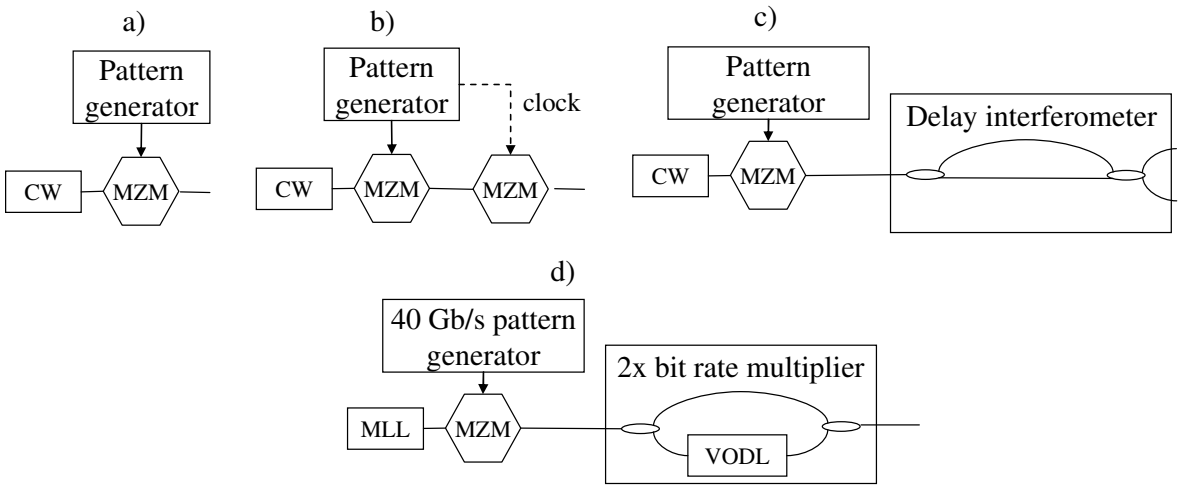

Fig. C.1 Transmitter setup of a) NRZ signal; b) RZ 33%, RZ 50% and CS-RZ 67% signal; c) AMI and ODB signal; and d) 80 Gb/s OTDM signal.

Appendix D. Simulation binary sequence size

This appendix is dedicated to the determination of the binary sequence size to be used in the simulations of chapter 3. It is highly desirable that the sequence size is as short as possible to minimize the simulation time. However, too small sequence sizes do not capture all the dynamics of the system and might yield misleading results when compared to longer sequences.

In order to assess the minimum binary sequence size to provide accurate results, two simulation setups for wavelength conversion were chosen. In the first setup the probe is a CW beam, as depicted in Fig. D.1. In the second one the probe is a short pulse beam, according to Fig. D.2. The bit rate is 40 Gb/s and the samples per bit are 64, that translates to a sampling period of about 0.4 ps, which is enough to describe pulses of a few ps of width. The 2^n-sized binary sequence is a pseudo-random binary sequence (PRBS) built from a de Bruijn sequence of size 2^n-1 padded with a zero at the end.

The required OSNR at a BER of 10^{-10} for both the input and output signals and the simulation time are presented in Fig. D.1 and Fig. D.2 for the conversion to CW and short pulse beams, respectively. In both figures the simulation time increases approximately linearly with the binary sequence size, with a simulation speed of about 2.9 and 3.5 bit/s, respectively for the CW and pulse probes, in an Intel 2.4 GHz Centrino 2 dual core laptop (processing with only one core). As for the required OSNR, the conversion to CW shows the same performance regardless of the binary sequence size, with a difference between the maximum and minimum observed required OSNR of 0.07 dB for both the input and output signals. However, for the conversion to short pulses, the required OSNR significantly depends on the binary sequence size for sequence sizes smaller than 2^7. Relatively to the 2^7 sequence, the sequences with larger size yield only a maximum difference of 0.05 dB of the required OSNR for both the input and output signals. Therefore the 2^7=128 bit binary sequence was chosen to perform the simulations of Chapter 3.

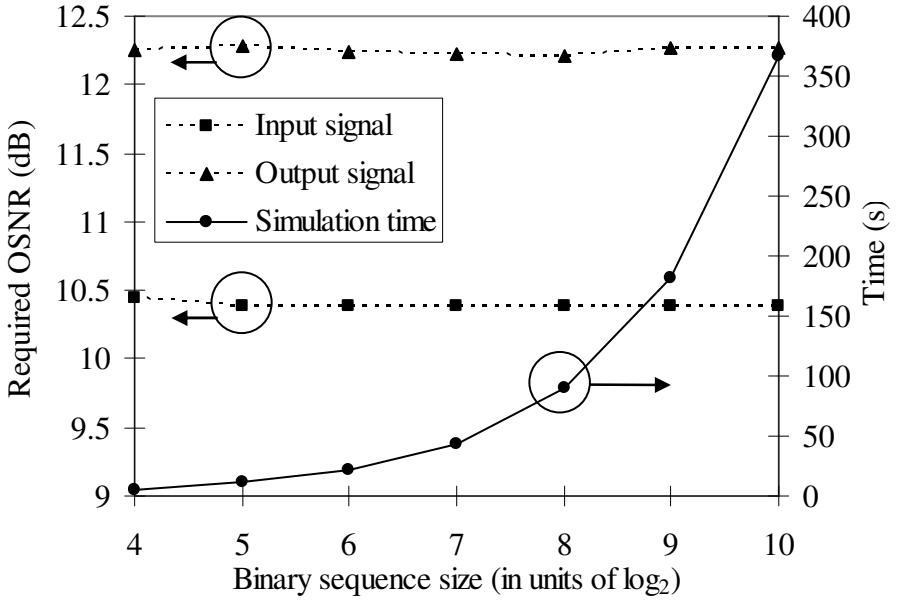

Fig. D.1 Required OSNR for the input and output signals and simulation time for wavelength conversion to a CW beam as a function of the binary sequence size. The lines are guides for the eyes.

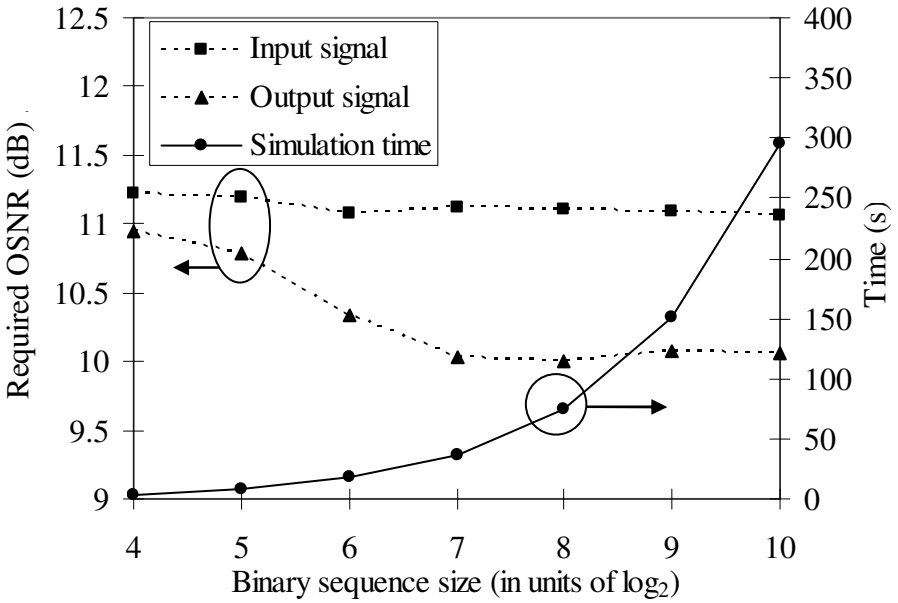

Fig. D.2 Required OSNR for the input and output signals and simulation time for wavelength conversion to a pulsed beam as a function of the binary sequence size. The lines are guides for the eyes.

Appendix E. ODL structure considerations

In this appendix, considerations are devised about the ODL structures in the packet compressor and decompressor presented in chapter 4. The ODL structure is built to create a number of packet replicas separated by a specific time interval. However, when phase modulation formats are used, not only the delay of the replicas must be accurate, but also the phase, as shown in chapter 4. In that chapter, margins for the maximum phase deviation were established. It was assumed that the ODL structure provided a null phase shift between ODL arms. Now, a more detailed analysis is provided in this respect.

A four arm delay line will be considered, suitable for four-fold compression and decompression, as in the examples of the figures of chapter 4. Two possible structures are investigated: the parallel structure that was considered in chapter 4 and that allows any natural number of replicas to be produced, and the cascaded Mach-Zehnder structure, which uses less ODLs to generate a power of 2 number of replicas than the former structure. Both are depicted in Fig. E.1. The ODL structures are built so that replicas are output with delays of 0, T, $2T$ or $3T$, with $T=T_p/N + T_s/N$, according to the explanation of the compressor and decompressor concept in chapter 4.

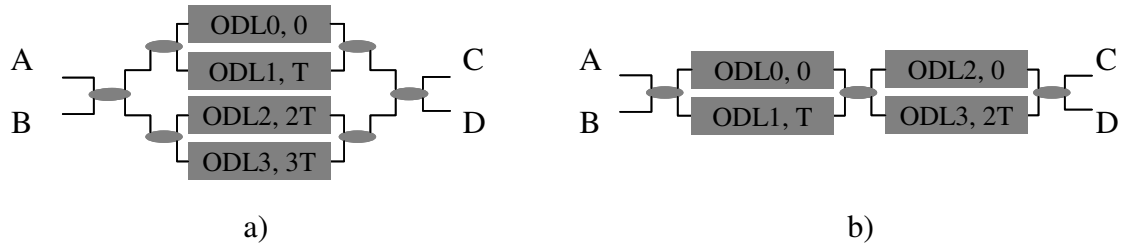

Fig. E.1 ODL structures: a) parallel and b) cascaded Mach-Zehnder. The delay of each ODL is represented as kT, k=0,1,2,3.

It shall be considered that the fibre or waveguide connections between elements (ODLs and couplers) do not introduce phase rotations. Furthermore, between the two couplers' outputs there is a phase difference of $\pi/2$. Consequently, phase differences will result between the packet replicas at the output of the ODL structure, according to the particular path inside the ODL structure. This is valid for both the ODL structure in the packet compressor and in the decompressor. The phase differences acquired for each packet replica at the ODL structure output have been calculated for both structures and the results are presented in Table E-1 and Table E-2, for the cascaded Mach-Zehnder and

parallel structures, respectively. The chosen ODL structure input and output are denoted by a pair formed by the letters A, B, C and D, according to the labels in Fig. E.1.

Table E-1 Phase difference introduced by the cascaded Mach-Zehnder ODL structure, for all paths and input and output ports combinations.

ODL	Total delay	Input output pair			
		A C	A D	B C	B D
		Phase difference			
0,2	0	0	π/2	π/2	π
1,2	*T*	π	3π/2	π/2	π
0,3	2*T*	π	π/2	3π/2	π
1,3	3*T*	π	π/2	π/2	0

Table E-2 Phase difference introduced by the parallel ODL structure, for all paths and input and output ports combinations.

ODL	Total delay	Input output pair			
		A C	A D	B C	B D
		Phase difference			
0	0	π	3π/2	3π/2	2π
1	*T*	0	π/2	π/2	π
2	2*T*	π	π/2	π/2	0
3	3*T*	2π	3π/2	3π/2	π

The first conclusion from the analysis of Table E-1 is that, independently of the chosen input and output pair, some of the packet replicas have phase differences among them, for both ODL structures. Consequently, the phase differences acquired in the packet compressor must be carefully matched to the ones acquired in the decompressor so that the overall phase differences after the compressor and decompressor combo are cancelled out and the phase information of the packet is not distorted. It should be remarked that a phase difference of π/2 and π corresponds, respectively, to the phase difference between symbols of the QPSK and BPSK formats. As a result, a completely wrong binary sequence might be created if a proper ODL structure configuration is not used. The information is preserved in the compressor and decompressor combo if the phase difference between the symbols that crossed different paths is a multiple of 2π.

After the compressor and decompressor combo, all symbols recover their original position in the bit sequence, which means that the sum of the delay that a particular symbol acquires in the compressor ODL and the decompressor ODL is the same for all symbols. Hence, the symbols acquiring a delay of 0, *T*, 2*T* and 3*T* in the compressor, will acquire delays of 3*T*, 2*T*, *T* and 0 in the decompressor, respectively. So, the phase differences corresponding to the previous delays should be summed to obtain the effective total phase difference.

After trying all the possible combinations, the following conclusions are attained, based on the assumptions made beforehand. It is not possible to have a cascaded Mach-Zehnder ODL structure and a parallel ODL structure on the same compressor decompressor combo. Both ODL structures must be of the same type. For the cascaded Mach-Zehnder structure, one of the following input and output pairs must be used: AC must be complemented by BD and AD must be complemented by BC. The parallel structure is more flexible and both AC and BD can be complemented by both AC and BD. The same applies to BC and AD.

Appendix F. Details of the implementation of MCB with simulated eye

In this appendix, the MCB method with the simulated eye diagram is discussed, for calculating the BER for a signal impaired by crosstalk, ASE noise and intersymbolic effects.

It was seen in chapter 5 that the BER for a signal in such conditions could be calculated by eq. (5.28), which is here reproduced:

$$BER_{Dopt} \approx \min_{z_0,z_1}\left\{\frac{1}{2L}\left[\left(\frac{z_1}{z_0}\right)^{\frac{z_0}{z_0+z_1}}+\left(\frac{z_1}{z_0}\right)^{\frac{z_1}{z_0+z_1}}\right]\times m_1(z_1)^{\frac{z_0}{z_0+z_1}}\, m_0(z_0)^{\frac{z_1}{z_0+z_1}}\right\} \tag{F.1}$$

where (eqs. (5.24) and (5.25))

$$m_0(z_0)=\sum_{l=1}^{L}\frac{1}{2^N}\sum_{k=1}^{N}C_k^N I_0(2A_{s,l}^{(0)}A_x^{(1)}z_0)^k\times I_0(2A_{s,l}^{(0)}A_x^{(0)}z_0)^{N-k}\,\frac{\exp\left[(\sigma_{tot}^{(0)})^2 z_0^2/2+z_0\left((A_{s,l}^{(0)})^2+k(A_x^{(1)})^2\right)\right]}{z_0\sigma_{tot}^{(0)}\sqrt{2\pi}} \tag{F.2}$$

$$m_1(z_1)=\sum_{l=1}^{L}\frac{1}{2^N}\sum_{k=1}^{N}C_k^N I_0(2A_{s,l}^{(1)}A_x^{(1)}z_1)^k\times I_0(2A_{s,l}^{(1)}A_x^{(0)}z_1)^{N-k}\,\frac{\exp\left[(\sigma_{tot}^{(1)})^2 z_1^2/2+z_1\left((A_{s,l}^{(1)})^2+k(A_x^{(1)})^2\right)\right]}{z_1\sigma_{tot}^{(1)}\sqrt{2\pi}} \tag{F.3}$$

and A_s and A_x represent the optical field amplitude at the sampling time for signal and crosstalk signal, respectively, and the (0) and (1) superscripts represent conditioning to a '0' or '1' bit, respectively.

However, in the MCB with the simulated eye, the new MGFs are written as (eqs. (5.31) and (5.32))

$$m_0(z_0)=\sum_{l=1}^{L}\frac{1}{2^N}\sum_{k=1}^{N}C_k^N I_0(2A_{s,l}^{(0)}A_x^{(1)}z_0)^k\times I_0(2A_{s,l}^{(0)}A_x^{(0)}z_0)^{N-k}\,\frac{\exp\left[(\sigma_{tot}^{(0)})^2 z_0^2/2+z_0\left(i_{s,l}^{(0)}+ki_x^{(1)}\right)\right]}{z_0\sigma_{tot}^{(0)}\sqrt{2\pi}} \tag{F.4}$$

$$m_1(z_1)=\sum_{l=1}^{L}\frac{1}{2^N}\sum_{k=1}^{N}C_k^N I_0(2A_{s,l}^{(1)}A_x^{(1)}z_1)^k\times I_0(2A_{s,l}^{(1)}A_x^{(0)}z_1)^{N-k}\,\frac{\exp\left[(\sigma_{tot}^{(1)})^2 z_1^2/2+z_1\left(i_{s,l}^{(1)}+ki_x^{(1)}\right)\right]}{z_1\sigma_{tot}^{(1)}\sqrt{2\pi}}. \tag{F.5}$$

where the squares of the electric field amplitude in the exponential have respectively been replaced by the simulated values of the current at the sampling instant. These are now

determined from the electrical eye diagram, which is filtered by the electrical filter, as shown in chapter 5.

For the conventional MCB method, there is no doubt of the meaning of the A_s which is unmistakeably the electric field amplitude of the signal. However, the optical and the electrical eye diagram are clearly different and therefore using $\sqrt{i_s}$ instead of A_s, where i_s is the electrically filtered current of the signal at the sampling time, will yield different results. Therefore, the replacement of A_s by $\sqrt{i_s}$ occurred only where appropriate, in the exponential of the MGF. However, the A_s also appears in the calculation of the total variance and in the part relative to crosstalk, as an argument of the modified Bessel function of the first kind. The total variance is

$$\sigma_{tot}^2 = \sigma_{s-ASE}^2 + \sigma_{ASE-ASE}^2 + \sigma_{el}^2 \tag{F.4}$$

where (eqs. (5.11) and (5.12))

$$\sigma_{s-ASE}^2 = 2S_{ASE}\left|A_s\right|^2 \int_{-\infty}^{+\infty} \left|H_e(f)\right|^2 \left|H_o(f)\right|^2 df \tag{F.5}$$

$$\sigma_{ASE-ASE}^2 = S_{ASE}{}^2 \int_{-\infty}^{+\infty} \left|H_e(f)\right|^2 \left[\left|H_o(f)\right|^2 * \left|H_e(f)\right|^2\right] df \,. \tag{F.6}$$

$\sigma_{ASE-ASE}^2$ does not depend on the A_s, but σ_{s-ASE}^2 does, which is the variance of the ASE noise – signal beating. It will now be analysed if the A_s^2 should, or not be replaced by i_s in the variance expression.

Consider the following example where the electrical filter is very narrow, but the optical eye diagram is clearly open and does not show any intersymbolic interference in the sampling instant. The electrical filter will introduce intersymbolic interference in the sampling time and the electrical eye will show a smaller aperture than in the optical domain. In particular, in the zero level at the sampling time, $i_s > A_s^2$. If A_s would be replaced by $\sqrt{i_s}$ in the signal – ASE beating, the beating variance would be overestimated. In fact, Eq. (F5) already considers explicitely the dependence of the optical and electrical filters. Fig. F.1 and Fig. F.2 show the crosstalk induced OSNR penalty as a function of the optical receiver filter bandwidth, calculated by semi-analytical simulation and the MCB method, with a simulated eye diagram. The MCB results presented in Fig. F.1 were calculated replacing A_s by $\sqrt{i_s}$ in the beating variance, whereas in Fig. F.2 A_s is kept.

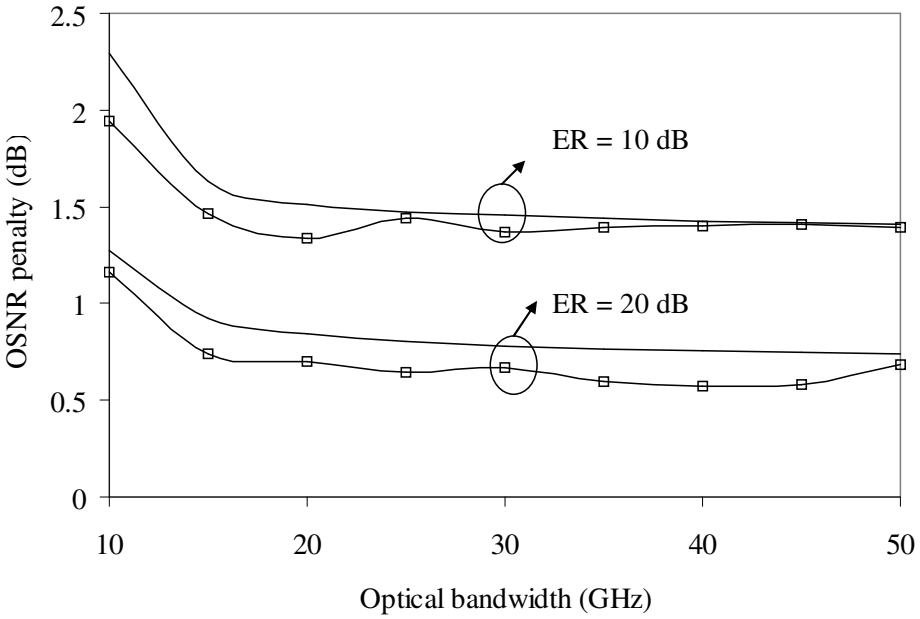

Fig. F.1 Crosstalk induced OSNR penalty as a function of the optical receiver bandwidth, for 10 and 20 dB of extinction ratio, calculated by semi-analytical simulation (squares plus lines to guide the eyes) and the MCB method with simulated eye diagram (line only). The variance of the signal - ASE noise is calculated from the electrical domain (i_s).

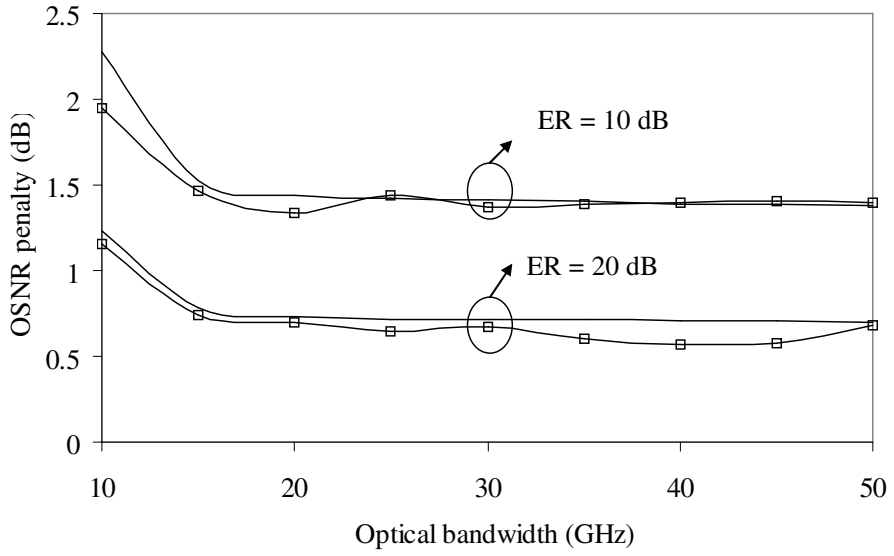

Fig. F.2 Crosstalk induced OSNR penalty as a function of the optical receiver bandwidth, for 10 and 20 dB of extinction ratio, calculated by semi-analytical simulation (squares plus lines to guide the eyes) and the MCB method with simulated eye (line only). The variance of the signal - ASE noise is calculated from the optical domain (A_s).

By comparing both figures, it can be concluded that using A_s in the signal – ASE variance, instead of i_s, gives OSNR penalties that are closer to the ones calculated by the semi-analytical simulation. The difference for high extinction ratios is larger due to the

effect explained before. For high extinction ratios, the ASE-beating in the zero level is very low, but using i_s in the beating variance exaggerates this beating and therefore gives overestimated BER values. However, for low extinction ratio signals, the zero level already has considerable power in the zero level and although $\sqrt{i_s}$ is still larger than A_s, this effect is not as pronounced as in the previous case.

Finally, the crosstalk impact in $m_k(z_k)$ is accounted for in $I_0(2A_s\ A_x z,)$, which came from the MGF of the signal - crosstalk beatings. Due to the approximation that the filters do not impact the signal - crosstalk beatings, $I_0(2A_s\ A_x z,)$, was kept with the optical field amplitudes and not the square root of the electrical current counterpart. In fact, since the signal - crosstalk beatings occur at the receiver, before electrical filtering, similarly to the signal - ASE noise beatings, A_s should not be replaced by i_s. Taking again the example of the narrow electrical filter, in the zero level, $\sqrt{i_s} > A_s$. So, if A_s was replaced by i_s in $I_0(2A_sA_x z,)$, the crosstalk effect would be overestimated. Therefore, A_s is kept in the $I_0(2A_sA_x z,)$ term.

Appendix G. OSNR penalties of a NRZ signal due to crosstalk from a RZ signal

Although not common nowadays, it is possible to have different modulation formats in the same hierarchy of an optical network. In such case, crosstalk between signals of different modulation formats could happen. In this appendix, cases of a NRZ signal impaired by crosstalk from RZ formatted signals are studied. First of all, since the RZ signal power is strongly dependent on time, i.e., the pulse occupies only a fraction of the bit slot, it is important to investigate if the crosstalk penalty is dependent on the bit delay between the signal and the crosstalk signal. The considered modulation formats of the crosstalk signal were NRZ, as a reference, RZ with 33% and 50% duty cycles, carrier suppressed RS (CS-RZ) with 67% duty cycle and alternate mark inversion (AMI) with 38% duty cycle. For the sake of simplicity these modulation formats will now be called RZ33, RZ50, CS67 and AMI38, respectively.

This study has been done by semi-analytical simulation, where the simulation setup is presented in Fig. G.1. Two CW lasers are modulated with data using pattern generators (PG) and Mach-Zehnder modulators (MZM), at 10 Gb/s. The NRZ signal is the output of one of the MZMs, which is the signal. The output of the other MZM is fed to a third MZM, which is driven by an electric clock signal, acting as a pulse carver, to create the crosstalk signal. Using appropriate clock frequencies, bias voltages and modulation amplitudes, a 50% or 33% duty cycle RZ, or 67% duty cycle CS-RZ is obtained, according to the details in Appendix C. For the 38% AMI signal, the transmitter is slightly different, as shown in Appendix C, The crosstalk signal is then delayed with a variable optical delay line (VODL) to adjust and vary the bit delay between the signal and the crosstalk signal. Signal, crosstalk signal and ASE noise are combined, optically filtered and fed to an optical receiver and a BERT. The OSNR penalty is the difference between the required OSNR, for a BER of 10^{-9}, for the crosstalk impaired signal and the crosstalk free signal. The optical bandpass filter has a 2^{nd} order Gaussian shape with 30 GHz of FWHM, and the ER is 30 dB. The SXR is set to 20 dB.

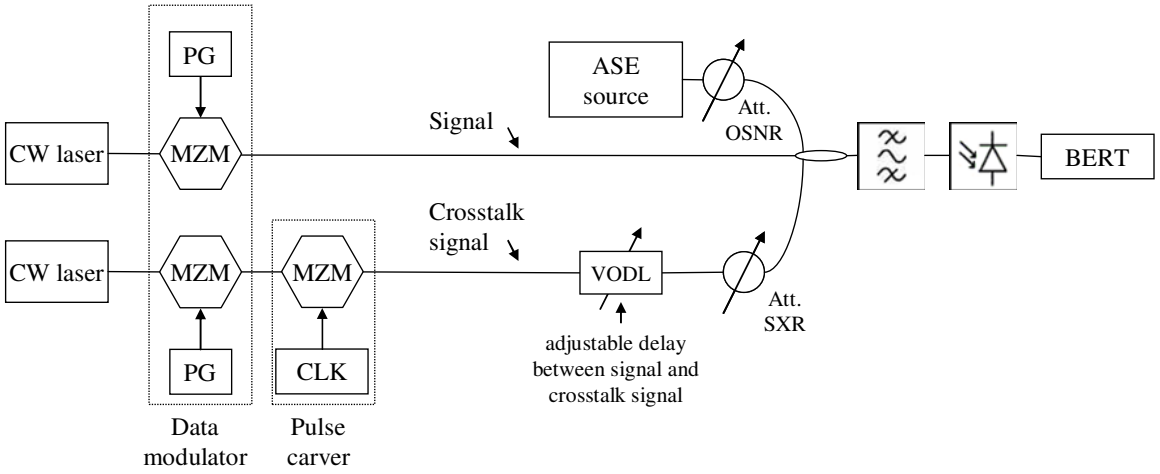

Fig. G.1 Simulation setup for calculating the OSNR penalty of a NRZ signal due to crosstalk induced by a RZ formatted signal.

The results of the crosstalk induced OSNR penalty from the different modulation formats as a function of the bit delay between signal and crosstalk signal are presented in Fig. G.2. In Fig. G.2 a) an electrical receiver with bandwidth of 7 GHz was used, while in Fig. G.2 b) the bandwidth was 10 GHz. It is clear from the results that for a NRZ crosstalk signal the OSNR penalty does not depend significantly on the delay between signal and crosstalk signal, either using the 7 GHz or the 10 GHz electrical receiver. This is due to the constant level of optical power in the "1"s level. However, for the RZ modulation formats, the constant level is not present anymore and the crosstalk induced OSNR penalty is strongly dependent on the delay between signal and crosstalk signal. When the optical pulse of the RZ signal coincides with the centre of the eye of the NRZ signal, the penalty is much higher when compared to when the "return to zero" part of the RZ signal coincides with the NRZ signal eye centre. In fact, when the RZ optical pulse is away from the NRZ signal eye centre, the optical power of the crosstalk signal that is coincident to the NRZ centre is very low and in this case the crosstalk induced penalty is nearly zero. This effect is augmented for the 10 GHz bandwidth receiver, relatively to the 7 GHz bandwidth receiver, since the larger bandwidth receiver does not filter the RZ signal as much, and the current peak of the "1"s is less attenuated. Therefore, a narrower electrical bandwidth should be used to minimize the crosstalk induced penalty from a RZ formatted signal. Regarding the different RZ formats, it can be seen that the highest OSNR penalty occurs at a different delay for the AMI38 case relatively to the other RZ formats. This is exclusively due to the different position of the optical pulses in the bit slot, at the output of the pulse

carver. Comparing different modulation formats, the largest OSNR penalty is quite similar for all of them. Although in the optical domain the narrower duty cycle formats have large peak powers, the electrical filter attenuates these differences. Again, for the larger bandwidth electrical receiver, these differences are more significant, and therefore, the larger duty cycle CS67 yields a lower penalty than the other formats.

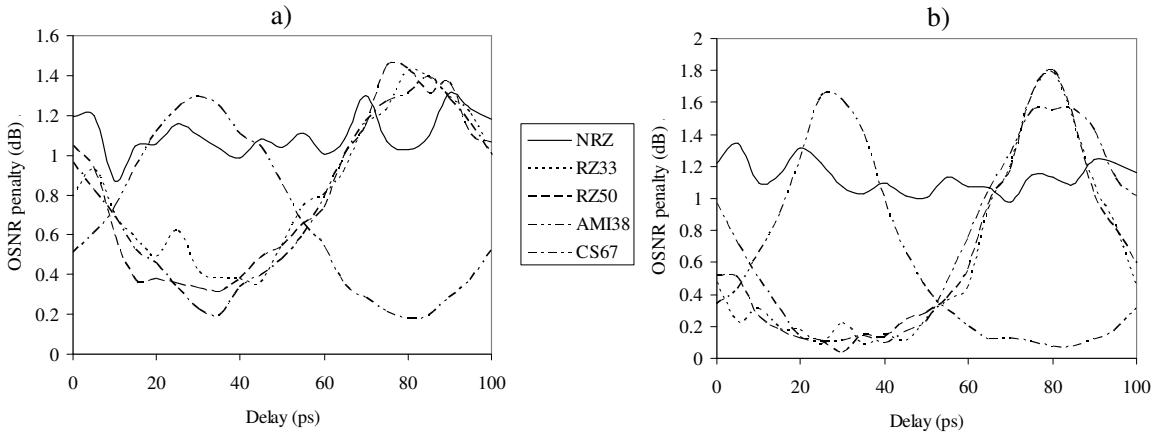

Fig. G.2 Crosstalk induced OSNR penalty on a NRZ caused by different modulation formats of the crosstalk signal, as a function of the bit delay between the signal and the crosstalk signal. a) 7 GHz bandwidth electrical receiver; b) 10 GHz bandwidth electrical receiver.

The delay between the signal and crosstalk signal that gives the worst OSNR penalty has now been determined, for the different modulation formats. The OSNR penalties calculated by simulation will now be compared to the OSNR penalties calculated by the MCB method, using a simulated eye diagram. However, at the time of the derivation of the MCB method it had been observed that the signal crosstalk beating is not so well characterized when the filters impact the crosstalk signals. This is precisely the case, since, for RZ formatted crosstalk signals, the electric filter will impact the signal shape. The crosstalk induced OSNR penalty for different crosstalk signal modulation formats as a function of the SXR, calculated by the semi-analytical simulation, is presented in Fig. G.3. For clearness, the corresponding MCB method results are plotted in a different figure, Fig. G.4.

Comparing the results obtained by the semi-analytical and MCB methods, it can be observed that the MCB method gives higher penalties than the semi-analytical method. For a SXR of 20 dB, the MCB penalties are about 0.3 dB higher than the semi-analytical penalties. This discrepancy is due to the approximate nature of the MCB method, and most

likely due to the inferior characterization of the signal-crosstalk beating term. Still, the MCB method correctly predicts that the NRZ crosstalk signal is the one that gives the lowest penalty, and the RZ33 is the format causing the highest penalty. The other RZ formats lie in between the previous, closer to the RZ33, since they are also RZ formatted.

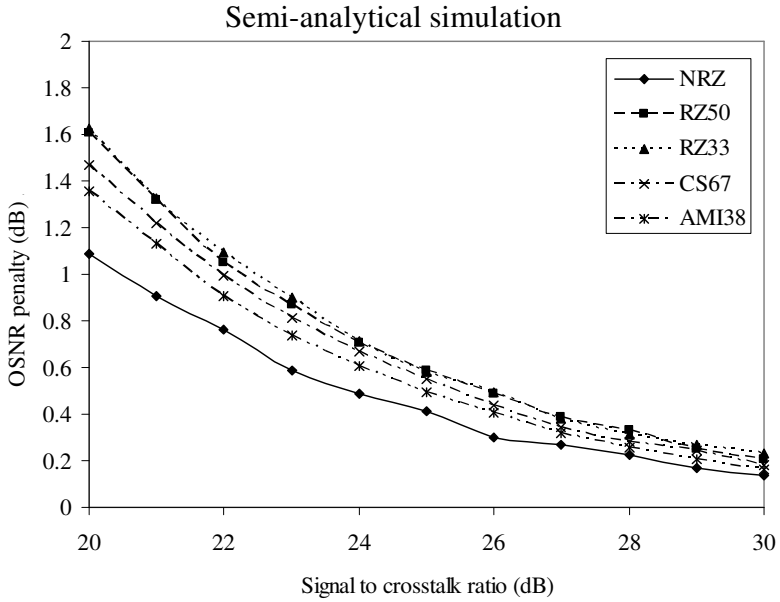

Fig. G.3 Crosstalk induced OSNR penalty as a function of the signal to crosstalk ratio, for different crosstalk signal modulation formats, calculated by semi-analytical simulation. The lines are guides for the eyes.

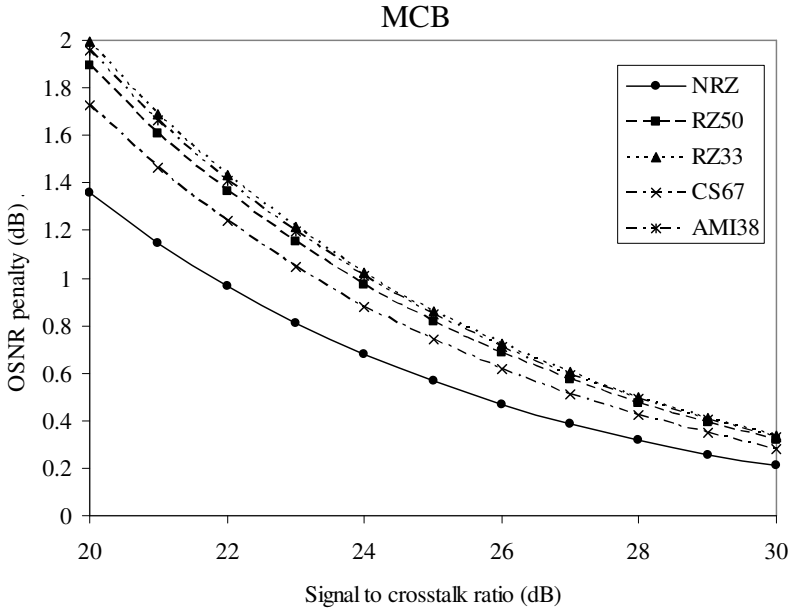

Fig. G.4 Crosstalk induced OSNR penalty as a function of the signal to crosstalk ratio, for different crosstalk signal modulation formats, calculated by the MCB method. The lines are guides for the eyes.

Appendix H. Comparison between crosstalk penalties between synchronized and unsynchronized signal and crosstalk signal

In real network conditions, the signal and the crosstalk signals are not synchronized, as it was considered in the results to determine the crosstalk impact in chapter 5. Therefore, in this appendix, the crosstalk induced OSNR penalty is assessed in the case where the crosstalk signal is synchronized to the signal, and in the case where the crosstalk signal and the signal are not synchronized, meaning that both signals have the same bit rate, but they are slowly drifting in time.

The simulation setup is similar to the one described in Appendix G, but the pulse carver is excluded. Therefore, both signal and crosstalk signal are NRZ. In each simulation run, the delay introduced by the VODL in the crosstalk path is varied randomly with a uniform distribution, so that two uncorrelated drifting signals are simulated.

The results of the simulation are presented in Fig. H.1. The crosstalk induced OSNR penalty was calculated as a function of the receiver optical filter bandwidth, for extinction ratios (ER) of 10 and 20 dB. Both synchronized and unsynchronized signal and crosstalk signal were considered. The synchronized penalties were obtained for the worst delay between signal and crosstalk signal, i.e., the delay resulting in the worst penalty, according to the results of Appendix G. The synchronized penalties are larger than in the unsynchronized case, but the difference in penalty is typically about 0.1 dB. This result agrees with the previous investigation of the dependence of the OSNR penalty on the delay between signal and crosstalk signal (Appendix G), where it had been shown that for the NRZ crosstalk signal the difference of the OSNR penalty between the worst and the best delay case is not very significant. As a conclusion, taking the case of worst delay between signal and crosstalk gives a slightly larger penalty than that considering time drifting between the signal and the crosstalk signal. Nevertheless, it is prudent to use the synchronized crosstalk penalty since, in a real network, the signals might be slowly drifting and the signal and crosstalk signal can have the worst delay for some periods of time, resulting in bursts of errors.

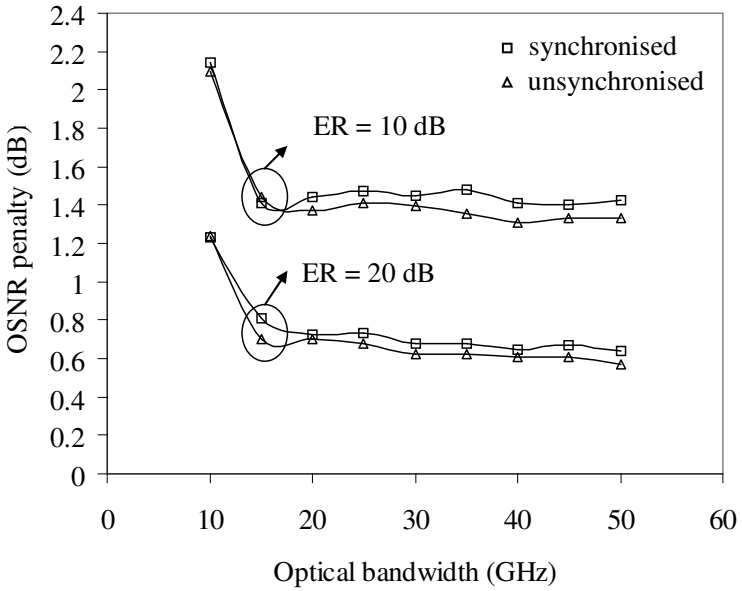

Fig. H.1 Crosstalk induced OSNR penalty as a function of the optical receiver bandwidth, for extinction ratios (ER) of 10 and 20 dB. Squares and triangles are for synchronized and unsynchronized signal and crosstalk signal, respectively. The lines are guides for the eyes.